Doctoral Dissertation
Doctoral Program in Energetics (35th Cycle)

An approach to building façade design to enhance acoustic and thermal comfort at the urban microscale

By

Elena Badino

******

Supervisors:
Prof. Arianna Astolfi
Prof. Valentina Serra
Prof. Louena Shtrepi

Doctoral Examination Committee:
Prof. C. Buratti, Referee/Examiner, University of Perugia
Prof. J. Kang, Referee/Examiner, University College London
Prof. M. C. Masoero, Examiner, Politecnico di Torino
Prof. A. Radicchi, Examiner, University of Siena
Dr. M. Zinzi, Examiner, ENEA

Politecnico di Torino
2023

Declaration

I hereby declare that, the contents and organization of this dissertation constitute my own original work and does not compromise in any way the rights of third parties, including those relating to the security of personal data.

Elena Badino
2023

* This dissertation is presented in partial fulfillment of the requirements for **Ph.D. degree** in the Graduate School of Politecnico di Torino (ScuDo).

Acknowledgments

I would like to thank my supervisors Profs. Louena Shtrepi, Valentina Serra and Arianna Astolfi for supporting me through this path. My deepest gratitude goes to those who have contributed the most to this work, Profs. Louena Shtrepi and Stefano Fantucci, whose precious guidance was essential for carrying out this research.

I would like to thank Henning Larsen. The visiting period there was one of the most enriching and motivating opportunities I had during my Ph.D., and I can't say how grateful I am for letting me stay in such a vibrant environment for a while. A special thanks to Jakob Strømann-Andersen, Mikkel Esrup Steenberg, Martha Lewis, Katrin Bindner, and to all the members of the sustainability team.

I am grateful to my colleagues for all the coffee, the sweets, the smiles, and the help (practical and not). Thanks also to the office mates that made this journey brighter: Andrea, Sonja, Cristina, Greta, Virginia, Giusi, and Farid. A special thanks goes to Giorgia Autretto, Manuela Baracani, Elisa Fenoglio, Giuseppina Puglisi, Gabriele Piccablotto, Giuseppe Vannelli, Alice Lorenzati, Fabrizio Bronuzzi, and all those who helped me through this journey.

I want to thank my friends and my family for the continuous support and empathy they showed me during these times. Many thanks to Marco for the support (and for the special risotto), and to the other Marco for keeping me grounded and for the never-ending podcasts from the other side of the ocean.

Abstract

Environmental noise pollution and heat stress threaten the health and well-being of the urban population. Under the challenges of increasing urbanization, urban heat island and climate change, the themes of outdoor thermal and acoustic comfort are gaining increasing research attention.

Both environmental noise levels and microclimatic conditions in urban open spaces are influenced by the morphological and material properties of the surrounding urban fabric. Therefore, architectural design, if properly conceived, can contribute to outdoor acoustic and thermal comfort in nearby urban areas. Among urban surfaces, building façades have the largest impact on thermal comfort in their surroundings and play a major role in the sound reflections occurring in urban areas. While in cities the urban fabric is often already fixed and there are limited chances to act on it, retrofit interventions of building façades are relatively common, making these elements strategic starting points to locally improve outdoor comfort and promote the well-being of the population. Nonetheless, the outdoor implications of façade design are generally overlooked, missing precious opportunities to enhance comfort conditions in urban areas.

The Ph.D. research activities aimed to shed light on some of the most relevant topics encompassing the improvement of acoustic and thermal comfort in outdoor urban spaces. The research work has investigated the methodologies that can be used to predict and optimize design proposals to improve outdoor acoustic and thermal comfort, with a focus on the role of building façades. The two themes have been addressed in parallel, ranging from the material scale to the urban microscale. The activities were mainly developed to support the definition of a methodological framework to address these topics from different standpoints, making use of laboratory and field measurements, and performance simulations.

An appropriate characterization of the material properties is essential to correctly set up the input data for performance simulations, whose outcome can

orient design processes, following the performance-based design approach. Part of the research has focused on the laboratory and in-situ characterization of innovative building envelope materials, with respect to acoustic and thermal properties. The reliability of performance simulation tools is crucial to inform design decisions in an efficient way. This aspect was investigated through a literature-based overview, and more in detail, through the comparison of simulated data with measured acquisitions in urban areas. In this framework, an evaluation of geometrical room acoustic tools i.e., Odeon ad Pachyderm, in an outdoor urban setting, and a validation study of the most well-known microclimatic simulation tool, i.e., ENVI-met, are presented. While good agreement between simulations and measurements was found for the use of room acoustic tools in an outdoor scenario, the evaluation of the microclimatic simulation program has highlighted some marked limitations in the tool's ability to correctly estimate microclimatic variables under extremely hot conditions, which may limit the reliability of the predictions. Finally, the practical application of performance simulation tools to orient design decisions was tested on both idealized scenarios and case-studies to explore the methodologies that can be followed, the complex interrelationship between the two aspects, and to highlight the potential benefits of the inclusion of outdoor comfort goals during design processes. The main contribution of this exploratory research work is to increase the knowledge on simulation approaches to estimate and improve outdoor thermal and acoustic comfort conditions by means of façade design choices, and on methodologies to assess the performance of innovative façade materials that are expected to influence, and potentially benefit, outdoor comfort conditions in their surroundings.

Contents

List of Figures

List of Tables

Chapter 1

Introduction

1.1. Overview and motivation

The improvement of acoustic and thermal comfort in outdoor urban areas is among the major challenges that cities are asked to face to protect public health and well-being in the framework of increasing urbanization and climate change. Moreover, enhanced outdoor comfort conditions can benefit indoor spaces. For example, low outdoor noise levels would allow exploiting natural ventilation without compromising on acoustic comfort, while improved outdoor microclimatic conditions can reduce the reliance on active systems to achieve indoor thermal comfort.

The research activity focuses on the themes of outdoor thermal and acoustic comfort and explores the methodologies that can be used to predict and optimize design proposals to improve comfort conditions in public and private open spaces (e.g., streets, squares, balconies and terraces). While architectural design choices, such as the form and material features of the buildings, can contribute to acoustic and thermal comfort in the surrounding of the design interventions, the performance consequences of design choices are often overlooked in practice, reducing the potential benefits of design interventions.

The contributions of building façades design to outdoor comfort conditions are the focus of the research activity. While the urban fabric is often already defined and there are limited opportunities to improve comfort conditions, retrofit interventions on building façades are relatively common in urban areas, making these elements strategic starting points to improve conditions in their surroundings. This research broadens the conventional conception of building façades, according to which they are only considered part of the envelope that modulates interior conditions based on exterior ones, by including the role played by them over outdoor conditions. The building façades are indeed seen as interfaces between indoor and outdoor environments, whose design can influence both conditions. In this frame, a multidisciplinary approach to façade design is endorsed to increase the designers' awareness and control of the proposals' implications on outdoor thermal and acoustic comfort and to allow to optimize the design proposal accordingly. A scheme illustrating the research theme is shown in Figure 1.

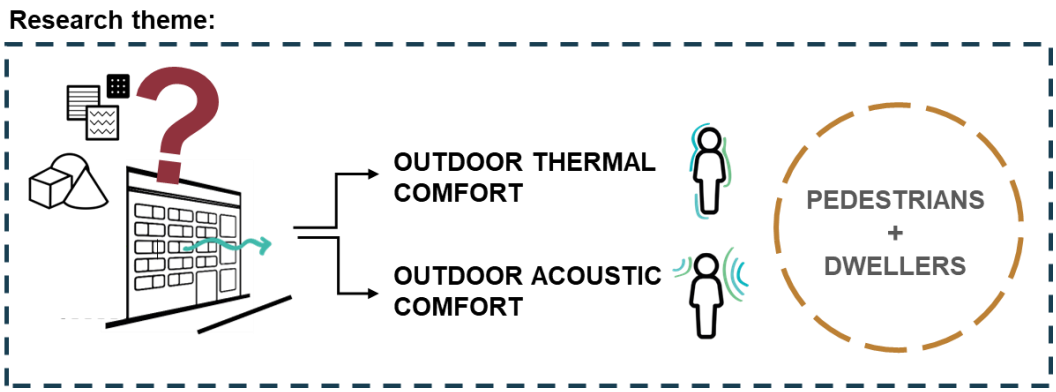

Figure 1. Scheme of the research theme.

The Ph.D. research work is exploratory in its character and covers different aspects of outdoor acoustic and thermal comfort, and of way façade design can be exploited to improve them in nearby areas. The research activities were mainly developed to support the definition of a methodological framework to address these topics from different standpoints.

The main goals of the research are the following:

a) the exploration of methodologies for the laboratory characterization and in-situ testing of innovative materials for building façades that can influence the surrounding acoustic and thermal conditions;
b) the identification of simulation tools able to provide useful performance feedback during the design processes to inform design decisions and their evaluation with respect to in-situ measurements;
c) the application of performance simulations to improve outdoor comfort conditions in different scenarios, ranging from idealized urban settings to actual design projects, to explore the potentialities of the proposed approach.

In this frame, a short-term visiting period spent at Henning Larsen in Copenhagen (Denmark) has allowed the testing of the research themes on some of the projects in development, used as case studies. This experience has contributed to a greater understanding of the multiple performance objectives and architectural goals to be combined in practice. This has helped to bridge the gap between the academic and professional realms, allowing to gain some insights into the practical implications of the Ph.D. research topics.

From the methodological point of view, the themes of acoustic and thermal comfort have been addressed in parallel during the research activities. The work has focused on different levels of details, ranging from the material scale to the urban microscale, and was carried out using laboratory and in-situ measurements, and performance simulations. The Ph.D. thesis has been articulated following the same scheme: it starts from the characterization of innovative materials for building envelope application and moves to a larger scale, at which in-situ measurements are conducted and performance simulations are used to support design decisions.

Appropriate characterization of the material properties is essential to correctly set up the input data for performance simulations, whose outcome can orient design processes, following the performance-based design approach. According to this method, performance simulation feedback is used to inform decision-making processes from the early design phases, allowing the designers to control and optimize the projects. The reliability of performance simulation tools is crucial to correctly predict the implications of different design alternatives and orient design decisions in an efficient way. This aspect was investigated through a literature-based overview, and more in detail, through the comparison of simulated data with in-situ measured acquisitions. This part was carried out for both acoustic and thermal realms, using two geometrical room acoustic tools in outdoor settings and evaluating the prediction of the most common microclimatic simulation tool under extreme heat.

Moreover, some practical applications are presented to illustrate how the simulation outcomes can be used to control and improve the final performance of the projects. The design applications were partly developed in the framework of the visiting period at Henning Larsen, where the candidate had the opportunity to use some of the projects developed by the architectural firm as case studies. To conclude, a parametric investigation is presented, to explore the effectiveness of green wall application in different urban settings, with respect to both outdoor acoustic and thermal comfort aspects, and evidence the complex interrelationship between the two performance goals.

The research activities, which are briefly summarized in the following section, have contributed to exploring some of the most relevant topics encompassing the improvement of acoustic and thermal comfort in outdoor urban spaces. The themes of the thesis are broad and have significant implications for life quality in present and future urban areas. This contribution presents an attempt to investigate several aspects revolving around outdoor acoustic and thermal comfort, considering different levels of details (from material scale to urban microscale) and using different approaches (literature reviews, measurement and simulations). While within the time constraints, the contributions could only be limited to specific aspects related to outdoor acoustic and thermal comfort, it will hopefully help paving the way to further research work on these themes.

1.2. Thesis outline

The Ph.D. research activity aimed to investigate the methodologies that can be implemented to improve outdoor thermal and acoustic comfort, with a focus on building façade design. The work includes the performance characterization of building envelope materials, review studies focusing on performance-based design approach and on the capability of performance simulation programs, validation studies to assess the reliability of simulation tools with respect to measured data, and presents some examples of design applications, where performance predictions were introduced as one of the major design drivers.

The themes of outdoor acoustic and thermal aspects are addressed in parallel in the thesis, which has been articulated in different chapters, starting from the material scale and moving up to the urban microscale. To better highlight the methodological approach followed, the chapters are named using A and B letters to distinguish between those related to the acoustic realm (A) and those focusing on thermal aspects (B). The thesis outline is schematized in Figure 2 and briefly summarized in the following. The correspondence between the thesis layout and research objectives previously introduced is evidenced by assigning the different Chapters with the colored squares identifying the different goals.

After the introduction, a brief overview of the themes of outdoor acoustic and thermal comfort is presented in **Chapter 2**. The objective of this part is to provide the reader with a short summary of the main issues associated with thermal stress and noise pollution and with a basic understanding of the design strategies, approaches, and simulation tools that can be used to improve outdoor comfort conditions, reporting also useful references to better frame the research topics.

Starting from the material scale, **Chapters 3A and 3B** focus on the acoustic and thermal characterization of innovative materials for the building envelope. A correct accounting of the material performance is indeed essential to understanding and predicting their effect when applied to the building envelope. Sound absorbing materials applied on the building envelope are among the most studied noise reduction strategies, while innovative materials with dynamic optical properties, such as thermochromic ones, have been proposed to reduce the building energy demand in climates where cooling and heating needs are balanced. Chapter 3A presents a study developed in collaboration with Cemex on the sound absorbing properties of porous concrete panels, which are among the few sound absorbing materials suitable for outdoor application. Chapter 3B proposes a methodology to investigate the dynamic behavior of thermochromic materials for building envelope application in the laboratory and in an outdoor test cell.

Starting from the following Chapters, the thesis moves to the urban microscale. **Chapter 4A** presents a review study on built projects developed with acoustic performance-based design (APBD). Despite its great potential, this approach still finds limited application in the acoustic realms. The research collects information on a series of built case studies developed with APBD to shed light on the methodology followed, and on the potentialities and limitations of the approach. Moving to thermal comfort aspects, a review of the mean radiant temperature models implemented in common simulation tools is reported in **Chapter 4B**. The mean radiant temperature is the most important environmental parameter influencing outdoor thermal comfort and reliable predictions of this variable are essential to correctly orient decision-making processes. Nonetheless, the simulation of mean radiant temperature in urban areas is challenging, and often marked simplifications are applied. The contribution aims to provide a preliminary understanding of the capabilities of the mean radiant temperature models implemented in different simulation tools, to shed light on the assumption and simplifications applied.

In order to better evaluate simulation tools, **Chapter 5A and 5B** compare the simulation results with in-situ measured acquisitions. In Chapter 5A the use of geometrical room acoustic simulation tools in outdoor settings is evaluated by comparing the sound pressure level predicted in different positions in a courtyard with the in-situ measured ones. Additionally, some design applications are presented, where the performance feedback of the simulation tools is used to guide the design process and improve the performance of the final design outcome. Among the case studies investigated is Wolfsburg Connect project, developed by the architectural studio Henning Larsen, whose analysis was carried out in the framework of a three-month visiting period spent by the candidate at the studio in Copenhagen, Denmark. With respect to microclimatic simulations, the prediction reliability of ENVI-met is evaluated in a validation study in Chapter 5B, with a specific focus on mean radiant temperature, air temperature, and the surface temperature of the urban facets. A measurement campaign was carried out under extreme hot weather conditions close to a south-oriented façade exhibiting a dark-colored appearance, to evidence the level of agreement between the measured and simulated data.

To conclude, **Chapter 6** presents a parametric investigation focusing on the effectiveness of green wall application to improve outdoor acoustic and thermal comfort. Simulation tools are used to predict the effect on outdoor acoustic and thermal comfort conditions of the application of green walls of the building façade according to different configurations in a set of idealized urban scenarios. The analysis is performed at the pedestrian level and over the façades, with the goal of providing guidance to identify the conditions in which such design strategy leads to the greatest improvement of comfort conditions, and evidence the interrelationship between acoustic comfort and thermal comfort goals in the tested scenarios.

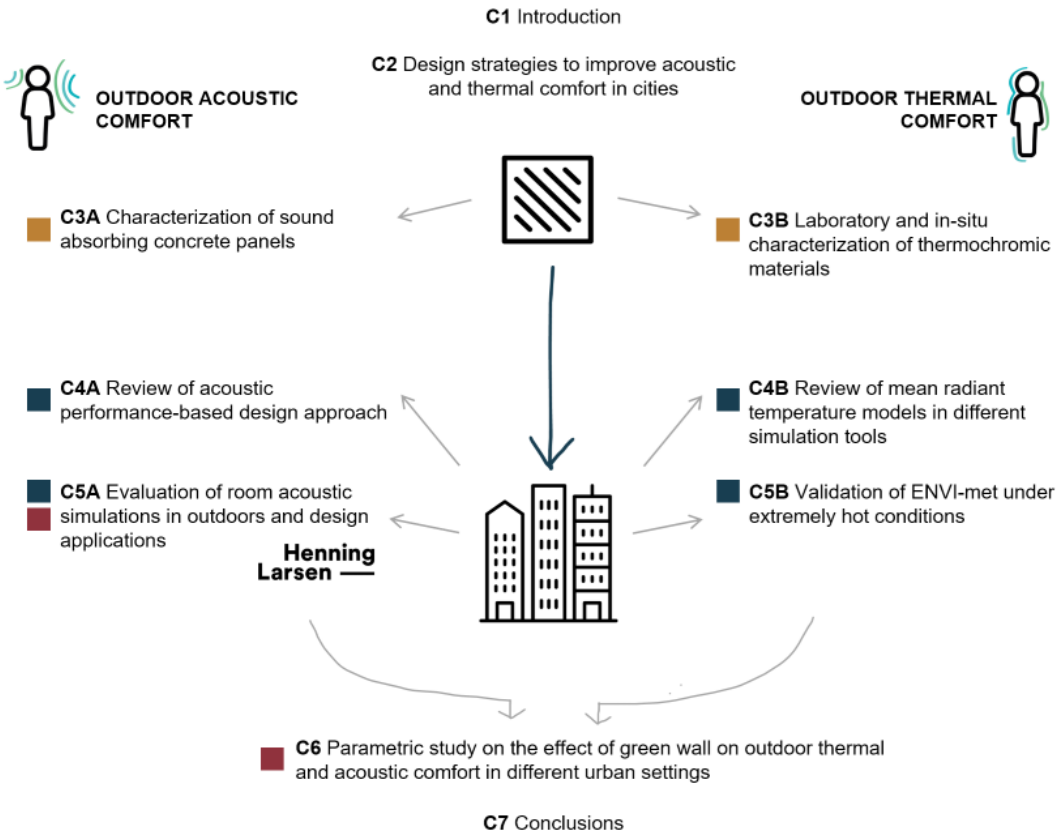

Figure 2. Scheme of the Ph.D. thesis outline.

Chapter 2

Outdoor thermal and acoustic comfort: a brief overview

Objective	To provide a general framework about the importance of outdoor thermal and acoustic comfort conditions in urban areas
Outcome	An overview of the main themes, on the design strategies and simulation approaches is presented
Highlights	• Improved outdoor acoustic and thermal comfort conditions help protecting public health. • Performance-aware design decisions, related to form and material properties of buildings, can benefits outdoor conditions. • Simulation tools can predict the design proposal' performance, allowing to optimize its features to improve the overall effectiveness of the design intervention.

2.1. Overview and motivation

By 2030, the world population is estimated to grow to 8.5 billion people, with 60% of the population living in urban areas [1,2]. Global climate change is projected to result in warmer air temperatures by day and night, more frequent or longer heat waves, changes in precipitation statistics, and in the intensity and/or duration of droughts and of high sea-level events [3,4]. The World Health Organization (WHO) estimates that heat will cause more than 90,000 additional deaths in 2030 and more than 250,000 in 2050 [5], and heat stress is listed among the causes of mortality. The Urban Heat Island (UHI) effect exacerbates the impact of global warming in cities, with increased risk of heat-related mortality [5–7], reduced workability and survivability [8], and increased energy demand and pollution [9–11]. The improvement of outdoor thermal comfort is therefore essential to protect public health. Additionally, since buildings operations and outdoor environments are thermodynamically looped, enhanced outdoor conditions may positively influence indoor ones, possibly leading to energy savings [10].

As evidenced by the WHO, the well-being of urban populations is also threatened by the increased health risks due to environmental noise pollution (e.g. cardiovascular disease, cognitive impairment in children, sleep disturbance, tinnitus and annoyance) [12]. In order to protect public health in cities, the WHO has suggested thresholds of outdoor sound pressure levels not to be exceeded in cities [12]. Moreover, low environmental noise levels would allow dwellers to stay comfortably indoors with open windows, exploiting natural ventilation [13,14]. This may also result in energy savings due to the reduced reliance on active systems to achieve indoor thermal comfort. The importance of this aspect has also been evidenced by the Acoustics, Ventilation and Overheating Guide [14], which endorses an integrated design approach, where acoustic requirements are combined with natural ventilation and thermal comfort in indoor spaces.

Under the challenges of increasing urbanization, population growth, UHI, and climate change, the research interest towards outdoor thermal and acoustic comfort in cities has increased [15–19].

Both environmental noise levels and outdoor thermal comfort in urban open spaces are influenced by the morphological and material properties of the surrounding urban fabric. The compact layout of urban environments and the sound reflective properties of common construction materials cause the environmental noise levels in cities to increase due to multiple sound reflections. At the same time, outdoor thermal comfort depends on the different microclimatic conditions within the urban canopy layer, which are influenced by both the geometric and material properties of the surrounding urban elements. Nonetheless, these aspects are generally not taken into account during design processes [20,21]. Since design decisions at the urban and building scales have long-lasting cumulative implications on the quality of outdoor spaces, performance-aware choices can enhance outdoor comfort and contribute to the protection of public health [22].

The design features of building façades can influence, and potentially benefit, both indoor and outdoor spaces. Nowadays, a large number of retrofit interventions on building façades are implemented to improve the energy efficiency of buildings.

These interventions, if properly conceived, have the potential to enable façades to work as public infrastructures and enhance comfort conditions in surrounding areas [21,23,24]. Among the urban surfaces, vertical ones have the largest impact over the thermal comfort perceived by pedestrians [25,26], and play a major role in the multiple sound reflections occurring in the urban environment [18]. Given the long-term implications of design decisions, the introduction of these aspects among the design goals would promote the well-being and health of the urban population.

A multidisciplinary design approach, in which relevant information on different performance goals is available to the designers since early design phases, would help maximizing the effectiveness of building façade design [27,28]. The use of simulation tools allows to predict performance aspects prior to construction to orient design decision making processes, following the performance-based design (PBD) approach. Addressing these aspects since the conceptual design phases is essential, as early design choices have the largest impact on the performance of the final design outcome and a reduced economic impact in comparison to late design modifications [29,30]. By providing adequate simulation tools to designers and consultants, it will be more feasible to integrate outdoor acoustics and thermal comfort objectives during design processes.

This Chapter presents a brief overview of outdoor thermal and acoustic comfort themes, in the attempt to frame the research activities carried out during the Ph.D. program. For more detailed information on these topics, the reader is referred to review studies and more comprehensive works reported in the references. For instance, as concerns thermal aspects, the themes of urban microclimate, UHI and thermal comfort are extensively described in [3]. An overview of the differences between indoor and outdoor thermal comfort assessment is in [31], the outdoor thermal comfort indices are summarized and described in [32], and a literature review on the comfort ranges of the indices based on subjective responses is presented in [33]. With respect to acoustics, a general overview of sound absorption and sound diffusive materials and phenomena is in [34], while design strategies to mitigate environmental noise are collected in general terms in [35,36], and with a specific focus on building envelope in [17,18].

2.1.1. A brief introduction to outdoor thermal comfort

Enhanced outdoor thermal comfort in cities would promote the well-being of the urban population, and also increase the attractiveness and the fruition of open spaces [5,15,37–39]. Thermal comfort is defined as “the state of mind, which expresses satisfaction with the thermal environment” [40]. While indoor comfort conditions have been extensively studied, little attention towards outdoor one was reported until the early 2000s, and since then it has gained increasing research interest [33,41].

The assessment of human thermal perception in outdoor environments is more challenging than in indoor spaces, given the rapid variability of the environment (e.g., wind speed, solar radiation) and the duration of exposure (from minutes to hours). Moreover, the activities of those in the outdoors, their demographic characteristics

and their clothing decision are very diverse with respect to indoor conditions. On the other hand, their expectations are far less stringent [3].

The assessment of outdoor thermal comfort is dynamic, i.e., involves adaptation, and subjective [38]. The human body can adapt to the thermal environment through physical, physiological and psychological adaptation mechanisms [42]. According to the physiological approach [43], people are considered comfortable when the heat flow of the human body is in balance, the core and skin temperature, and the sweat rate are within comfort range [31,32]. All these variables are related to a set of environmental parameters (i.e., air temperature, mean radiant temperature, wind speed, and humidity) and personal ones (i.e., body metabolism and clothing level). The mean radiant temperature, which quantifies shortwave and longwave radiative exchanges, is considered the most relevant environmental parameter affecting outdoor thermal comfort [26].

The exposure time to the outdoor environment influences the human ability to acclimatize. According to [31], under hot conditions, the human body reaches steady state levels in shorter time, while the time needed in cold conditions is much longer. This highlights the need for non-steady state models to quantify outdoor thermal comfort [44]. A series of thermal indices have been developed on the basis of outdoor human comfort models describing the human body energy balance. The latter is defined considering the interrelation between the previously described personal and environmental parameters. The outdoor thermal comfort indices are all based on steady-state assumption, and are therefore suitable to situations when people stay outdoors for a sufficiently long time [31]. While a more than 165 indices has been developed and used to assess thermal comfort conditions in outdoor spaces, only four of them are widely used in practice, i.e., PET (Physiological Equivalent Temperature), UTCI (Universal Thermal Climate Index), PMV (Predicted Mean Vote) and SET* (New Standard Effective Temperature) [33]. PET is the most widespread index and describes the environment to which the human body is exposed in terms of the air temperature that would be required in reference conditions to produce the same thermal response in the human body [45].

Despite a number of different factors are involved, the environmental stimulus is the most important factor affecting the thermal sensation of people [38]. From the perspective of human health and well-being, the most relevant conditions are those within the urban canopy layer, where the ambient environment is dynamic and highly variable over very short distances [3].

Several simulation programs can simulate the microclimatic conditions in a given environment and quantify outdoor thermal comfort consequently. These tools can be used to predict the effect of the form and material features of the built environment on the thermal comfort conditions, allowing the designers to be aware on the implications of the project on the perceived thermal sensation. Among the currently available simulation tools, ENVI-met can be considered the most well-known one; nonetheless other programs, such as Ladybug Tools, RayMan, and SOLWEIG, can be used to support design decisions.

Several studies have suggested design solutions able to enhance thermal comfort in outdoor urban spaces, considering the geometrical and material features of urban

fabrics, the use of vegetation and water bodies. However, in general, outdoor thermal comfort issues should be considered at the earlies opportunities, since once the main urban features are fixed, the opportunities to improve thermal conditions are limited.

The design solutions to reduce heat stress mitigate some of the environmental parameters affecting thermal comfort. For example, they may reduce the radiation to which the human body is exposed, lower the air temperature, or promote wind, by exploiting different mechanisms, such as shading, evaporative cooling, by reducing the emission of longwave radiation, or through specific urban layouts. Comprehensive reviews of these mitigation strategies can be found in [15,46], while a literature review on materials to counteract UHI is presented in [47]. While the microclimatic implications of horizontal surfaces, such as roofs and paving, have been object of several researches [48–52], little attention has been given so far to those of vertical surfaces, such as building façades [21,53–60].

With respect to material features, the application of “cool” materials with high solar reflectance (also named “high albedo” materials) on building envelopes and urban surfaces was advanced [48,51]. Thanks to their high solar (i.e., shortwave) reflectance and high infrared (i.e., longwave) emittance, these materials maintain lower surface temperatures with respect to conventional ones. Since visible light is included in the shortwave range, typically materials with high solar reflectance present a light-colored appearance; vice-versa low solar reflectance properties are associated to a dark color. However, solar reflective non-white surfaces are also available, exhibiting a reflective behavior limited to the near infrared (NIR) range [57]. “Cool” materials with high solar reflectance are used to reduce building energy demand for cooling and to mitigate UHI. The lower surface temperature of these materials results in less heat transferred to the building interior, in a reduced amount of heat exchanged with the air, and in lower longwave radiation emitted by the surface. Recent studies have investigated the impact of these materials on outdoor thermal comfort conditions. Different simulation studies have suggested that the resulting increase in reflected solar radiation may offset the reduction of emitted longwave radiation and thus increase thermal discomfort in urban open spaces [25,57,61]. The same outcome was found by some measurement studies [62,63]. Other innovative solutions for outdoor application are the “dynamic” materials, such as thermochromic ones [64,65], that are able to reversibly switch their optical properties in response to changing surface temperatures. Their application to the building envelope can reduce the energy demand of building for both cooling and heating throughout the year in climates where these needs are balanced.

Despite the variety of design strategies presented in [15,46], designers and consultants generally deal with design projects located in already built contexts, offering relatively limited opportunities to improve the microclimatic conditions [3]. In urban environments, the urban fabric is already defined, and it is possible to act at a localized scale, for instance by altering materials, and introducing vegetation or shading elements.

2.1.2. A brief introduction to outdoor acoustic comfort

The compact urban layouts of contemporary cities lead to the uprising of problems such as environmental noise pollution [66,67]. This issue constitutes a relevant and widespread cause of disturbance, with considerable effects on human health and well-being [68–70].

Environmental noise is generated by different sources related to human activities [71], among which road traffic is generally the most relevant one in the urban areas [72,73]. Other relevant noise sources are railway noise, aircraft noise and, in certain circumstances, also leisure noise. Leisure noise can be generated by the presence of people talking in the urban open spaces, and can be the most significant noise sources in certain areas, such as touristic or nightlife ones [73–76].

Environmental noise is often quantified using the A-weighted sound pressure level in outdoor positions, that quantify the frequency-dependent noise intensity perceived by human ear in a given location in space. Typically, improved acoustic comfort conditions are associated to lower environmental noise levels. Nonetheless acoustic comfort can be assessed using other acoustic parameters (e.g., clarity, definition, speech transmission index) [77], through perceptive evaluations [77–80] or soundscape approach, which focuses on the perception of sound environment in a given context using an interdisciplinary approach [18,81–83]. While several tools are available to predict the outdoor propagation of environmental noise (e.g., SoundPLAN, CadnaA), the effect of localized form or material changes can hardly be predicted by them. In this frame the employment of room acoustic simulation tools (e.g., Odeon, CATT-Acoustic, Pachyderm) in outdoor settings can be useful tools to estimate the effect of form or material changes at a detailed level and orient design decisions accordingly.

In urban environments, noise levels are enhanced by the multiple sound reflections occurring on the surrounding surfaces, and primarily on façades. Therefore, façade design, if properly conceived, is expected to promote acoustic comfort in urban environments [18,84]. Nonetheless, little attention has been given so far to the role played by these building elements in noise propagation in cities [18,85]. In general terms, the most effective noise mitigation approach is to reduce the noise emission at the source level, for example by using quieter car engines, by applying low-noise asphalt whose porous texture can reduce the rolling noise of cars, or by lowering speed limits. Nonetheless, these approaches are often difficult to implement in practice for several reasons (e.g., economic, political, city planning), and other strategies focusing on the propagation path to receiver positions are needed.

Beyond the noise mitigation strategies related to building façades, briefly presented in the following, are the use of tree belts and noise barriers and several others, including soundscape approaches (e.g., noise masking, the introduction of wanted sounds). Overviews of urban design strategies to mitigate environmental noise levels are presented in [35,36].

Dense urban environments, such as street canyons and courtyards, are reverberant spaces with multi-path sound propagation, in which the direct sound is enhanced by the sound energy reflected on the building fronts, that increase the sound pressure level [86,87]. Sound absorption and diffusion [34] can be exploited

to reduce the noise level in cities. Differently from sound reflective materials, when sound energy strikes a sound absorbing surface, part of its energy is lost and a relatively low fraction of the incident energy is reflected back in the space, contributing to a reduction in sound pressure level. Sound diffusing materials are able to reflect the incident energy in non-specular way, i.e., in a diffuse fashion, potentially promoting the redirection of the energy towards the sky, exiting the urban environment [88–92]. The role of diffuse reflections in urban canyons has been investigated in [89,93–95], which reported noticeable noise reductions at great distances from the sound source. However, building façades typically present low diffusion values [96]. The application of sound absorbing materials to reduce noise levels in cities is among the most investigated strategies [18]. Although in general sound absorbing materials are intended for indoor spaces, sound absorbing solutions suitable for outdoor applications have started appearing on the market (e.g., porous concrete, perforated panels). Similarly, vegetated surfaces such as green walls and roofs can exhibit excellent sound absorption performance, and therefore can be considered effective noise mitigation strategies for outdoor application.

A number of researches have shown that different shapes and cladding materials of a façade can greatly reduce the sound pressure level over the façade itself, by measurements [97–104] and performance simulations [80,88,97,102–107]. The main findings of the studies related to façade design features to reduce environmental noise have been collected by the reviews presented in [17,18]. Previous studies have investigated the potential of the geometrical and material features of façades [88,107–111] as environmental noise reduction strategies. The shielding effect provided by balconies over the façade was studied in [88,100,107,112], as well as the effect of different balcony depths, and of the inclination of the parapets and of the inferior surfaces of the balconies [88,97,102,106]. These studies highlight that the shielding effect provided by the balconies is compromised by sound reflections occurring over the inferior surfaces of the upper balconies, and this occurs mainly at the lowest floors [97,100,112]. The benefits of the application of sound absorbing materials to the façade have been reported in many studies, such as in [80,88,101,102,107].

Despite the growing awareness on the health impact noise pollution and the increased research effort towards the identification of mitigation strategies, the acoustic consequences of architectural and urban design are generally overlooked in practice [20,88,113].

Chapter 3A

The performance of concrete-based acoustic panels

Objective	To systematically investigate the effects of concrete mix design, sample thickness, and mounting conditions on the sound absorption properties of porous concrete panels in a scaled reverberation room
Outcome	Based on the testing of 30 panels configurations, the effect of the mix design, panel thickness and mounting conditions on the sound absorption coefficient could be assessed to highlight the most promising strategies
Highlights	• Concrete mix design D, with round lightweight aggregate of 0.5-1 mm, is the most effective sound absorbing option. • In most cases, solutions with single panels or double layered panels of an equivalent thickness provide similar performance. • The mounting method is shown to greatly influence the sound absorbing performance.

3A.1. Overview and motivation

Sound absorbers and sound diffusers are generally used to control the acoustic performance of architectural spaces. While sound absorbers have been extensively studied within the research community, significant knowledge regarding sound diffusers has been developed only over the past 40 years [34]. While sound absorbers reduce of the amount of energy which is reflected back to the main ambient after being stroke by the soundwaves, sound diffusers are used to control the spatial and temporal dispersion of the reflected energy. Sound absorbers are generally used to prevent undesired phenomena such as echoes, by reducing the amount of reflected sound energy, and to reduce reverberation and sound pressure level. Differently, sound diffusers are used when the conservation of the sound energy within the room is essential, but there is the need to control or randomize the direction of the reflected sound energy [34]. Although the use of sound absorbers and diffusers have been traditionally associated to indoor spaces, outdoor application of such materials has started being explored in the recent years, particularly in the attempt to mitigate noise pollution in urban environments. In this framework, the development of wear-resistant sound absorbers and sound diffusers, which are suitable for outdoor applications, is gaining increasing attention.

Indeed, both sound absorbing and diffusing strategies can help improving outdoor acoustic comfort in cities [17,18], either by dampening the sound energy being reflected by urban facets or by promoting the diffusion of reflected energy, to redirect part of it out outside of the urban fabric or to prevent echoes.

This Chapter focuses on the performance characterization of concrete-based sound absorbing panels, reporting the outcomes of a research project held in collaboration with Cemex Research Group AG (referred to as "Cemex" in the following sections). The mentioned characterization study was carried out in a scaled reverberation room, considering different porous concrete panels and mounting conditions (§ 3A.2). Additionally, sound diffusive surfaces are briefly introduced, with a short presentation of the random incidence scattering coefficient, and by reporting some preliminary guidelines for the design of sound diffusive surfaces (§ 3A.3).

The content of Section 3A.2 has been published in the journal article *"More Than Just Concrete: Acoustically Efficient Porous Concrete with Different Aggregate Shape and Gradation"* [114] and in the contribution *"Acoustically efficient concrete: acoustic absorption coefficient of porous concrete with different aggregate size"* presented at Forum Acusticum 2020 e-conference [115], both authored by Louena Shtrepi, Arianna Astolfi, Elena Badino, Giovanni Volpatti and Davide Zampini.

3A.2. The sound absorbing performance of porous concrete panels with different concrete mixtures and mounting methods

Given the noise reduction potential of the application of sound absorbing materials on urban facets, such as building façades [17,18], the development of broadband sound absorbers solution suitable for outdoor application can promote their introduction in practice. Most commercial sound absorbing materials are intended to acoustically treat indoor spaces and are not suitable for outdoor application, where appropriate mechanical properties and resistance to the weather elements are required. While some sound absorbing materials for outdoor applications are available, they are often intended for noise barrier application and exhibit a visual appearance that often doesn't meet the aesthetic requirements for architectural design projects. In this frame, porous concrete panels can be considered a promising solution for outdoor application as they can offer wear resistance and broadband sound absorbing performance combined to a neutral visual appearance. The research project reported in this Section focuses on the characterization of the sound absorbing performance of porous concrete panels developed by Cemex. The panels, manufactured with different concrete mixtures and different thicknesses, are tested considering either single-layer and multiple-layers panel combinations, as well as different mounting conditions, i.e., panels directly laid against a solid backing or with an air gap at the back, either empty or filled with rock wool. The outcome of this research may provide useful insights on strategies to increase the sound absorbing performance of concrete based porous concrete panels, to further improve their noise reduction potential. Moreover, the systematic investigation on the influence of thickness, layers and mounting conditions can provide useful insights for the testing of other types of innovative porous sound absorbing materials, such 3D printed ones [116,117] or sustainable solutions, as those developed using waste materials [118–121].

3A.2.1. Introduction

The implementation of noise control strategies in outdoor environments is a challenging task for several professionals and an increasing number of studies highlight the importance of the architectural design on urban noise mitigation in canyon streets [107,122] squares [78] and inner yards [80]. A detailed overview of the acoustic strategies used for the building envelope design in order to improve the urban acoustic environment is given in [17]. These studies have pointed out the need for sound absorbing and scattering materials suitable for outdoor environments. Moreover, several indoor spaces such as airports, train stations, schools etc. are characterized by requirements similar to those of outdoor spaces regarding highly durable and resistant acoustic materials. Therefore, this work aims to investigate the sound absorbing properties of porous concrete of different mix design, thicknesses and mounting conditions, as this material results suitable for outdoor and indoor applications. Compared to other porous sound absorbers, porous concrete has the

capability to withstand the atmospheric elements and therefore it is suitable for applications in outdoor and indoor environments when resistance, low deformability and high durability are required.

Porous absorbers are the most widespread type of sound absorbers. According to their microstructure, porous absorbers can be further classified into granular, cellular and fibrous [34,123]. In porous absorber sound propagation occurs in a network of interconnected pores in which the sound energy is dissipated into heat through viscous and thermal effects. In order to provide effective sound absorption, porous materials must feature an open pore structure on its surfaces, and interconnected networks of pores. This enables the impinging sounds to enter the panel and propagate through it, dissipating energy. In particular, the primary mechanism is viscous boundary layer effect occurring in sub-millimeter air layers adjacent to the pore walls, while part of the energy is also lost due to thermal conduction [34]. On the contrary, isolated pores, i.e., those that are not connected to other pores, do not contribute to the sound absorbing properties of the material. The most fundamental properties of porous materials influencing their sound absorbing properties are flow resistivity and porosity and secondarily, pore shape factor and tortuosity [34].

Conventional concrete is generally characterized by poor sound absorbing properties, as the prevailing phenomena occurring are sound reflections. In general, normal concrete has an absorption coefficient value of 0.05-0.10 [124]. However, porous concrete has the capability to work as a porous sound absorbing material as it is characterized by high porosity, i.e., open pore structure on its surface and an interconnected network of pores. It is also known as pervious, gap-graded, permeable or enhanced porosity concrete [125] and is currently widely used in urban environments as paving material to support environmentally sustainable rainwater management [126]. It has been exploited also for its acoustic absorbing properties in traffic noise barriers and railway noise reduction [118,127,128]. Pervious concrete mainly consists of normal Portland cement, coarse aggregates (aggregate dimension greater than 5mm) and water, which generate a void content that generally ranges from 15% to 35% [126,129–131].

Pervious concrete acoustic panels belong to the class of granular sound absorbers with pores created by the presence solid aggregates which are bonded together by a cementitious binder. The key factor to allow sound absorption to occur is the accurate definition of the quantity of binder to ensure that there is enough binder to keep the aggregate together without clogging the pore network and still allow for an appropriate resistance for its use and handling. Overall, the sound absorbing properties of granular materials tend to be uneven in frequency and to be characterized by peaks [132].

Different strategies have been proposed with the intent to improve the sound absorbing properties, i.e. with the aim to enhance the rate and the evenness of the sound absorption provided, by altering the microstructural properties of the pervious concrete. As concerns the aggregates, several studies have investigated the effect of using aggregate material of various nature (cenospheres, crumb rubber, recycled aggregates, bottom ash, expanded perlite, plant particles, etc.) [118,127,128,133–

140], of varying the aggregate size and of using different aggregates types by blending or combining them in multiple layers [118,127,141,142]. Other researches focused on the effect of the addition of fiber content, chemical admixtures, and the influence of varying the values of indices used to describe the overall composition (Water/Cement ratio, void content, paste flow, compaction index). The addition of fibers in the mixture has been proposed in [127,142,143] to promote absorption by splitting bigger pores into smaller ones. Other studies [142,144] analyzed the increases in sound absorption resulting from the addition of aluminum powder, air entraining admixtures and foam agents to the concrete matrix. Finally, the variations of the acoustic properties of the pervious concrete mixture, described by indices such as W/C ratio, void ratio, paste volume, cement flow have been assessed [127,128,134,135,142,144]. It should be noted that these strategies applied to the mix design aim to vary the fundamental properties i.e. flow resistivity, porosity, pore shape factor and tortuosity, which control the absorbing performance. Therefore, it is important to adequately control the void ratio and aggregate type, which influence tortuosity and flow resistivity [145], pore size and pore aperture size, which are used to control porosity [124]. Moreover, as for all the acoustic porous materials also the thickness of the porous layer results important for the acoustic absorption coefficient spectra. The principal maximum peak of the absorption coefficient is displaced to lower frequencies when the thickness increases [118,141,145]. However, there is a threshold regarding the thickness of granular materials above which the absorption does not increase further [34]. A comprehensive review of the strategies that have been proposed to enhance the sound absorbing performance of concrete has been recently presented in [132].

Objectives of the study

Some design guidelines for sound absorbing concrete emerging from the past research works have been adopted in this research regarding the aggregate shape and size. The present study aims to investigate through a systematic research approach the effects of concrete mix design (four different conditions), sample thickness (three different conditions), and mounting conditions (three different conditions) on the absorption properties of porous concrete tested in a small-scale reverberation room (SSRR). Therefore, the main aim of this study is to define the sample configuration that could lead to an increase of the sound absorption properties of concrete panels. More than 30 different combinations of the afore-mentioned variables have been considered.

This work aims to increase awareness on the porous concrete properties among several professionals such as architect, designers, acousticians, policy makers, etc. that deal with noise control strategies in outdoor and indoor environments.

3A.2.2. Materials and Methods

The research has been organized through the following steps:

1) Selection of different concrete mix design and preparation of samples for the measurements;
2) Selection of different mounting methods;
3) Measurement of the frequency dependent sound absorption α in the SSRR;
4) Computation of the weighted sound absorption coefficients as single index α_w and comparisons.

Tested concretes

Information regarding the porous concrete types, identified with the letter A, B, C, D, are summarized in Table 1. The selected concrete types A, B and C can be considered representative of different concrete mixtures of common usage, while concrete type D was manufactured in the attempt to combine the lightweight and void ratio properties with reduced aggregate dimensions. Two different types of aggregates have been used in the mix design, that is normal weight and lightweight. The normal weight aggregates have been used in concrete type A and have an irregular shape with an average dimension of 4-8 mm, while the lightweight aggregates have an almost perfect round shape, i.e., spherical, with different dimensions ranging between 4-8 mm, 2-4 mm and 0.5-1 mm for concretes B, C, and D, respectively. Pictures of the samples and details of the aggregate shape can be visualized in Figure 3.

Table 1. Four mix design of porous concrete.

Concrete type	Aggr. Typology	Aggr. Size [mm]	Aggr. Particle Density [kg/m^3]	Void Ratio [%]	Flexural Strength [MPa]	Pervious Concrete Density [kg/m^3]	Water Permeability [mm/s]
A	crushed normal weight	4-8	2650±30	25±2	3.5±0.5	1955±20	9.5±1.1
B	round lightweight	4-8	905±85	25±3	1.5±0.3	932±35	10.9±1.7
C	round lightweight	2-4	325±35	25±2	1±0.2	514±20	7.4±0.9
D	round lightweight	0.5-1	510±70	20±2	0.5±0.1	682±15	3.6±0.5

Figure 3. Sample A: crushed normal weight aggregates 4-8 mm; Sample B: round lightweight aggregates 4-8 mm; Sample C: round lightweight aggregates 2-4 mm; Sample D: round lightweight aggregates 0.5-1 mm.

Concretes A differs significantly from the other three regarding the concrete density value, which is strongly affected by the higher values of the aggregate particle density. The four concretes present a similar void ratio. However, while this parameter is constant for concretes A, B and C, it decreases for concrete type D, which features smaller aggregates. It can also be noticed that there is a decrease in the flexural strength for lower densities and smaller aggregate dimensions.

For each concrete, three different sample types have been manufactured with three different thicknesses, i.e., 20 mm, 40 mm and 60 mm (Figure 3); for each of them, three samples have been produced. The panels are square shaped in plan with a side dimension of 60 cm. Three different mounting conditions were tested for the samples with a thicknesses of 20 and 40 mm, that is, coupling different samples in multiple layers (Figure 4), adding a 50 mm air gap between the sample and the room floor (Figure 5), and adding a layer of fibrous material (rock wool) in the air gap itself (Figure 6). The identification codes of the samples and mounting conditions have been summarized in Table 2. The coupling of different samples in multiple layers has been performed only within the same concrete in order to compare their performance with single layers of the same thickness and investigate any anisotropy at the back surface of each layer. The multiple layers configuration is obtained by superimposing one panel to the other, with no joint or glue connecting them. This mounting solution could be practically useful when modular solutions are explored and would limit the need for different formwork thicknesses. The introduction of a rock wool layer in the air gap has been tested with sample D of 20 mm thickness only since it resulted in the highest sound absorption performance compared to the 20 mm samples of A, B and C concretes. In this case, two thicknesses of the rock wool layer, that is, 30 and 50 mm have been introduced in the air gap.

The assessment of the sound absorbing performance has been conducted in the small-scale reverberation room (SSRR) of Politecnico di Torino (Italy), following the procedure indicated in the ISO 354 Standard [146]. The reliability of the measurement was tested with respect to reproducibility and repeatability, by repeating the measures three times on three different samples of the same typology and considering their arithmetic mean to describe the performance of each type. The sound absorbing properties are expressed as 1/3 octave band sound absorption coefficients (α) and also as weighted sound absorption coefficients (α_w) for an easier comparison.

Figure 4. Multiple layers of 20+20 mm and 20+40 mm. Sample A: crushed normal weight aggregates 4-8 mm; Sample B: round lightweight aggregates 4-8 mm; Sample C: round lightweight aggregates 2-4 mm; Sample D: round lightweight aggregates 0.5-1 mm.

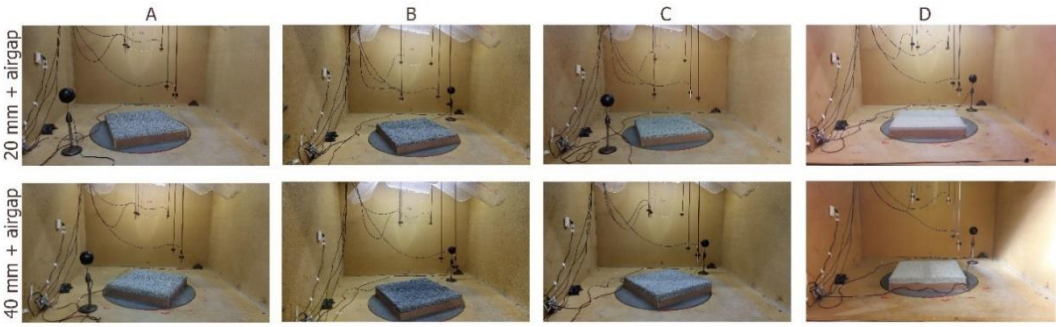

Figure 5. Mounting on 50 mm air gap. Sample A: crushed normal weight aggregates 4-8 mm; Sample B: round lightweight aggregates 4-8 mm; Sample C: round lightweight aggregates 2-4 mm; Sample D: round lightweight aggregates 0.5-1 mm.

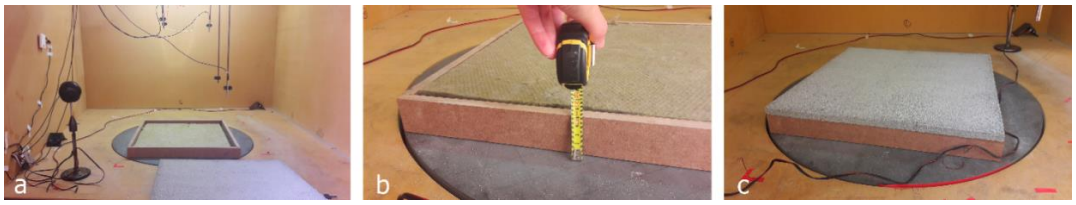

Figure 6. a) 30 mm and b) 50 mm rock wool filling 50 mm air gap. c) Sample D of 20 mm over one of the two conditions.

Table 2. Summary of the tested samples and configurations of the porous concrete. Single layers have been tested in configurations of multiple layers, with air gap and with rock wool in the airgap (+ tested and -untested configurations of single layers).

Concrete Type	Overall thickness [mm]	Layer thickness [mm]		Air gap 50 mm	Rock wool thickness [mm]
		Single layer	Multiple layers		
A	20	20		+	-
	40	40	20+20	+	-
	60	60	20+40	-	-
B	20	20		+	-
	40	40	20+20	+	-
	60	60	20+40	-	-
C	20	20		+	-
	40	40	20+20	+	-
	60	60	20+40	-	-
D	20	20		+	-
					30
					50
	40	40	20+20	+	-
	60	60	20+40	-	-

Sound absorption coefficient measurements

The small-scale reverberation room (Figure 3 to Figure 6) is installed in the Applied Acoustics laboratory at DENERG (Department of Energy, Politecnico di Torino, Italy). The room has been primarily built for random-incidence scattering coefficient measurements according to ISO 17497-1 [147], but is also suitable for measurement of sound absorption coefficient according to the ISO 354 [146,148,149]. It is an oblique angled room with pairs of nonparallel walls with a volume of 2.86 m^3 and a total area of 12.12 m^2. A more detailed description of the room construction has been provided in Shtrepi and Prato [149].

The measurement procedure consists in using the integrated impulse response method [146] for simultaneous measurements on six different microphone positions in two conditions, i.e. with and without the sample inside the room. The measurement chain consists of six 1/4" BSWA Tech MPA451 microphones and ICP104 (BSWA Technology Co., Ltd., Beijing, China); two ITA High-Frequency Dodecahedron

Loudspeakers with their specific ITA power amplifiers (ITA-RWTH, Aachen, Germany) and a sound card Roland Octa-Capture UA-1010 (Roland Corporation, Japan). This set-up allows to perform 12 measurements, which refer to the minimum number required by ISO 354:2003 [146]. The software used for the measurements, i.e. sound generation, recording and signal processing, is MATLAB combined with the functions of the ITA-Toolbox (an opensource toolbox by RWTH-Aachen, Germany) [150].

For each of the 12 measurements the reverberation time relative to a 20 dB decay, i.e., T_{20}, is evaluated and used to estimate the T_{60}, i.e. the reverberation time occurring for a 60 dB decay, as done in the full scale reverberation room (FSRR) data processing. The data are spatially averaged with the ensemble averaging method in order to obtain the reverberation times T_1 and T_2, which are obtained without and with the sample inside the room, respectively. Equations (1) and (2) are applied to estimate the random-incidence absorption coefficient α.

The difference between T_1 and T_2 measurements is used to calculate the variation of the equivalent sound absorption area A_T [m^2] based on Sabine's theory, according to Equation (1) :

$$A_T = 55.3V\left(\frac{1}{c_2 T_2} - \frac{1}{c_1 T_1}\right) - 4V(m_2 - m_1) \quad (1)$$

where T_1 and T_2 [s] are the reverberation times of the empty reverberation room and of the reverberation room with the test specimen, respectively; V [m^3] is the volume of the empty reverberation room; c_1 and c_2 [m/s] is the propagation speed of sound in air in the room without and with the sample: c_1 = 331 + 0,6 t_1, t_1 [°C] is the air temperature; m_1 and m_2 [m^{-1}] is the power attenuation coefficient of the climatic conditions in the reverberation room without and with the sample (calculated according to ISO 9613-1 [151].

The random-incidence absorption coefficient α is defined following Equation (2):

$$\alpha = \frac{A_T}{S} \quad (2)$$

where S [m^2] is the area covered by the test sample. It should be noted that the edge area is included in the calculations of S considering the four concretes as isotropic materials [152].

3A.2.3. Results and discussion

The results of the measured sound absorption coefficients are reported in the graphs in Figure 7, Figure 9, Figure 10 and discussed in separate sections, based on the tested conditions, i.e. thickness and mounting method for each concrete type (A, B, C, D). In the end, more general conclusions are drawn to compare the performance of the different sample types. Moreover, the single index for weighted sound absorption (α_w) in SSRR measurements have been estimated and used for comparisons.

Effect of sample thickness and concrete type

Figure 7 shows the graphs of the four samples A, B, C and D for three different thicknesses of the single layers. Overall, the absorption spectra of panels A is uneven, and tend to provide poor absorption (< 0.25) at frequencies lower than 630 Hz, while at higher frequencies, the sound absorption coefficients ranges between 0.40 and 0.70 for panels with either 40 mm or 60 mm thicknesses. The 20 mm thick panel features an absorption peak at 3150 Hz which reaches the value of 0.90 and provides a poor absorption (<0.25) at frequencies lower than 2000 Hz. As expected, the sound absorbing properties of the panel are extended toward the lower frequencies for thicker panels [118,141,145]. The 40 and 60 mm panels present a higher absorption coefficient with respect to the 20 mm panels in the 500-2000 Hz frequency range.

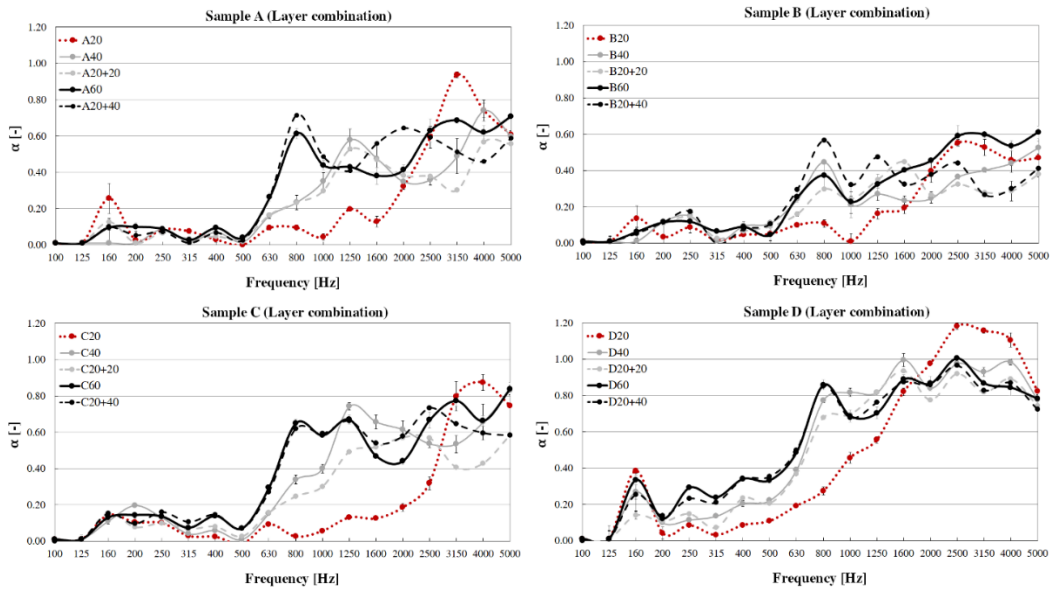

Figure 7. Comparison of the absorption coefficients for samples A, B, C and D with different thicknesses obtained from multiple layer combinations (20, 40, 20+20, 60, and 20+40 mm). Sample A: crushed normal weight aggregates 4-8 mm; Sample B: round lightweight aggregates 4-8 mm; Sample C: round lightweight aggregates 2-4 mm; Sample D: round lightweight aggregates 0.5-1 mm.

The absorption spectra of samples B are uneven and tend to provide poor absorption (< 0.25) at frequencies lower than 630 Hz for panels with either 40 mm or 60 mm thicknesses, while at higher frequencies the absorption coefficient ranges between 0.20 and 0.60. The 20 mm thick panel features an absorption peak at 2500 Hz of about 0.60 and provides poor absorption (< 0.25) at frequencies lower than 1600 Hz. As expected, the sound absorbing properties of the thicker panels are higher at lower frequencies compared to the 20 mm sample, as it can be seen in the 500-1600 Hz frequency range. However, the 20 mm sample outperforms the 40 mm one in the range 1600-4000 Hz, which does not result coherent with the expected behavior for a porous material. This might be due to the concrete mix design used for the 40 mm sample, which might have led to lower porosity of these samples. Moreover, increasing the thickness from 40 to 60 mm should have led to a shift of the

maximum peak at lower frequencies [118,141,145]. In this case, however, the peak is present at 800 Hz for both 40 and 60 mm thick samples. These two aspects may suggest that the superficial and inner porosity are not uniform among the different thicknesses. Moreover, it can be argued that for this typology the thickness threshold is around 40 mm, i.e. no further increase of the absorption coefficient below 800 Hz is obtained with the thickness increase from 40 to 60 mm [34].

The absorption spectra of panels C is also slightly uneven and tend to provide poor absorption (< 0.25) at frequencies lower than 630 Hz for panels with either 40 mm or 60 mm thicknesses, while at higher frequencies the absorption ranges between 0.40 and 0.80. The 20 mm thick panel features an absorption peak around 4000 Hz, achieving a value of 0.90 and provides poor absorption (< 0.25) at frequencies lower than 1600 Hz. The absorption coefficient for this thickness becomes lower than 0.25 at frequencies below 2000 Hz. As expected, the sound absorbing properties of the panel are extended toward the lower frequencies for thicker panels [118,141,145]. The 60 mm sample reaches significant high values of absorption coefficient (> 0.40) at 800 Hz, while the 40 mm panel at 1250 Hz.

The absorption spectra of panels D is more even than the other three typologies, and tend to provide significant absorption (> 0.40) at frequencies higher than 630 Hz for panels with either 40 mm or 60 mm thicknesses, where the sound absorption ranges between 0.40 and 1. The 20 mm thick panel feature an absorption peak between 2500 Hz and 4000 Hz, achieving a value of 1.20; the peak is broader than those featured by 20 mm thick panels of type A, B and C. Values higher than 1 may occur in the measurements with finite sample size for materials with high absorption properties [153,154]. The 20 mm sample of panel D achieves significant absorption (> 0.40) above 1000 Hz while for panels A, B and C this occurred above 2500 Hz, 2000 Hz, and 3150 Hz, respectively. As expected, the sound absorbing properties of the panel are extended toward the lower frequencies for thicker panels [118,141,145]. This is evident below 1600 Hz. Indeed, for the thicker panels, the significant absorption range is extended in a similar way down to 630 Hz.

When comparing samples with round lightweight aggregates, i.e., B, C and D, it can be observed that there is a decrease of the sound absorption when the aggregate size increases from 0.5-1 mm (sample D) to 4-8 mm (sample B). This is due to an increase in the median pore size when increasing aggregate size [141], which would reduce the tortuosity of the pore network and thus result in lower absorption values. Moreover, it can be noticed that sample A with crushed normal weight aggregates results in higher values of the absorption coefficient when compared to sample B, which has similar void ratio (25%) and aggregate dimensions (4-8 mm) to sample A, but features different aggregate shapes and densities, i.e., round lightweight aggregates. This might be due to a higher tortuosity enabled by internal pores with varied size connected to the surface [127]. This kind of difference was not observed in previous studies, that is [142], in which no significant differences between round-shape (lightweight) and irregular shape (normal weight) aggregates with the same gradation were found.

Effect of sample mounting in multiple layers

The graphs in Figure 7 show the absorption coefficients of the four sample types both in the single layer and multiple layer configurations with panel thicknesses of 20, 40 and 60 mm, for an easier comparison. Sample A graph shows that the sound absorbing performance achieved when coupling two panels of 20 mm thick is comparable to that achieved by a single panel with a thickness of 40 mm. A similar trend is observed comparing the 60 mm thick panel with the combination of 20+40 mm thick panels. However, there are some differences occurring above 1250 Hz. It can be observed that above 2500 Hz both the 20+20 mm and the 20+40 mm combination show lower values of sound absorption compared to the 40 and the 60 mm single layers samples, respectively. It can be noticed that the multiple layer 20+40 mm of sample A outperforms the 60 mm sample only at the 800 Hz peak and in the frequency range 1250-2500 Hz.

Sample B graph shows that the sound absorbing performance achieved when coupling two panels 20 mm thick is comparable to that achieved by a single panel with a thickness of 40 mm. However, the combination 20+20 outperforms the 40 mm single layer panel in the range 1000-2000 Hz. Differently the performance of the 60 mm thick panel are higher than those of 20+40 mm thick panels combined for frequencies higher than 1600 Hz. The multiple layer 20+40 outperforms the 60 mm sample in the range 630-1250 Hz.

Sample C results show that the sound absorbing performance achieved when coupling two panels 20 mm thick is slightly lower than that achieved by a single panel with a thickness of 40 mm, particularly for frequencies range 800-2000 Hz and above 3150 Hz. The performance of the 60 mm thick panel is comparable with that achieved by the combination of 20+40 mm thick panels. However, the multiple layer 20+40 outperforms the 60 mm sample in the range 1250-2500 Hz.

Sample D results show that the sound absorbing performance achieved when coupling two panels 20 mm thick is comparable to that achieved by a single panel with a thickness of 40 mm. A similar trend is observed comparing the performance achieved by a 60 mm thick panel with that of the combination of 20+40 mm thick panels. This might be due to the high and uniform porosity obtained for all the samples of type D. In these samples both sides of the panel present a uniform distribution of the pores apertures and the measurement results also suggest a higher connection of the internal pores to the surface [127]. Indeed, for the other three typologies the back side of the panels (Figure 8) present a higher number of closed pores which do not allow to fully activate the absorption of the second layer. In these cases, further care should be put in the treatment of the mix design and its curing in samples since heavier aggregates might sediment and result in non-uniform distribution of the pores within the panel and its front/back surfaces.

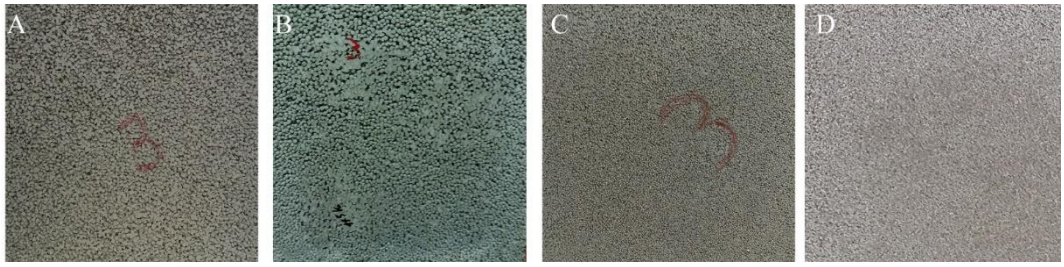

Figure 8. Back surface for Sample A: crushed normal weight aggregates 4-8 mm; Sample B: round lightweight aggregates 4-8 mm; Sample C: round lightweight aggregates 2-4 mm; Sample D: round lightweight aggregates 0.5-1 mm.

It should be highlighted that the concrete with higher acoustic performance (sample D with round lightweight aggregate of 0.5-1 mm) presents poor performance related to wear resistance compared to the other types, which may hamper their application in actual scenarios if no facings or other protective solutions are used. Another option is to use panels of type B and C, which, when coupled in layers of 20+40 mm, reaches sound absorbing performance close to that of the same configuration of panels type D for frequencies higher than 800 Hz. Alternatively, a systematic investigation may be useful to detect the thresholds values of the concrete parameters (e.g., paste volume) in order to obtain acceptable mechanical properties and still preserve highly efficient acoustical properties.

Effect of sample mounting with an air gap

The graphs in Figure 9 show the four sample types A, B, C and D mounted with an air gap of 50 mm between the panel and the rigid backing, i.e. the SSRR floor. Sample A graph shows that the performance is enhanced at the lower frequencies when an air gap is left between the panel of 20 mm and the backing, while the sound absorption at high frequencies decreases. The maximum peak is shifted at lower frequencies, i.e., around 630 Hz, with an absorption coefficient of about 0.60. The 40 mm layer seems to be less affected by the presence of the air gap and the maximum peaks remain unvaried in frequency for this thickness. However, a slight decrease is reported at high frequencies and an increase of about 0.10 is observed at the peak value corresponding to 1250 Hz.

Sample B shows different trends for the 20 mm and 40 mm layers. However, when an air gap is left between the panels and the backing, the performance is enhanced at the lower frequencies for the 20 mm and 40 mm layers. The high frequency sound absorption decreases for the 20 mm layer when the air gap is added, while the maximum peak is shifted at lower frequencies, i.e., around 630 Hz, with an absorption coefficient of about 0.60. The 40 mm layer seems to be less affected by the presence of the air gap at high frequencies above 2000 Hz. Conversely, the air gap seems to decrease the absorption over the 630-2000 Hz for the 40 mm layer. A peak value appears at the frequency of 200 Hz with a value of about 0.55 of the absorption coefficients.

Sample C shows a decrease of the absorption coefficient at high frequencies for both 20 mm and 40 mm layers when an air gap is left between the panels and the

backing. For the 20 mm panel this is significant above 2500 Hz, while for the 40 mm panel it is more evident in the 1000-2500 Hz. The performance is slightly enhanced at the lower frequencies in the range 315-800 Hz for the 20 mm sample and in the range 315-2500 Hz for the 40 mm sample, with the maximum peaks that are shifted at 630 Hz and 800 Hz, respectively.

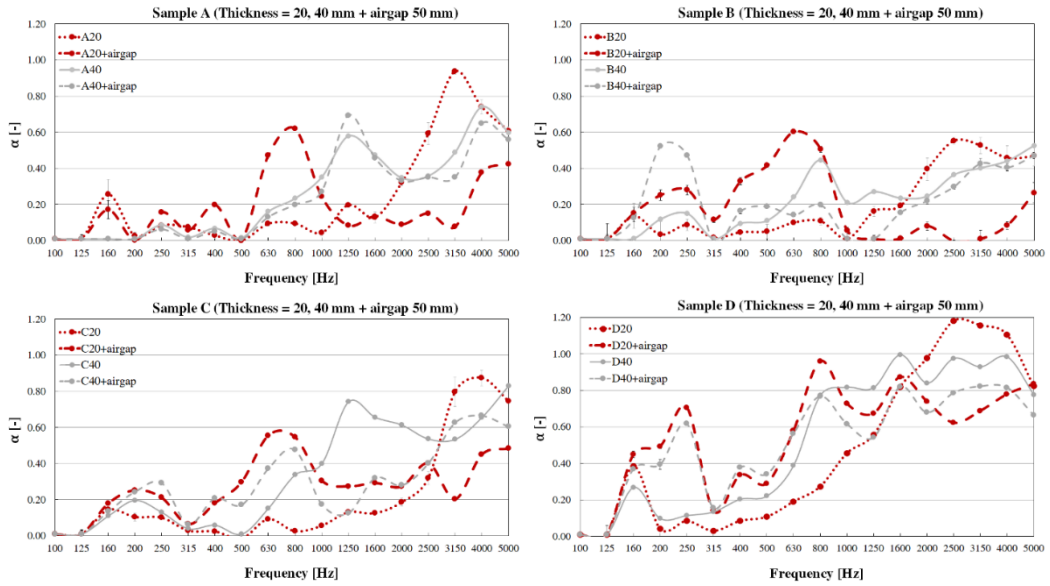

Figure 9. Comparison of the absorption coefficients for samples A, B, C and D of different thicknesses (20 and 40 mm) mounted with an air gap of 50 mm. Sample A: crushed aggregates 4-8 mm; Sample B: round lightweight aggregates 4-8 mm; Sample C: round lightweight

Sample D shows a decrease at high frequencies when an air gap is left between the panels and the backing above 1600 Hz and above 800 Hz for the 20 mm and 40 mm panels, respectively. Nevertheless, the sound absorption coefficients in those ranges result above 0.55. The performance is enhanced at the lower frequencies, where several peaks appear around 250 Hz, 400 Hz and 800 Hz. The absorption coefficient increases for both thicknesses in the 160-630 Hz when the air gap is added, showing a very similar trend for both 20 mm and 40 mm panels.

By comparing the sound absorbing performance of the different panel types measured, it emerges that the panel type D outperforms the other typologies also when mounted with an air gap of 50 mm. It presents a more uniform frequency-dependent sound absorption a broader frequency range of high values of absorption coefficient and absorption coefficients higher than those of other panel typologies. The performance of panels type C is slightly better than those of panels A and B. The worst performance is presented by panel type B, which is generally associated with the lower sound absorbing coefficient throughout the spectrum. This might be due to the effect of regular and bigger aggregates, which lead to reduced tortuosity of the pore network [141]. Generally, it should be highlighted that the performance of the 20 mm sample behaves as a layer of microperforated panel mounted with an air gap, i.e. presenting a clear sound absorption coefficient peak at low frequencies with poor

values at higher frequencies [34]. This similarity is more evident for sample A and B, which are expected to have a pore networks with lower tortuosity due to the greater dimension of the aggregates (4-8 mm) [141]. The 40 mm sample shows a similar behavior, which can resemble that of a multilayer microperforated panel. In this case, the thickness of the panel allows for a higher tortuosity of the pore network, which still allows for some absorption at higher frequencies. The microperforated panel sound absorption model presented by Maa [155] has been used in several studies to describe the acoustic behavior of concrete [138,144].

Effect of sample mounting with an air gap filled with porous material

The previous sections showed that sample D presents the highest sound absorption coefficients extended over the broader range of frequencies. In order to further improve the performance of the combination of panel D with an air gap, another strategy has been used considering the air gap filled with porous material. The introduction of rock wool layer in the air gap has been tested with the sample of 20 mm thickness only. Two thicknesses of the rock wool layer, that is, 30 and 50 mm have been introduced in the air gap. It should be recalled that the air gap considered here is of 50 mm. Therefore, the first layer of rock wool (30 mm) allowed to have a 20 mm air gap left between the concrete sample and the rock wool layer, while the 50 mm rock wool allowed to test a fully filled air gap.

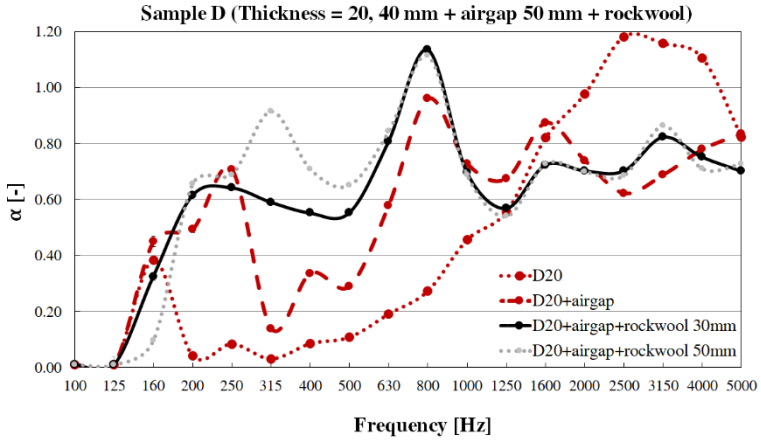

Figure 10. Sample D single layer of 20 mm combined with an air gap of 50 mm filled with a rock wool layer of 30 and 50 mm.

Figure 10 shows that the with the insertion of 30 mm and 50 mm rock wool in the air gap the sound absorption coefficients have very similar trends above 630 Hz. Generally, the combination of an air gap with a porous material (e.g. rock wool) is shown to improve the acoustic performance down to 250 Hz. A peak value at 800 Hz is further increased when the air gap is filled with rock wool compared to the empty condition. Furthermore, a significant improvement is obtained in the 250-800 Hz frequency range reaching values of sound absorption coefficients of 0.60-0.90. This solution result appropriate for several outdoor applications dealing with railway noise and traffic noise reductions, that feature a spectrum of interest in the range 125-4000

Hz [156]. Moreover, the investigated mounting systems could be integrated with structural multilayer building façades [157].

Single number acoustic index α_w

Based on the above results, the weighted sound absorption coefficients α_w derived from the SSRR measurements were calculated. These single indices are useful for an immediate and practical comparison of the performance of different conditions. The higher the α_w values, the better is the material capability in sound absorption. Their values normally range from 0 to 1, with 1 meaning 100% sound absorption.

The weighted sound absorption coefficient α_w is derived from practical sound absorption coefficients, α_p which is calculated as average of the one-third octave sound absorption coefficients within the octave in accordance with ISO 11654 [158]. Weighted sound absorption coefficient α_w can be obtained with the reference curve (α_{250}=0.8; α_{500}=1; α_{1000}=1; α_{2000}=1; α_{4000}=0.9), which is shifted in steps of 0.05 towards the α_p values until the sum of unfavorable deviations is less or equal to 0.10. The unfavorable deviations occur when the measured value is lower than the value of the reference curve. Finally, the weighted sound absorption coefficient is the value of the adjusted reference curve at 500 Hz.

Table 3. Comparison of single acoustic indices related to the weighted absorption coefficient (αw) for the four concrete types (A, B, C, and D).

Sample characteristics	A	B	C	D
20 mm	0.10	0.10	0.10	0.20
40 mm	0.15	0.25	0.15	0.30
60 mm	0.25	0.25	0.25	0.45
20 + 20 mm	0.15	0.25	0.15	0.30
20 + 40 mm	0.20	0.25	0.25	0.40
20 mm + 50 mm air gap	0.20	0.10	0.35	0.50
40 mm + 50 mm air gap	0.20	0.10	0.30	0.50
20 mm + 50 mm air gap (rock wool 30 mm)				0.70
20 mm + 50 mm air gap (rock wool 50 mm)				0.75

Table 3 shows that there are a few differences among the single indices within each concrete data. It is evident from these values that the highest performance is obtained for panel type D. The α_w values for the single layer of type D samples become significant (> 0.40) for a thickness of 60 mm. The single layer 20 mm and 40 mm present an improvement of the α_w values when they are mounted with an air gap behind (α_w = 0.50). This mounting condition performance is further improved when the air gap is filled with a porous material. It can be noticed that when the entire gap is filled with rock wool (50 mm), the highest α_w is obtained. A significant improvement due to the air gap is also obtained for sample C, while a slight improvement is reported for sample A. Conversely, depending on the sample thicknesses, sample B values of

α_w are either not affected or reduced when the air gap is added at the back of the 20 mm and 40 mm thick layers, respectively.

3A.2.4. Conclusions

The present study has been carried out in order to characterize the sound absorbing performance of a set of porous concrete panels varying in concrete mix design (A, B, C, D), thickness and mounting method. The measurements have been conducted in the 1:5 scale reverberation room of the Politecnico di Torino, in accordance with the ISO 354-1:2003 standard. The sound absorbing performance of the different panels has been described as 1/3 octave band and as weighted sound absorption coefficient α_w. The following conclusions have been drawn:

1. The mix design with the smallest round lightweight aggregate dimensions (0.5-1 mm), referred to as panel D, gave the most effective sound absorption coefficient for all the three sample thicknesses as well as for the mounting condition with an air gap at their back. It was shown that the worst performing mix design feature round lightweight aggregate with the greater dimensions (4-8 mm) referred to as panel B.
2. Samples with crushed normal weight aggregates of 4-8 mm, referred to as panel A, showed higher values of absorption coefficients compared to samples with round lightweight aggregates of the same dimensions. The performance is comparable to that of the sample with round lightweight aggregates of smaller gradation (2-4 mm) referred to as panel C. This was attributed to the pores dimensions and inner distribution which affects the pores tortuosity.
3. The sound absorbing performance of the porous concrete panels tends to increase at low frequencies for greater panel thicknesses. In most cases, solutions with single panels or double layered panels of an equivalent thickness provide similar performance. This mounting solution could be useful in practice for modular solutions and to limit the need for different formwork thicknesses.
4. The mounting method is shown to greatly influence the sound absorbing performance. For all porous concrete types considered, the sound absorption performance is enhanced for lower frequencies by leaving a 50 mm air gap behind the panel. However, the air gap significantly lowers the high frequencies performance of the thinnest samples (20 mm).
5. The frequency dependent absorption coefficient and the weighted absorption coefficient α_w comparisons showed that, depending on the mounting method, the performance of the concrete samples with aggregate dimensions of 0.5-1 mm, i.e., panel D, can be further improved. The α_w reaches values 0.50 and 0.75 for the condition with an empty air gap of 50 mm and air gap completely filled with a rock wool layer, respectively. These values are comparable to those of most used conventional porous materials.

It should be highlighted that the mix design mechanical properties remain a crucial aspect that need to be considered when the applicability of such materials is discussed. It was observed that the material with higher acoustic performance (round

lightweight aggregate of 0.5-1 mm) presents poor performance related to wear resistance, which make the application of such panels in actual scenario hardly possible. Therefore, it is endorsed to conduct further testing in the attempt to find the most performing solution balancing sound absorption with wear resistance. Alternatively, when wear resistance is required, it is possible to use panels of type B and C, which, when coupled in layers of 20+40 mm, reaches a sound absorbing performance close to that of the same configuration of panels type D for frequencies higher than 800 Hz.

Further research could be conducted along this line of research to explore other mix design and mounting method strategies to hopefully increase awareness about the potential benefits of the application of sound absorbing porous concrete in the frame of the architectural and urban design strategies. Such research may include: (1) acoustic absorption of materials with blended aggregates of different dimensions, weights and shapes, (2) acoustic absorption for alternative mounting methods, (3) acoustic absorption modeling of porous concrete of single layers and multi-layer structure, and (3) possible applications in case studies for outdoor and indoor environments.

3A.3. A brief overview of sound diffusers

The effect sound diffusion in outdoor settings has been investigated in [92,93,107,159,160]. In comparison to conventional construction materials, which often exhibit a flat sound reflective surface, these materials can generate diffuse reflections, meaning that the reflected sound energy is spread in multiple directions. On one hand, this can damp the sound reflected energy in a given position in comparison to a specular-reflecting surface and on the other hand can counteract sound trapping in urban areas, by promoting the redirection of the reflected sound towards the sky. While some past studies, such as [107], have predicted negligible variations of outdoor noise levels due to the application of sound diffusing façade materials, sound diffusers can still be useful in urban scenarios affected by strong specular reflections and to mitigate acoustic nuisances such as echoes.

The following sections briefly introduce sound scattering phenomenon and its measurement procedure and summarize a series of design guidelines that can support the definition of the geometric features of sound diffusive elements.

3A.3.1. Sound scattering: the physical phenomenon

When a soundwave strikes a surface, a part of the incident sound energy is absorbed by the material, a part is reflected, and a part is transmitted through the component. Although in actual conditions all these phenomena take place at the surface interface, acoustic materials are commonly classified as either “sound reflective” or “sound absorbing” based on the prevailing physical phenomenon occurring at their interface. Sound reflections can occur in a specular manner, i.e., with the reflection angle equal to incident angle, or in a diffuse fashion, when the sound energy is reflected in different directions, i.e., scattered, as shown in Figure 11.

Surfaces which reflect the incident soundwaves in a diffuse way are referred to as "sound diffusers".

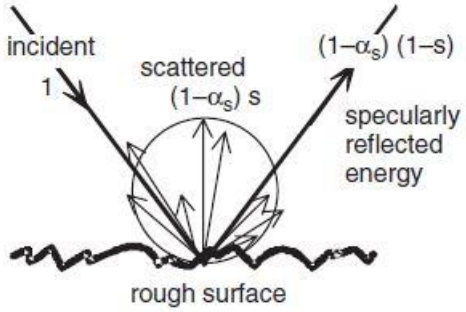

Figure 11. Specular reflection and scattered reflection occurring at the interface with a surface.

The phenomenon of sound diffusion is mainly influenced by the geometrical features of the surface impinged by sound. Irregularities and curved shapes are commonly used to promote the diffusion of the reflected sound. Sound diffusion can occur both spatially - when the sound is reflected in different directions, and temporally - when such reflections occur over a large timespan. The phenomenon of sound scattering depends on the relationship between the wavelength of the incident sound and the dimensions of the surface irregularities, as shown in Figure 12 (taken from [161]). At lower frequencies, when the half-wavelength is much larger than the surface irregularities, a specular reflection occurs, while at higher frequencies, where the half-wavelength is much smaller than the surface irregularities, the sound is reflected specularly over the facets of the irregularities. Sound scattering occurs in-between these conditions, when half-wavelength of the incident sound is close to the irregularity dimensions [161].

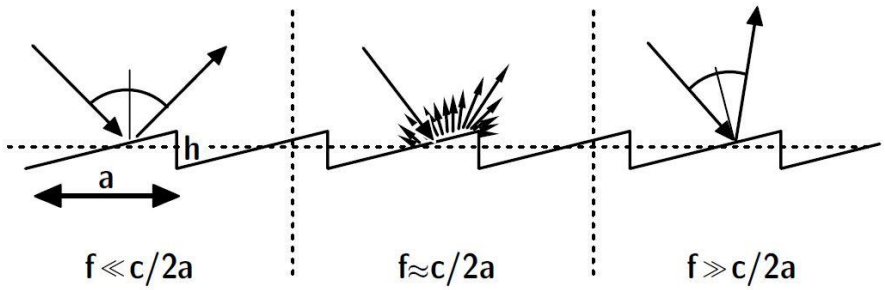

Figure 12. The influence of relationship between the wavelength of the incident soundwave and the dimensions of the surface irregularity on the type of reflection occurring at the surface interface

The scattering performance of a given surface refer to its ability to reflect sound energy in directions other than specular. This property can be described by two coefficients: the sound scattering coefficient and the diffusion coefficient. The random-incidence scattering coefficient (*s*), defined in ISO 17497-1:2004 Standard [147], is a quantitative descriptor that quantifies how much the sound reflection from a surface deviates from the specular direction. The diffusion coefficient (*d*), defined in

ISO 17497-2:2012 Standard [162], is used to describe the spatial evenness of the diffused sound energy. It quantifies the similarity between the polar response of the reflected sound energy and a theoretical uniform distribution; this index is useful to compare diffusers according to their performance [34].

Definition and measurement of the random-incidence sound scattering coefficient

The random-incidence scattering coefficient (s) of a surface is defined as the ratio of sound reflected in direction other than specular to the overall reflected energy. It is the most widely used descriptor of the sound scattering occurring at the surface interface. It is commonly included in the datasheets of commercial diffusers and is the input value required by geometrical room acoustic simulation tools to model sound diffusion in virtual environments. These programs generally require irregular geometries to be simplified to planar surfaces, and to assign them a proper scattering coefficient, to account of their actual sound diffusive behavior. The scattering coefficient is calculated throughout the frequency spectrum to account to the variation in the relation between the dimensions of the surface irregularities and the sound wavelength at the different frequencies. The value of s ideally ranges from 0 to 1, in which 0 indicates when the reflection only occurs specularly, while 1 indicates that all the sound energy is reflected towards direction other than specular.

The measurement procedure to obtain the random-incidence scattering coefficient of a surface in diffuse field is detailed in the ISO 17497-1:2004 Standard [147]. In case of scaled reverberation rooms, the dimensions of the panel sample, of the technical equipment and the wavelength of the acoustic signal need to be scaled with the same scale factor of the reverberation room. The use of a scaled reverberation room allows for the testing of smaller samples and offers practical and economic advantages over the full-scale measures, as it eases the manufacturing and shipping of the samples. According to ISO 17497-1:2004 Standard [147], s is determined indirectly from the measured random-incidence absorption coefficients of the panel (α), and the random-incidence specular sound absorption coefficient α. The latter equals one minus the ratio of specularly reflected acoustic energy to the incident energy. The test sample is laid on a turntable with a circular rigid base inside the reverberation room. A series of reverberation time measurements is carried out while the turntable performs a 360° rotation. The values of α_{spec} and α are determined from four reverberation time measurements inside the reverberation room, under different measuring conditions, i.e., either with or without the sample and with either rotating or fixed turntable. From the obtained α_{spec} and α, the random-incidence scattering coefficient can be derived.

3A.3.2. Design guidelines for sound diffusers

The sound scattering properties of sound diffusers are strongly informed by their geometrical features and several design strategies can be implemented to enhance their performance. Table 4, taken from the work in [163,164], summarizes a series of design ground rules for geometric diffusers. The reported strategies aim to maximize the portion of energy which is reflected by the panel in directions other than specular

(i.e., scattered), thus allowing to increase the scattering coefficient value. These guidelines can provide a valid support to designers for the definition of the geometric features of sound diffusive surfaces, especially in early design phases.

Table 4. Design guidelines for scattering surfaces.

Variable	Pattern	Design rule	Effectiveness on scattering and diffusion	Ref.
Size	Pyramids	Increased height	Increase at Low and Mid frequencies	[165]
	Extruded profiles (Schroeder diffusers)	Increased height	Increase at Low and Mid frequencies	[166]
	3D diffusers	Height > 20 cm	Increase at 500-3150Hz.	[167]
	Rib structures	Height > 18 cm and width of 10 cm	Increase at < 500Hz	[168]
		Use of different heights in the same panel	Increase at 125-4000 Hz (smoother curve of the frequency dependent scattering)	
	Periodic type diffusers based on rib structures	Square section (5cm, 10cm and 22cm)	Increase at Low and Mid frequencies	[169]
	Fractal order	Use of different sizes simultaneously	Broadband; Higher uniformity in the polar distribution	[170]
Configuration	Random array of cubes (20cm)	Randomization	Increase at 500-1000Hz and at high frequencies, starting from 3.15 kHz	[148,168,171]
	Penrose configuration.	Aperiodic	Increase at 500-1000Hz	[170]
Coverage density	Cubes of 20cm	Coverage density around 50%.	Broadband	[168]
	Hemispheres	Coverage density around 57 - 58 %	Broadband	[171]
	1D, 2D and 3D diffusers	38%, 46% and 57%, respectively.	Broadband	[167]
Distance	Structures of 2.5 cm	20 cm and 40 cm	Increase at 500-2000Hz	[170]
	Periodic rectangular ribs of 4.7 cm	15.1 cm and 30.2cm	Decrease of the scattering values in the frequency range 500-3150Hz	[172]
Profile shape	periodical profiles	Rectangular, triangular and semicircular profiles	High frequencies are improved by triangular and semicircular shapes; mid frequencies benefit by the rectangular profile	[173]
	Wave	Sine sweep profile	Increase High frequencies	[174]

	Extruded triangles	Triangular profile	only for specific generator angles. ($30° < \chi < 45°$)	[34]
	Alternation of concave and convex surfaces	Oriented orthogonal to each other	Broadband	[175]
	Prismatic elements	Prismatic elements	Lead to higher scattering values compared to pyramids or plates of the same dimensions	[170]
	Deep triangular prisms	Asymmetric profile	Broadband	[176]

Chapter 3B

Testing procedures to assess the thermal and optical performance of thermochromic building coatings

Objective	To suggest procedures for the outdoor and laboratory testing of the dynamic behavior and performance of thermochromic (TC) coatings for building envelope application, including the assessment of photodegradation effect.
Outcome	Black and green TC materials were tested in an outdoor test cell as outer layer for roof and façade application. The same materials were analyzed in the laboratory under steady-state and transient thermal conditions. Additionally, the progressive effect of photodegradation was investigated
Highlights	• TC panels exhibit lower surface temperatures (up to 35 °C) with respect to reference ones. • The color switching occurs in the visible range, with a difference in reflectance of ~0.6. • The solar reflectance of the TC panel was reduced by 0.1 after three days of outdoor exposition due to photodegradation. • TC panels exhibit a limited hysteresis phenomenon during the switching process.

3B.1. Overview and motivation

Outdoor thermal comfort conditions are influenced by the properties of surrounding urban facets. In the most recent years, several innovative materials for building envelope applications have been proposed. Most of these materials have been developed in an attempt to increase the energy efficiency of the building to which they are applied. Among them are the so-called "cool materials", such as those exhibiting high-solar reflectance properties, which are meant to be applied on as the outer layer of the building envelope and enable to reduce the energy consumption of buildings for cooling. This feature makes them effective in cooling-dominated climates, while they may result in heating penalties in winter in scenarios characterized by more balanced cooling and heating demand throughout the year. To overcome the limitation of cool materials with static optical properties, dynamic materials, such as thermochromic (TC) ones have been proposed for building application. These materials exhibit a light color appearance at higher temperatures, that results in prevailing solar reflecting properties, while presenting a dark-colored appearance, leading to greater solar absorbance, at lower temperatures.

This Chapter focuses on the characterization of TC materials in the laboratory and in an outdoor test cell. The dynamic behavior of these materials makes their characterization challenging in comparison to the more conventional materials exhibiting static optical properties.

Therefore, this research aims to suggest characterization procedures for materials with dynamic optical properties, such as thermochromic ones, including their testing in an outdoor facility, the study of their dynamic behavior under transient thermal conditions and the analysis of the effect of photodegradation on their dynamic performance.

The content of this Chapter is based on the journal article *"Development of testing procedures for assessing the thermal and optical performance of thermochromic coatings for buildings"* that has been submitted to Solar Energy Journal for publication, and on the contribution titled "*Laboratory and In-situ assessment of thermochromic coatings for building application: Testing on dynamic properties and photodegradation*" presented at COBEE 2022 Conference in Montreal, Canada [177]. Both contributions are authored by Elena Badino, Giorgia Autretto, Stefano Fantucci, Valentina Serra and Michele Zinzi,

3B.2. Introduction

The interest towards innovative design solutions to reduce building energy demand is increasing, given the large impact of the building sector, which nowadays accounts for about 30-40% of the global energy end use [178]. Moreover, in cities, it is of crucial importance to counteract urban overheating, which further increases building cooling demand and compromises thermal comfort conditions. In this frame, innovative building envelope materials, such as thermochromic (TC) ones, can benefit

both indoor and outdoor settings, thus contributing to more comfortable and sustainable urban environments.

TC technologies have been proposed for both opaque and transparent building components, in the attempt to manage the amount of solar radiation either absorbed by the envelope or entering the building, and improve energy efficiency [64,179]. While TC glazing have been object of several past studies and is increasingly gaining popularity and market position [179], the application of TC coating for opaque components has emerged more recently.

In climates with balanced cooling and heating demand, thermochromic coatings applied to the external surfaces of buildings can be used to reduce energy consumption for heating and cooling and to improve the urban microclimatic conditions. TCs can reversibly change their optical properties based on their surface temperature and are considered to belong to the next generation of construction materials [64]. TCs exhibit a dark-colored appearance (colored phase) at temperatures lower than the design switching temperature, to maximize solar gains in winter, and a light-colored appearance (colorless phase) at higher temperatures, to minimize solar gains in summer. TC building coatings have the potential to overcome the limitation of high albedo ones in climates where both heating and cooling demands are relevant throughout the year; indeed, in such climates, high albedo materials, while being effective energy-saving solutions during summertime, are reported to result in a heating penalty, i.e., an increase in heating demand during winter [180]. In scenarios where cooling and heating needs are balanced, TC building coatings can modulate the sensible heat flow through the envelope in different seasons, thus reducing both cooling and heating demands [65,181,182]. For instance, the potential annual energy saving for a TC roof with respect to a high albedo one was estimated up to 8.5% in [65] and up to 11% in [181]. As concerns the indoor air temperature, a TC building envelope was predicted to provide reductions up to 11°C during summertime, and increases up to 2.7°C during wintertime [182]. Moreover, considering the outdoor environment, the color change of TCs can counteract UHI during summertime, and support it in wintertime, which would in turn have a positive effect on energy demands and carbon emissions [183,184]. It must be however highlighted that the energy saving potential of TC coatings greatly depends on the climatic scenarios, and TCs are not effective in either cooling- or heating-dominated climates, where materials with static optical performance are preferable [65,185].

TC materials can be divided into two categories: those based on dyes, and non-dye types [64]. The working mechanism of dye based ones depend on the interplay between the components (i.e. pH-indicator dye and polymer matrix), while non-dye ones work mostly based on molecular re-arrangement or nano-scale optical effects [64,186]. Reviews on the state of the art of dye and non-dye TC materials are presented in [64,186].

Leuco dye-based TC materials belong to the category of dye-based TC solutions, and their working principle is grounded on a proton transfer reaction. These materials can switch from a colorless phase (also called “leuco”, or “bleached”) to a colored (“zwitterionic”) one as a result of temperature change. Leuco dyes TC materials are

composed of a color former (leuco dye), a color developer, and a co-solvent. The color former is an electron-donating component, the color developer is an electron-acceptor (proton donor), the co-solvent is a long chain alkyl alcohol whose melting point determines the transition temperature [64]. Despite their dynamic behavior is promising for building coating application [187], photodegradation is a major limitation of leuco dye-based materials, that results in a quick loss of switching properties due to solar exposition. As reported in [188], the photodegradation causes the colored state of dye-based TCs to gradually fade, while the colorless state gradually becomes darker. The phenomenon occurs especially in the first hours of exposition [189] and it is thought to be caused by an irreversible photochemical reaction activated by UV radiation [64]. Several studies report that applications of dye-based TC materials have been investigated comparing their optical, thermal and mechanical properties with cool or common samples, either in outdoor environments or climatic chambers [188,190,191]. According to [64], leuco dyes-based TC materials were the only type of TCs tested for applications in the built environment, either as the building envelope coating [188] or for pavement application [190,191]. In this framework, little attention has been given so far in an defining an outdoor and laboratory testing procedure for TC building coatings and on systematic studies on the effect of photodegradation on their performance, considering longer period of outdoor exposition.

Since the practical application of leuco dye-based TCs to the building sector is currently hindered by photodegradation, there is an increasing research effort towards strategies to improve the optical stability of these materials using UV and optical filters [192] and protective topcoats [193], as well as towards the development of non-dye based TCs, such as nanoscale engineerable ones (e.g. temperature sensitive quantum dots [194–197], plasmonics [198,199], and photonic crystals [186,200,201]). All these research lines let suggest that in the future the current limitations of TC materials will be addressed, allowing for their application in the built environment. However, despite the dynamic performance and durability of these materials were already investigated, the literature lacks studies aimed at sharing among the research community both laboratory characterization procedures and outdoor testing methods. This work aims to contribute to filling this research gap by suggesting testing methodologies for the characterization of the dynamic behavior of TC coatings for building application in the laboratory and in an outdoor test facility, where the TCs are tested for several consecutive days.

This study presents the results of a measurement campaign on a set of TC paints based on leuco-dye that were used as a building envelope external coating, and includes the assessment of the photodegradation impact on their properties. The objectives of the study are:

a) The identification of a procedure for the outdoor measurement of the dynamic behavior and performance of TC materials applied as outer coating of building envelope components, including the monitoring of their surface temperatures and the solar reflectance variations.
b) The definition of experimental techniques to assess the progressive impact of the photodegradation process on the TC performance occurring over time, when exposed to solar irradiance.

c) The development of a laboratory method to characterize the dynamic optical properties of TC paints as a function of their surface temperature.

3B.3. Method

The research study is composed of an outdoor experimental campaign and a laboratory testing of panels coated with TC paint, that are addressed separately in § 3B.3.1 “Thermochromic panels”, § 3B.3.2 “Outdoor experimental campaign” and § 3B.3.3 “Laboratory testing”. In the outdoor campaign, TC paints were employed as external coating on multilayer components for roof and façade application; the experimentation was performed in an outdoor test facility during summer conditions in Turin, Italy. The laboratory, spectrophotometric measurements were conducted to characterize the outdoor exposed (naturally aged) TC panels and on unexposed (pristine) ones. Tests were carried out both in steady state and in transient thermal conditions.

3B.3.1. Thermochromic panels

The tested samples are squared aluminum panels coated with a TC paint composed of microencapsulated leuco dye with a nominal switching temperature of ~25°C. The TC paint and the panels were manufactured in different colors and sizes. All the aluminum panels were coated with the following functional layers:

- an elastic white layer (Solar Reflectance Index>100), with a thickness of about 1 mm, applied directly over the aluminum panels;
- a TC paint (3 layers) which coat the first elastic layer.
- a protective finishing transparent top coat (2 layers) which contains additives working as UV filter and HALS (Hindered-Amine Light Stabilizer).

For the sake of simplicity, the above-described panels will be referred to in the following as “TC panels”. The panels are in black and green colors. Those for the laboratory testing, identified as type A, have a side length of 20 cm, while those meant to be tested outdoors, identified as type B, have a side length of 55 cm. The overall thickness of the coated samples is ~1.6 mm. It must be highlighted that, the optical properties of the green and black TC panels were different between type A and B, as a result of different production batches. Therefore, for the sake of completeness, the laboratory testing was conducted on both panel types, i.e., green type A and B, black type A and B. A set of panels with static optical properties were used as reference for the outdoor testing and the laboratory measurements. The reference panels are coated with a conventional static paint of the same color of the TC ones in the colored phase and are in the same dimensions.

Pictures of type A reference panels are shown in Figure 13; the visual appearance of this panels resemble that of the corresponding TC panels (type A) in the colored phase.

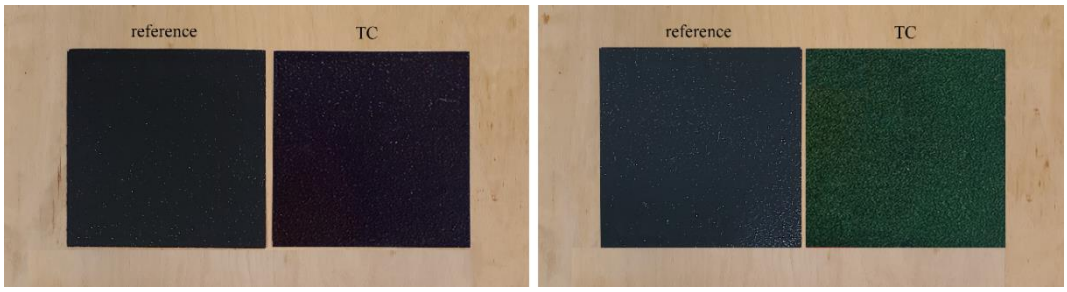

Figure 13. Pictures of the black (left) and green (right) reference and TC panels (type A)

3B.3.2. Outdoor testing

For the outdoor testing, the TC and reference panels were used as cladding solutions on the exterior sides of multilayer components for façade and roof application, that are described in detail in the following section. The components were installed on an outdoor experimental facility of the Department of Energy of Politecnico di Torino in Turin (Italy). The façade components were installed on a test cell (non-conditioned space) while the roof ones were applied directly over the roof slab of the university building. For the façade components, black and green TC/reference panels were applied as exterior layer, while for the roof application only black TC/reference panels were installed. In all tested positions, TC and reference panels of the same color were located close to each other to minimize the variation of the boundary conditions. The experimental setup is shown in Figure 14.

Figure 14. Picture of the outdoor test facility with the experimental set-up highlighted in red; the picture was taken on the first day of experimentation.

The experimental campaign was carried out for 13 days, between June 30 and July 12, 2021. During the campaign, the variation of surface temperatures and solar reflectance of the panels were continuously monitored, along with the environmental boundary conditions.

At the end of each monitoring day of experimentation, a patch of aluminum tape (~30x40 mm) was used to screen and protect a small portion of the panel from solar radiation and to stop the photodegradation process at different natural aging stages and collect data on its development over time. This procedure was performed on both the façade TC samples and on the roof one, which are expose to different amount of solar irradiance resulting from their horizontal or vertical position. Figure 15 shows a picture taken on the 3rd day of outdoor experimentation with two screening patches applied on the TC façade samples.

Figure 15. Picture of the TC façade components with two screening patches applied.

Multilayered components

Two types of envelope components with the TC/reference panels were prepared for the testing, i.e., a façade component and a roof one, consisting of multiple layers, where the TC/reference panels are the exterior one. The components were designed in the attempt to represent typical building thermal insulating solutions (insulated roof and façade External Thermal Insulating Composite System, i.e., ETICS).

The roof components are composed of a 50 mm thick extruded polystyrene layer (XPS) over which the black TC/reference panels type B (side length of 55 cm) are directly fixed with adhesive silicone, as shown in Figure 16a. The roof components are cladded by 4 black TC/reference panels, that results in squared panels with a side length of 110 cm. The roof components are leant horizontally against the roof slab of the university building. The façade components are composed of a 50 mm thick layer of XPS covered by ~3 mm thick layer of ETICS render. The façade components were cladded with TC/reference panels that are fixed to the external render substrate with adhesive silicone layer. The panels applied over the façade are of type B and are in green and black color. Figure 16b shows a picture taken during the preparation of the façade components is shown in, in which a layer of mortar is being laid on the XPS panes, already equipped with temperature sensors, while the application of adhesive silicone is shown in Figure 16c. At the end of the preparation, the panels were covered

with rigid panels, compressed using weighting elements, and left to dry for several hours (see Figure 16d).

Figure 16. Pictures of the preparation of the (a) façade components, (b) the application of a mortar layer and (c) of the adhesive silicone for roof components, and (d) the drying phase, where weights were used to compress the panels.

The façade components were installed on the aluminum frame of the outdoor test cell, while the roof ones were laid upon the roof slab. The TC panels of both components were screened with aluminum foil to prevent any exposition to the solar radiation before the start of the measurement campaign. A picture of the screened façade components is shown in Figure 17.

Figure 17. Photograph of the test cell with the screened façade components

Experimental setup

During the experimentation, the external surface temperature of the TC/reference panels applied on the façade and roof components and the solar reflectance of the roof component was monitored, along with the environmental boundary conditions. The surface temperatures of the TC/reference panels were measured using T-type thermocouples, with ± 0.3°C accuracy in the range between 0 and 60 °C, in accordance to ASTM E220-19 Standard [202]. In both the roof and the façade multilayer components, the thermocouples used to measure the external surface temperature (T_s) of each panel were installed below the thin aluminum coated panel, to avoid the disturbance of the direct solar radiation. Both sensors were set in correspondence to the center of the TC/reference panel to minimize the edge effect.

Furthermore, on the roof component, a double pyranometer set-up was used to estimate the in-situ solar reflectance of the TC/reference panels (ρ_{e_TCb} and ρ_{e_Rb}), which is calculated as the ratio between the horizontally reflected solar irradiance (I_{sol_ref}) and the global horizontal irradiance (I_{sol_h}). The set-up consists of two second class pyranometers (model: Hukseflux LP02-05) installed 20 cm above the panel's surface, one upward and one downward oriented, over the center of the panels. The height of the sensors was set to ensure for the downward oriented one a view factor of the panel equal to 90%, to minimize the influence of the radiation reflected by the surrounding surfaces. To estimate solar reflectance of the panels, a self-shading correction was applied to the reading of the downward-oriented sensor, following the indications found in [203]. The location of the thermocouples and pyranometers used to measure the behavior of the TC/reference panels is shown in Figure 18 for the façade and roof components.

Figure 16b shows sensors that are not present in the sensor scheme in Figure 18 for the façade components. Indeed, a larger number of sensors was actually used during the measurement campaign with respect to those described in Figure 18, that are the ones selected for the result reporting. For the sake of convenience, it was however chosen not to include the data obtained by these sensors in the Results (§

3B.4) since the effect of the dynamic behavior of TC materials on the collected data was relatively marginal in comparison to those selected and shown in Figure 18.

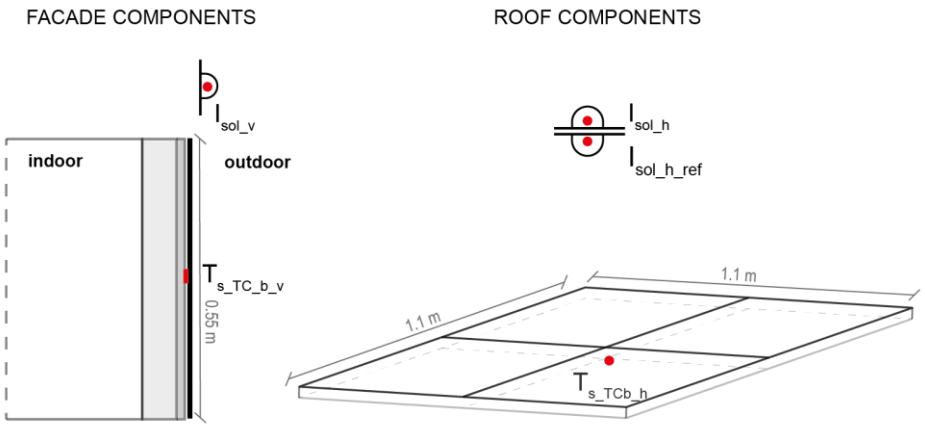

Figure 18. Scheme of the experimental setup with the sensor positions. Please note that the identification codes used are referred to black TC panels, as an example.

In addition, an infrared (IR) camera (model: Testo 882) was used to visually account for the surface temperature variation of the panels during the switching period. The thermal images were elaborated assuming a long-wave thermal emissivity of 0.9, which was calibrated by comparing the surface temperature measured with the thermocouples with that estimated with the IR camera.

The boundary conditions were measured for the entire duration of the experimentation, consisting of outdoor air temperature, relative humidity, wind speed and the solar irradiance incident on the façade and roof. The outdoor air temperature (T_{a_o}) was monitored with a calibrated T-type thermocouple placed outdoors in a shaded position. The relative humidity (RH) and wind speed (w) were measured by a weather station located over a nearby building in the university campus. The global solar irradiance on the façade of the test cell (I_{sol_v}) and that incident on the roof (I_{sol_h}) are measured using second Class pyranometers (model: Hukseflux LP02-05).

The details and identification codes of the measurements carried out during the experimental campaign with respect to the TC/reference panels and boundary conditions are summarized in Table 5 and Table 6, respectively.

All the measured data was continuously monitored using a datalogger (model: Datataker DT85) with a time-step of 5 minutes, except for wind speed and relative humidity values that were collected with a time-step of 15 minutes by the campus weather station.

Table 5. Details of the measurements on the TC/reference panels during the outdoor experimental campaign.

Measurement	type	color	Application	ID code
External surface temperature [°C]	TC	black	roof / horizontal	$T_{s\_TC\_b\_h}$
	reference			$T_{s\_R\_b\_h}$
	TC	black	façade / vertical	$T_{s\_TC\_b\_v}$
	reference			$T_{s\_R\_b\_v}$
	TC	green		$T_{s\_TC\_g\_v}$
	reference			$T_{s\_R\_g\_v}$
Solar reflectance [-]	TC	black	roof / horizontal	$\rho_{e\_TC\ b}$
	reference			$\rho_{e\_R\ b}$
Reflected solar irradiance [W/m²]	TC	black	roof / horizontal	$I_{sol\_ref\_TC\_b}$
	reference			$I_{sol\_ref\_R\_b}$

Table 6. List of the boundary conditions monitored during the outdoor experimental campaign.

Measurement	Application	ID code
Air temperature [°C]	outdoor	T_{a_o}
Solar irradiance [W/m²]	roof / horizontal	I_{sol_h}
	façade / vertical	I_{sol_v}
Wind speed [m/s]	outdoor	w
Relative humidity [-]	outdoor	RH

3B.3.3. Laboratory testing

The laboratory testing consists in four spectrophotometric campaigns that were carried out directly on the aluminum panels coated with the TC paints. The campaigns consisted of:

- a spectral reflectance measurement of the unexposed TC panels in the visible, solar and near-infrared (NIR) ranges;
- a light reflectance measurement of TC panels in different colors in the colored and colorless phases;
- a study in the visible range of the exposed TC panels at the different stages of photodegradation in steady state thermal conditions;
- a study in the visible range of the switching process on unexposed TC panels in transient thermal conditions.

The spectral reflectance measurements were conducted in the 300-2500 nm range with a Perkin Elmer Lambda 900 spectrophotometer equipped with a 150mm diameter integrating sphere, suitable to carry out measurements on diffusing and scattering samples. The light reflectance measurements (400 nm to 700 nm wavelength) were carried out in the laboratories of Politecnico di Torino with a portable spectrophotometer (model: Minolta CM 600d). Based on the spectral reflection coefficients, the broad band coefficients (i.e., light/solar/NIR reflectance) are

calculated after being weighted with the normalized relative spectral distribution of global solar radiation, following the procedure in ISO 9050:2003 Standard [204].

Measurement of light, solar and NIR reflectance under steady state conditions

As a preliminary step, the spectral reflectance of the TC panels was assessed in their colored and colorless phases considering the light (ρ_v), solar (ρ_e) and NIR ranges (ρ_{NIR}) to analyze the wavelength distribution of the optical properties. The analysis is performed at 15°C and 50°C, i.e., at temperature far below and above the switching temperature of 25°C. This test was conducted on black and green TC panels, i.e., green TC type B, black TC type B. In addition, the same analysis was conducted on the reference panels, for comparison purposes.

Light reflectance measurement and colorimetric analysis of TC panels in the colored and colorless phases

A light reflectance analysis was conducted to study the color variation in the colored and colorless phases of the unexposed TC panels of type A in two different colors, i.e., black and green. The color variation of these panels was analyzed through the light reflectance (ρ_v) and, in more detail, through a colorimetric analysis, using the CIELAB coordinates. The latter method describes the color using L^*, a^* and b^* coordinates, where L^* quantifies the lightness, and the two coordinates for color a^* and b^* range respectively from green ($-a^*$) to red ($+a^*$) and from blue ($-b^*$) to yellow ($+b^*$) [205]. The panels were tested after being exposed to steady state thermal conditions at 0°C and 50°C for 4 hours, by placing the panels in a thermally insulated basin filled with ice, and in a ventilated oven set at 50°C, respectively. For each panel, the CIELAB coordinates were calculated as the arithmetic average of three measurements carried out in different positions of the panel, to account for potential color inhomogeneity of its surface. In order to have an overall assessment of the color difference exhibited by the panels between the colored and colorless phases, the color distance ΔE^* was determined based on the measured L^*, a^* and b^* coordinates of each panel. According to the CIE 1976 definition, ΔE^* is the Euclidean distance between the coordinates exhibited by each panel in the colored phase (L^*_1, a^*_1, b^*_1) and colorless one (L^*_2, a^*_2, b^*_2), according with Equation (3):

$$\Delta E^* = \sqrt{(L_2^* - L_2^*)^2 + (a_2^* - a_2^*)^2 + (b_2^* - b_2^*)^2} \quad (3)$$

Light reflectance measurement and colorimetric analysis of the outdoor exposed TC panels at different photodegradation stages

After the conclusion of outdoor experimental campaign, a laboratory testing was carried out to study the photodegradation effect on the green and black TC panels type B, that were previously tested in the outdoor experimental campaign. Light reflectance (ρ_v) measurements were performed in the areas of the panels that were

protected by the patches applied during the outdoor exposition, which were meant to block the photo-degradation process at different stages (please refer to the beginning of §3B.3.2 for further details). The measurements were performed at steady state thermal conditions far below and above the switching temperature of the TC paint, for the colored and colorless phases, respectively. The measurement procedure is the same described previously, i.e., the panels were tested at 0°C (colored phase) and 50°C (colorless phase), and three measurements were carried out in each portion of the panel, i.e., photodegradation stage; the two testing conditions are shown in Figure 19.

Figure 19. Pictures of the two testing conditions for the measurements used to assess the unexposed panels and the photodegradation of the exposed ones (shown in the pictures), i.e., a) the ice basin, b) the ventilated oven.

Besides the light reflectance (ρ_v) of the panel in the colored/colorless phase at each photodegradations stage, also the CIELAB were reported, for a more detailed evaluation on the color degradation exhibited by the panels.

Measurement of the light reflectance of the TC panels under transient thermal conditions

The switching process of the unexposed TC panels was studied in the laboratory by measuring the light reflectance (ρ_v) of the coating under transient thermal conditions for green TC panels type A and B and black TC panels type A and B. The panels were placed inside a climatic chamber (model: ATT DM340) performing temperature ramps in the range between 15°C and 35°C with a temperature variation of 0.1°C/min. Three different rates of temperature variation were initially used, with a variation of 0.1, 0.05 and 0.033 °C/min (1°C of variation every 10, 20 and 30 minutes). However, the light reflectance results obtained in the case of the 0.05 and 0.033 °C/min ramps were not considered reliable. Indeed, those measurements required more than 1 working day to be carried out, meaning that the temperature ramp was stopped and then resumed the day after. The results highlighted that during the stop the switching process continued, leading to uneven light reflectance variation as a function of temperature; these results were therefore discarded and are not included in § 3B.4.

Considering the operating temperature of the spectrophotometer, the upper temperature of the transient temperature range was limited to 35°C and a punctual data of ρ_v measured in steady state conditions at 50°C was added for completeness. The panels were tested at every 1°C variation of the climatic chamber under increasing and decreasing temperature ramps, to evaluate the behavior of the TC panels switching from the colored to the colorless phase and vice-versa. To have a more accurate accounting of the surface temperature variation, a calibrated T-type thermocouple was glued on the bottom side of each panel to collect temperature data every 30 seconds. The surface temperature of the panels was calculated as the average value of three acquisitions, considering the time needed to conclude the testing of the panels. The light reflectance of each panel is calculated as the average of three light reflectance measurements taken in different points.

3B.4. Results

3B.4.1. Outdoor testing

Boundary conditions

The graph in Figure 20 shows the variation of the boundary conditions from June 30 to July 12. The outdoor air temperature (T_{a_o}), relative humidity (RH) and sol-air temperature ($T_{sol\text{-}air}$) calculated using the global horizontal solar irradiance (I_{sol_h}) are plotted in Figure 20a, while I_{sol_h}, the solar irradiance incident on the façade (I_{sol_v}) and the wind speed (w) are shown in Figure 20b. $T_{sol\text{-}air}$ allows to describe the environmental boundary conditions with a single figure, and it was calculated considering the measured solar absorbance of the black reference panel applied on the roof, equal to 0.9, and the horizontal or vertical solar irradiance (I_{sol_h} or I_{sol_v}), depending on the position of the samples. The radiative and wind-dependent convective coefficients used in the $T_{sol\text{-}air}$ calculation were determined according to ISO 6946:2017 [206] assuming an emissivity of 0.85, and considering the mean thermodynamic temperature of the surface and of its surroundings equal to the outdoor air temperature. The daily trends of the environmental variables suggest that the starting three days of the campaign exhibit comparable conditions, being sunny days with a clear sky. In the following days, the weather conditions are less stable, with a cloudy sky leading to a less regular solar radiation profile.

Figure 20. Variation of the boundary conditions during the outdoor experimental campaign, with respect to a) outdoor air temperature (T_{a_o}), sol-air temperature ($T_{sol\text{-}air}$) and relative humidity (RH); b) the solar radiation on the horizontal plane (I_{sol_h}) and on the façade (I_{sol_v}) and of wind speed (w).

Roof components monitoring results

The appearance of TC panels installed on the roof and façade cladding components at the beginning and after the switching process on the first day of experimentation is shown in Figure 21. As it can be noticed, the TC panels shift from a color comparable to that of the reference ones to a markedly lighter one at the end of the switching process.

Figure 21. Picture of the experimental set-up on the first day of the campaign, before and after the switching process.

Figure 22 shows the thermal images, taken every 30 minutes, between 7:45 a.m. and 9:00 a.m. during the switching process on the second day of experimentation (please notice the impact of photodegradation in comparison to the photographs in Figure 21). The images demonstrate how the temperature difference between the TC and reference panels quickly increases after sunrise, ranging from about 2°C at 7:45 to around 17°C at 9:00 a.m.

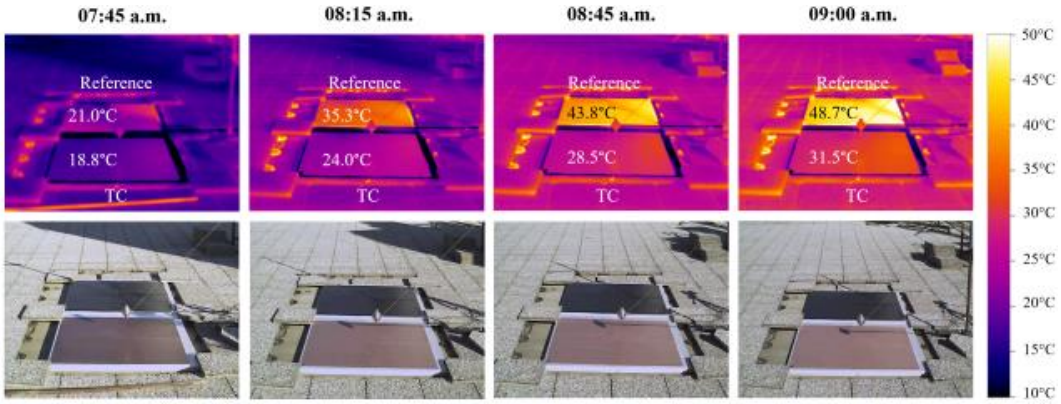

Figure 22. Thermal images and corresponding true-color pictures of the TC/reference roof components during the switching process on the 2nd day of experimentation.

Figure 23 shows the plots of the variation of the external surface temperature of the TC and reference roof components (i.e., $T_{s\_TC\_b\_h}$ and $T_{s\_R\_b\_h}$) and the solar reflectance of the TC panel applied on the roof component (ρ_{e_TCb}) as a function of $T_{sol-air}$ during the first three days of experimental campaign. For the sake of clarity, the I_{sol_ref} has been omitted from the graph, since ρ_{e_TCb} is calculated as the ratio between the I_{sol_ref} and I_{sol_h} (see Figure 20b), and thus the former can be easily derived from this relation. As already pointed out, the $T_{sol-air}$ trend confirms that the boundary conditions during the first three days were favorable and comparable to each other. Since during those days the photodegradation effect was still relatively limited, the dynamic behavior of the TC panels was analyzed in this timeframe only. Due to the jeopardized switching performance of the TC paint, the data collected during the remaining days of experimentation (from July 3rd to July 12th) was used to study the photodegradation effect only.

The plot shows the switching process of the TC panels, reported as the increase in solar reflectance occurring after sunrise, as a result of the surface temperature increase induced by the absorbed solar radiation. This variation in optical properties results in remarkably different surface temperatures between the TC panels and the reference ones during daytime. Conversely, at nighttime no sensible difference in surface temperature between the TC and reference panels is observed, thus indicating comparable long-wave thermal emissivity between the two panels' surfaces.

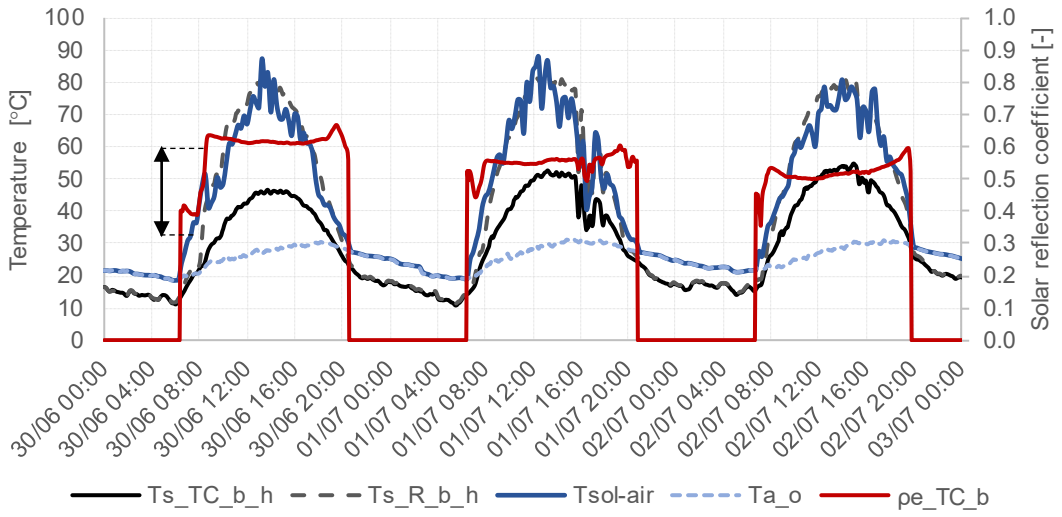

Figure 23. Variation of the $T_{s\_TCb\_h}$, $T_{s\_Rb\_h}$ and ρ_e of the TC roof component and of T_a and $T_{sol\text{-}air}$ in the first three days of experimental campaign. $T_{sol\text{-}air}$ and T_{a_o} are also plotted for completeness.

The ρ_{e_TCb} trend reveals that the switching phase occurred over a very short time frame (around 30 minutes) just after sunrise. Therefore, it can be generally considered that the ρ_{e_TCb} readings between 8:50 a.m. and 8:15 p.m. describe the colorless phase of TC panels, while those referred to the colored phase can hardly be evaluated due the limited number of data collected in this short phase. Nevertheless, only for the first monitoring day, ρ_{e_TCb} in the colored phase of ~0.4 could be measured, while in the second and third day the occurred photodegradation has limited the difference between the colored and the colorless phases.

Despite the plot is limited to the first three days of outdoor experimentation, the effect of photodegradation is already visible. The solar reflectance of the TC panel in its colorless phase tends to decrease by 0.1 in three days, varying from a mean value of about 0.62 on the first day of exposition to about 0.52 on the third day. This reduction is caused by the photodegradation process that gradually compromises the TC panel's performance, whose colorless phase tends to become darker over time.

The external surface temperature of the reference panel reaches peaks of about 80°C during the central hours of the days, while the maximum surface temperatures reached by the TC one range between 45°C on day one to 55°C on the third day. The maximum surface temperature difference between the TC ($T_{s\_TCb\_h}$) and the reference panels ($T_{s\_Rb\_h}$) is about 35°C on the first day, when the effect of photodegradation is relatively limited in comparison to the following days. Indeed, in the third day of experimentation, the surface temperature difference between the reference and the TC panel is reduced to about 25°C.

To convey information on the statistic distribution of the measured quantities for each day of outdoor experimental campaign, $T_{s\_TCb\_h}$, $T_{s\_Rb\_h}$ and $T_{sol\text{-}air}$ collected during the first three days have been also represented using boxplots in Figure 124 in the Appendix 3B.

Façade components monitoring results

The trend of external surface temperatures of the TC/reference panels applied over the façade of the test cell during the first three days of experimentation is shown in Figure 24a for the black TC/reference panels ($T_{s\_TC\_b\_v}$ and $T_{s\_R\_b\_v}$, respectively) and in Figure 24b for the green TC/reference panels ($T_{s\_TC\_g\_v}$ and $T_{s\_R\_g\_v}$, respectively). The $T_{sol\text{-}air}$ trend is added for completeness. The surface temperatures of the black and green TC/reference panels follow comparable trends, suggesting that, regardless the color difference, the reflectance of the coatings is similar.

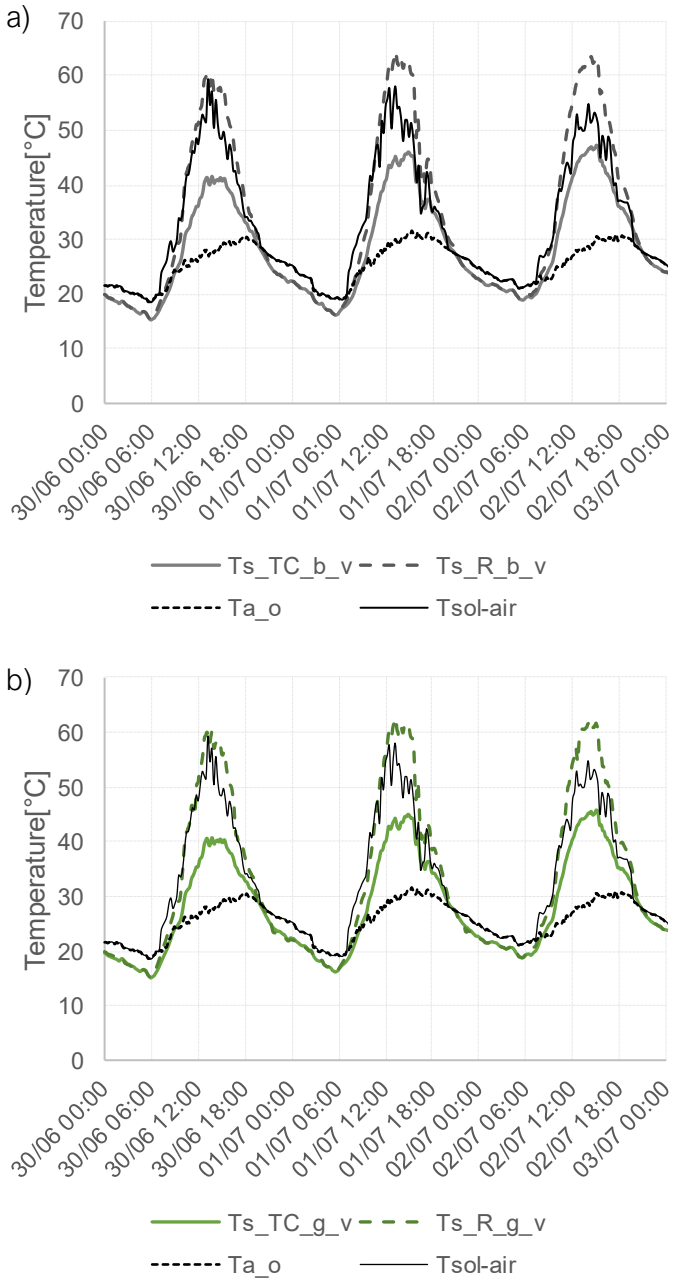

Figure 24. Surface temperature of the TC/reference panel for façade application during the first three days of outdoor experimentation.

As observed in the case of the roof components, the surface temperature of the TC panels is markedly lower than that of the corresponding reference components during daytime. In absolute terms, the surface temperature exhibited by the panels applied over the façade are lower than those applied horizontally on the roof, given the different amount of solar radiation impinging on them. The maximum temperature observed for the reference panels ($T_{s\_R\_b\_v}$ and $T_{s\_R\_g\_v}$) is around 60-62°C while that measured on the TC panels ($T_{s\_TC\_b\_v}$ and $T_{s\_TC\_g\_v}$) is between 40°C (day 1) and 47°C (day 3), for both color options, depending on the day. The maximum temperature difference between the reference and TC panels shifts from about 20°C on the first day, to about 15°C on the third one, independently of the color. Overall, the graph shows that the absolute surface temperature values and relative loss of thermochromic performance over the days (i.e., trends in maximum surface temperature difference) are smaller in case of the façade panels with respect to the roof ones, as a result of the reduced amount of solar radiation impinging on them.

As for the roof components, $T_{sol\text{-}air}$, $T_{s\_TC\_b\_v}$ and $T_{s\_R\_b\_v}$ on the first three days of outdoor experimentation are shown using boxplots in Figure 125 in the Appendix 3B.

3B.4.2. Laboratory testing

In the following sections, the results of the laboratory analysis are collected by grouping the results concerning the light and solar reflectance of TC panels, the colorimetric analysis, the photodegradation study and the analysis of the switching process of the TC panels.

Light, solar and NIR reflectance of the TC panels

The result of the reflectance measurement for the black TC panels type B and corresponding reference panels are collected in Table 7, considering the solar, visible and NIR ranges. The results on the same analysis on green TC panels type B and reference panels is reported in Table 8. For a more detailed analysis, the graph in Figure 25 shows the measured solar reflectance trend in the visible range of the black and green TC samples type B in the colored and colorless phases, along with that of the black and green reference panels.

For the black TC panel, the solar reflectance (ρ_e) in the colorless and colored measured in the laboratory can be also compared to that measured in-situ on the first day of experimentation with the double pyranometer setup on the horizontal roof component, showing a good matching (see Table 7).

The reference panels were meant to be comparable to the corresponding TC ones in the colored phase. Nonetheless, despite a good agreement between the reference and TC panels is reported in the visible range (ρ_v), a marked mismatch is observed in the near-infrared one (ρ_{NIR}), where the TC panels exhibit a reflective behavior in contrast to the absorptive one of the reference panels (see Table 7, Table 8 and Figure 25). While these properties highlight a questionable degree of comparability between the reference and TC panels in the colored phase, they were however considered acceptable given the methodological purpose of the present research contribution.

Table 7. Reflectance of the black unexposed TC panel and reference panels in the solar/visible range (laboratory measured) and on day 1 of exposition (in-situ measured solar reflectance). (*Value measured at about 45°C).

	black TC panel				black reference panel			
	ρ_e (in-situ, 1st day)	ρ_e (lab)	ρ_v (lab)	ρ_{NIR} (lab)	ρ_e (in-situ)	ρ_e (lab)	ρ_v (lab)	ρ_{NIR} (lab)
colored phase	~0.40	0.39	0.05	0.71	0.10	0.05	0.05	0.05
colorless phase	0.62*	0.70	0.66	0.75				

Table 8. Reflectance of the green unexposed TC panel and reference panels in the solar/visible range (laboratory measured).

	green TC panel			green reference panel		
	ρ_e (lab)	ρ_v (lab)	ρ_{NIR} (lab)	ρ_e (lab)	ρ_v (lab)	ρ_{NIR} (lab)
colored phase	0.42	0.08	0.73	0.07	0.06	0.08
colorless phase	0.72	0.75	0.74			

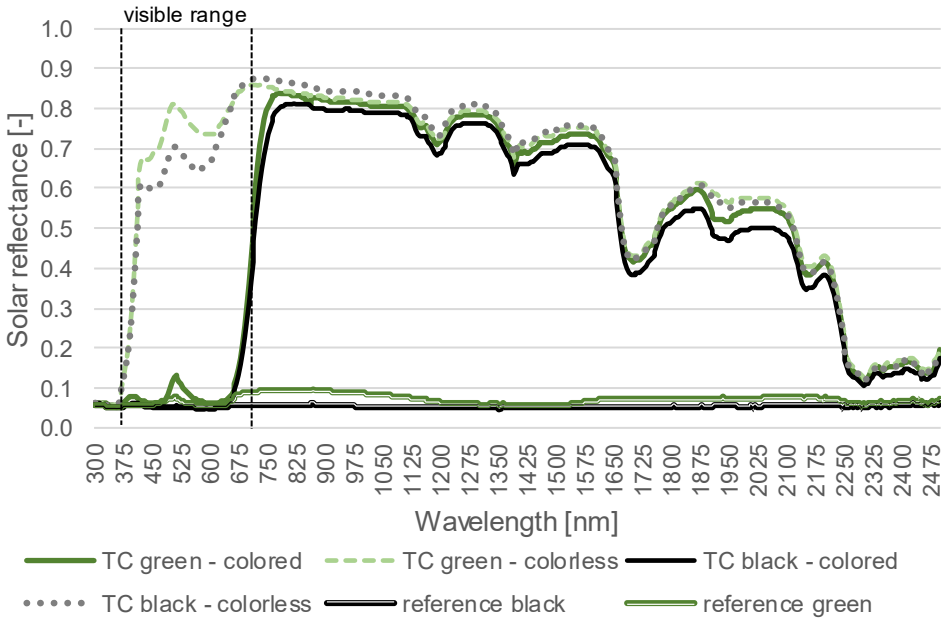

Figure 25. Solar reflectance trend of the green and black TC panels type B in the colored and colorless phases

As concerns the TC panels, a good agreement between the in-situ measured and laboratory measured solar reflectance (ρ_e) of the black TC panel is found, with a maximum difference of 0.08 in case of the colorless phase, which confirms the reliability of in situ measured data. Moreover, the comparison of the reflectance in the different ranges for the colored and colorless phases highlights that the switching process affects the reflectance of both TC panels only in the visible range (ρ_v), while spectral reflectance of the TC panels in the NIR range (ρ_{NIR}) remains unaltered. In

case of the black TC panel, ρ_v varies between 0.66 (colorless phase) to 0.05 (colored one), while for the green TC panels, ρ_v varies between 0.75 (colorless phase) and 0.08 (colored phase). This result suggest that the dynamic properties of the tested TC materials can be adequately investigated through reflectance measurements limited to the visible range.

Light reflectance and colorimetric analysis of the TC panels of type A in the colored and colorless phases

Table 9 collects the results of the spectrophotometric investigation of the unexposed TC panels in green and black color, carried out in steady state thermal conditions at 0°C and 50°C to characterize them in the colored and colorless phases, respectively. For a more detailed accounting of their properties, the graph in Figure 26 plots the measured light reflectance of the same panels along the visible range.

Table 9. CIELAB coordinates and light reflectance of the unexposed TC panels type A in green and black color in the colored phase (0°C) and colorless one (50°C).

	0 °C				50 °C				Δ 0-50 °C	
	L^*	a^*	b^*	ρ_v	L^*	a^*	b^*	ρ_v	ΔE^*	$\Delta\rho_v$
green type A	25.1	-9.8	5.0	0.06	84.0	0.3	9.7	0.64	59.99	0.58
green type B	27.6	-16.8	9.3	0.07	88.9	-3.0	7.1	0.73	62.85	0.66
black type A	19.4	1.5	-0.3	0.05	79.4	2.3	10.6	0.57	60.96	0.53
black type B	21.7	1.5	1.8	0.06	87.2	-0.8	6.2	0.70	65.72	0.64

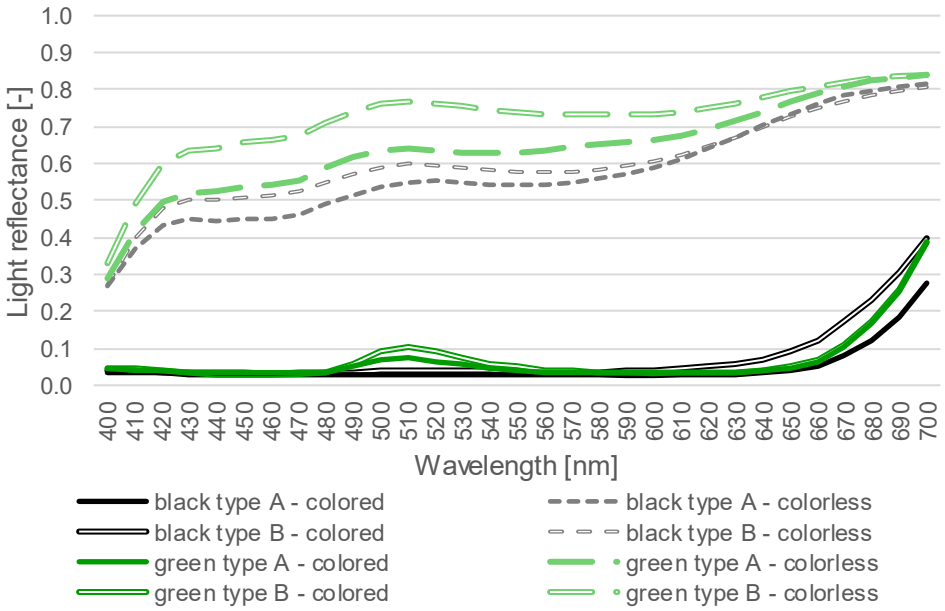

Figure 26. Light reflectance of the black and green TC panels type A and B in the colored and colorless phases along the visible range

The results highlight that the differently colored panels show, in the colored phase, ρ_v values in the range of 0.05 to 0.07, while a greater dispersion of the ρ_v values in the colorless phase is observed, with values ranging from 0.57 to 0.73. Overall, the difference of light reflectance between the colored and colorless phases ($\Delta\rho_v$) is between 0.53 to 0.66, that corresponds to a color distance ΔE^* in the range between ~60 and ~66. The smallest variation in $\Delta\rho_v$, equal to 0.53 (ΔE^*= ~61), occurs for the black TC panel type B, while the greatest ones, i.e., 0.66 and 0.64 (ΔE^*= ~ 63 to 66), are exhibited by the green and black TC panel type B. The comparison between the green and black TC panels type A and B show marked differences in the ρ_v values in the colorless phases, evidencing a different production process for the two panels' types. This trend is also evidenced in the graph in Figure 26, which shows greater light reflectance values of the green and black panels type B in comparison to type A ones.

Light reflectance of the photodegraded TC panels in the colored and colorless phases

The analysis on the photodegraded TC panels aims to assess the extent to which the photodegradation processes had affected their color switching ability of the TC over time. In Figure 27 the visual appearance and CIELAB coordinates of the TC panels type B used in the outdoor experimentation in the colored and colorless phases is shown at the different stages of photodegradation, i.e., days of experimental campaign.

The image shows how the color difference exhibited by the pristine panel in the two phases gradually vanished due to the photodegradation process when exposed to outdoor conditions, leading to a final stage, at the end of the experimentation (13 days of exposure), where the dynamic properties of the TC panels are heavily compromised and the color difference in the two phases is barely noticeable.

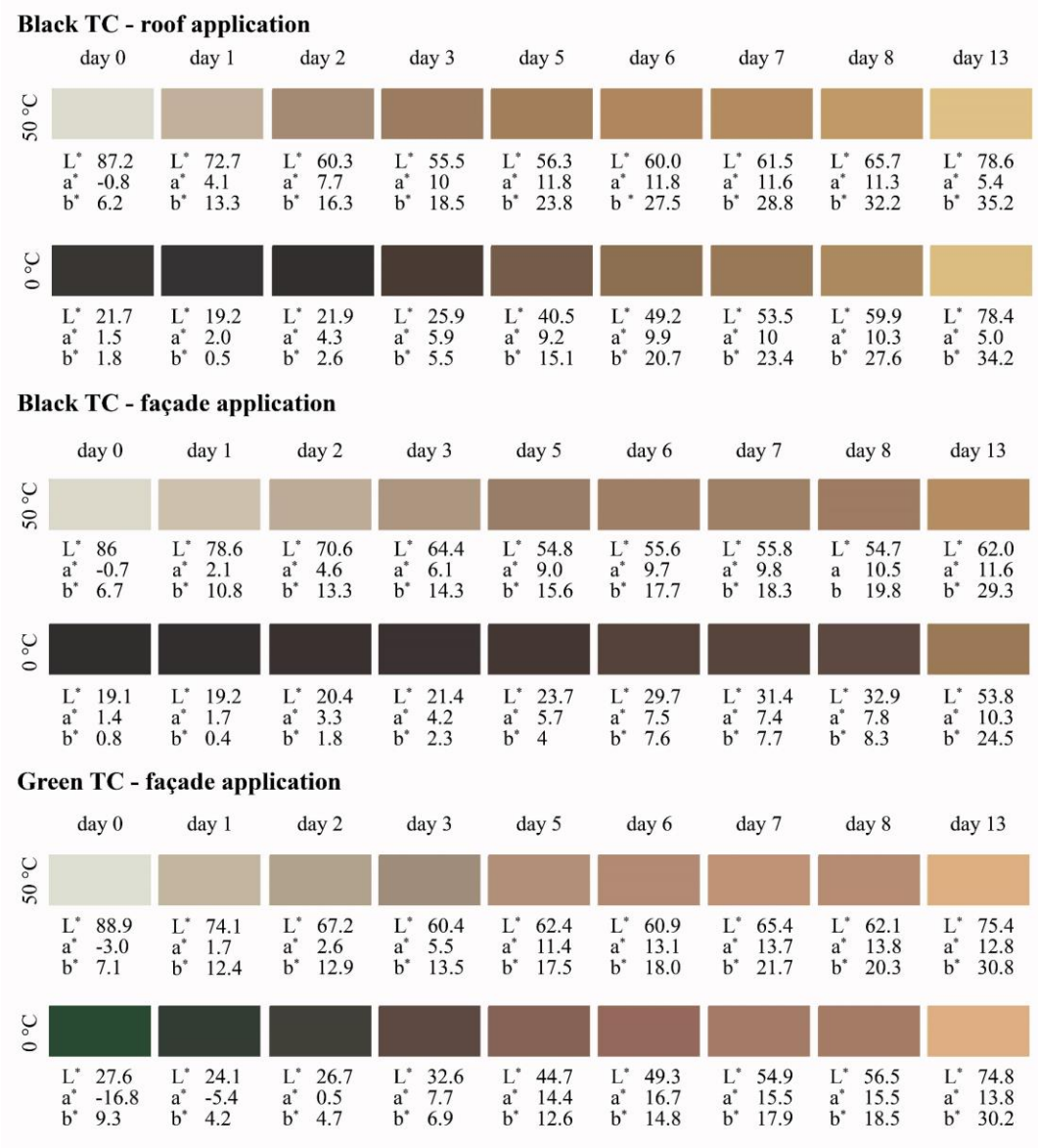

Figure 27. Visual appearance and corresponding CIELAB coordinates of the TC panels at the different stages of photodegradation, in the colored and colorless phases.

To provide a more quantitative evaluation of the photodegradation process, the graphs in Figure 28 plots the light reflectance of the TC panels of type B used for the outdoor experimentation, in the colored and colorless phases, as a function of the cumulative solar irradiance at the different stages of photodegradation. The cumulative solar irradiance quantifies the amount of solar radiation to which the panels were exposed at the different photodegradation stages and is referred to the horizontal irradiance (I_{sol_h}) in case of the roof component and to the vertical one (I_{sol_v}) in case of the façade ones. The data referred to the TC panel applied on the roof component is shown in Figure 28a, while in Figure 28b and Figure 28c are reported those of the black and green TC panels applied on the façade, respectively.

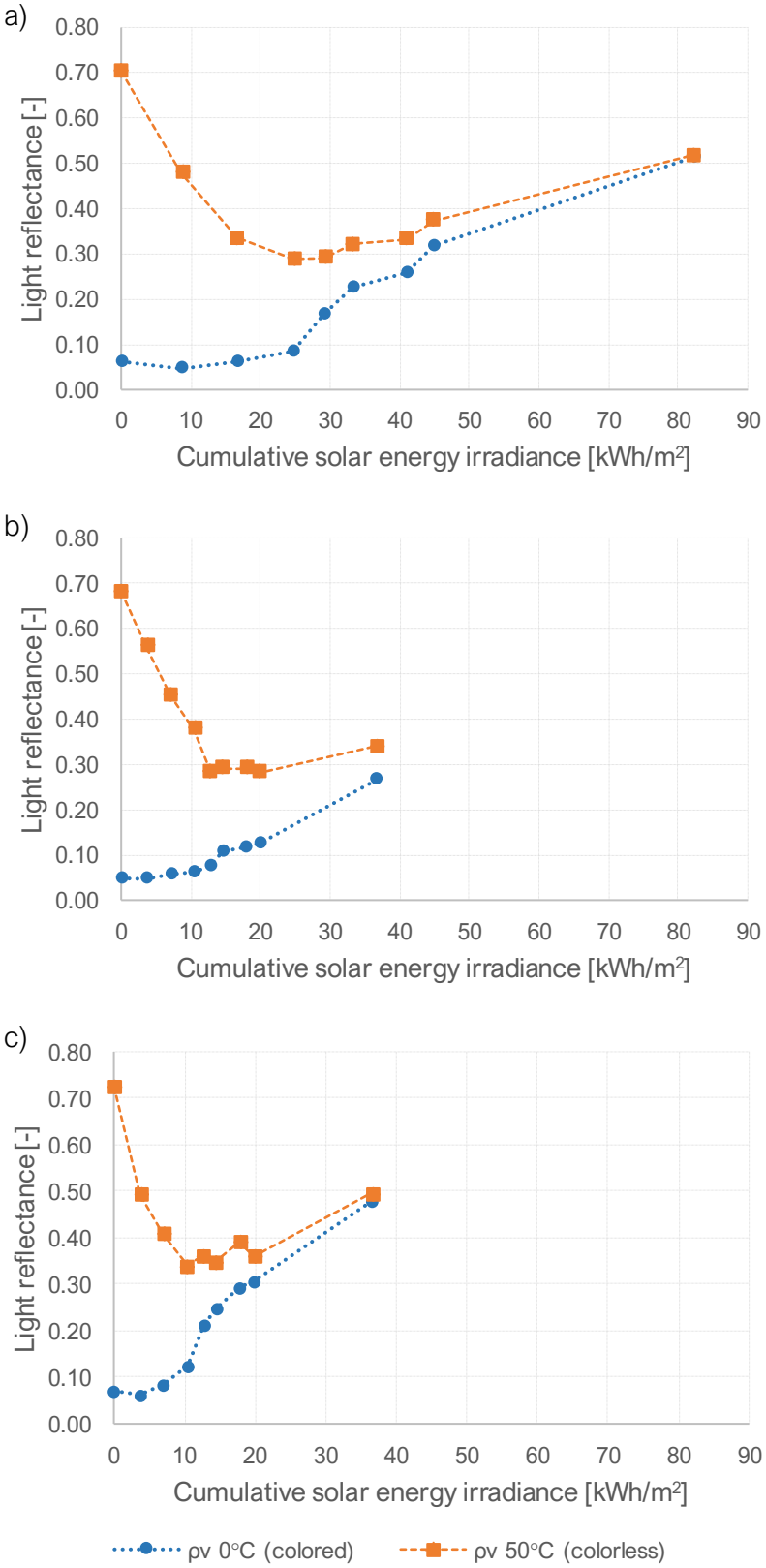

Figure 28. Light reflectance plotted as a function of the cumulative solar irradiance for a) black TC panel type B installed on the roof; b) black TC panel type B installed on the façade; c) green TC panel type B installed on the façade.

The results show progressive loss of switching ability of the TC panels due to photodegradation. The light reflectance of the TC panels before the outdoor exposition (i.e., the value plotted for a cumulative solar irradiance of 0 kWh/m^2) varies between ~0.7 in the colorless phase to ~0.05 in the colored one, as already noted. Starting from the first day of exposition to solar irradiance there is a marked drop of the ρ_v of the panels in the colorless phase; the reduction of ρ_v in the colorless phase continue over the following days, with a slightly more attenuated trend until it tends to the stabilization. These more stable data was collected from the 4th day to the 7th day, where the weather was often cloudy, so the solar irradiance was quite limited. The ρ_v of the panels in the colored phase seems to be affected more gradually by the photodegradation effect, as the variation is much more limited during the first days of outdoor exposition, while for most panels seems to increase from the 4th day to the 7th day, i.e., the days in which the photodegradation impact on the colorless phase was less significant. The ρ_v values for the colored and colorless phases collected on the 7th day (~20 kWh/m^2 for the façade component and of ~45 kWh/m^2 for the roof one) are very close to each other with a difference smaller than 0.1 in case of the black TC panel applied on the roof and the green one installed on the façade, and of about 0.15 in case of the black TC panel applied on the façade. The final value plotted in the graphs, referred to the end of the outdoor experimentation (on the 13th day, at ~82 kWh/m^2 for the roof panel, and ~37 kWh/m^2 for the façade one), clearly show that the ρ_v in the colored and colorless phases have converged to a single value, meaning that the panels have fully lost their ability to switch their optical properties.

Light reflectance of the TC panels during the switching process

The graphs in Figure 29 plots the measured variation of ρ_v under transient thermal conditions, of the green and black TC panels type A and green and black TC panels type B as a function of their surface temperature. The graphs show the measured value of ρ_v considering an either increasing (i.e., heating, shown in red color) or decreasing (i.e., cooling, shown in blue) temperature variation. The switching process of the panels, that in the graphs corresponds to a steep variation of ρ_v, occurs for most TC panels at around 24°C, i.e., slightly below the nominal switching temperature of 25°C. At temperature far above and below such temperature, almost no variation of light reflectance was observed. The comparison of the ρ_v values measured following the increasing and decreasing temperature trends, highlights that the switching process is not instantaneous and occurs around slightly different temperatures, with a variation of 0.5 to 1°C, suggesting that they are subject to a limited thermal hysteresis phenomenon, whose magnitude is comparable for all the tested panels. While the phenomenon of hysteresis is reported to occur in other thermochromic solutions, such as TC glazing [207], and has been included in the simulation model of TC roofs in [65], to the best knowledge of the authors, it has not been studied experimentally on TC coatings so far.

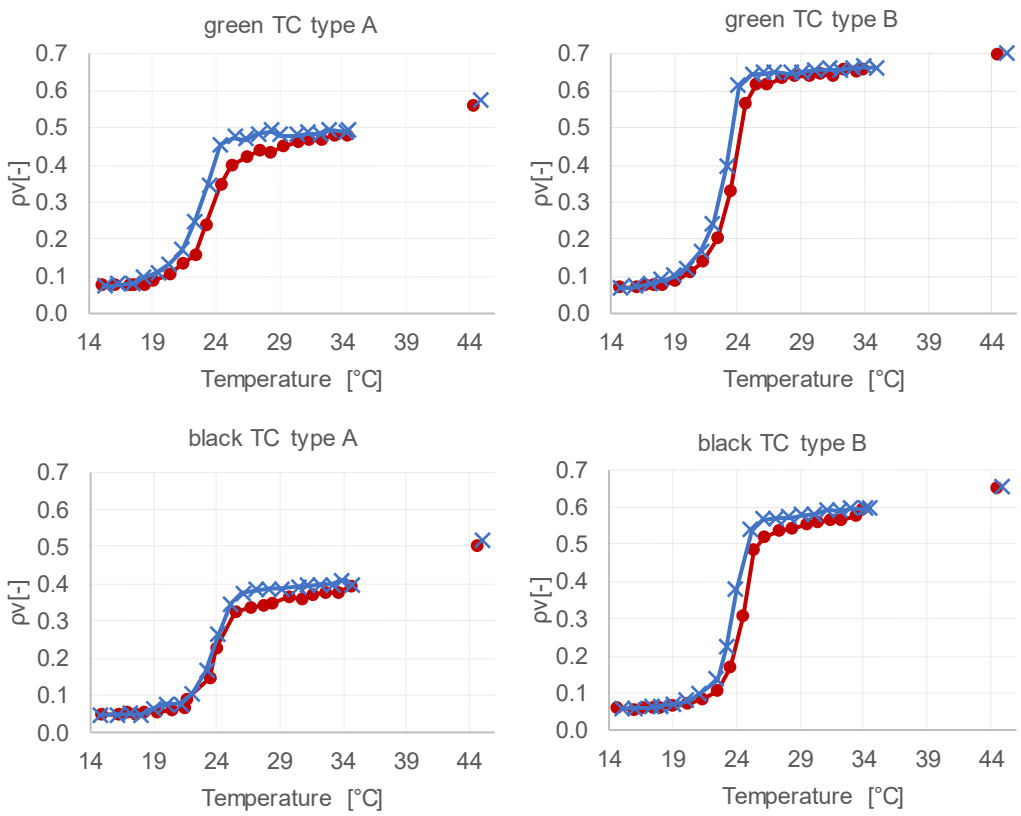

Figure 29. Graphs of the light reflectance of the test TC panels in either decreasing (blue line) or increasing (red line) thermal conditions.

3B.5. Conclusions

This study focuses on TC materials for building cladding applications that present dynamic optical properties and are a promising energy-saving solution to reduce the heating and cooling demands in climates where they are balanced throughout the year, while also contrasting urban overheating in summer. This research presents a methodology to monitor the behavior of TC materials in outdoor conditions and to characterize their dynamic performance in the laboratory. Despite being originally developed for TC materials, the proposed methodology may be adapted for other types of switchable coatings.

In an outdoor experimental campaign conducted during summertime, TC and reference panels were applied as the outer layer of roof and façade components to monitor the external surface temperature and solar reflectance of the panels over the days. Different laboratory studies were carried out, with the goals of characterizing the spectral and light reflectance of the TC panels in the colored and colorless phases, investigating the progressive performance loss exhibited by the outdoor exposed thermochromic panels caused by the photodegradation, and studying the switching process of unexposed TC panels under transient thermal conditions. The results of the outdoor experimentation suggest that the application of TC building cladding is an effective strategy to reduce building energy consumption to achieve indoor thermal comfort without occurring in heating penalties in wintertime. While a maximum

difference in the surface temperature of TC in their colorless phase and reference panels of about 35°C was found in case of the roof application, this result should be considered specific of this study. Indeed, it was observed that the TC paint shows a greater near infrared reflectance compared to the reference (conventional) paint, meaning that the measured temperature difference is influenced also by this property and not only by TC behavior. Therefore, the results of this study should be interpreted in light of these considerations.

A methodological approach to assess the in-situ reflection properties of TC coatings is also presented, showing good agreement with the values measured in the laboratory.

The spectral reflectance analysis on the TC panels in the colored and colorless phases have highlighted that the panels exhibit dynamic properties in the visible range, while a negligible switching behavior is observed in the near infrared region. The light reflectance of TC panels in the colored and colorless phases was measured on a set of panels in green and black colors; in addition, a colorimetric investigation was performed on them to gather more information on the visual appearance of the panels in the two phases. Overall, the difference of light reflectance between the colored and colorless phases ($\Delta\rho_v$) is between 0.53 to 0.66, that correspond to a color distance ΔE^* in the range between ~60 and ~66.

Despite their potential, the dynamic performance of TC materials based on leuco dye quickly degrades when exposed to solar radiation. This phenomenon was observed in the outdoor testing, where the solar reflectance of the TC panel was reduced by 0.1 after three days of outdoor exposition. Consequently, the difference in surface temperature between the TC and reference panel applied on the roof was reduced by 10°C. A light reflectance analysis on the degraded panels at different photodegradation stages in the colored/colorless phases suggests that, at first, the process mainly affect the ability of the TC dye to fully reach the colorless phase, while it impacts on its ability to switch to the colored phase at a later time.

To conclude, a light reflectance study was conducted to investigate the switching process of the TC panels under transient thermal conditions, with increasing and decreasing temperature variations. The study has allowed to observe a limited hysteresis phenomenon exhibited by the TC panels, evidencing that the switching process is non-instantaneous and occurs at slightly different temperature based on the previous thermal state of the panel.

Further investigations may include the extension of the monitoring campaign to both summer and winter condition, the testing of more stable TC paint solutions and the characterization of TC behavior in outdoor settings over longer period of time. Moreover, the study of the microclimatic effect of TC materials is endorsed to investigate how such innovative solutions can influence outdoor conditions.

Acknowledgements

The authors wish to thank Gabriele Piccablotto from LAMSA (Analysis and modelling of environmental system Laboratory) of Politecnico di Torino for the support on the spectrophotometric measurement, and Dario Cervellati and Arlen Ferrari from GFC Chimica s.r.l. that provided the testing samples and useful feedback on data.

Chapter 4A

Acoustic Performance-Based Design: A Brief Overview of the Opportunities and Limits in Current Practice

Objective	To provide an overview of the application of performance-based design approach (APBD) in acoustics by gathering information on built case-studies and evidence the main opportunities and limits of such approach
Outcome	19 built examples of APBD were collected and described in order to highlight the design features to which such approach was applied, the tools and methodologies used in the digital workflow
Highlights	• APBD is normally applied due to the combined use of parametric modeling (e.g., Grasshopper) and acoustic performance simulation tools (e.g., Odeon) + optimization (e.g., Galapagos, Octopus). • Most simulation tools used rely on geometrical room acoustic principles, although in some cases wave-based once were used. • There is generally poor integration between modelling and simulation environments, and many case studies were developed with the aid of custom tools.

4A.1. Overview and motivation

This Chapter focuses on the performance-based design (PBD) approach and its application in the acoustic field. This approach is based on the introduction of performance goals early on during the design process and relies on performance simulation tools, whose estimations can be used to orient design decisions. PBD approach allows designers and consultants to have greater control over the project performance and to optimize the design project accordingly, overall increasing the efficiency of the design process and the quality of the final design outcome. While the advantages of such an approach in addressing complex design problems are straightforward, its application in acoustics is still limited.

The review study here presented collects and describes a series of built case-studies developed according to the acoustic performance-based design (APBD) approach. The design features to which this approach was applied, the method followed during the design process, the digital workflow and the tool used (for modeling and performance simulation) are collected with the aim to highlight the advantages of the APBD and suggest some possible ways to promote its application among practitioners.

The content of this Chapter has been published in the journal article *"Acoustic Performance-Based Design: A Brief Overview of the Opportunities and Limits in Current Practice"* authored by Elena Badino, Louena Shtrepi and Arianna Astolfi [208].

4A.2. Introduction

4A.2.1. Performance-Based Design

Architectural problems generally combine a great multitude of objectives, which pertain to different fields, such as cultural, aesthetic, economic, structural and energetic ones. As these objectives often contrast with each other, it is crucial for the design team to find the most favorable solution in overall terms.

According to the classification proposed by Shi [209], architectural objectives can be divided into three categories: structural performance, performance of the physical environment - both of which can be quantified - and aesthetic and cultural performance, which relates to unquantifiable aspects. Digital simulations and measurements on scale-models allow for the evaluation of the quantifiable performance of the design proposals prior to their construction. In common practice, such tools are generally used in late design phases to verify the adherence to the performance requirements prescribed in codes, standards and laws, and evaluate the need for late design adjustments [210–212].

However, in the recent years, another approach has gained popularity, according to which performance simulations are used to drive the design process. This approach is known as performance-based design (PBD): pertinent information on one or more performance aspects is gathered since early design phases, and the proposals are

iteratively optimized based on the performance feedbacks. The design process follows the loop of generation–evaluation–modification, until a solution that meets the performance goal is achieved. While not discouraging the inclusion of unquantifiable goals and aesthetical considerations, pertinent information on quantifiable performance can greatly support decision-making processes in the conceptual design stages.

In early design phases, designers consider a wide range of possible design solutions. Design decisions made at this stage have the greatest impact on the final performance, while late-time design adjustments can rarely compensate poor decisions made in early stages [213–216]. Moreover, design modification taken in early design phases is less costly to implement than those taken in subsequent phases [29,212]. Therefore, PBD approach benefits both design workflow and final outcome, combining a decrease in cost and time, and enhances design quality [217–219]. Indeed, with PBD designers have a greater control over the performance since early design phases and, as a result, the need for late-time design modifications or "a posteriori" measures is prevented, enhancing the overall efficiency of the design process.

The PBD approach emerged in the 1970s and has become increasingly more appealing to architects due to the technological advancement and, in particular, to the development of performance simulation and parametric modeling tools [209,220–223]. Some educational experiences, such as those in [223,224], suggest that architectural students are increasingly being encouraged to use these tools and include performance feedback to support design decisions during the early-stage design exploration.

PBD marks the paradigm shift from the traditional "form-making" to the "form-finding" approach [225]. It allows one to displace traditional know-how, enabling designers to understand the effects of different design features of the proposal on performance, and to identify design scenarios that best fulfill the unique requirements of each project.

The PBD method can be subdivided into two subclasses according to the way the design optimization process is conducted. In "formation models" the modifications are applied manually by the operator, while in "generative models" the design proposals are directly optimized by the computer [226]. The latter subclass is also known as "performance-driven design" [209].

Following the manual procedure, the designers control the form-generation process, allowing for the introduction of unquantifiable criteria and the technical expertise of the operator. For instance, based on performance simulation feedbacks and technical knowledge, the operator generates new design alternatives and tests them until a satisfying solution is achieved. The generation of design proposals can be eased by the use of parametric modeling tools, such as Grasshopper [227] for Rhinoceros [228] and GenerativeComponents [229]. These tools allow one to define complex geometries and to easily modify them by controlling their parameters, thus preventing the need for the operator to manually redraw each design iteration. Adequate technical skills are required in manual processes, since the success of the optimization greatly relies on the correct understanding of the relations between

design features and performance [210]. However, the time and manpower required in the processes may limit the number of iterations pursued and the effectiveness of the design optimization [209,230].

On the other hand, generative models allow one to explore a wide number of design options with a limited involvement of the operator, exploiting the functionalities of optimization tools (e.g., Galapagos [231] and Octopus [232]) [209,210,225,233]. These tools, when paired to a parametric model and a performance simulation tool, allow one to automate the search of the most performing solution within the variation space defined by the operator, while also narrowing the space of possible solutions based on the estimated performance [234]. The population of candidate solutions evolves over many generations, until a satisfactory solution is reached. This enables one to explore a wide solution space and to find potentially unconsidered design options to address the specific requirements of the project [211,235]. In automated processes it is also possible to effectively combine different performance goals in multi-objective optimization procedures, which can hardly be implemented manually. In automated procedures, the involvement of the designer is generally limited to the definition of the target performance objectives and of the boundaries of the variation space within which the generative process operates, which may reflect quantifiable and unquantifiable criteria [218]. Despite these advantages, manual procedures may be preferred by professionals to allow the design exploration to be guided by their intuition and expertise gathered by working in the field.

Manual and automated procedures are often combined in different ways in hybrid methods, allowing one to exploit the advantages of both approaches, based on the requirements of the design process.

The PBD approach enhances the efficiency of the design process by enabling to optimize the architectural proposal with respect to the performance analyzed. However, the application of PBD method is still relatively limited currently. Indeed, current architectural practice often relies on experience-based know-how and performance simulations are mainly introduced in late design phases with the aim to verify the adherence to the performance requirements.

4A.1.1 Performance-Based Design in Acoustics

The implementation of PBD in the architectural acoustics field would allow the designer to better combine acoustic performance objectives with architectural goals. Architectural design and acoustic performance are strictly linked: the emitted sound is altered by the architectural space within which it is deployed, due to sound reflection, absorption and diffusion phenomena occurring over its surfaces. In common practice, however, acoustic concerns are mainly restricted to the design of spaces intended for artistic performances, such as music venues and theatres. In such spaces, the architectural environment is meant to support the sound generated by the artists, and acoustic design is critical for both audience and performers [219].

However, as the benefits of acoustic comfort on the well-being of the population are being acknowledged, acoustics concerns are introduced in a wider variety of design problems [12]. Indeed, acoustic requirements are being increasingly extended to the design of spaces not related to artistic performances, such as classrooms,

workplaces and urban environments, where an appropriate acoustic performance would benefit the hosted activities and the well-being of the users [12,107,236,237].

The acoustic performance of architectural spaces can be described by a number of parameters (e.g., sound pressure level, sound strength, reverberation time, clarity, etc.), each accounting for different perceptual aspects [238,238]. The acoustic requirements vary in accordance with the function hosted in the space. For instance, in spaces intended for speech, as classrooms and conference rooms, early sound reflections need to be adequately controlled to ensure the speech intelligibility [239]. In music venues, i.e., concert halls, opera houses, theatres and open-theatres, a number of parameters are usually considered to account for different perceptual aspects [240]. The proper management of early and late reflections is crucial, and it is generally obtained by opportunely treating the ambient with reflective and diffusive surfaces. Differently, the acoustic performance of sound reproduction rooms, like home theatres and recording studios, should be neutral, to prevent the space to alter the perception of recorded sounds; in this case a combination of sound diffusing and sound absorbing surfaces is preferred [34].

Currently, different commercial acoustic simulation tools are available (e.g., Odeon [241], CATT-Acoustic [242], Pachyderm Acoustics [243], etc.), allowing professionals to estimate the performance of design proposals using the geometrical acoustic method. The acoustic performance of a given environment is predicted based on its geometrical features and the acoustic properties of the materials applied to the surfaces. Normally, the acoustic analysis is run in an external application from the modeling environment, and a specific virtual model need to be prepared (e.g., geometrical simplification, surfaces divided into layers based on material and specific format) in order to be fed to the acoustic simulation tool. Besides geometrical acoustic simulations, some more sophisticated simulation methods, such as wave-based ones, have been applied to concert halls and other bigger environments [244–246]. However, these methods still require long simulation time and are not currently supported in any commercial acoustic simulation tool.

Although architectural design should pursue aesthetical quality in parallel with acoustic performance objectives, the process of conciliating acoustic requirements and architectural quality is often difficult and time-consuming, given the different design approaches and criteria of the two disciplines [30,247]. In most cases, the architectural and acoustic specialists work rather independently, with relatively few exchanges between them [235,248]. For instance, the most common approach followed in the design of concert halls relies on well-known typologies (e.g., shoe-box, fan-shaped, vineyard, etc.) and integrates acoustic simulations in late phases of the design process to verify the adherence of the project to performative requirements. In the design of spaces intended for other purposes, acoustic performance is often overlooked, recurring to acoustic treatments to adjust the performance only in late design phases or after the construction. Since the projects at the final stages are already defined, normally, major form-modifications cannot be pursued anymore, and improvements can only be obtained by altering minor design features, resulting often in costly and little effective solutions [213,214,249,250].

In this frame, the implementation of the PBD method in the acoustic field, known as acoustic performance-based design (APBD), would be able to overcome some of the main drawbacks of the traditional method and set-up an effective collaboration between architectural and acoustic specialists. The feedback of the simulations enables one to identify the dependencies between the design features and the acoustic performance, and to optimize the project accordingly. However, despite the mentioned advantages, the application of APBD in current architectural practice appears to be limited.

4A.1.2 Objectives

The aim of this paper is to provide an overview of the state of the art of the application of the acoustic performance-based design method through the gathering of a set of built case studies. The design procedures followed in the development of the case studies are briefly described, to highlight the benefits of the application of APBD and suggest possible improvements to extend its application.

4A.2 Research Methods

This paper presents and investigates a set of 19 built case studies developed with APBD, which were gathered through literature research. The methodology followed in this work is similar to that applied in review studies pertaining to the architectural field, as in [251]. For this work, unbuilt examples, as well as examples built as scaled prototypes or which lacked adequate documentation, were excluded from the analysis. The research is limited to the publicly available information on the built case studies, which was mainly gathered from journal articles, conference proceedings, books and web articles. Therefore, the presented collection cannot be considered comprehensive, as it excludes the projects, which are not documented in literature, as it is often the case of projects developed by professionals. Moreover, it must be highlighted that, with the exception of case studies developed for research purposes, the publicly released information regarding the design workflow and the performance parameters considered in the optimization process is generally rather limited. Despite these limitations, the presented collection will be hopefully meaningful and will help to delineate the state of the art of the APBD method, by briefly describing the design outcomes, as well as the design processes and the strategies followed to enhance their performance.

4A.2.1 Selection of Case Studies

The research was conducted on the literature available on online databases as Scopus [252] and ResearchGate [253], on Google search, and in the academic libraries of Politecnico di Torino. Although scientific literature has been privileged, the support of Google search engine was exploited to extend the collection of case studies and to find further information. It must be noted that, for certain projects, further details were asked to the professionals involved in the projects via personal communications. Common keywords used in the search enquiries to filter results

were: “performance-based design”, “form-finding”, “performative design”, “performance”, “architecture”, “design”, “generative”, “optimization”, “simulation”, “acoustics” and “sound”. Only built examples with adequate documentation were selected for the analysis.

According to these criteria, 19 built examples were collected. In the following section, the case studies were briefly described and information on the design method and the tools used were gathered.

4A.2.2 Case Studies

The 19 case studies, which were briefly described in the following sections, were clustered according to their primary purpose and architectural characteristics. The first section, named “music venues” (Section 2.2.1) collected the projects that were designed to support of music and other artistic performances (i.e., concert halls, acoustic shells, etc.), while the second section, named “other spaces” (Section 2.2.2), gathered projects that were meant to host other functions or were developed as artistic installations.

Music Venues

The Philharmonie de Paris

Design: Ateliers Jean Nouvel, Brigitte Métra Associés; Acoustics: Marshall Day Acoustics, Nagata Acoustics, Studio DAP, Kahle Acoustics, Altia Acoustique, Jean-Paul Lamoureux and ASC; Paris, France, 2015

The project is the winning proposal of an international competition for the Philharmonie de Paris, whose main venue is a 2400 seats concert hall primary used for orchestral acoustic music performances (Figure 30). The acoustic brief for the “Grande Salle” explicitly called for an innovative shape for the concert hall with a limited distance between stage and seats, optimization of both early and late acoustic responses and also defined more than 10 acoustic requirements to be met (sound strength, reverberation time, clarity, etc.). The acoustic design started with the study of the sound reflections through laser measurements in scale models and continued with the support of parametric modeling and acoustic simulation tools, using Grasshopper, Maya [254] and Odeon. The solution adopted is made of two nested chambers that balance early and late reflections: the inner provides acoustical clarity and visual intimacy; the outer provides high reverberation, with an overall volume of 37,700 m^3. The inner chamber is characterized by the presence of suspended reflectors, called “nuages”, along with the balconies’ fronts and walls, namely “ribbons”, which provide early sound reflections. The design of the “nuages” and “ribbons” was developed though the APBD method, following an iterative form-optimization process guided by the relations between their geometry and the acoustic performance at the audience positions. Initially, the form optimization process was carried out manually, while in subsequent phases it was pursued with the aid of automated processes using Grasshopper and Maya. The “nuages” and “ribbons” have been optimized to provide the desirable amount of early sound reflection over

the audience in order to meet the acoustic requirements, such as time delay and level difference between direct and reflected sound, while also considering architectural and theatrical requirements. Odeon simulations were used after the optimization procedure to further verify the design outcome. Such simulations evidenced that the optimization process lead to significant performance improvements without compromising the architectural concept [255–261].

Figure 30. Philharmonie de Paris. Image courtesy © William Beaucardet.

Elbphilharmonie Concert Hall

Design: Herzog and de Meuron, Acoustics: Nagata Acoustics; Hamburg, Germany, 2017

The design of the main concert hall of the Elbphilharmonie, the "Grosser Saal" (Figure 31), is based on the vineyard configuration and features 2100 seats and a volume of 23,000 m^3. The APBD approach informed the design of the 10,000 unique acoustic diffusive panels that line the ceiling, walls and balustrades of the venue, whose engraved pattern has been defined through a generative design process. The development of the project involved the use of an acoustic simulation tool, parametric modeling and optimization systems. Moreover, a 1:10 scale model was also used to test the efficacy of the customized diffusing panels in eliminating long path echoes. Each group of seating of the audience is served by unique gypsum fiberboard panels, to create a balanced reverberation across the entire hall. Their design, which is the result of a close collaboration between acousticians and architectural designers, combines acoustic performance and aesthetics through an irregular pattern of "seashell" cells engraved in their surfaces. The APBD method has been followed in the design of the "seashell" pattern, which is optimized to diffuse sound waves over

the seating of the audience and to eliminate detrimental echoes. The cells of the pattern feature a width ranging from 40 to 160 mm, and a depth ranging from 10 to 90 mm. In particular, in locations where it was required to eliminate echoes, the sound scattering performance of the panels were enhanced by the greater depth of the engraved cells, which measures 50–90 mm, while when soft reflections are desired, the cells feature a depth in the range of 10–30 mm. The generation of the pattern of the panels was performed by a custom algorithm, able to define a unique solution for each panel to meet the acoustic requirements. In addition to acoustic simulations, also scale model measurements were used to verify the results of the simulation and ensure the effectiveness of the pattern in echoes suppression [262–266].

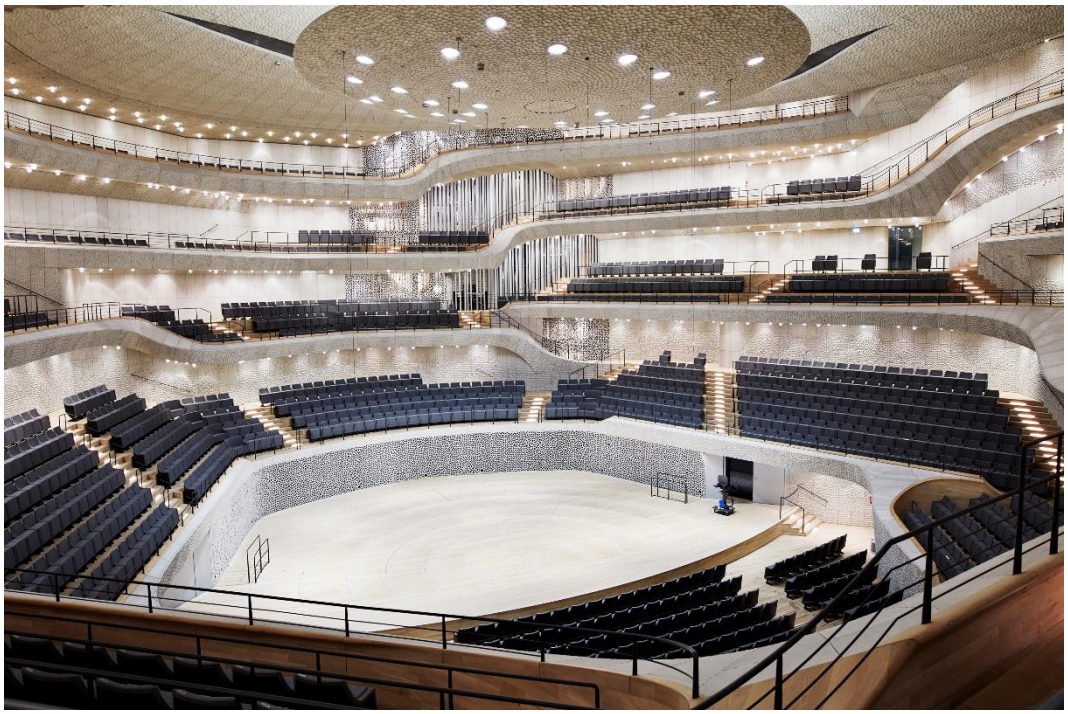

Figure 31. The "Grosser Saal" of the Elbphilharmonie. Image courtesy © Maxim Schulz.

Anneliese Brost Musikforum Ruhr

Design: Bez + Kock Architekten; Acoustics: Kahle Acoustics, Müller-BBM; Bochum, Germany, 2016

The project is the winning proposal of the design competition for the concert hall for the Bochum Symphony Orchestra, which called for a shoe-box venue with a volume of 14,000 m^3, visual intimacy and less than 1000 seats. The concert hall developed by Bez + Kock Architekten conciliates these conflicting goals by locating almost 1/3 of the required volume above the sound-transparent grid-ceiling (Figure 32). The final solution combines elements of the shoe-box and of the vineyard configurations, as the audience surrounds the orchestra. The sense of intimacy is further enhanced by the concave-curved shapes featured by the fronts and undersides of the balconies located at the sides of the venue. The APBD method informed the design of these surfaces as well as that of the acoustic canopy

suspended above the stage. The architectural team collaborated with the acoustic consultants in the design process of these elements, which was developed using parametric models created in Grasshopper and a custom acoustic simulation tool integrated in the modeling environment. In plan, the curved profiles of the sides and undersides of the balconies were initially determined on the basis of two center-points, one in the conductor's position and one in the middle of the parterre. In order to prevent the creation of sound focuses and echoes resulting from the curvature, these surfaces were segmented, and the curvature and vertical tilting of each portion was optimized based on acoustic simulation feedbacks to provide beneficial sound reflections, enhancing clarity and acoustic envelopment. The acoustic canopy located above the stage is made of five double-curved and dynamically shaped panels made of gypsum fiber board. The form of the panels of the canopy was optimized iteratively considering acoustic and architectural goals and their final configuration, which features varying curvatures in cross section, enhances the diffusion of the percussion and brass in the venue. Odeon simulations were performed in late design phases for verification purposes and found good agreement with the results of the simulations employed to support the design optimization [267–269].

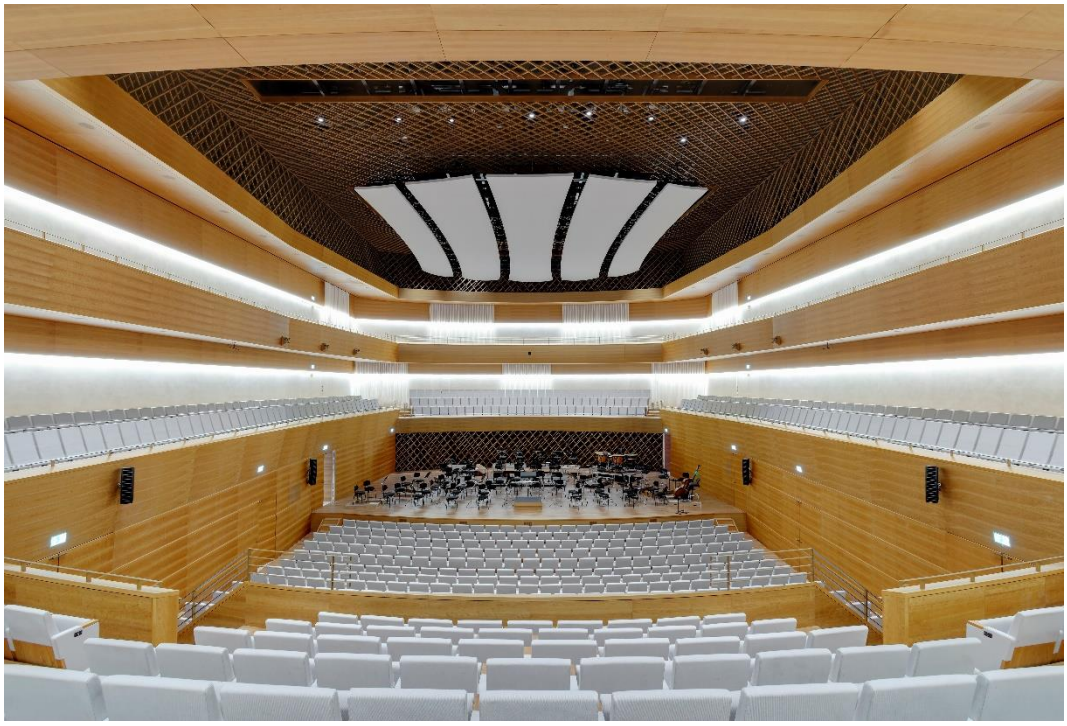

Figure 32. Anneliese Brost Musikforum Ruhr. Image courtesy © Mark Wohlrab/architektur-photos.de.

Concert Hall of Ureshino Cultural Center

Design: AnS Studio, SUEP Architects; Acoustics: Nagata Acoustics; Ureshino, Japan, 2014

The concert hall (463 seats) is part of the Cultural Center of the city of Ureshino and features a shoe-box configuration with a folding roof (Figure 33). In the design of

the roof of the concert hall, origami design and acoustic engineering were combined in order to meet the acoustic performance requirements. APBD informed the design of the folding roof of the venue, whose final shape is the outcome of an interactive design method, which combined a parametric origami software (i.e., a software able to generate different folding patterns based on origami rules), a custom acoustic simulation program and an optimization tool. The acoustic performance requirements for the venue proposed by the acoustic consultants were a uniform distribution of sound over the hall and audience within 30–90 ms, and the absence of echoes and sound focuses. The design method followed three steps. Initially, all the possible design alternatives for the folding roof were generated by the origami program, according to origami rules and the constraints set by the design team, which were related to building regulations, budget, structural aspects and other criteria. Each solution was then analyzed with the custom acoustic simulation program, with respect to the sound propagation and the distribution of sound at the audience positions. Finally, based on the simulation feedbacks, the optimization tool was used to find the solution, which showed the best combination of parameters to balance architectural and acoustic goals. The final solution for the roof, which was selected by the optimization program among a pool of about 200 design alternatives, is based on the Miura-ori folding pattern [270], where the folding depths and angles have been selected based on acoustic simulation feedback [235,271].

Figure 33. Concert Hall of Ureshino Cultural Center. Image courtesy © Kai Nakamura.

University of Iowa Concert Hall

Design: LMN Architects, Neumann Monson Architects. Acoustics: Jaffe Holden; Iowa City, IA, USA, 2016

The 700 seats-concert hall represents the main venue of the Voxman Music Building of the University of Iowa. The concert hall is based on the shoe-box

configuration and features a sculpted structure suspended from the ceiling, made of 946 unique folded aluminum composite modules, which was generated through performance-based design (Figure 34).

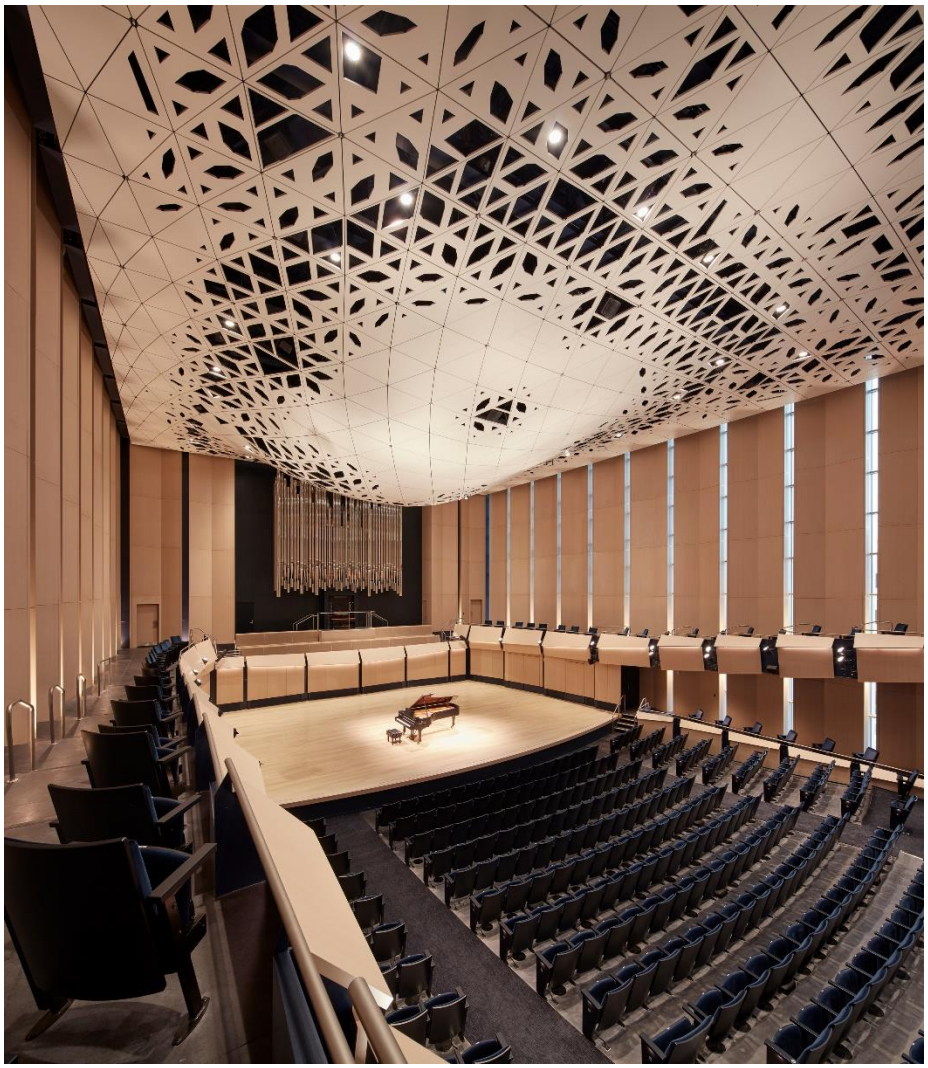

Figure 34. University of Iowa Concert Hall. Image courtesy © Tim Griffith.

The structure integrates and rationalizes in a unique and aesthetically unified solution five technical systems: acoustics, stage lighting, house lighting, audio-visual and fire protection. The form-finding process, which guided the design of the structure was enabled by a collaborative parametric model developed in Grasshopper, which was optimized in light of the objectives defined by the consultants of the different disciplines involved. The project was guided by an iterative design method and was also optimized for fabrication and to be delivered in a low-bid procurement environment. As regards acoustics, the feedbacks from a custom ray-tracing simulation tool, developed in collaboration with the acousticians, were used to drive the design optimization process of the ceiling system. This enabled the architects to autonomously run preliminary acoustic analyses to test the design iterations in early design phases. In particular, the form of the ceiling system was progressively refined to ensure an even distribution of the reflected sound waves towards the audience and

toward the upper portion of the side walls. Given the number of disciplines involved, SketchUp [272] and Revit [273] versions of the parametric model had to be used to allow exchanges among the different consultants. Early prototypes of panels and connections of the ceiling system were produced at different scales and tested. Iterations between physical and digital models were used to further refine the project and explore different fabrication strategies. Great commitment was placed in optimizing the fabrication of the system, and direct-to-fabrication data for construction could be generated from the model [274–276].

Symphony Hall of the Fuzhou Strait Culture and Art Centre

Design: PES-Architects, Acoustics: Tongji Architectural Design Group, Kahle Acoustics and Akukon; Mawei New Town, Fuzhou, China, 2018

The Fuzhou Strait Culture and Art Centre includes a 1000 seat symphony hall and a 1600 seat opera hall, both of which were developed with the APBD approach.

The symphony hall of the Strait Culture and Art Centre in Fuzhou features a vineyard configuration and, despite the relatively modest seat capacity, is meant to host a full symphony orchestra of more than 100 musicians (Figure 35). In order to prevent overly loud acoustics, its volume was set at 17,000 m^3 and was visually divided in two parts by the suspended reflectors, which overlook the audience. The curvature of the suspended reflectors ensures an even coverage of early reflections, but the major role is played by the walls of the halls, which are shaped as convex sphere portions. The walls that separate the terraces of the audience and those at the periphery of the hall are inclined in a petal-like configuration. The lower portions of these elements generate early reflections, while the upper parts spread the sound energy in the venue. The surface of the petals is coated with ceramic tiles with different textures and patterns, to provide either specular or diffuse reflections. The APBD approach informed the design of the geometrical features and surface patterns of these petals. Grasshopper was used to generate the parametric models, while a custom tool integrated in the modeling environment was used to analyze the acoustic performance according to the early acoustic efficiency approach [277]. As regard the geometrical features, the distribution and vertical tilting angles of the “petals” were optimized to provide early lateral reflections to all the audience blocks. The surface pattern of specularly reflecting or diffusing ceramic tiles was used generate useful early reflections and to prevent undesired echoes from the upper portions of the petals. Since it was considered crucial to maintain strong early reflections, the sound diffusing tile pattern was applied only in the portion of the petals creating potentially harmful late reflections, while the remaining part was left with a specularly reflective finish. Such surfaces were identified by using a custom algorithm able to categorize the surface facets based on the delay of the reflections they may generate, considering the combined data from four sound source positions. Although the surfaces were identified by the algorithm, when conflicting feedbacks were found, the final decision was left to the operator. Odeon simulations were used in late design phases for verification purposes [278].

Figure 35. Symphony Hall of the Fuzhou Strait Culture and Art Centre. Image courtesy © Marc Goodwin.

Opera Hall of the Fuzhou Strait Culture and Art Centre

Design: PES-Architects, Acoustics: Tongji Architectural Design Group, Kahle Acoustics and Akukon; Mawei New Town, Fuzhou, China, 2018

The 1600-seat opera hall (volume 14,500 m^3) is based on the horseshoe configuration and features a continuous skin, with convex and concave curvatures, which defines and unifies walls, balconies and ceiling (Figure 36). The APBD approach was applied to define the form of the skin, which was optimized in order to meet the acoustic requirements of creating a homogenous coverage of strong early lateral reflections over the entire audience and to avoid undesired focusing effects. The acoustic simulations were performed with a custom tool based on a differential ray-tracing technique [279], integrated in the modeling environment. Since the architectural elements are not present as individual entities but are interlinked by the skin, they could not be singularly adjusted, as any form change would impact on the other elements. Therefore, the continuous envelope was modeled parametrically in Grasshopper, and directly optimized based on the acoustic feedbacks, due to the close collaboration between the architectural and acoustic teams. In particular, the skin was subdivided in smaller patches, and each was assigned with an acoustic target, such as creating early reflections or enhancing late reverberation. The orientation of the different skin portions was then iteratively optimized by the operators in order to achieve their target performance requirements and then combined to create the final smooth curved skin. A fine-scale texture of flower-shaped ceramic tiles is applied to the surfaces of the continuous skin; the small irregularities of the pattern provide sound scattering at high frequencies. The final outcome of the optimization was further tested in Odeon; the verification confirmed the benefits provided by the application of APBD [278,280].

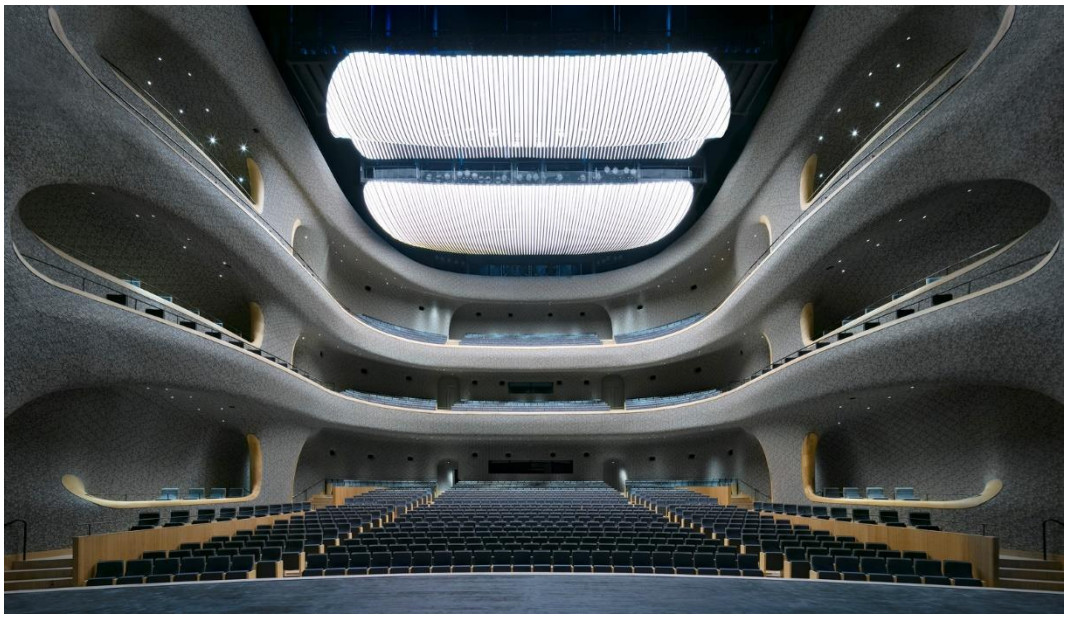

Figure 36. Opera Hall of the Fuzhou Strait Culture and Art Centre. Image courtesy © Marc Goodwin.

Conga Room

Design: Belzberg Architects, Acoustics: Newson Brown Acoustics; Los Angeles, CA, USA, 2008

The Conga Room dance club hosts a series of a multitude of programs (dance hall, stage, restaurant, bars and VIP areas) and is located at the second floor of a multipurpose building, mainly occupied by offices. Due to a retrofit intervention, the existing spaces were acoustically insulated and adapted to host the new mixed functions. The bold design of the undulating ceiling system is meant to visually attract clients while also providing acoustic treatment for the dance hall (Figure 37). The ceiling was indeed identified as the most effective location for acoustic treatments to provide sound insulation and amplification. The ceiling system was developed through performance-based design, exploiting the functions offered by CATIA [281] and Rhinoceros for modeling, and Ecotect [282] for the simulations. The ceiling system, made of CNC-milled plywood panels whose pattern and fashion changes differentiate the various environments of the club, was designed to address acoustic issues and to integrate several building infrastructures (house lighting, mechanical, audio-visual, fire protection, etc.). The model of the ceiling structure was iteratively optimized based on the feedback from the various specialists involved and performance simulation. In particular, the ceiling panels over the dance hall are morphed into flower-like structures, which control the acoustic performance of the ceiling. The different arrangements and tilting of the flowers' petals have been optimized based on acoustic simulation feedback to provide the desired amount of sound absorption [283–286].

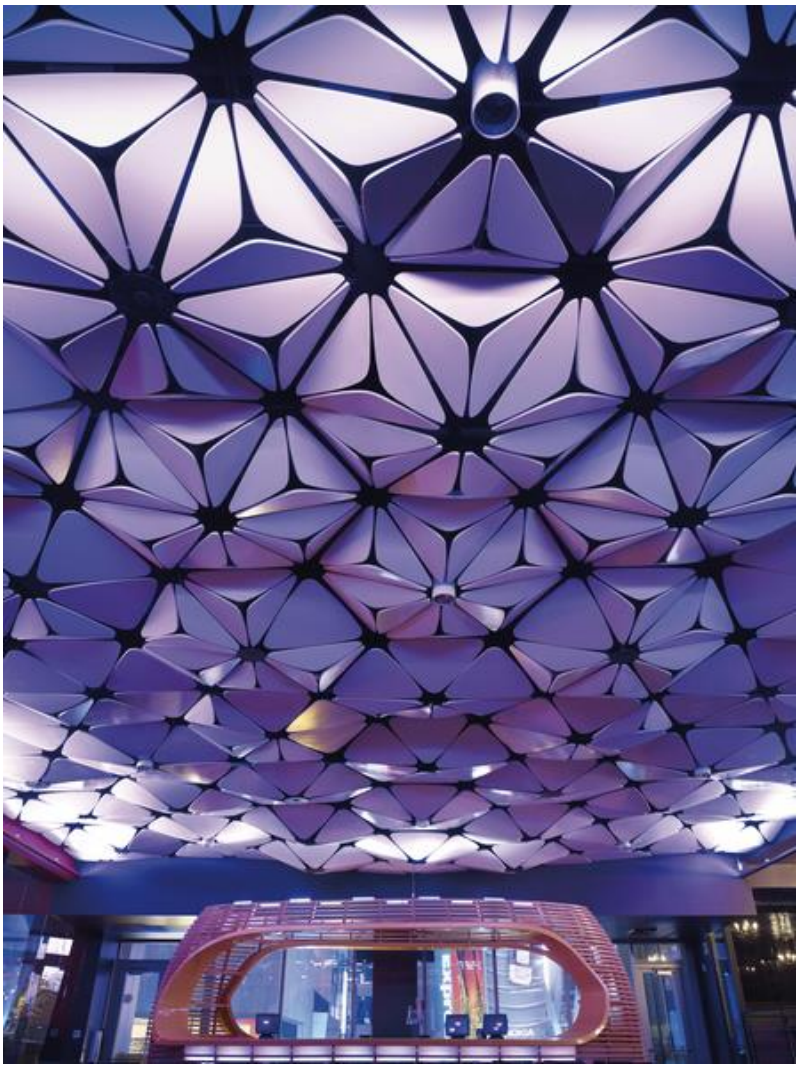

Figure 37. Conga Room. Image courtesy © Benny Chan/Fotoworks.

Stage by the Sea

Design: Flanagan Lawrence Architects; Acoustics: Arup Acoustics; Littlehampton, UK, 2014

The project consists of two double-curved concrete shells located close to the coastline of Littlehampton, United Kingdom. The smaller shell works as a shelter, while the bigger one is an acoustic shell that is used as a stage for outdoor concerts and projects the sounds towards the listeners (Figure 38). During the design process of the acoustic shell, great commitment was placed in combining structural, acoustics and aesthetic goals in a unique solution. The final design of the acoustic shell is the result of an ABPD process, and conjugates the key acoustic performance requirements with architectural and structural objectives to create a durable, effective and inexpensive solution. The design process involved the use of Grasshopper for Rhinoceros for modeling, Dynamo for Revit [273,287] for the acoustic simulations and Galapagos for the design optimization. The design of the structure was developed in a tight collaboration between architects and technical consultants, which enabled us

to find the best compromise in overall terms. The digital model of the shell was exchanged among the professionals involved more than twenty times before its final configuration was achieved. The acoustic analysis enabled one to define a shape for the acoustic shell able to effectively support outdoor concerts by reflecting the sounds towards the audience located in the facing sunken garden, allowing the music to be perfectly heard in windy conditions at a distance of 50 m from the stage [288–292].

Figure 38. Stage by the Sea. Image courtesy © Flanagan Lawrence.

Resonant String Shell (ReS) 6.0

Design: Sergio Pone, Bianca Parenti, Daniele Lancia, Sofia Colabella; Acoustics: Serafino Di Rosario; Acireale, Italy, 2017

ReS is a temporary outdoor acoustic shell that hosts the classical music concerts of the yearly festival “Villa Pennisi in Musica”. The shell design combines acoustic concerns with structural and technological ones. During each edition of the festival, a prototype of a temporary outdoor acoustic shell is built in the framework of a summer school, and its performance is tested though acoustic measurements. From year to year, the design of the shell is optimized based on the measured acoustic performance and a new design is developed to be built in the following edition. The acoustic shell built in 2017, named ReS 6.0 (Figure 39), was developed exploiting a multiobjective optimization process to define the geometry of the shell. In particular, the inner profile of the shell, which is composed of wooden reflective panels, anchored to an already defined structural system made of arches, was optimized within a magnitude of 50 cm. The process was enabled by Octopus [232], a multiobjective optimization tool, Grasshopper and a custom acoustic simulation tool based on an image-source method. Considering three pairs of sound sources located within the shell (i.e., music performers), the profile of the shell was optimized to maximize the evenness of sound energy in the audience positions. The sound energy was described by the sound pressure level and the standard deviation was calculated to quantify its

rate of homogeneity. For each couple of sound sources, the sound pressure level has been estimated using the custom acoustic simulation tool, and Galapagos was used to search for solutions able to minimize the standard deviation. The optimization process identified a set of "equally optimal" solutions, among which the final configuration was selected by considering also aesthetic criteria. CATT-Acoustic was used in late design phases to run more accurate analyses of the optimized shell. The field measurement confirmed that the form optimization leads to a greater and more uniform distribution of sound energy in the audience [248].

Figure 39. ReS 6.0. Image courtesy © Daniele Lancia.

Soundforms

Design: Flanagan Lawrence Architects; Acoustics: Arup Acoustics; London, UK, 2012

Soundforms is a movable acoustic shell designed to support outdoor classic music performances, by improving the ability of musicians of the ensemble to hear each other, and by projecting the sound generated towards the audience. A prototype of the shell, developed for small chamber music orchestra, was built and tested in London's Dockland, and was then selected to be installed in the Olympic Park for the 2012 London Olympic Games to host music concerts during the event (Figure 40). The acoustic performance was one of the major drivers of the design process, aside with the development of the structure and its optimization for transport and assembly. The shell form was developed from a portion of torus, and features an upper peak, which was designed to project as much sound as possible towards the listeners, playing a role similar to that of the ceilings of concert halls. The shell has an inflatable skin made of eight PVC coated polyester cushions, fixed to the truss structure. The side walls of the acoustic shell, which performs as reflectors, are integrated in the

inner structure of the shell and are visually covered by an acoustically transparent fabric liner, thus enabling one to maintain the visual aspects of the shell without compromising their acoustic performance. Removable reflective panels are installed within the shell, with the objective to balance the amount of sound energy diffused towards the orchestra and projected towards the audience. The APBD method informed the development of the convex profiles of the reflectors, as well as their deployment within the shell, which, in the built prototype, were optimized for a small chamber orchestra. The optimized reflectors were developed by the acoustic consultants in close collaboration with the design team, following a process of subsequent optimization combining architectural and acoustic objectives with fabrication and constructability criteria. The reflectors facets were parameterized in Grasshopper, the acoustic simulations were run using a custom ray-tracing script in Dynamo for Revit, while the optimization process was performed with the support of automated routines using Galapagos. The final solution was then further tested in Odeon to validate the results [234,293–295].

Figure 40. Soundforms. Image courtesy © Nick Guttridge.

Tiara Acoustic Shell

Design and acoustics: Alban Bassuet, Willem Boning, Arup Acoustics; Fishtail, MT, USA, 2014–2015

The design of the acoustical shell for the Tippet Rise Art Center was commissioned to Arup Acoustics in 2014. The demountable and transportable shell was initially designed to host and support outdoor chamber music concerts for an audience of 50–60 people, by creating an intimate performance space, visually open to the surroundings natural environment (Figure 41). The shell is made of wooden

panels, which represent the upper corners of the side and front corners of a fan-shaped room, while the rest of the enclosing surfaces were removed to open the view towards the natural setting.

Figure 41.. Tippet Rise Art Center, MT. Photo: Erik Petersen © 2017 Tippet Rise.

The goal was to generate a unified acoustic environment for both audience and performers and an enveloping sound impression, despite the lack of reverberation. The virtual model of the shell was parameterized using Grasshopper. The acoustic performance of the structure was investigated using a custom simulation tool based on an image-source method; a source position and 50 receiver positions were used. Based on the performance feedbacks, Galapagos was used to optimize the parametric model by adjusting six parameters controlling the shell form, in order to ensure a broad spread of early energy over the entire audience. The variation space of the model parameters was set based on structural requirements, and in order to prevent the shell from obscuring the view of the mountain in the background. The fitness function counted the second and third order of reflections over the “poorest” receivers of the audience. From the two solution regions found by Galapagos, the design team selected the final one based on structural criteria. In 2015, the initial design solution was further expanded in order to accommodate up to 80 people, by the addition of two kinks to the structure, which were optimized with a procedure similar to that used for the initial solution. The final configuration of the shell provides on average 5.6 s- and third-order reflections to each receiver, with a minimum of one from the front, one from the right side and one from the left side [296].

Aalborg Acoustic Pavilion 2011

Design and acoustics: AREA, Electrotexture Lab; Aalborg, Denmark, 2011

The temporary acoustic pavilion was developed within a research framework. The structure is meant to host electronic music performance and its design was optimized for both acoustic performance and constructive feasibility. The structure is composed of CNC milled plywood plates, which works as sound reflectors (Figure 42).

Figure 42. Aalborg Acoustic Pavilion 2011. Image courtesy © Isak Worre Foged.

The design process was enabled by the combined use of Grasshopper, a custom acoustic simulation tool and Galapagos solver, which allowed one to combine acoustic goals with production and assembly criteria. The pavilion was also optimized with the aim to open its geometry towards the water while closing it towards the close-by road, to shield it from traffic noise. During the design process, the design problem has been progressively reformulated, in order to reduce the variation space evaluated by the Galapagos solver. With respect to acoustics, the volume of the pavilion and the configuration of the reflectors, which define the envelope of the shell, were optimized in two subsequent steps. In order to prevent the structure from altering the electronic music spread via a loudspeaker, the optimization processes aimed to minimize the reverberation time within the pavilion, calculated with the Sabine equation. This goal was reached by maximizing the number of reflections occurring among reflectors, thus enhancing sound absorption, and by directing the reflected sound away from the pavilion. The optimization was performed considering different sound source positions, which marked the loudspeaker locations in the corners of the pavilion. In particular, the arrangement of the specific set of reflectors serving each loudspeaker was optimized to maximize sound absorption by increasing the number of reciprocal

reflections. In the end, the final solution was slightly refined to meet the fabrication requirements [297,298].

Aalborg Acoustic Pavilion 2012

Design and acoustics: AREA, Mads Brath Jensen; Aalborg, Denmark, 2012

The pavilion is composed of an origami folded structure made of triangular wooden panels (Figure 43). The temporary pavilion was developed for research purposes and is intended to host two subspaces with different purposes, which are therefore characterized by dissimilar acoustic performance. A design optimization process was set in the in order to create two areas with opposite acoustic proprieties within the pavilion: a zone intended for classical music performances, featuring a long reverberation time, and an area intended for speech, with a short reverberation time. The tools used in the development of the acoustic pavilion are Grasshopper, a custom acoustic simulation tool and Galapagos solver. The acoustic performance on the listener positions was described by the reverberation time, calculated with the Millington-Sette equation, and by sound pressure level, simulated using a custom ray-tracing tool. The parametric model of the pavilion was composed of two subsystems: the first controls the overall space form, which resemble a tunnel; the second defines the folding structure and presents a higher control point resolution. The panels of the pavilion feature a sandwich structure with foam in the middle layer and plywood on both sides. Three panel variants were developed in order to provide three different rates of sound absorption, by opportunely perforating the interior plywood side of the panel, and therefore exposing the sound absorptive foam layer to the impinging sound waves. The optimization process was able to control the orientations of the control point of the primary and secondary subsystems, as well as the acoustic variants of the wooden panels, which compose of the structure. After 700 iterations, the reverberation times in the two subzones of the design solutions generated by the optimization process stabilize at values of 0.2 s and 1.4 s [299].

Figure 43.. Aalborg Acoustic Pavilion 2012. Image courtesy © Isak Worre Foged.

Resonant Chamber

Design: RVTR; Acoustics: Arup Acoustics; Ann Arbor, MI, USA, 2012

Resonant Chamber is a responsive acoustic envelope system, based on rigid origami principles, that is able to dynamically alter the sound environment in which it is installed based on a set of inputs collected in real time by sensors or using preprogrammed configurations (Figure 44).

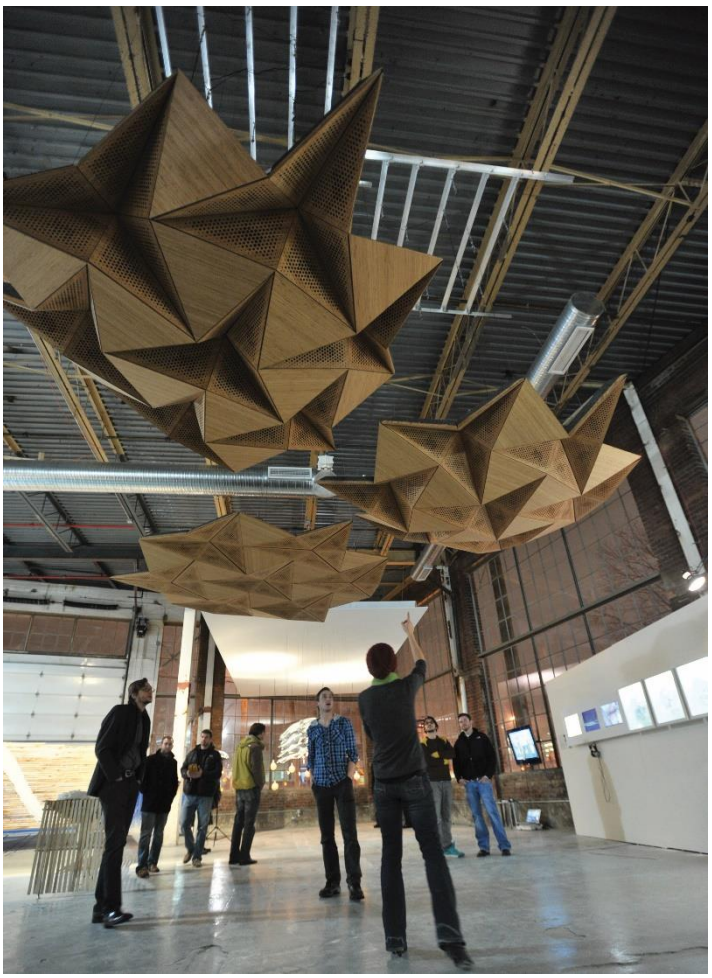

Figure 44.. Resonant Chamber. Image courtesy RVTR © Adam Smith.

The flexible structure can be deployed in a music venue to alter the sound during the performance, playing the role of an instrument at the architectural scale itself, or can be installed in more ordinary spaces, to calibrate their acoustic performance to given requirements. The faceted "sound cloud" is able to dynamically transform its configuration in response to acoustic changing conditions and to variations in the listeners' positions. The tools used to develop the project were Grasshopper, a ray-tracing tool for acoustic simulations and Kangaroo [300], to model the dynamic deformation of the system. The structure is made of a combination of different plywood panels, featuring either sound reflective, sound absorbing or electroacoustic properties, arranged around an electronic panel that contains circuit controls and sensing inputs. In response to the inputs, such as ideal reverberation time, absorption

coefficient, directional amplification and early/late acoustic response, the system adjusts its acoustic properties. In particular, resonant chamber modifies the acoustic performance of the space within which it is installed by gross deformations of its shape, able to alter the aural volume, and by locally adjusting the folding configuration, to change the panels exposed to the sound waves. The optimal geometry and the characteristics of the materials were determined by acoustic simulations and measurements on physical prototypes [301–305].

Courtyard Enclosure of Smithsonian Institute

Design and acoustics: Foster + Partners; Washington, DC, USA, 2007

The design of the courtyard enclosure for the Smithsonian Institute's Patent Office, an historic building in Washington, was developed in the framework of an invited international competition, won by Foster + Partners. APBD informed the design of the courtyard enclosure, which is a complex roof structure meant to perform at the same time as a solar shade, an acoustic absorber and a weather protection device. The proposal consists of a glazed undulated canopy, which features a diagonal grid of structural beams and is supported by eight columns arranged in three domes (Figure 45). Since the space underneath was meant to be flexible and hosts a variety of events, such as receptions, seated dinners and music and theatrical performances, the acoustic treatment was integrated in the bearing structure of the canopy. The Specialist Modeling Group, a research team within Foster + Partners, developed a custom generative script able to control the entire roof system based on a set of parameters, allowing for exploration of a wide range of design alternatives. During the design process, the different design goals were mutually related and synthesized by the generative tool, which was constantly adapted as the design requirements became more specific. The acoustic performance goal was to reduce the reverberation time between 2 and 3.5 s. To this aim, the structural beams of the canopy were designed to work as sound absorbing devices. The sound absorbing layers of mineral wool were mounted at the sides of the core steel structure of the beam and were covered by layer of thin steel tubes. The latter layer, while visually hiding the sound absorbing material, is "transparent" to sound, exposing the sound absorbing filling to the impinging sound waves. To provide the desired reduction of reverberation time, the area of the sound absorbing material was a key parameter in the generating algorithm. Although acoustic simulations were not integrated in the modeling tool, the digital models of the enclosure could be easily exported to be analyzed in the external software. Ultimately, the final solution for the roof was the result of more 400 design iterations explored during a period of 6 months [306–309].

Figure 45. Courtyard Enclosure of Smithsonian Institute. Image courtesy © Brady Peters.

Other Spaces

FabPod

Design and acoustics: Nick Williams, Brady Peters, John Cherrey, Jane Burry, Mark Burry, Alexander Peña De León, Daniel Davis; Melbourne, Australia, 2013

The project is an acoustic enclosure for meetings, able to host eight people, housed in an open-plan office at RMIT University (Figure 46).

The FabPod project is part of a research investigating the sound diffusing properties of hyperboloid surfaces, which was previously explored on a prototype wall in 2011. The acoustic design imperatives were to reduce the sound transmission through the enclosure and to provide a homogeneous internal acoustics that was conductive to small meetings, without creating an acoustically "dead" space. In order to meet these objectives, the FabPod combines sound absorption and sound diffusion within the cell, creating a diffuse sound field by exploiting the sound scattering properties of hyperboloid surfaces. A similar strategy was applied also to the outer side of the installation, with the aim to improve the auditory experience in its surroundings. The project is intended as a flexible structure, able to be applied to a range of scenarios, and therefore great consideration was dedicated to fabrication quality and mass-customization. APBD was applied to the definition of the overall

enclosure form and to the geometrical and material properties of the surface pattern. Three material options were developed for the facets of the interior surface (plexiglass, metal and felt), featuring different rates of absorption. The parametric model of the structure was defined in Grasshopper and four different workflows were developed, each one using a different acoustic simulation tool, to design either the enclosure form or the pattern of hyperboloid blocks. Pachyderm Acoustics and Odeon, which are based on geometrical acoustics, were used to analyze the form of the enclosure, and two custom wave-based acoustic simulation tools were used to simulate the acoustic performance of the hyperboloid surfaces. Different acoustic parameters were taken into account, including reverberation time, sound pressure level, speech transmission index (STI) and the scattering coefficient. The final design consists in a semi-enclosed envelope, which wraps around the meeting area and is composed of an irregular pattern of 180 unique hyperboloid blocks, featuring different acoustic properties [310–315].

Figure 46. FabPod. Image courtesy © John Gollings.

Manufacturing Parametric Acoustic Surfaces (MPAS) project

Design and acoustics: Brady Peters, Martin Tamke (CITA); Barcelona, Spain, 2010

The temporary project was installed at the Smart Geometry 2010 Workshop and Conference and consists of a curved wall composted of different panel types, which generates different types of acoustic subspaces (Figure 47). The project explores new forms and material compositions and digital fabrication techniques. The APBD approach was applied to the design of the undulating from of the wall and to the panel composition. The design of the installation was developed in GenerativeComponents with the support of generative computer scripts, while acoustic simulations were run

in Odeon. The acoustic goal was to create different acoustic subspaces in the surroundings of the installation: from a quiet, enclosed area, characterized by a high rate of sound absorption, to an amplified sound area, generated by sound reflective surfaces, with a gradient of acoustic performance between the two conditions. Such different acoustic performance could not be effectively described by the reverberation time alone; therefore, a number of other acoustic parameters were introduced in the analyses, such as early decay time, speech transmission index and sound pressure level. Moreover, auralizations were used to listen to the sonic environments generated by the installation prior to its construction. The acoustic performance drove the design of both the overall shape of the installation and its panel composition. Nine panel types with different acoustic performance were designed and opportunely integrated in manufacturing parametric acoustic surfaces (MPAS) in order to produce the desired acoustic effects. The collection of panel typologies includes a sound absorbing panel, different types of sound diffusing panels, variously perforated screens, a panel with different properties depending on the direction of the impinging sound and a "sound window", which provided visual connection from one acoustic space to the other. Based on acoustic performance feedbacks, the geometrical form of the wall and its panel composition were controlled to generate the different acoustic subspaces in the surroundings of the installation [306,316–318].

Figure 47. MPAS project. Image courtesy © Brady Peters.

Distortion II

Design and acoustics: Brady Peters, Martin Tamke, Stig Nielsen (CITA); Niels Jacubiak Andersen (Krydsrum); Magnus Gustafson and Patric Gustafson (Akustikmiljo)); Copenhagen, Denmark, 2011

Distortion II is an experimental research project developed to create a bending acoustic surface able to create visual and acoustic effects within an open-plan space (Figure 48).

Figure 48. Distortion II. Image courtesy © Anders Ingvartsen.

The temporary structure is composed of a folded surface, made of composite plates arranged in a series of trihedral corners with different dimensions and orientations. Four different digital production techniques were used in the installation, i.e., laser cutting, knife cutting, CNC routing and metal bending, and fabrication files were generated by a custom tool. The installation explores the potentials of acoustic subspaces (see also MPAS project) and creates a sound-amplified area and a sound-dampened zone. To this aim, the APBD approach was applied to define the materials, the level of enclosure of the structure and the geometry of the panels to control sound reflections. The acoustic parameters used to define and measure the inhomogeneous acoustic space surrounding the installation were reverberation time, early decay time, sound strength and an experimental parameter (STV IA-diff) [319,320]. Two design workflows were used in the development of the project: in the first Odeon was used to run the acoustic simulation, while in the second the acoustic analyses were directly run within the modeling environment using a custom ray-tracing tool, to provide instantaneous performance feedback for the optimization process. The latter workflow was only used in conceptual phases, while Odeon was extensively used in subsequent ones to accurately calculate the different acoustic parameters considered. The plates that compose the installation feature opposite acoustic properties on their sides, being composed of a layer of sound absorbing material, a structural MDF panel and a layer with a sound-reflective aluminum face. The arrangement and materials of the plates of the trihedral corners were optimized through an iterative routine to generate the two acoustic subzones. In the sound-amplified zone, the plates sides feature sound reflective properties and are arranged in order to create focusing, while on the sound-

dampened area, the faces of the plates feature sound absorptive properties and their configuration promotes sound diffusion [319,321].

4A.3 Discussion

The information regarding the design processes of the case studies is summarized in Figure 49- where the case studies within the categories “music venues” and “other spaces” have been further classified in accordance with their architectural typologies. The table gathers information regarding the primary functions, the design features developed with APBD, as well as regarding the procedures and tools used in the development of the projects.

		NAME	PRIMARY FUNCTION	FEATURES TO WHICH APBD WAS APPLIED	AUTOMATED/ MANUAL	DIGITAL TOOLS EMPLOYED
MUSIC VENUES	concert halls	PHILHARMONIE DE PARIS	music performance	geometry of nuages, fronts and walls of balconies	with automated processes	Rhinoceros, Grasshopper, Maya, Odeon
		ELBPHILHARMONIE	music performance	surface pattern of the diffusing surfaces	with automated processes	Rhinoceros, parametric modeling software, custom acoustic simulation tool, optimization program
		ANNELIESE BROST MUSIKFORUM RUHR	music performance	overall geometry of the canopy, balcony front and undersides	manual processes	Rhinoceros, Grasshopper, custom acoustic simulation tool, Odeon*
		CONCERT HALL OF URESHINO CULTURAL CENTER	music performance	overall geometry and folding pattern of roof	with automated processes	parametric origami generator, custom acoustic simulation tool, optimization program
		UNIVERSITY OF IOWA CONCERT HALL	music performance	overall geometry and surface pattern of the ceiling system	manual processes	Rhinoceros, Grasshopper, custom acoustic simulation tool
		FUZHOU SYMPHONY HALL	music performance	geometry and surface pattern of the “petals”	manual processes	Rhinoceros, Grasshopper, custom acoustic simulation tool, Odeon
	opera hall	FUZHOU OPERA HALL	music performance	geometry of the continuous skin	manual processes	Rhinoceros, Grasshopper, custom acoustic simulation tool, Odeon
	dance club	CONGA ROOM	music performance	panel configuration of the ceiling system	manual processes	CATIA, Rhinoceros, Ecotect*
	outdoor acoustic shells	STAGE BY THE SEA	music performance	overall shape of the acoustic shell	with automated processes	Rhinoceros, Grasshopper, Dynamo for Revit, custom acoustic simulation tool, Galapagos*
		RESONANT STRING SHELL (ReS) 6.0	music performance	overall shape of the acoustic shell, components	with automated processes	Rhinoceros, Grasshopper, custom acoustic simulation tool, Octopus, CATT-Acoustic
		SOUNDFORMS	music performance	overall shape of the acoustic shell and reflectors	with automated processes	Rhinoceros, Grasshopper, Dynamo for Revit, custom acoustic simulation tool, Galapagos, Odeon*
		TIARA ACOUSTI SHELL	music performance	overall shape of the acoustic shell	with automated processes	Rhinoceros, Grasshopper, custom acoustic simulation tool, Galapagos
	pavilions	AALBORG ACOUSTIC PAVILION 2011	music performance	overall geometry of the pavilion and surface pattern	with automated processes	Rhinoceros, Grasshopper, custom acoustic simulation tool, Galapagos
		AALBORG ACOUSTIC PAVILION 2012	speech / music performance	overall geometry of the pavilion and surface pattern	with automated processes	Rhinoceros, Grasshopper, custom acoustic simulation tool, Galapagos
	indoor inst.	RESONANT CHAMBER	various performances (including music)	overall shape and configurations of the responsive system	manual processes	Rhinoceros, Grasshopper, custom acoustic simulation tool, Kangaroo
	enclosure	ENCLOSURE OF SMITHSONIAN INSTITUTION	various performances (including music)	overall shape of the courtyard enclosure	with automated processes	custom generative script, acoustic simulation tool
OTHER SPACES	meeting room	FABPOD	speech	overall geometry and surface pattern	manual processes	Rhinoceros, Grasshopper, Pachyderm Acoustics, Odeon, custom acoustic simulation tool
	indoor installations	MANUFACTURING PARAMETRIC ACOUSTIC SURFACES PROJECT	other	overall shape of the wall and panel configuration	with automated process	GenerativeComponent, Odeon, custom generative script
		DISTORTION II	other	overall shape of the wall and panel configuration	manual processes	parametric modeling tool, Odeon, custom acoustic simulation tool

* E. Badino, personal comunication

Figure 49. The table offers an overview of the projects, gathering relevant data on their architectural features and on the design development.

4A.3.1 Architecture and APBD

The collection of case studies shows a great degree of variation with respect to their functions and profiles: from world-renowned concert halls to more ordinary architectures, research projects and artistic installations.

Most of case studies are major projects, such as concert halls venues, developed by renowned architectural firms and acoustic consulting groups, or were developed as research projects. In the first case, the resources and specialized expertise that are often available to major architectural firms, along with the reliance on external consultants, enable an innovative approach such as APBD to be effectively applied. However, such resources are generally not available in more ordinary projects, especially when the architectural firms involved have no technical expertise on parametric modeling, acoustics and programming, as it is often the case. This result suggests that this procedure requires specialized expertise and resources, which are not commonly available for ordinary architectural projects.

Most projects are spaces meant to host music performance (16 projects out of 19), while only a small fraction of the projects is developed for other purposes (e.g., artistic installation, meeting room and multipurpose space). This suggest that the application of APBD is in line with the general trend of including acoustic concerns mainly in the development of spaces intended for music performances. However, certain projects, such as FabPod, Resonant Chamber and the Courtyard Enclosure of the Smithsonian Institution, shows the application of APBD for spaces intended for a wider variety of purposes.

Across the collection, APBD has been applied to either major or minor architectural features of the design, ranging from reflectors and pattern textures in concert halls, to the overall shape of smaller architectures, such as acoustic shells or artistic installations. In the design of concert halls, the main structure of the venue is generally based on well-known typologies (e.g., shoe-box, vineyard, etc.), while APBD is applied to reflective surfaces or diffusive pattern. In smaller intervention, such as pavilion and acoustic shells, APBD has been applied also to entirely shape the structures, often combining other goals, such as fabrication criteria. This highlights that PBD approach is often paired with a more conventional approach in large projects to better combine the large number of requirements, which need to be considered.

4A.3.2 Digital Workflows in APBD

APBD is normally applied due to the combined use of parametric modeling and acoustic performance simulation tools. Moreover, optimization tools can be exploited to automate the search of the most favorable solutions with respect to the target performance goals.

The parametric modeling tool that was used in the great majority of the considered projects is Grasshopper [227] for Rhinoceros [228]. Acoustic analyses were mainly run using custom tools based on geometrical acoustics, while the commercial package that was used the most is Odeon [241]. In many cases, optimization tools based on evolutionary algorithms, such as Galapagos [231] and Octopus [232], have been utilized to support the design process.

Parametric modeling eases the design optimization process, by allowing one to easily modify the design by controlling the model parameters. Grasshopper is one of the most commonly used parametric modeling tools. It is a graphical algorithm editor integrated in Rhinoceros, which is a commercial modeling tool widely employed in architectural practice. Grasshopper enables one to generate parametric models of complex geometries on the basis of algorithms set by the designer. Grasshopper does not require any programming knowledge and is therefore employed by designers with relative ease.

Currently, a wide number of acoustic simulation tools, such as Odeon, CATT-Acoustic, etc., are available, allowing professionals to quickly perform simulations based on geometrical acoustic methods. Odeon is the commercial package that was more widely employed in the collected case studies. Acoustic simulation tools require a solid acoustic knowledge base to correctly set up the simulation and interpret its results. In most cases, the acoustic knowledge of architectural professionals is not adequate to correctly employ these systems, making the reliance on external acoustic consultants unavoidable.

Another limitation is due to the lack of integration among simulation and modeling tools, which are generally stand-alone applications, and the limited interoperability resulting from the specific formats or geometrical models required to run the acoustic simulation. Some tools, such as the SketchUp plugin of Odeon [322], ease the file exchange between the modeling and simulation environments. However, the generation of specific model for acoustic analyses is often mandatory to meet the requirements of the simulation tools (e.g., geometrical simplification, watertight model and layer division by materials). Therefore, architectural design and acoustic performance analyses need to be run into two separated environments on specific virtual models, resulting in a time-consuming process, which often limits the number of model exchanges among professionals. As a result, design optimization in early design phases can be difficult to achieve from the feedback provided by these tools, which are more commonly used in late design phases for verification purposes, as shown in many case studies. A noteworthy exception in this frame is Pachyderm Acoustics [243], an open-source acoustic simulation tool integrated in Rhinoceros/Grasshopper, which was used in the development of FabPod.

In many case studies custom tools were employed to avoid the issues resulting from the poor level of interoperability and to perform specific analyses. For instance, the use of custom tool has been reported in 16 out of 19 case studies. Such tools are generally used in early design phases to provide quick estimations of the acoustic performance directly in the modeling environment.

Currently, different modeling platforms offer the possibility to the users to create custom programs (e.g., Rhinoscript, Grasshopper, Python, etc.) within their environment, widening the possibilities offered by the regular preset functionalities. In most cases, custom tools have been used in early design phases to run simplified performance analyses, easily visualize the results and optimize the design proposal accordingly. By clarifying the relation between acoustic and architectural design, these tools support an effective collaboration between architect and acousticians, and possibly the other technicians involved, enabling one to integrate different goals in the

design proposal. Custom acoustic simulation tools are generally based on geometrical acoustic technique and apply ray-tracing or image-source methods. The performance feedback obtained, although simplified, is considered accurate enough to orient the design decision in early design phases. In many cases, more accurate analyses were run in late design phases with commercial acoustic simulation tools to further validate the results. Following a different approach, custom tools can be used to run sophisticated acoustic analyses, such as wave-based ones, which at the time of writing are not included in any commercial acoustic simulation package. In wave-based simulations, the wave behavior of sound phenomena, which are normally neglected in geometrical acoustic simulations, can be accurately simulated in 2D and 3D environments. For instance, in the development of FabPod, wave-based acoustic simulations were used to assess the scattering performance of the surfaces, which could not be accounted with geometrical acoustic techniques. In the most recent times, wave-based tools as Treble Acoustic Simulation Suite [323], has markedly widen the simulation possibility to architectural designers and consults, allowing to quickly run wave-based simulation and to hear in real time the auralizations of the space. This allows to experience the difference among design proposals, facilitating the understanding of the acoustic implications of design options, especially for acoustically untrained decision makers.

Despite the wide range of possibilities offered by custom tools, the programming skills and acoustic knowledge required in their development and application are normally not available to architectural firms. However, currently the availability of several online coding courses and of platforms such as ACOUCOU [324], which offers free education materials on acoustics, may help to fill the gap. Furthermore, the introduction of PBD approach in architectural education would help students to become more familiar with building performance and simulation tools. Some of the case studies analyzed (e.g., ReS 6.0, Aalborg Acoustic Pavilions, MPAS project and Distortion II) were developed in an educational framework, and students were actively involved through summer schools and workshop; previous educational experiences with the PBD approach have been also documented in [223,224].

The design optimization can be performed either manually, for subsequent iterations by the operator, or in an automated matter. In the latter case, the parametric model is automatedly optimized on the basis of performance feedback until one or more satisfying solutions are achieved, resulting in a quick and efficient process. The support of automated processes has been reported in the development of most case studies (11 out of 19). The optimization tools that were used in the case studies analyzed are Galapagos and Octopus, which are based on evolutionary algorithms, and are directly integrated in Grasshopper for Rhinoceros. Such tools enable one to run either single objective or multi-objective optimization of parametric models defined in Grasshopper, based on target requirements and variation space set by the user. The performance feedbacks needed to set up the optimization process are generally obtained from the custom acoustic simulation tool integrated in the modeling environment.

The design proposal can be optimized since early design phases based on the simplified performance feedbacks from the custom acoustic simulation tools, while

more sophisticated simulation systems, such as Odeon, can be employed in late design phases when most design features have been already defined. These tools can be used to verify the performance of the preselected design proposals and provide the designers with detailed suggestions for further design improvements. For instance, commercial packages were used in late design phases to validation purposes in the Philharmonie de Paris, in the music venues in Fuzhou and in ReS 6.0.

4A.4 Conclusions

As the impacts of acoustic performance on human well-being are being acknowledged, acoustic concerns are expected to be increasingly integrated in the design of spaces with a variety of functions. In common practice, acoustic consultants are rarely involved since early design phases, and acoustic optimization and architectural design tend to be rather independent processes. In this frame, the application of performance-based design in acoustics seems very promising to optimize design proposals in light of performance feedbacks obtained from acoustic simulation tools. However, the method finds little application in current architectural practice, and is mainly restricted to notable architectures and research projects. A set of case studies developed with APBD has been collected in the attempt to shed some light on the state of the art of the application of the method in current architectural practice, evidence the design strategies followed and suggest some possible fields of improvement to further encourage its application.

The development of integrated platforms that combine acoustic analyses and architectural modeling, the increased interoperability among modeling and simulation tools, would ease performance analyses in early design phases, and will allow for an effective collaboration among architectural and acoustic specialists.

The enhancement of acoustic and coding skills of designers, which can be promoted by the provision of specialized teaching platforms, would support the development and application of custom tools to run simplified analyses in the modeling environment during early design phases, hopefully encouraging the application of APBD in practice.

Acknowledgements

The authors would like to thank the professionals that provided useful information to the authors on the design processes, and the copyright owners of the photographs that granted the permission to use the images in this work.

Chapter 4B

Modeling mean radiant temperature in outdoor environments: comparing the approaches of different simulation tools

Objective	To compare the mean radiant temperature (T_{mrt}) models of different simulation tools to allow for a preliminary assessment of their capabilities
Outcome	The T_{mrt} models of ENVI-met, Ladybug Tools, CitySim, TRNSYS, Solene-microclimat, RayMan and SOLWEIG are presented, and the simplifications applied to the radiative components are reported
Highlights	• The models apply several simplifications to the radiative components accounted. • Most of the simplifications are related to reflected radiative components, which are either approximated or neglected. • ENVI-met v5, TRNSYS, Solene-microclimat exhibit the most complete models and have the greatest capability to reliably assess complex urban scenarios.

4B.1. Overview and motivation

This Chapter focuses on the mean radiant temperature (T_{mrt}), the most important environmental variable affecting outdoor thermal comfort, by comparing the T_{mrt} models implemented in different simulation tools. Detailed information on the tools' capability is often not clearly stated by program developers, making the selection of performance simulation tools and the interpretation the predicted outcome not always straightforward for potential users. This contribution presents an overview on the shortwave and longwave radiative components accounted for the T_{mrt} estimation and on the simplifications applied to them, for each of the considered simulation tools. The contribution can support a preliminary assessment of the modeling capability of the simulation tools, increasing the awareness on the underlying calculation assumptions and can provide guidance for a correct interpretation of the simulation outcome. Nonetheless, comprehensive validation studies are needed to quantify the accuracy of simulated T_{mrt}, by comparing the results to in-situ measurement acquisitions (see Chapter 5B).

The content of this Chapter has been partly published in "*Modelling mean radiant temperature in outdoor environments: contrasting the approaches of different simulation tools*" authored by Elena Badino, Maria Ferrara, Louena Shtrepi, Enrico Fabrizio, Arianna Astolfi, Valentina Serra and presented at the 8th International Building Physics Conference (IBPC 2021) Conference [325]

4B.2. Introduction

Human thermal perception in outdoor urban environments is influenced by the microclimatic conditions within the urban canopy layer, where the ambient environment is dynamic and highly variable over very short distances [3,38].

As already discussed in Chapter 2, the morphological and material properties of the urban fabric influence the thermal perception in their surroundings, and therefore performance-aware choices in architectural practice can contribute to the enhancement of outdoor thermal comfort conditions [15,16,326]. Despite the increased awareness on this theme, the microclimatic impacts of design projects are often overlooked [21,327], and cities are often built without considering bioclimatic criteria, potentially hampering their ability to cope with the challenges posed by climate change [24].

In this frame, performance simulation tools enable designers to evaluate and control the microclimatic effect of their design solutions prior to construction, allowing them to test the effect of different dimensions, arrangements, and material properties of the design proposals [10,26,38,41,326]. Therefore, simulation tools able to provide reliable estimations of the microclimatic effects of the surrounding urban fabric are required to identify effective climate-sensitive design solutions and enhance outdoor thermal comfort conditions in cities.

4B.3. Modeling of the mean radiant temperature in the outdoors

The environmental parameters used to describe the microclimatic conditions to which the human body is exposed are mean radiant temperature, air temperature, relative humidity and wind speed [15,26,32]. These environmental parameters allow to derive outdoor thermal comfort indices (e.g., PET, UTCI, SET*) to evaluate the thermal stress perceived by the human body. Among the mentioned parameters, the mean radiant temperature (T_{mrt}) is the one that has the greatest influence over outdoor thermal comfort during summertime [26,328,329]. Moreover, T_{mrt} is more accurate than the air temperature as a predictor of heat related mortality [330].

According to the ANSI/ASHRAE Standard 55, the mean radiant temperature is defined as "the temperature of a uniform, black enclosure that exchanges the same amount of heat by radiation with the occupant as the actual surroundings" [331]. The Standard explicitly states that both longwave and shortwave radiation components are included in the definition. Indeed, while indoor T_{mrt} calculation can often be limited to the longwave (i.e., thermal infrared) components, the calculation of the T_{mrt} in the outdoor environment requires the inclusion of the shortwave (i.e., solar) radiation.

The T_{mrt} can be estimated by modeling the whole radiation field in a given environment. According to [26], this procedure requires data related to: a) meteorological parameters (e.g. air temperature, relative humidity, cloud cover, atmospheric turbidity); b) temporal parameters (day of the year, time of the day); c) geographical location; d) artificial and natural obstacles reducing sky view from calculation point (described by Sky View Factor); e) geometrical properties of buildings and vegetation in the study area (to calculate the view factors); f) the solar reflectance, transmissivity and emissivity of the model surfaces; g) the geometrical features (e.g. standing/seating) and the emissivity and shortwave absorbance of the human body.

The main challenges in outdoor T_{mrt} calculation are posed by the spatial and temporal variability of radiant exchanges due to the heterogeneity of urban environments, that are composed of various geometric and material features, and by the correct accounting of the human body geometry [26,332]. In the following, a general procedure to calculate the T_{mrt} from the longwave and shortwave radiative components is described, according to [26].

The longwave radiation includes that either emitted or reflected by the built environment and atmospheric longwave radiation from the sky. The calculation procedure proposed by Fanger [333] enables to calculate the longwave irradiance (also referred to as flux density) emitted by the surfaces of the environment that reaches the human body by subdividing the environment surrounding the human body into n isothermal surfaces. For each i-th surface (i = 1, ..., n), the surface temperature T_i, the emissivity ε_i and the view factor F_i are defined. According to the Stefan-Boltzmann's law, the longwave irradiance L_i emitted by each isothermal surface in the surrounding environment can be determined according to Equation (4):

$$L_i = \varepsilon_i \cdot \sigma \cdot {T_i}^4 \qquad [\mathrm{W/m^2}] \tag{4}$$

where σ is the Stefan-Boltzmann constant ($\sigma = 5.67 \cdot 10^{-8}$ W/m^{2}K^4). Since the emissivity values of common construction materials is usually greater than 0.9, the contribution of reflected longwave radiation is usually minor, but not inconsequential [3,334]. In particular, low-emissivity surfaces, such as metal ones and low-emissivity glazing, reflect a significant fraction of the incident longwave radiation [3]. Indeed, according to Kirchhoff's law, longwave emissivity equals absorptivity, and since construction materials transmit no longwave radiation, low-emissivity surfaces behave as longwave reflectors. Besides the longwave radiation from the built environment, the calculation needs to include the atmospheric radiation, that is the downwelling longwave radiation from the sky.

The solar radiation components are direct solar radiation, diffuse sky radiation and reflected shortwave radiation. Direct solar radiation on the human body can be calculated based on the direct normal irradiance S_b [W/m^2], i.e., the solar irradiance on a surface perpendicular to the radiation, and the projected area factor f_p, that quantifies the portion of the human body that is exposed to direct solar radiation based on solar altitude and azimuth and human body posture; f_p values can be found in different Standards and studies [331,335–337]. The reflected shortwave radiation accounts for the direct beam and diffuse sky radiation reflected by the surfaces surrounding the human body, and depends on the surfaces' solar reflectance, i.e., the fraction of incident shortwave radiation being reflected by the surfaces. Diffuse sky radiation is the solar radiation reaching the Earth surface after being scattered by the atmosphere. Different sky models are available to estimate diffuse and direct solar irradiance [338,339].

To estimate T_{mrt}, both the emitted and reflected longwave radiation L_i and the diffuse and reflected shortwave radiation K_i from the i-th surrounding surface are weighted according to the view factors F_i between the i-th surface and the human body. View factors are also called shape factors, configuration factors, and angle factors [340] and are used to determine the fraction of radiation leaving a given surface that strikes the human body. The human body geometry is often approximated to more simple forms in order to reduce the computational load. For instance, a seated person can be approximated to a cube or sphere, while a standing one can be approximated to a cylinder, an oval cylinder or an octagonal prism [341–344]. However, more accurate descriptions of human body are also possible [341,342,345]. An overview on view factor calculation and a comparison of the most common approximations of the human body geometry used to calculate the view factors is presented in [342].

The radiation fluxes reaching the human body are calculated based on the sum of the n contributions of the longwave and shortwave radiation, and the direct solar radiation. In order to quantify the radiation fluxes absorbed by the human body, the longwave and shortwave irradiances from the i-th surrounding surfaces (L_i and K_i) striking the human body (weighted by the corresponding F_i) are multiplied by the human body's absorption coefficients, i.e., α_l for longwave radiation and α_k for shortwave radiation. Direct solar radiation is calculated considering the direct normal irradiance (S_b), the projected area factor (f_p) and shortwave absorption coefficients of the human body (α_k). For a clothed human body, α_l is generally assumed equal to 0.97

and α_k equal to 0.7 [26,328,346]. As a result, the mean radiant flux density S_{Str} [W/m^2] can be calculated following Equation (5) [26]:

$$S_{Str} = \alpha_l \cdot \sum_{i=1}^{n} F_i \cdot L_i + \alpha_k \cdot \sum_{i=1}^{n} F_i \cdot K_i + \alpha_k \cdot f_p \cdot S_b \quad [\mathrm{W/m^2}] \qquad (5)$$

T_{mrt} is defined as the temperature of fictive isothermal enclosure that behaves as a perfect black body emitter and causes the same amount of radiative exchange with the human body as the actual environment where it is located. Therefore, T_{mrt} can be calculated following Equation (6):

$$T_{mrt} = \sqrt[4]{\frac{S_{str}}{\varepsilon_p \cdot \sigma}} \quad [\mathrm{K}] \qquad (6)$$

where ε_p is the emissivity of the human body ($\varepsilon_p = \alpha_l$ according to Kirchhoff's law).

Given the key role played by the T_{mrt} in outdoor thermal comfort conditions, accurate estimations of this parameter at the urban microscale are crucial to orient design decisions. The validation of the simulation results with respect to measured data it is an essential step to evaluate the accuracy of T_{mrt} models [347–349]. Measurement of T_{mrt} are mainly performed using globe thermometers or with the integral radiation measurement (IRM) technique (also known as six-direction radiation measurements), that was suggested by Höppe [350]. There is good agreement that in outdoor environments IRM approach is the most accurate [26,328,346,351–354]. A comparison of the measurement techniques is presented in [328,351,353]. In order to evaluate the accuracy of simulated results with respect to measured ones, difference performance statistics can be used, such as the mean bias error (MBE), root mean square error (RMSE) and its systematic and unsystematic components, mean absolute error (MAE), the Wilmott's index of agreement (d) and correlation metrics such as the coefficient of determination R^2 [347,348]. The ISO 7726:1998 Standard [337] specifies the requirements of instruments for measuring the physical quantities characterizing an environment, providing acceptable ranges of accuracy for different physical variables, including the T_{mrt}. The Standard has also been used in past studies, such as [348,355], to define an acceptable error range for simulated T_{mrt}, that is considered equal to ± 5°C for thermal stress conditions.

Reliable estimations of T_{mrt} in outdoor settings can be useful to understand the implications of design decisions on outdoor thermal comfort during design processes and define effective climate-sensitive design solutions. To this aim, several simulation tools can be used to model the T_{mrt} in complex urban environments. ENVI-met, SOLWEIG and RayMan are some of the most widely employed tools in past studies to calculate the T_{mrt} in outdoor settings [355,356]. More recently, some other tools, such as Ladybug Tools, CitySim, TRNSYS, CityComfort+ and Solene-microclimat, have been employed to the same purpose. Despite the availability of several tools, details on the capability and assumptions of the T_{mrt} models and full descriptions of the implemented calculations are often not declared or of limited accessibility, as also

noted by previous works [10,355,357]. This may generate difficulties for potential users in the selection of the most appropriate simulation tool, as well as in the interpretation of the results. Several previous works have proposed comparison of T_{mrt} calculation implemented in simulation tools, either from a qualitative or a quantitative standpoint [26,326,332,355–362]. However, only few studies have presented detailed descriptions of the underlying calculation procedures of T_{mrt} models, in the attempt to shed light on the model assumption and capabilities, evidencing the design scenarios in which such simplifications may limit the accuracy of the predictions.

4B.3.1. Objectives

This work aims to contribute to fill this gap by collecting information on the T_{mrt} models implemented in the simulation tools and evidencing their capabilities and calculation assumptions. The study integrates previous works and specifically focuses on some the most advanced simulation tools available, that are able to deal with complex outdoor settings. Based on the T_{mrt} model descriptions, the tools' ability to account for the different radiative components either emitted or reflected by the urban surfaces is compared and summarized. The analysis is limited to the built elements of the urban environments, such as the ground and the building walls, without considering the role of vegetation. The primary focus on this contribution is to highlight which shortwave and radiative components from the surrounding urban elements are accounted in the T_{mrt} models, along with the main simplifications applied to them. In addition, some information or references are provided on other relevant aspects for T_{mrt} estimation (e.g., surface temperature estimation, view factors, projected area factor, sky model) that are outside the scope of this overview. Moreover, information regarding the degree of interoperability or integration between the simulation tools and the modeling environments, the level of geometric detail supported for the virtual environment, and the geometric approximation used in the tools to model the human body is provided. In light of the collected data, a quick summary on the radiative component included in the calculations has been compiled with the aim to support potential users in the selection of the most appropriate simulation tool, based on the design complexity and the required accuracy of their projects.

4B.4. Method

This study compares the modeling techniques implemented in a set of advanced performance simulation tools to estimate T_{mrt} in the urban environment. Several tools enable to predict the mean radiant temperature in outdoor environment, such as ENVI-met, SOLWEIG, RayMan, Ladybug Tools, CitySim, TRNSYS, CityComfort+ and Solene-microclimat. Among them, this this study primarily focuses on the publicly available tools that supports complex 3D environments, i.e., ENVI-met, CitySim, Ladybug Tools, TRNSYS and Solene-microclimat. Additionally, in light of their wide popularity, SOLWEIG and RayMan are briefly described, despite their ability to evaluate complex urban scenarios is more limited [26,346,363]. CityComfort+ is excluded from the analysis as it was not released publicly.

The resources used to collect information of the T_{mrt} models implemented in the tools include journal articles, conference papers, manuals, scripts, PhD theses, web pages of official forums and personal communication. Whenever possible, the most recent sources were privileged to report the most updated description found in literature to the best knowledge of the authors. However, it must be noted that potential implementations in the calculation procedure that were not published could not be included in this overview. Within these limitations, the T_{mrt} calculation procedures of the tools have been described and analyzed to shed light on the underlying assumptions. Based on the gathered data, the ability of the models to account for different radiative components is summarized according to the classification proposed in [355,359]. For the purposes of this work, the summary is limited to the radiative components emitted or reflected by the built environment, in addition to those coming from the sky (i.e., diffuse sky radiation and atmospheric counter radiation) and to direct solar radiation. Additionally, information on the tool licensing and interoperability, as well as on the modeling of the surrounding context and human body geometry is provided.

This contribution is articulated into two sections. In the first (§ 4B.5), the T_{mrt} models implemented by the tools is presented, while in the second section (§ 4B.6) the tools are compared based on the different longwave and shortwave radiative components included in the calculation.

4B.5. Description of T_{mrt} models implemented in the simulation tools

In the following sections the selected simulation tools are briefly presented, and information is provided on the implemented T_{mrt} models along with the main formulation and the calculation assumptions/simplifications. The T_{mrt} models implemented in these tools differ in the simplifications of the radiative exchanges, in the levels of geometric approximations applied to the virtual environment and the human body, and in the degree of integration and interoperability with common modeling environments.

4B.5.1. ENVI-met

ENVI-met is a 3D microclimate model designed to simulate surface-plant-air interactions with high resolution, from the micro to the local scales. It is a non-hydrostatic, obstacle-resolving computational fluid dynamics (CFD) model that relies on Reynolds Averaged Navier-Stokes (RANS) equations [355]. ENVI-met is one of the most widely used and complete tools to assess outdoor thermal comfort [347]. It is released under a commercial license, while a lite version of the tool is also available for free. The tool is a stand-alone program that requires the user to generate the virtual model directly within the simulation environment. However, Dragonfly Legacy plug-in for Grasshopper can ease the creation of the virtual environment file and can be used to run the simulations and visualize the results. The tool support complex 3D models with localized material changes, and the model geometries need to be defined

according to an orthogonal 3D grid, with a resolution up to 0.5 m. It must be evidenced that finer grid resolutions result in markedly increased computational efforts, which may make them unpractical to implement. The approximation of the geometry to a 3D grid limits the tool's ability to deal with tilted and irregular geometries and may influence the tool predictions, as noted in [364]. The calculation is performed for all grid points of the model domain.

ENVI-met is in constant development, and the most recent releases include a series of improvements that are expected to increase the model accuracy. The optional Indexed View Sphere (IVS) mode, introduced in version 4, allows to provide site-specific evaluation of the radiative fluxes from surrounding building elements. The detailed material accounting enabled by IVS allows to replace the otherwise do main-wide mean material properties, potentially increasing the model accuracy, especially for T_{mrt}. Further details on IVS model and on the preceding one can be found in [365]. In addition, a crucial improvement in the T_{mrt} estimation in ENVI-met has been introduced in the most recent release, i.e., version 5, in which the calculation is performed by default following the IRM approach, in contrast to the former two-directional approach.

While several validations of the ENVI-met with observed data are available in literature, many of them are referred to air temperature only, as evidenced in [347]. ENVI-met validation studies referred to T_{mrt} report a wide range of variability in its accuracy and, at the time of writing, are almost only related to ENVI-met versions 4 or precedent, without IVS mode enabled. As also noted in [348], many of the validation studies referred to T_{mrt} have highlighted large modeling errors, that often exceed the acceptable error range of ± 5°C suggested by ISO 7726:1998 Standard [337] for thermal stress conditions. The meta-analysis in [347] (published in 2018), although related to outdated model versions, evidences that the model tends to overestimate daytime and underestimate night-time T_{mrt} values, while it is able to reproduce the daytime peak values. In the following, some more recent model evaluations are briefly presented. The research in [348] evaluates the reliability of T_{mrt} simulations by ENVI-met in Arizona (USA). The study was conducted by comparing ENVI-met v 4.3 results with T_{mrt} data measured in different positions and periods of the year, including under extreme hot conditions. The results of the study evidenced a poor agreement between the simulation and the measured results suggesting that ENVI-met model should not be used under micrometeorological or morphological extremes without in-situ validation to quantify errors and assess directional bias due to model limitations. A detailed model evaluation of ENVI-met v4.4.2 (no IVS) has been presented in [355] and found underestimations of T_{mrt} during in sunlit locations and overestimations in the shade. In [366], observation of T_{mrt} in a courtyard in Seville, (Spain) were compared with the one simulated by ENVI-met (v 4.4.5) without IVS, finding a more promising agreement between measured and simulated data. Similar results were found by another study [367] carried out in mild autumn conditions to Tehran (Iran). The study in [368] evaluate the accuracy of simulated T_{mrt} using ENVI-met v 4.4.5, finding an overestimation in T_{mrt} values during daytime in summer. A systematic analysis in [369] tested different simulation approaches using ENVI-met v 4.4.6 with respect to T_{mrt} in various locations in Hong Kong during summertime,

evidencing a marked variation in the tool's capability to provide accurate predictions based on the simulations settings. To conclude, the only validation available at the time of writing referred to ENVI-met v 5 with IVS was carried out during summer in Hong Kong and found good agreement between measured and simulated T_{mrt} values [370]. The same study has reported a drastic improvement in T_{mrt} accuracy for the new calculation model implemented in ENVI-met version 5 with respect to the previous one.

In light of the already mentioned ENVI-met developments, in the following, the T_{mrt} calculation in ENVI-met is described separately for ENVI-met releases up to version 4 and for version 5 including the IVS mode.

The first description of the two-directional T_{mrt} model, implemented in ENVI-met releases up to v 4 (without IVS), is presented in the PhD thesis by Bruse [371] while, the most recent description of the T_{mrt} calculation is given in the PhD dissertation by Huttner in 2012 [372], and has been presented also in [370]. Based on the information in [347,370,372], T_{mrt} [K] is calculated based on Equation (7):

$$T_{mrt} = \left[\frac{1}{\sigma}\left(L + \frac{\alpha_k}{\varepsilon_p}(D + S)\right)\right]^{\frac{1}{4}} \qquad [\mathrm{K}] \tag{7}$$

where α_k and ε_p is the shortwave absorbance and the longwave emissivity of the human body, assumed equal to 0.7 and 0.97, respectively [360,372], L is the longwave radiation, D is the total diffuse shortwave radiation and S is the direct shortwave radiation absorbed by the human body. The following analysis is based on the work in [355], that has attempted to understand the calculation assumptions included in version 4 with respect to previous model description. The study provides a systematic comparison of the simulation results obtained by ENVI-met (v4.4.2) without IVS with respect to T_{mrt} data measured with the IRM in Szeged (Hungary) that have allowed to shed light on the calculation assumptions of the tool in the calculation of the longwave and shortwave radiation [355]. As reported in [355,372] the model subdivides the 3D environment into an upper and a lower hemispheres, each of which accounting for 50% of the emitted or reflected radiation from the environment. According to [355,372], the longwave and shortwave fluxes from the surrounding elements are estimated for both hemispheres by means of individual view factors calculated for the specific grid point using ray-tracing, i.e., approximating the human body to a sphere [355,365,373]. As suggested in [355], the model applies several simplifications to the reflected and emitted radiation components. With respect to shortwave radiation, the upper hemisphere accounts for diffuse sky and wall-reflected solar radiation, while the lower hemisphere accounts for the ground reflected solar radiation (direct and diffuse) only. This latter simplification can be considered accurate enough for pedestrian positions (predominant ground view factor at limited heights above ground). As reported in [355,370], direct solar radiation is calculated based on the projected area factor (f_p) of a standing human body following [335]. The diffuse sky radiation is calculated based the sky view factor and assuming isotropic radiation from the sky [355]. Shortwave radiation reflected by walls is calculated for the direct solar radiation only, thus neglecting the reflections of diffuse sky radiation. The

ground-reflected shortwave radiation is based on the domain-wide mean ground solar reflectance (ρ) [355,370]. The direct solar radiation reflected by walls relies on the use of domain-wide mean ρ values of building walls. Multiple reflections of solar radiation are not accounted by the model. Considering longwave radiation, the lower hemisphere only includes the longwave radiation emitted by the ground, disregarding other elements. The upper hemisphere accounts for the radiation emitted by walls and for atmospheric longwave radiation, including its wall-reflected contribution [355]. The atmospheric longwave radiation reflected by the ground is not accounted by ENVI-met. Despite an advanced 7-nodes wall model [374] is implemented in ENVI-met, the emitted radiation by walls and ground is approximated considering domain-wide mean emissivity and surface temperature values for the walls and ground, separately. As evidenced in [355,372], these simplification may lead to overestimated longwave fluxes in shade and underestimated ones when the sites are sunlit and cause the amount of emitted longwave fluxes sensible to of the domain configuration, even though they occur beyond the site of investigation [355]. Overall, the simplifications applied to the reflection of shortwave and longwave radiation limit the model ability to run site-specific estimations. Due to these limitations, the microclimatic effect of localized material changes in urban environment can hardly be evaluated with accuracy in ENVI-met version up to 4 without IVS. This hampers the reliability of the tool to evaluate and compare design scenarios with localized material changes. Nonetheless, the recently implemented IVS option is expected to overcome some of the above-mentioned issues [355,357,359], and an evaluation in [369] reported an increase in T_{mrt} accuracy with IVS.

The new six-directional T_{mrt} calculation model, introduced in ENVI-met version 5, is based on IRM and, when coupled with IVS, allows for site-specific T_{mrt} estimations. The only description found at the time of writing is in [370]. The model allows for grid cell based T_{mrt} calculation. It accounts for the sum of all the calculated longwave and diffuse shortwave irradiances in the 6 orthogonal directions (i.e., L_j and D_j, respectively), while the direct solar radiation impinging on the human body can be calculated based on three different projected area factors f_p that can be selected by the user [335,336,350,375].

The T_{mrt} calculation described in [370] is based on the Equation (8):

$$S_{Str} = \alpha_l \cdot \sum_{i=1}^{n} W_i \cdot L_i + \alpha_k \cdot \left(\sum_{i=1}^{n} W_i \cdot D_i + \cdot f_p \cdot S_b \right) \quad [\mathrm{W/m^2}] \qquad (8)$$

where W_i are the directional weighting factor used to account for the shape of a standing human body, and equal 0.22 for cardinal directions (north, south, east, west) and 0.06 for vertical ones (upward/downward) [26,370]. Therefore, differently from the previous T_{mrt} model, the one here described takes into account the shape of a standing human body, which is considered more representative in outdoor settings. L_i quantifies the sum of the atmospheric longwave radiation and that emitted by the surrounding built environment, while D_i accounts for diffuse shortwave radiation and diffusely reflected contributions, and S_b is the direct normal solar irradiance. As concerns shortwave radiation, direct and diffuse fluxes are considered, as well as

diffusely reflected contributions, including multiple reflections. While the longwave radiation emitted by surrounding surfaces is evaluated in detail, longwave radiation reflections are not accounted except for the wall-reflected atmospheric radiation, potentially reducing the calculation accuracy in case of low-emissivity surfaces (steel, low-emissivity glass, etc.). Nonetheless, this limitation is expected to be fixed in the next ENVI-met releases with the inclusion of longwave reflections in the model.

4B.5.2. Ladybug Tools

Ladybug Tools [376]. is a free and open-source simulation tools built on top of several validated simulation engines, i.e., Radiance, EnergyPlus/OpenStudio, Therm/Window and OpenFOAM [376]. The tool is under continuous development and several learning resources are available in addition to the official forum (i.e., Discourse). With Ladybug Tools it is possible to run the simulation and visualize the results directly in the same modeling environment. Moreover, the tool is open to some modifications of the code to better fit it to the project requirements [377]. The tool supports complex virtual models defined using thermal zones, with different geometries and materials, while the calculation points are set according to a user defined horizontal grid [378]. At the time of writing two versions of Ladybug Tools are available: a new version, i.e., Ladybug Tools (LBT) v1, and one based on the legacy tools (Ladybug 0.0.69 and Honeybee 0.0.66). The legacy tools are released as plug-in for Grasshopper, while the newest LBT Tools is integrated in Grasshopper (free version), Revit and Rhinoceros (commercial versions). Starting from LBT Tools v1.4 (released in 2022), an improved T_{mrt} calculation based on Radiance has been introduced, which is more detailed than the one in legacy tools. The T_{mrt} modeling of the legacy version is presented in the following, while the new LBT is just briefly introduced at the end of the section, based on the little information available on its T_{mrt} calculation at the time of writing.

In the legacy tools, T_{mrt} modeling can be performed within Honeybee module using the Microclimate Map Analysis component, as presented in [360,378,379]. T_{mrt} validations are presented in [21,53,360,378]. In [360] T_{mrt} values are validated against IRM-measured value obtained during summer in Szeged (Hungary), finding a RMSE of 6.2 °C, and in [21] against measurement with globe-thermometer documented in [380] for a winter day and a summer day in Taiwan, concluding that the model results are in the acceptable range defined by ASHRAE Guideline 14 [381]. Other studies, such as [53,378], concluded that the observed deviations with respect to the measured T_{mrt} values were acceptable, reporting greater errors in sunlit conditions than in shaded ones [378].

The radiation model used to calculate the T_{mrt} is described in [359,378,382–384]. The T_{mrt} is calculated by correcting the mean radiant temperature referred to longwave exchanges only (reported in the following as "longwave T_{mrt}", $T_{mrt,lw}$) with the contribution of the shortwave radiation computed with the SolarCal model described in [382,383] and included in ASHRAE 55 Standard [40].

The calculation of longwave mean radiant temperature from the surfaces of the environment (except for the sky) $T_{mrt,lw,env}$ [°C] is described in [359,377,378,384], and is based on the surface temperatures of each surrounding element calculated by

EnergyPlus (see [385] for detailed information) and view factors calculated for each grid point using ray-tracing. It is possible to define the resolution for the view factor calculation (i.e., to change the number of rays emitted). Since the calculation in [359,377,378,384] doesn't consider the emissivity of the surfaces of the built environment, they are assumed as black body emitters (ε=1) and reflections of longwave radiation are neglected. However, in [21], variation of emissivity are taken into account, suggesting that emissivity values can be included in the calculation. In order to account for the contribution from the sky, the sky temperature T_{sky} [°C] is determined with a formulation in [386] as a function of the atmospheric longwave radiation contained in the Typical Meteorological Year (TMY) weather file [378,384].

The solar adjusted T_{mrt} is obtained by calculating the solar radiation according to SolarCal model presented in [382,383]. The model is based on the calculation of the "effective radiant field" ERF_{solar} [W/m^2] and accounts for the direct solar radiation, diffuse sky radiation and ground reflected radiation. Diffuse radiation from the sky D_{sky} is assumed to be distributed on the upper half of the radiatively exposed portion of the human body f_{eff}. Ground reflected solar radiation is calculated on the lower half of f_{eff}, considering the global horizontal irradiance I_{TH} (including direct and diffuse horizontal irradiance) and a default value of ground solar reflectance set at 0.2 [377]. Moreover, direct solar radiation incident on a standard seated person is calculated based on ANSI/ASHRAE Standard 55 [40,378]. The calculation (valid for sunlit conditions) is performed in accordance to Equation (9) [384]:

$$ERF_{solar} = \left(0.5 \cdot f_{eff} \cdot F_{sky} \cdot \left(D_{sky} + I_{TH} \cdot \rho_{grd}\right) + f_{eff} \cdot f_p \cdot S_b\right) \cdot \frac{\alpha_k}{\alpha_l} \quad (9)$$

where f_{eff} is the fraction of the human body that can is exposed to solar radiation, and is set by default as equal to 0.696, i.e. for a seated person, F_{sky} is the sky view factor computed through ray tracing, f_p is the projected area factor for a seated person is defined according to ANSI/ASHRAE Standard 55 [40] and S_b is the direct normal irradiance. The shortwave absorptivity of the human body α_k is assumed equal to 0.7 [378] and the longwave absorptivity/emissivity α_l is assumed 0.95 [384]. According to [359], S_b, D_{sky} and I_{TH} are collected from the TMY weather file. While, as previously noted, the ground solar reflectance is set by default at 0.2, it can be changed by manually editing the code, as done in [377].

From the above mentioned components, the T_{mrt} is calculated following Equation (10) [377,378]:

$$T_{mrt} = T_{mrt,lw,env} \cdot \left(1 - F_{sky}\right) + T_{sky} \cdot F_{sky} + \frac{ERF_{solar}}{h_r \cdot f_{eff}} \quad (10)$$

where h_r is the radiant heat transfer coefficient [378], T_{sky} is the sky temperature, and F_{sky} is the sky view factor. The view factors used to calculate the incoming diffuse shortwave and longwave radiation are calculated for each grid point, i.e., approximating the human body geometry to a sphere. Similarly, the projected area factors f_p used to account for the direct solar radiation are by default referred to a seated person, according to the ANSI/ASHRAE Standard 55 [40]. However, with

limited editing of the code, it is possible to consider a standing person and to customize the value of h_r (e.g. for indoor/outdoor conditions), as described in [377,378].

The surfaces of the environment are assumed to behave as black body emitters and reflection of longwave radiation are neglected by the model. This can lead to reasonably accurate results for common construction materials, although it may result in errors when considering low emissivity materials, as noted in [3,334]. The above-mentioned procedure only accounts for shortwave radiation reflected by the floor, neglecting the contribution of reflections by other elements, such as building walls. Diffuse shortwave radiation from the sky and ground-reflected shortwave radiation are weighted for the corresponding view factor and assumed to be distributed respectively on the upper and lower halves of the radiatively exposed portion of human body. This has been evidenced as one of the limitation of the tool in [378], and can be considered a valid approximation for calculation points close to the ground, as previously noted. T_{mrt} inaccuracies due to the neglection of shortwave radiation reflected by the building walls is expected to be greater within the built environment (i.e., with reduced F_{sky} values) with reflective walls (with high ρ values).

In the newest LBT (from v 1.4 on) a more advanced T_{mrt} calculation is implemented, using Radiance. Given its recent release, limited information on the model was found, and no detailed formulation or published validation studies are available at the time of writing. Based on the information collected of the official forum Discourse, the T_{mrt} estimated within the Comfort Map components takes into account direct and diffuse shortwave radiation, allowing for the inclusion of multiple reflections (however no information was found if reflections include both direct and diffuse fractions). As concerns longwave radiation, the model estimates the longwave radiation emission from surrounding surfaces. The tool relies on Radiance for the calculation of the surface view factors, while no information was found on the inclusion of surface emissivity in the calculation. Reflections of longwave radiation are not included in the calculation [387], which therefore may fail at correctly estimating longwave exchanges in presence of low emissivity materials.

4B.5.3. CitySim

CitySim is a free urban energy modeling tool developed by the Solar Energy and Building Physics Laboratory of EPFL [388]. CitySim Pro is a graphical user interface built upon CitySim released by Kaemco under a commercial license [389]. It is a stand-alone program primarily developed to predict energy consumption of urban settlements at a district scale [390,391], however it has been used to calculate T_{mrt} in outdoor conditions in [343,357,392]. According to [357], the calculation position can be defined by the user and the virtual model can feature complex geometries and it needs to be prepared and organized in layers to be imported in CitySim. The tool implements localized material variations and is able to recognize façade, roof, shading, surface, ground and floor [393]; while localized windows cannot be modeled, their presence can be accounted using glazing ratios. A SketchUp extension that enables the operator to directly import the model is available. Moreover, CitySim can be integrated in Grasshopper for Rhinoceros by means of GHCitySim [394]. A guide

of the CitySim Pro is available in [393] although it does not cover T_{mrt} calculation. The model referred to diffuse sky radiation (direct and reflected) has been validated with respect to the results of Radiance in [395]. The calculated T_{mrt} is compared to the one obtained by other tools in conference papers, such as [357]. However the only validation with respect to measured data was found in the PhD thesis by Coccolo [343] using the globe thermometer in Lausanne (Swiss) and Dubai (United Arab Emirates), finding a RMSE between 4-6 °C. The T_{mrt} calculation is presented in the PhD thesis by Coccolo [343], while the modeling of shortwave radiation is based on the Simplified Radiosity Algorithm (SRA) described in [395–397]. No officially released information was found in literature on the calculation procedure and human body geometry assumptions, a part form the mentioned PhD thesis [343]. Based on the description, the T_{mrt} calculation is performed in accordance to the IRM [350], i.e., based on the shortwave and longwave irradiances in the six directions (K_j and L_j, respectively).

The SRA model, which is thoroughly described in [395–397] is used to calculate the shortwave irradiance K [W/m^2] impinging on the standing human body, whose geometry is approximated to a prism. The model accounts for the direct, diffuse and reflected components of shortwave radiation. Direct beam irradiance is determined from direct normal irradiance, its incident angle to the calculation surface, and the insolated surface fraction. For the diffuse sky radiation D_{sky} [W/m^2] a discretization of the sky vault into patches is applied [398] in combination to the Perez all-weather sky model [338]. The D_{sky} calculation accounts for the presence of obstructions (i.e., the built environment), and includes the reflection of shortwave radiation occurring over the obstructions. For the reflection calculation, the ρ value of the dominant obstructing surface is considered for each patch, thus allowing to evaluate the effect of localized material changes. The reflections of shortwave radiation include the contribution of direct beam, diffuse sky and that of the reflections from other patches, i.e., multiple shortwave reflections. The reader is referred to [395–397] for further information and the detailed formulation.

The calculation of longwave radiation flux density L_j on the surfaces of the human body is described in the PhD thesis by Coccolo [343] and relies on the determination of equivalent temperature of the environment (T_{env}) "seen" from the centroid of each surface composing the human body. According to the formulation, T_{env} [K] is calculated with Equation (11):

$$T_{env}{}^4 = \frac{1}{\pi}\left[\varepsilon_{sky} \cdot T_{sky}{}^4 \cdot \Omega_{sky} + \varepsilon_{grd} \cdot T_{grd}{}^4 \cdot \Omega_{grd}\right] + \sum_{i=1}^{n} \varepsilon_i \cdot T_i^4 \cdot F_i \qquad (11)$$

where the T_{sky} and T_{grd} [K], ε_{sky} and ε_{grd} are the temperature and emissivity of the sky and ground, respectively, Ω_{sky} and Ω_{grd} are projected solid angle of the unobstructed sky and the ground as seen from the centroid of the receiving surface, T_i [K] is the surface temperature of the i-th surface (see [396,399] for further details on surface temperatures calculation), ε_i is the emissivity and F_i is the view factor of the i-th surface surrounding the human body, that are deterministically estimated [359]. The emissivity ε_{sky} is assumed equal to 1 and the sky temperature T_{sky} is calculated as a

function of air temperature based the work in [400]. The longwave radiation flux density L_i [W/m^2] received by the human body in the i-th direction is calculated according to Stefan-Boltzmann law from T_{env}, following the formulation in [343].

In order to estimate T_{mrt}, the mean radiant flux density S_{str} is calculated as the sum of the shortwave radiation densities (K_j) and longwave radiation densities (L_i) impinging in the 6 orthogonal directions multiplied by the corresponding weighting factors W_i, and by the shortwave and longwave absorption coefficient, respectively (assuming α_k = 0.7 and ε_p = α_l = 0.95 [343,401]). The weighting factors W_i are calculated for a standing human body (0.22 for the cardinal position and 0.06 from upward/downward ones) [328]. Therefore, the mean radiant flux density S_{str} [W/m^2] is calculated following Equation (12):

$$S_{Str} = \alpha_k \cdot \sum_{i=1}^{6} W_i \cdot K_i + \varepsilon_p \cdot \sum_{i=1}^{6} W_i \cdot L_i \quad [\mathrm{W/m^2}] \tag{12}$$

From the mean radiant flux density, the T_{mrt} is calculated according to Equation (6). The T_{mrt} calculation is based on a detailed model for shortwave radiation, that enables to calculate multiple reflections of radiation among the surfaces of the environment. However, reflections of longwave radiations are not accounted by the model, with the already mentioned shortcomings for low-emissivity surfaces [3,334]. Moreover, the tool does not allow for the detailed inclusion of windows, which limits the ability of the tool to account for the heterogeneity of urban environments.

4B.5.4. TRNSYS

TRNSYS is a transient systems simulation program with a modular structure to calculate energy and climatic conditions of building environments, thermal and energy systems [402]. It is a commercial stand-alone tool, with a SketchUp plugin named TRNSYS3D to ease the preparation and importation of the virtual model, and a Rhino plugin named TRNLizard enables to run the simulation and visualize the results in the modeling environment. Several official learning resources are available for the tool. TRNSYS supports virtual model with complex geometries and user-defined calculation positions [403]. Starting from version 17, the radiation model includes detailed modeling of shortwave radiation (direct, diffuse and reflected components) in addition to longwave radiation [404]. It has been used in [327,334,405–407] to estimate the T_{mrt} in outdoor spaces by extending the modelling capability of the tool, that was originally developed for indoor studies and only deals with enclosed volumes. The method followed to run outdoor T_{mrt} analysis, that is detailed in [334,407], is based on the creation of enclosed thermal zones with fictive windows to which ad-hoc properties are applied. The calculation procedure of shortwave and longwave radiation, and T_{mrt} is described in [334,407,408]. A validation of the predicted T_{mrt} with respect to globe thermometer measurements in a climatic chamber is included in [408] showing good consistency with TRNSYS calculation. In [405] the T_{mrt} obtained by TRNSYS were compared to those of ENVI-met.

The calculation $T_{mrt,lw}$ is based on the surface temperature of each surrounding surfaces (whose calculation is described in [409]), and Gebhart factors [404] for longwave radiation [334,408]. These factors quantify the fraction of the diffuse radiation leaving a given surface (by emission or reflection) that is eventually absorbed the human body, including reflections from all other elements [410]. Gebhart factors are calculated considering the emissivity values of the surrounding surfaces and that of the person (ε_p=α_l). Notably, this calculation allows to include longwave reflections, thus enabling to accounts for the presence of low-emissivity surfaces. The atmospheric longwave radiation can be estimated by modeling a fictive window with specific properties (refer to [334,407] for further details).

Direct solar radiation is calculated based on f_p for a standing human body, as defined in VDI 3787 [336]. Different sky models can be used to estimate diffuse sky irradiance [411]. The model includes direct and diffuse shortwave radiation, and the reflections of both fractions rely on Gebhart factors (in this calculated for shortwave radiation) and take into consideration the specific solar reflectance of the surfaces of the built environment. The use of Gebhart factors allows for the accounting of multiple shortwave reflections over surrounding surfaces [334,408].

From the above-mentioned radiative components, the T_{mrt} [K] is calculated with Equation (13):

$$T_{mrt} = \left[\left(T_{mrt,lw}\right)^4 + \frac{1}{\varepsilon_p \sigma A_s} \left(D_s^* + S_s^*\right) \right]^{\frac{1}{4}} \quad \text{[K]} \tag{13}$$

where ε_p and A_s are respectively the emissivity and the effective radiation area of the human body (or sensor) and S_s* [W/m^2] is the direct solar radiation, D_s* [W/m^2] is the diffuse solar radiation, both including also multiple reflections.

According to [408], the human body geometry is accounted for in detail with respect to the direct solar radiation, through the introduction of projected area factors varying based on solar altitude according to the VDI 3787 Standard [336]. For the remaining components of diffuse and reflected direct solar radiation, as well as emitted and reflected longwave radiation, the human body is approximated to a sphere [334,408]. Although TRNSYS was not developed to run outdoor calculations, the T_{mrt} model is detailed and considers multiple reflections of both longwave and shortwave radiation. Moreover, the tools allows to take into account the material properties at a very detailed level, allowing to model and test the effect of innovative materials, as done in [56].

4B.5.5. SOLENE-microclimat

SOLENE-microclimat is a urban microclimate simulation tool that consists of a thermo-radiative model, a CFD model and a thermal building model. It is a free tool originally developed for research purposed at CRENAU Laboratory of the Nantes School of Architecture [412]. A SketchUp plug-in [413] eases the coupling between the simulation tool and the modeling environment, while no official documentation or free learning resources are publicly available to the best knowledge of the authors.

The tool supports complex 3D scenarios with emissivity and solar reflectance values defined for the urban surfaces, despite no detailed information on the virtual model was found. More specifically, the available references appear to use specific material properties for all building walls in the domain, allowing to use glazing ratios [414] without localized material changes, while material variation for ground surfaces are instead tested in [412,415]. These considerations let suggest that the tool has limited ability to reproduce the material heterogeneity of urban environments. The thermo-radiative model enables the calculation of outdoor comfort conditions, and has been used to estimate the T_{mrt} in [412,414]. The thermo-radiative model is described and validated in [416] with respect to upward and downward radiation measurements performed over the canopy layer. However, no validation of simulated T_{mrt} results with respect to measurement was found. An early description of the T_{mrt} calculation procedure, which seems however outdated based on more recent references, is detailed in [417].

According to [414], the T_{mrt} is calculated for a standing human body represented by a multi-faceted cylinder. For each composing surface, the longwave and shortwave radiation fluxes have been considered.

According to [417], the T_{mrt} is calculated based on Equation (14):

$$T_{mrt} = \left[\sum_{j=1}^{n} F_{i,j}\, \varepsilon_j {T_j}^4 + F_{i,sky} \varepsilon_{sky} T_{sky}^4 + \frac{f_p \alpha_k U_{sol} S_{\downarrow}}{\sigma f_{eff}} + \frac{\alpha_k U_{sol} \left(D_{\downarrow} + \rho (S_{\downarrow} + D_{\downarrow}) \right)}{\sigma} \right]^{0.25} \quad [\mathrm{K}] \tag{14}$$

where $F_{i,j,}$ ε_j and T_j are respectively the view factor between surface i and j, the emissivity and the temperature of surface j (details on the calculation are available in [415,417,418]); $F_{i,sky,}$ ε_{sky} and T_{sky} are the sky view factor, the sky emissivity and the sky temperature.

Based on the formulation above, longwave radiation exchanges between the human body and the surrounding environment include longwave radiation emitted by the built environment and atmospheric radiation from the sky, while the formulation does not account for reflections of longwave radiation. However, it must be noted that this calculation is in contrast with the description of the radiative model included in more recent publications [412,416], that states that reflections of longwave radiation are accounted with the radiosity method up to the first reflection order.

With respect to shortwave radiation, the model accounts for direct, diffuse and reflected direct and diffuse solar radiation. In the early model formulation in [417], a complex method is used to account for clothing in the absorption of solar radiation, based on the "heating efficiency factor due to the sun" U_{sol}. It estimates the fraction of incident solar radiation absorbed by the body and varies depending on clothing characteristics. The detailed calculation of U_{sol} is described in [417].

Direct and diffuse shortwave radiation fluxes are calculated based on an anisotropic sky model [338,415,416]. The absorbed solar radiation is calculated for

each mesh of the virtual environment considering direct and diffuse solar radiation and the contribution of the multiple reflections of solar radiation over the surrounding surfaces of the environments, by means of the radiosity method [412,416]. This overcome the original T_{mrt} formulation in [417] in which only one reflection of solar radiation was considered.

Longwave radiation fluxes are calculated with the same principle. For each surface mesh, the absorbed infrared radiation flux is calculated considering the atmospheric radiation from the sky and longwave radiation from surrounding surfaces, minus the radiation emitted and reflected by the surface itself [416]. In the case of longwave radiation only one reflection is considered, given the high emissivity value of common construction materials [412,416].

4B.5.6. RayMan Pro

RayMan tool [346,419] is able to simulate T_{mrt} on the basis of the VDI 3787 and VDI 3789 Standard [336,420]. It is a stand-alone tool released for free for academic use and an official manual is available [421]. RayMan has been validated against field measurement in several studies [59,328,352,355,356,362,363] evidencing it ability to obtain reasonably accurate results, with a variation in accuracy depending on the tested scenario. RayMan model is firstly presented in [346] and the T_{mrt} calculation is based on [333,422]. The T_{mrt} calculation can be performed for a user-defined point at a time. The 3D model of the environment is divided in two hemispheres at height 1.1 m from the ground. The virtual model of the surrounding context is accounted in a rather simplified way to determine the sky view factor from the calculation point and the radiative exchanges. The geometric properties of the context can be input either fish-eye photography, free drawing of the horizon limitation, a topographic raster, or an obstacle dataset created in RayMan [421]. The emissivity and solar reflectance values of each obstacle (i.e., building) can be defined using a single value (i.e., localized materials within the same obstacle, such as windows, are not supported), while only a single value of solar reflectance and emissivity for the surfaces of the lower hemisphere can be set. The description of the T_{mrt} model implemented in RayMan presented in the following is referred to RayMan Pro v 3.1 Beta and is based on the information in [346,355,421,423]. Equation (15) is the overall formulation reported in [346], that is valid for sunlit locations (in shaded ones, $S_b = 0$):

$$T_{mrt} = \left[\frac{1}{\sigma}\left(\sum_{i=1}^{n}\left(L_i + \frac{\alpha_k}{\varepsilon_p} D_i\right) F_i + \frac{f_p \alpha_k S_b}{\varepsilon_p}\right)\right]^{\frac{1}{4}} \quad (15)$$

The calculations for the upper hemisphere accounts for the sky view factors and built environment while the lower hemisphere only accounts for the surrounding built environment. The calculation is referred to a point in space, meaning that the human body is approximated to a sphere (with $\alpha_k = 0.7$ and $\varepsilon_p = 0.97$) for the diffuse shortwave and longwave radiation fluxes, while direct solar radiation is calculated defining f_p for either a seated or a standing person based on [424]. According to [355], no detailed information on how the T_{mrt} model accounts for long and shortwave radiation beyond

[346,423] is available. The direct and diffuse shortwave radiation is accounted by the model, however no information was released on the way shortwave radiation reflections are accounted, as reported in [355,425]. Nonetheless, an illustration in [423] let suggest that the shortwave radiation reflections by buildings and grounds are accounted considering their solar reflectance values. While reflections of shortwave radiation appear to be included in the model, their properties are not discussed, given the lack of detailed information available. As concerns longwave radiation exchanges, the model accounts for the radiation emitted by the ground and wall surfaces, considering their emissivity values and surface temperatures. The description in [423] reports that the surface temperature of walls and ground is estimated based on [426], while [425] suggests that the wall surface temperature is assumed equal to air temperature, which is expected to provide unreliable estimations for surfaces with low emissivity or low solar reflectance. The T_{mrt} model also accounts for atmospheric longwave radiation, including its reflections on ground and wall surfaces [423].

4B.5.7. SOLWEIG

SOLWEIG is a free tool developed by the Urban Climate Group of the University of Gothenburg. SOLWEIG was originally released as a standalone tool and has been recently integrated in UMEP (Urban Multi-scale Environmental Predictor) plugin for QGIS, with a user manual available at [427]. The model supports 2.5D virtual environments (i.e., digital surface models), where bulk user-defined solar reflectance and emissivity values are used for all the buildings and ground surfaces in the domain [427]. Based on these considerations, SOLWEIG has limited ability to account for complex urban scenarios and for the actual material properties of the built environment. SOLWEIG has been object of several validation studies, such as [59,355,356,362,428], with variegated results overall reporting reasonable accuracy. The T_{mrt} calculation is performed at user-defined positions at 1.1 m from the ground for a standing human body approximated to a squared prism or to a cylinder [427,428]. The T_{mrt} calculation is described in [355,428,429] and is based on the six-directional approach (IRM method) [350]. The calculation is performed according to Equation (16):

$$S_{str} = \alpha_l \cdot \sum_{i=1}^{n} F_i \cdot L_i + \alpha_k \cdot \sum_{i=1}^{n} F_i \cdot K_i \qquad [\mathrm{W/m^2}] \tag{16}$$

where K_i is determined as a function of global, direct and diffuse shortwave irradiances. Reflections of shortwave radiation over the building and ground surfaces are accounted by the model, considering both direct and diffuse fractions [425,429]. L_i is calculated considering the ground and wall emissivity values.

Longwave radiation L_i includes atmospheric, wall-emitted, ground-emitted radiation and wall-reflected radiation while, based on [425,429], the longwave radiation reflected by the ground is neglected. The longwave radiation reflected by walls includes the atmospheric radiation and, for the lateral orientations, also that

emitted by the ground [425,429]. The surface temperatures are based on [430] and, depending on the considered orientation (received from upward or lateral directions), different approximations are applied to the wall surface temperatures to estimate of L_i, (e.g. domain-mean T values, different assumptions made for wall temperatures in sunlit/shaded conditions, etc. refer to [429] for further details). The study in [355] have highlight some model approximations which may reduce its accuracy. The amount of reflected radiation is equally split among the cardinal directions, limiting the tool's ability to correctly estimate the directional radiative fluxes in heterogeneous built environments. Other sources of potential inaccuracy, also discussed in [355], are the assumption that surface temperature will return equal to air temperature after 2 h of shade or at night, the surface temperature parametrization for different ground covers, which is questioned in [355], the use of domain-wide mean surface temperatures, and the use of bulk solar reflectance and emissivity values for ground/building walls.

4B.6. Summary of the tools and of the radiative components included in the T_{mrt} models

Table 11 collects information on the selected tools, with respect to their release (free/commercial license) and their level of interoperability / integration with common modeling environments. The majority of the considered simulation tools are stand-alone programs released under a commercial license. Most of the tools enable to directly import the virtual model to run the simulation, often with the aid of ad-hoc plug-ins for common modeling environments. Ladybug Tools and the most recent version of SOLWEIG are the only tools directly integrated in the modeling environment (Rhino/Grasshopper or QGIS), allowing the user to set the virtual model, run the simulation and visualize the results directly within the same program. A similar degree of integration can be achieved within Rhinoceros/Grasshopper for TRNSYS and ENVI-met, by means of TRNLizard and Dragonfly plug-ins, respectively.

Table 10 briefly summarizes how the virtual model of the context is approximated by the simulation tools, in terms of geometry and material properties, i.e., emissivity and solar reflectance. Additionally, information is provided on the accounting of the human body geometry in the T_{mrt} calculation.

While most of the selected simulation programs support complex virtual environments, the digital models often need to be prepared with some degree of geometrical simplification. As an example, in ENVI-met virtual models are based on an orthogonal 3D grid, in RayMan obstacles can be modeled as hexahedral shapes and SOLWEIG support 2.5D geometries. These can represent significant limitation when dealing with for non-standard geometries, such as irregular or curved shapes or textured surfaces. Another shortcoming is the limited ability of some of the tools to model material heterogeneity and localized materials: some tools, such as ENVI-met (up to v4, without IVS), CitySim, RayMan and SOLWEIG don't implement, or implement in simplified terms, localized materials within the built environment (e.g. material variation on ground and building surfaces, windows, etc.) often using default,

bulk or domain-wide mean values for the emissivity and solar reflectance properties. All these assumptions may result in significant errors based on the characteristics of the scenarios under analysis and limit the ability of the tools to achieve reliable predictions of local T_{mrt} variations when comparing design scenarios exhibiting different material properties.

With respect to the accounting of human body geometry, many simulation tools calculate T_{mrt} for a standing person or apply a "hybrid" accounting of the human body geometry. In the latter case, direct solar radiation is calculated by means of projected area factors (f_p) for standing/sitting body postures, while for diffuse radiation, the human body is approximated to a sphere, i.e., representative of a sitting person, and view factors are calculated from its center. In this frame, Ladybug Tools is the only one that by default performs the calculation for a seated person, although with little code editing [377,378] it is possible to adapt the estimation of direct shortwave radiation to a standing person. In outdoor settings, where people often have standing position, the approximation of human body geometry to a sphere may lead to an underestimation of the lateral radiation exchanges, that are prevailing for a standing person [26,55,346], and an overestimation of those in the vertical directions. However, despite the differences in the calculation approaches, the analysis in [342] suggests that the calculation of view factors for a standing or seated person have a limited influence on the calculated T_{mrt}.

Table 11. Summary of the main features of the selected tools.

	ENVI-met up to v4 (no IVS)	ENVI-met v5 (with IVS)	Ladybug + Honeybee (legacy)	CitySim	TRNSYS	Solene-microclimat	RayMan	SOLWEIG
License	commercial (free Lite version)	commercial (free Lite version)	free	commercial/ free	commercial	commercial	free	free
Tool type	standalone	standalone	integrated in Grasshopper	standalone	standalone	standalone	standalone	standalone/ integrated in QGIS
Interoperability	Grasshopper plug-in	Grasshopper plug-in	-	SketchUp + Grasshopper plug-ins	SketchUp + Grasshopper plug-ins	SketchUp plug-in	-	-

Table 10. Summary of the geometric and material features of the virtual models and of the human body shape implemented in the selected simulation tools.

	ENVI-met up to v4 (no IVS)	ENVI-met v5 (with IVS)	Ladybug + Honeybee (legacy)	CitySim	TRNSYS	Solene-microclimat	RayMan	SOLWEIG
Virtual model geometry	complex (orthogonal 3D grid)	complex (orthogonal 3D grid)	complex	complex	complex	complex	complex (hexahedral obstacles)	2.5D
Emissivity	domain-wide mean for buildings/ground	detailed	detailed	detailed[#]	detailed	unknown*	building specific/single value for ground	single value for all building walls/ground
Solar reflectance	domain-wide mean for buildings/ground	detailed	detailed	detailed[#]	detailed	unknown*	building specific/single value for ground	single value for all building/ground
Human body shape	seated/standing (direct)	standing	seated°	standing	seated/standing (direct)	standing	seated/standing (direct)	standing

* the available references show localized ground materials and single material for all building walls

° f_p for direct shortwave radiation can set for a standing person by editing the code.

[#] windows accounted using glazing ratio

Based on the information on the T_{mrt} models collected in the previous sections, the radiative components included in the T_{mrt} calculation of the simulation tools are evaluated. The proposed summary is based on the classification of the radiative components in [355,359], that for the purposes of this work is limited to the radiative components from the sky and the sun and those from by the built environment (i.e. ground and building walls). Shortwave radiation is composed of direct solar radiation, diffuse sky radiation, single and multiple reflections of shortwave radiation over surrounding elements (considering direct and diffuse components). Longwave radiation exchanges include the component from the sky, the radiation emitted and reflected by the surrounding built environment (differentiating between single and multiple reflections). The considered radiative component are shown in Figure 50

The summary of the radiative components included in the T_{mrt} models of the selected simulation tools is presented in Table 12 and graphically in Figure 51. The summary provides an overview of the radiative exchanges included in the models, evidencing the radiative components neglected by the calculation and the major simplifications applied to the components considered.

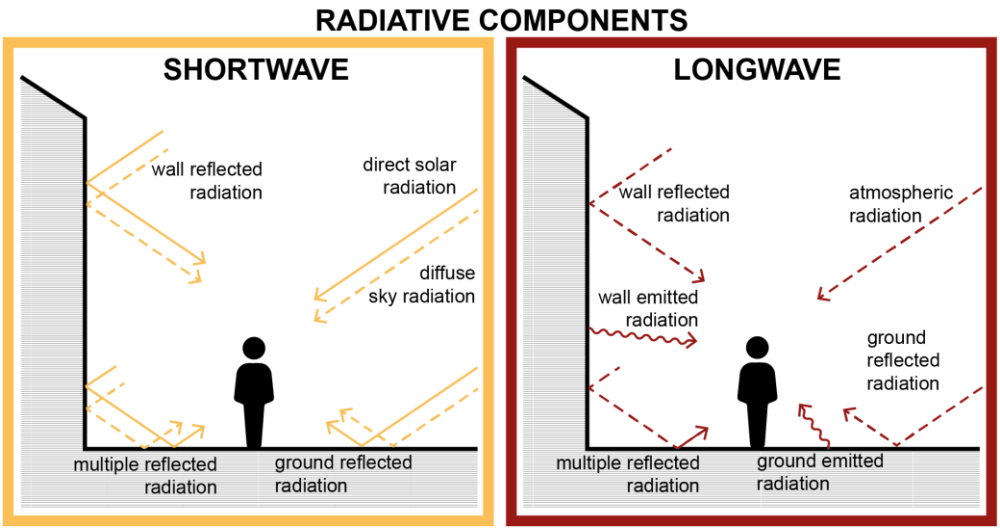

Figure 50. Schematic drawing of the classification of shortwave and longwave radiative components for T_{mrt} calculation.

Table 12. Summary of the radiative exchanges included in the T_{mrt} models of the selected programs.

				ENVI-met up to v4 (no IVS)	ENVI-met v5 (with IVS)	Ladybug + Honeybee (legacy)	CitySim	TRNSYS	Solene-microclimat	RayMan	SOLWEIG
SHORTWAVE	direct			accounted	accounted	accounted	accounted	accounted	accounted	accounted	accounted
	diffuse sky			accounted	accounted	accounted	accounted	accounted	accounted	accounted	accounted
	reflected	ground	direct	accounted*	accounted	accounted*	accounted	accounted	accounted	accounted*	accounted*
			diffuse	accounted*	accounted	accounted*	accounted	accounted	accounted	accounted*	accounted*
		building walls	direct	accounted*	accounted	neglected	accounted	accounted	accounted	accounted*	accounted*
			diffuse	neglected	accounted	neglected	accounted	accounted	accounted	accounted*	accounted*
	multiple reflections		direct	neglected	accounted	neglected	accounted	accounted	accounted	neglected	accounted*
			diffuse	neglected	accounted	neglected	accounted	accounted	accounted	neglected	accounted*
LONGWAVE	atmospheric			accounted	accounted	accounted	accounted	accounted	accounted	accounted	accounted
	emitted	ground		accounted°	accounted	accounted°	accounted	accounted	accounted	accounted	accounted°
		building walls		accounted°	accounted	accounted°	accounted	accounted	accounted	accounted°	accounted°
	reflected	ground		neglected	neglected	neglected	neglected	accounted	accounted	accounted#	neglected
		building walls		accounted#	accounted*	neglected	neglected	accounted	accounted	accounted#	accounted#
	multiple reflections			neglected	neglected	neglected	neglected	accounted	neglected	neglected	neglected

ENVI-met up to v4 (no IVS)
- * domain-wide mean solar reflectance values for ground/building walls
- ° domain-wide mean emissivity and surface temperatures for ground/building walls
- # atmospheric fraction only

ENVI-met v5 (with IVS)
- * atmospheric fraction only

Ladybug + Honeybee (legacy)
- * fixed value for ground solar reflectance (default = 0.2)
- ° fixed value for emissivity (default = 1)

RayMan
- * based on illustration; no details on the model are available
- ° T_s of wall assumed equal to air temperature according to [355]
- # atmospheric fraction only

SOLWEIG
- * bulk value of solar reflectance for ground/building walls
- ° bulk value of emissivity for ground/building walls + surface temperature approximations
- # for lateral directions only + atmospheric and ground emitted fraction only

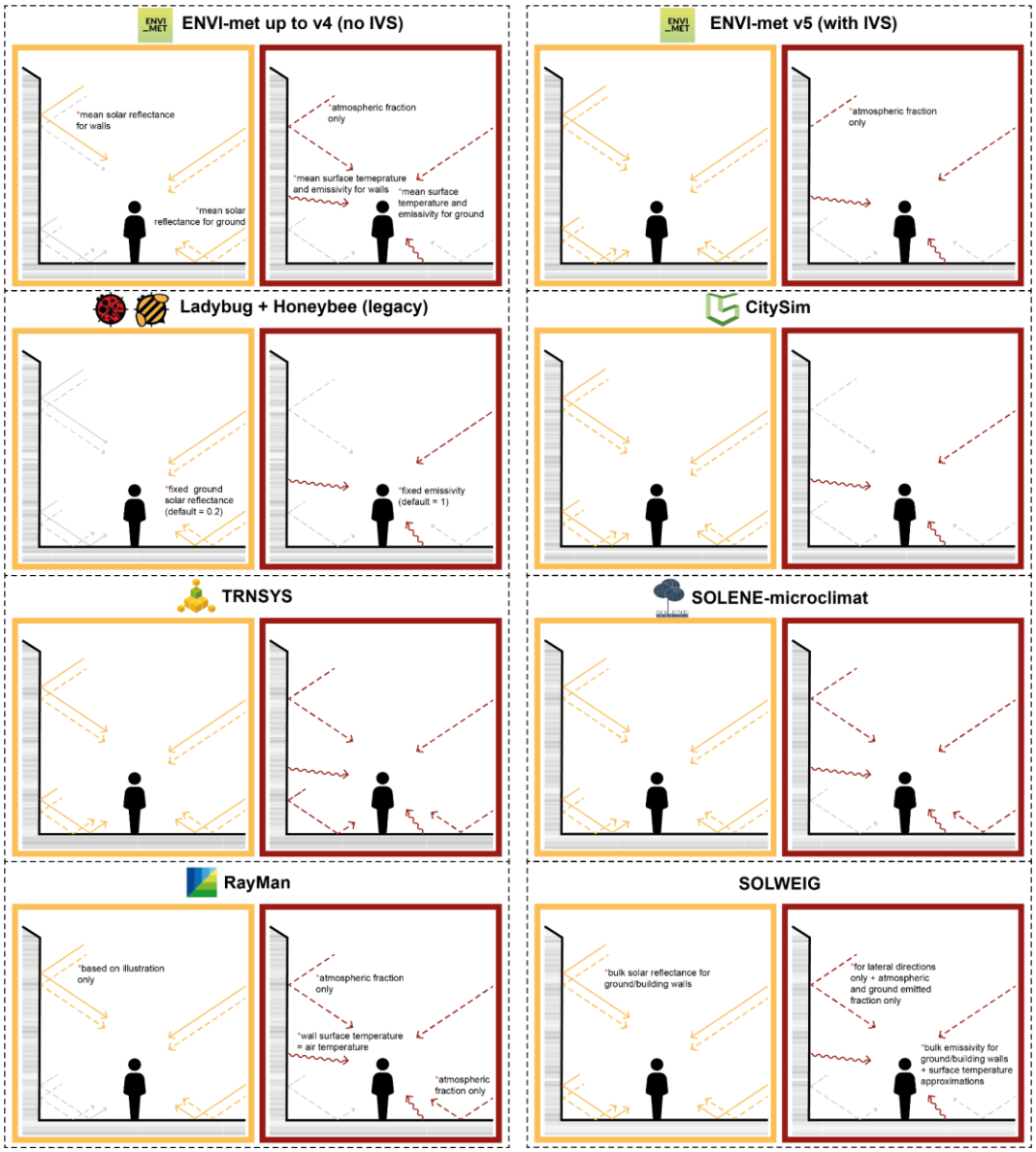

Figure 51. Schemes of the radiative components included in the T_{mrt} models of the selected simulation tools. Radiative components in grey color are neglected.

The descriptions of the T_{mrt} calculation evidence the rate to which the complex radiative exchanges occurring in actual scenarios are simplified by the selected simulation tools. The T_{mrt} models often account only for part of the radiative exchanges between the environment and the human body, with different degrees of simplification, neglecting the remaining ones. The tools that appear to implement the most complete T_{mrt} models, when considering the radiation component accounted and the simplification applied to them, are ENVI-met v5, TRNSYS and Solene-microclimat. Notably, ENVI-met v5 shows a marked improvement over the previous releases in terms of radiative component included in the model. RayMan and SOLWEIG, despite accounting for most radiative components, apply a series of simplifications to the virtual model (e.g., material properties, geometric features, calculation assumptions) which limit their ability to correctly estimate complex scenarios and localized material variations. The radiative components accounted in Ladybug and Honeybee (legacy

version) shows marked simplifications in the T_{mrt} calculation, although they are expected to be at least partially addressed in the most recent releases, LBT Tools v 1.4 and following ones, that rely on Radiance. Overall, most simplifications are referred to reflected shortwave and longwave radiation components, whose calculation is often either neglected or performed using averaged or default values. Reflections of longwave radiation is often neglected, in light of the great emissivity value of most construction materials. Similarly, shortwave radiation reflected by the building walls and multiple reflections are often simplified and, in some cases, neglected. The significance of the errors resulting from these simplifications cannot be stated a priori, as it depends on specific characteristics of the design problem under investigation (e.g., the presence of surfaces with high solar reflectance or low emissivity values). Nonetheless, while reducing the complexity of the calculation procedure, these simplifications may potentially lead to significant errors in the results. Therefore, users should be aware of the simplification and underlying calculation assumptions to being able to select the most appropriate simulation tools and to correctly set-up the simulation and interpret the results, based on the design problem and the degree of accuracy required.

A further consideration is related to the validation studies, which were briefly introduced for each tool. Several works have attempted to validate the T_{mrt} results simulated by the tools with respect to measured data, often evidencing a wide range of variation in accuracy, depending on the scenario considered. Nonetheless, many of the considered tools still lack comprehensive validations of the T_{mrt} models.

In general, the comparison of simulated and observed T_{mrt} is rather problematic [341,355,360]. Indeed, various T_{mrt} measurement techniques with different accuracy (e.g. different types of globe thermometers, IRM approaches) can be used [328], while other issues are linked to the specific properties of the considered scenario, which may evidence or minimize the importance of certain radiative exchanges, the different spatial and temporal scales adopted in modeling and measurement, to the heterogeneity of reporting of the measurement conditions (e.g. for radiation and site) and to the statistical metrics used to evaluate the results [360]. Lastly, as noted by [348], in certain validation studies the accuracy of the simulated results has been considered acceptable despite large errors were errors were demonstrated.

The summary of the radiative components presented in this Chapter can support potential users in the selection of the most appropriate tools based on the characteristics and specific requirements of the design problems. Nonetheless, it must be remarked that any information of the accuracy of predicted T_{mrt} cannot be directly inferred from the proposed comparison. Therefore, it is essential to validate the simulation outcome with observed data to evaluate the results accuracy, as also evidenced in [347–349].

4B.7. Conclusions

This Chapter provides an overview of some of the most advanced simulation tools able to estimate T_{mrt} in outdoor settings, i.e., ENVI-met, Ladybug Tools, CitySim, TRNSYS, Solene-microclimat, RayMan and SOLWEIG. The primary goal is to analyze

the shortwave and longwave radiative components included in the T_{mrt} calculation, with a focus on those either reflected or emitted by the surfaces of the urban environment, to evidence how the surrounding built environment can be modelled (geometric approximations for buildings, material properties applied to urban surfaces) and the way the human body shape is accounted. Additionally, general information on the tools is provided, to shed light on their licensing and their level of integration / interoperability with modeling environment.

Overall, the considered tools are often standalone programs with some plug-ins to ease the integration with modelling environment. The virtual model of the surrounding context is generally simplified to different extents with respect to its geometric and material properties. The tools apply some simplifications to the radiative components accounted for the estimation of T_{mrt}, that are in most referred to reflected shortwave and longwave radiation components, which are either approximated or neglected. With respect to the radiative component accounted in the calculation, ENVI-met v5, TRNSYS, Solene-microclimat, RayMan and SOLWEIG emerge as the most complete tools, although RayMan and SOLWEIG apply marked simplification to the modelling environment which limit their ability to deal with complex and heterogeneous contexts. The presented summary can provide guidance to practitioners, increasing the awareness on the simplification applied by common simulation tools to estimate T_{mrt} in outdoor settings, allowing for a preliminary assessment of their simulation capability. Nonetheless, in order to quantify the accuracy of the tools, comprehensive validation studies are needed to compare the simulated T_{mrt} with respect to in-situ measurement acquisitions (see Chapter 5B).

4B.8. Chapter Nomenclature

α_k	absorption coefficient for shortwave radiation of the human body	[-]
α_l	absorption coefficient for longwave radiation of the human body	[-]
ε_{grd}	emissivity of the ground	[-]
ε	emissivity	[-]
ε_p	emissivity of the human body	[-]
ε_{sky}	emissivity of the sky	[-]
ρ	solar reflectance	[-]
σ	Stefan-Boltzmann constant	[-]
A_s	effective radiation area of the human body/sensor surface	[m^2]
D	diffuse shortwave irradiance	[W/m^2]
D_{ref}	reflected solar irradiance	[W/m^2]
D_{sky}	diffuse sky irradiance	[W/m^2]
$D_{s,i}$	diffuse solar irradiance transmitted through component i	[W/m^2]
D_s*	diffuse solar irradiance on the human body/sensor surface including multiple reflections	[W/m^2]
$D_\downarrow$	downward diffuse irradiance	[W/m^2]
ERF_{solar}	effective radiant field	[W/m^2]
F	view factor	[-]
f_{eff}	radiatively exposed portion of the human body	[-]
f_p	projected area factor of the human body	[-]
F_{sky}	sky view factor	[-]
I_{TH}	global horizontal irradiance	[W/m^2]
h_r	radiant heat transfer coefficient	[W/m^2K]
K	shortwave irradiance	[W/m^2]
L	longwave irradiance	[W/m^2]
S	direct solar irradiance	[W/m^2]
S_s*	direct solar irradiance of the human body/sensor surface including multiple reflections	[W/m^2]
S_b	direct normal solar irradiance	[W/m^2]
S_{str}	mean radiant flux density absorbed by the human body	[W/m^2]
$S_\downarrow$	downward direct solar irradiance	[W/m^2]
T	surface temperature	[°C][K]
T_{env}	equivalent temperature of the environment	
T_{grd}	ground temperature	[°C][K]
T_{mrt}	mean radiant temperature	[°C][K]
$T_{mrt,lw}$	longwave mean radiant temperature	[°C][K]
$T_{mrt,lw,\ env}$	longwave mean radiant temperature from the surfaces of the built environment	[°C][K]
T_{sky}	sky temperature	[°C][K]
U_{sol}	heating efficiency factor due to the sun	[-]
W	weighting factor	[-]

Chapter 5A

Outdoor acoustic comfort: evaluation of room acoustic simulations and design applications

Objective	To evaluate the potentialities of the use of geometrical room acoustic simulation tools for *SPL* predictions in outdoor settings, with a comparison between simulated and measured data and design applications.
Outcome	The use of Odeon and Pachyderm acoustics for outdoor *SPL* estimations is evaluated in outdoor settings, and some design examples are provided, where acoustic simulations inform the decision-making process.
Highlights	• Geometrical room acoustic simulations can be useful tools to compare design alternatives with the objective of improving outdoor acoustic comfort. • Odeon and Pachyderm are reported to predict noise levels in outdoor settings with reasonable accuracy. • Some design applications are proposed as examples of the methodologies that can be followed in practice to improve outdoor acoustic comfort with minor design modifications.

5A.1. Overview and research goals

This Chapter focuses on the use of room acoustic simulation tools to analyze outdoor scenarios. After a brief introduction to architectural means to reduce environmental noise in urban areas (§5A.2) and geometrical room acoustic tools (§ 5A.3), the reliability of room acoustic simulations in outdoor settings is investigated, and some design applications are reported.

The first part (§ 5A.4) presents a preliminary study aimed to evaluate the reliability of the *SPL* prediction of room acoustic simulation tools based on geometrical acoustic principles in an outdoor scenario. Past research works have evidenced that material and geometric design features at the urban microscale can contribute to reducing environmental noise levels, thus enhancing the well-being of the urban population. While several simulation tools for outdoor propagation are available, they often exhibit a limited ability to predict the effect of design strategies at the architectural scale (material variations on the façade, presence of protrusions, etc.). The possibility of using geometrical room acoustic simulation tools in outdoor settings has emerged in this frame. While room acoustic tools are originally developed for indoor applications, their use at the urban microscale can provide useful feedback to orient design decisions to improve acoustic comfort in cities. Therefore, the use of Pachyderm and Odeon in an outdoor scenario is evaluated by comparing the *SPL* simulation results with in-situ measured acquisitions. This study can therefore provide a preliminary understanding of the capability of these tools to predict outdoor *SPL*, which is the most used acoustic parameter used to estimate environmental noise impact.

The second part of the Chapter (§ 5A.5) presents two applications of the acoustic performance-based design approach at the urban microscale. Both studies are carried out using room acoustic simulations to analyze and optimize architectural features of buildings at the urban microscale. One application (§ 5A.5.1) focuses on a courtyard and evaluates the environmental noise level variation resulting from a set of geometric and material design alternatives of the building façade surrounding the courtyard. The second application (§ 5A.5.2) focuses on Wolfsburg Connect project by the architectural firm Henning Larsen in Copenhagen (Denmark), that was in development during the candidate's visiting period at the firm. The project is related to a new multifunctional area in Wolfsburg (Germany) and is located in an acoustically challenging position. The contribution investigates the effect of façade material variations on the façade of a portion of Wolfsburg Connect project, also considering minor geometric variations for the buildings.

The content of the first part of the Chapter (§ 5A.4) has been partly included in *"An evaluation of geometrical room acoustic simulations in outdoor settings"* submitted for presentation at Forum Acusticum 2023 Conference authored by Elena Badino, Louena Shtrepi, Arianna Astolfi and Valentina Serra, and in "*L'uso di Odeon per simulazioni a scala microurbana: un confronto con misure in campo*" (English title: The use of Odeon simulation at the urban microscale: a comparison with in field measurements) [431] presented at the 49th Congress of the Italian Acoustician Association in 2023, authored by Elena Badino, Louena Shtrepi, and Arianna Astolfi.

The content of § 5A.5.1 has been partly published in "*Façade design through parametric modelling for environmental noise mitigation in a courtyard*" presented at EuroNoise 2021 Conference [432] and in "*Studio parametrico sulla riduzione del rumore ambientale in vari scenari urbani*" (English title: Parametric investigation of environmental noise reduction in different urban scenarios) [433], presented at the 48th Congress of the Italian Acoustician Association in 2022, both authored by Elena Badino, Louena Shtrepi, Arianna Astolfi.

5A.2. Introduction

Environmental noise is a rising concern in contemporary cities, where several potential noise sources are present, and the noise is exacerbated by the combination of sound reflective construction materials and compact urban layouts. Noise pollution is considered a relevant and widespread cause of disturbance worldwide, which threatens the health and well-being of the urban population (e.g., cardiovascular disease, cognitive impairment in children, sleep disturbance, tinnitus, and annoyance) [434]. According to the last report by the European Environmental Agency, at least 20 % of the EU population live in areas where traffic noise levels are harmful to health, and this figure is projected to increase because of future urban growth and an increased demand for mobility [435]. Environmental noise is generated by different sources related to human activities [71]. While vehicular traffic noise is considered the most common noise source worldwide [72,73], in certain contexts other sources may prevail, such as railway, aircraft o leisure noises. In this frame, the World Health Organization (WHO) has suggested source-specific outdoor sound pressure level thresholds to protect public health [12]. While the report does not include the noise generated by people talking in the street, which in the following is referred to as leisure noise, it can nonetheless be considered a major noise source in some scenarios, such as restaurant districts or nightlife areas [107,436]. Moreover, the relevance of leisure noise has increased due to the restrictions of the COVID-19 pandemic, which have forced bar and restaurants to host clients in outdoor spaces instead of indoor ones. Urban courtyards, where outdoor areas of restaurants are often surrounded by residential buildings, represent examples of settings where leisure noise plays a crucial role, which may compromise the acoustic comfort of dwellers, especially during nighttime.

The benefits of the promotion of outdoor acoustic comforts are multiple and include the possibility for dwellers to stay comfortably in balconies and terraces as well as indoors with open windows, to exploit natural ventilation [13,14]. This latter aspect may result in energy savings due to the reduced reliance on active systems to achieve indoor thermal comfort and has also been evidenced by the Acoustics, Ventilation and Overheating Guide [14].

Environmental noise levels in cities are influenced by the morphologic and material properties of the surrounding urban fabric. The compact layout of urban environment and the sound reflective properties of common construction materials cause the environmental noise levels in cities to increase due to multiple reflections. A number of researches have evidenced the environmental noise reduction potential

of performance-wise architectural design in urban areas [17]. In particular, the geometric and material design of building façades can promote acoustic comfort in indoor spaces and surrounding urban areas. Therefore, the energy retrofit interventions on existing buildings that are commonly carried out to enhance the thermal insulating properties of the building envelopes, if properly conceived, may have the potential to contribute to more comfortable indoor and outdoor acoustic conditions. Nonetheless, despite the growing awareness on the importance of addressing urban noise pollution, acoustic concerns are hardly considered during design processes [437].

Previous studies have investigated the potential of the geometrical and material features of façades [107–111,122] as environmental noise reduction strategies. Recent review article has collected the main findings of the research studies related to façade design features for noise reduction [17,18]. Based on previous works, sound absorbing materials applied to urban facets can lower environmental noise levels by reducing the amount of sound reflections occurring in the urban environments. Moreover, the geometry of the façade can help shielding the receivers from the incoming sounds, although this contribution seems to be generally limited compared to that obtained with sound absorbing strategies.

The theme of noise reduction by means of architectural building features has been mainly addressed considering isolated buildings (e.g., [438,439]), street canyons (e.g., [107,122,440]) and courtyards (e.g., [79,80,441,442]).

5A.3. Brief introduction to geometrical room acoustics simulations

The way the sound reaches a given position in space after being modified by the surrounding environment can be described by the space's impulse response. Several methods exist to predict the room impulse response of a given space prior to construction, based on which relevant information on its acoustic behavior can be evaluated. The acoustic prediction models can be classified as wave-based ones or those relying on geometrical acoustics (GA) principles. The reader is referred to [443–445] for an extensive overview of geometrical room acoustic techniques, and to [446] for a comparison between GA and wave based methods. In theory, wave-based ones are the most accurate as they numerically solve the actual wave equation, allowing to model the phenomena associated to the wave behavior of sound (e.g., diffraction, interference). Nonetheless, their practical application is still limited given the detailed data on material properties required to characterize the surfaces, and the computation power required to run the simulations.

Therefore, most of the currently available room acoustic simulation tools rely on GA principles, which are computationally more efficient and also requires more easily available data to define the acoustic properties of the surfaces (i.e., random incidence sound absorption and sound scattering coefficients). GA tools are based on the approximation of soundwaves to rays, and are widely used to estimate the room behavior in mid and high frequency ranges, where the ray assumption can be

considered valid [443]. In contrast, the reliability of GA simulations in the low frequency range is more problematic given the role of wave phenomena in this range. While sound diffraction is not included in classical GA methods, it can be estimated to some extent through different approaches [443]. GA tools allow to estimate the effect of the geometric and material properties of a given environment, considering one or more sound sources emitting sound energy as rays, which in the end reach the receiver position through a direct propagation path and through reflections over the surfaces of the surrounding environment. The amount of sound energy reflected and the fashion in which the reflection occur are based on the sound absorbing and sound scattering properties of the considered surface. The accuracy of these input values is therefore essential to ensure the reliability of the predictions. The sound-receiver path can be calculated deterministically using the image-source method, or stochastically, using raytracing. Common simulation tools, such as Odeon, CATT-Acoustics, EASE and Pachyderm, apply a hybrid approach where image-source method is used for the early reflections, and raytracing one for the later ones.

5A.4. Evaluation of geometrical room acoustic simulation in outdoor settings

This study aims to investigate the extent to which acoustic simulation tools based on GA principles can provide reliable sound pressure level (*SPL*) estimations in outdoor settings. To this aim, two simulation tools were used, i.e., Odeon, a commercial standalone program, and Pachyderm Acoustics, a free tool integrated in Rhinoceros. Traditionally, GA tools have been developed and used to predict acoustic conditions in indoor settings, and both Odeon and Pachyderm have been validated with respect to indoor conditions. However, given the potential noise reduction benefits provided by a performance-aware design of building façade, the ability to test the effectiveness of different façade solutions has emerged.

While several simulation tools for outdoor sound propagation are available (e.g., CadnaA, SoundPLAN), they generally apply simplifications to the material and geometric properties of urban façades. Therefore, such tools are not suitable to test the noise reduction effectiveness of façade design strategies, such as the presence of screening elements or sound absorbing materials. In this frame, the possibility to use room acoustic simulation tools in outdoor settings has emerged. While past research studies have used room acoustic simulation tools in outdoor settings [79,80,107,240,439,447,448], to the best knowledge of the author, their reliability was not assessed so far with respect to in-situ measurements in urban settings.

In this framework, the study in this Section contributes to filling this gap and assesses the reliability of room acoustic simulations in an outdoor scenario, i.e., a case-study courtyard, by comparing the simulation results with in-situ measured acquisitions. The selected scenario represents a condition in which the sound source is “seen” by the receivers’ positions, and in which wave-based phenomena such as diffraction, that are simplified or neglected by geometrical acoustics, are considered of minor importance. The virtual model of the case-study courtyard is fed to Odeon

and Pachyderm to compare the measured and predicted sound pressure levels in the courtyard and over the façade, thus evaluating the reliability of the estimations.

5A.4.1. Research method

The methodology followed to evaluate the reliability of the simulation tools with respect to *SPL* estimations is based on the following steps, described in the following sections:

a) an in-situ measurement campaign in a courtyard, in which reverberation time and sound pressure level was measured in different positions;
b) the calibration of the acoustic model in Odeon and Pachyderm based on the measured reverberation time at the courtyard level.

The comparison of the simulated and measured *SPL* at the different measurement positions is then performed on the calibrated acoustic models (see § 5A.4.2).

Measurement campaign

An in-situ measurement campaign was carried out to collect data to set up and calibrate the acoustic model in Odeon and Pachyderm Acoustics and to assess the reliability of their predictions.

Figure 52. Photograph of the courtyard used as case-study

To this aim, a measurement campaign was carried out in a case-study courtyard of the Politecnico di Torino, in Turin (Italy). The courtyard is 18.7 m wide and 29.7 m long and is located between 4 educational buildings of the Department of Energy (DENERG) and the Department of Structural, Geotechnical and Building Engineering (DISEG). The heights of the buildings on the three sides of the courtyard are between 15.4 and 17.1 m, corresponding to 4 floors, while the remaining side is lined by a smaller building (7.25 m high and 5 m deep), backed by a taller building (7 floors

above ground, ~ 25 m height). The courtyard has cobblestone paving and the fronts of the buildings exhibit a pattern of windows in different sizes and their opaque portions have a brick finishing. Pictures of the courtyard are shown in Figure 52.

Figure 53. Photographs taken during the measurement campaign showing a) the sound source and sound level meter in the courtyard; b) the microphone hold at 2 m distance from the façade; c) the indoor microphone position.

The measurement campaign was carried out in the courtyard on May 6th, 2021, with favorable weather conditions, with a clear sky and negligible wind. The goal of the measurement campaign was to characterize the way the sound emitted within the courtyard propagates at the courtyard level (i.e., at the pedestrian level) and over the façades of the side buildings. To this aim, the reverberation time (T_{20}) and the sound pressure level (*SPL*) were measured in different outdoor positions at the pedestrian level and over the façade of the building. T_{20} acquisitions are used to ensure that the simulation tools capture the key acoustic parameters of the courtyard that affect sound propagation within it, while the *SPL* quantifies the sound energy at certain positions. The two measurements are described separately in the following. Additionally, *SPL* measurements were also performed in indoor spaces with open windows (at 1 m distance from the windows and at a height of 1.5 m). While these latter measurements were not used for the evaluation of the geometrical room acoustic software, the collected data is reported in Table 47 in Appendix 5A for

completeness. The measurement equipment used consists of two calibrated Class 1 sound level meters (model NTI XL2), an omnidirectional sound source (model: B&K model 4296), shown in Figure 53.

The sound source was located on a tripod at a height of 1.5 m above ground and was kept in a fixed position at the courtyard level, while the sound level meters were moved to acquire data in the different measurement positions.

A set of measurement positions at the courtyard level and in outdoor positions at the different floors over the façade were defined. The number of measurement positions was defined in light of the relatively simple and symmetric form of the case-study courtyard. The selected measuring points and corresponding identification codes are shown in the courtyard plan in Figure 54, along with the main dimensions and distances.

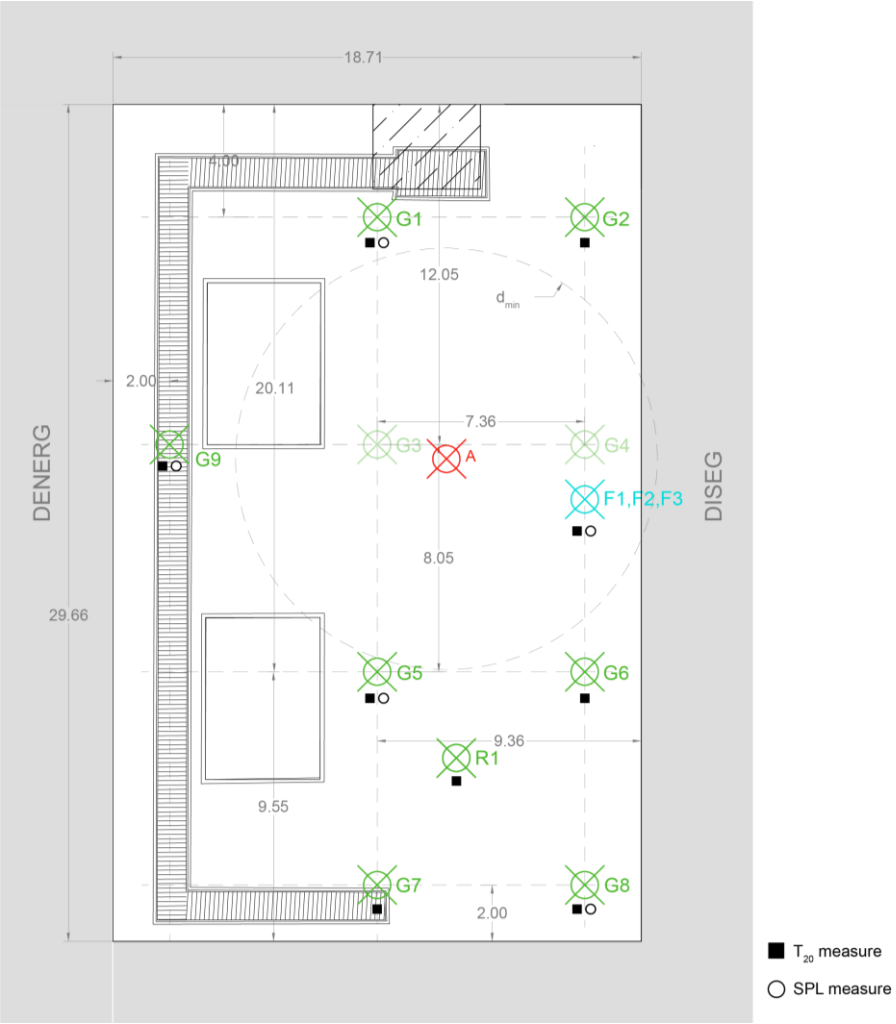

Figure 54. Courtyard plan with the courtyard receiver (in green), the façade receivers (in blue) and source position (in red). The measurement positions in light green are excluded.

Ten microphone positions were defined at the courtyard level, 9 of which were set according to a grid and identified with the codes G1 to G9, while the position of another point was selected randomly in the area and was identified as R1. The measuring points located over the façade were set in a central position of one of the

side buildings, at 2 m distance from the façade, following the indications in ISO 140-5:1998 Standard [449]. These measurement positions are at the 1st, 2nd and 3rd floor of the building and are respectively identified as F1, F2 and F3. The sound source was located in a central position in the courtyard, identified as A (shown Figure 54). All the measurement positions in the courtyard are set at a height of 1.5 m, similarly to the sound source. The outdoor measurement points at the different floors of the building are set at the center of the lower edge of the window, which is at a height of ~1 m above the corresponding building floor.

Reverberation time measurement

The reverberation time (T_{20}) measurements were carried out using an exponential sine-sweep signal [450] in the range 50-20000 Hz with a duration of 6 s that was repeated three times for each sound-receiver position. The use of sine-sweep signal is reported to be advantageous as it allows the achievement of greater signal-to-noise ratio [451,452]. The data processing to determine the reverberation time was performed on the impulse response signals using Audacity [453] in combination with Aurora plug-in [454]. The measurement data is collected from 125 Hz to 4000 Hz octave bands. The reverberation time measurements were carried out at all microphone positions detailed in Figure 54, i.e., the courtyard positions and the façade ones, in combination with the sound source in position A. Nonetheless, the results obtained in positions G3 and G4 are not considered as they do not respect the minimum distance (d_{min}) from the source positions required by ISO 3382-2:2008 Standard [238] (see Figure 54). The minimum distance was calculated considering the inner volume of the courtyard and is shown in Figure 54 with a dashed line circumference. Therefore, the data gathered by these receivers was not considered for the purposes of this analysis. The reverberation time values reported in the following for the courtyard and façade positions are respectively calculated as the arithmetic mean of those obtained at the courtyard level and over the façade.

Sound pressure level measurement

The *SPL* measurements were carried out by emitting a white noise signal and by measuring the *SPL* with the sound level meter at considered the measuring positions and, in parallel, at 1 m distance from the source. The latter measure was performed to obtain a reference *SPL* value for all measurement positions and to characterize the sound source in view of the acoustic simulations. From the *SPL* value at 1 m, the sound power level (*SWL*) of the source could be estimated analytically for an omnidirectional sound source under free field propagation. The *SPL* measurements were carried out with the sound source located in A and the *SPL* meter set in a representative subset of the microphone positions, i.e., in G1, G5, G8 and G9 at the courtyard level, and F1, F2, and F3 over the façade (see Figure 54). During the measurement campaign, the equivalent sound pressure level of background noise was 55.0 dB in the noisiest position (in G8 that is close to the university hallway). Two slightly different source set-ups were used, one for the façade measurement and one for the courtyard one. The equivalent *SPL* at 1 m distance from the source was respectively 86.6 dB and 88.0 dB; from these values, the two corresponding *SWL*s of

the sound source were determined. Detailed information on the *SPL* at 1 m distance from the source and on the calculated *SWL* of the sound source can be found in

Table 49 in Appendix 5A for the source set-up used for the courtyard measurement, and in Table 50 in Appendix 5A for the one used for the façade measurement.

Simulation tools and acoustic model calibration

The simulation models set in Odeon [455] and Pachyderm Acoustics [243] were calibrated based on the measured T_{20} at the courtyard level and at the three floors in outdoor positions over the façade.

Odeon (version 16) is a commercial room acoustic simulation tool based on GA principles, based on a hybrid approach combining image source method for early reflections with ray tracing one for later ones. Odeon has been validated in various studies [456–462]. It is a stand-alone tool which requires to model the virtual environment in a separate modeling environment, such as SketchUp and to import it in the simulation tool. Since Odeon only supports enclosed spaces, in order to analyze an outdoor setting, the modeled environment needs to be enclosed within a perfectly sound absorbing box. The acoustic properties of the materials are specified by the operator: the sound absorption coefficient is specified for each octave band in the frequency range from 63 to 8000 Hz, while a single value of the scattering coefficient is used, referred to 707 Hz, that represents the logarithmic average between the scattering values at 500 and 1000 Hz. A comprehensive material database is available in Odeon, collecting sound absorption coefficients of commonly used materials; in addition, the user can add custom materials. Odeon is also able to estimate edge diffraction effect up to the second order. The coordinates of the points representing the receivers and the sources positions are set manually by the operator.

Pachyderm (version 2.0.0.2) is a free and open-source acoustic simulation tool based on GA (hybrid method, similarly to Odeon). Pachyderm has been validated in [463,464] and a software intercomparison with Odeon is included in [107]. The tool is directly integrated in Rhinoceros and can be accessed either from Rhinoceros or from Grasshopper interfaces. Since Grasshopper is also a parametric modeling environment, it is possible to optimize the design geometry and directly analyze its performance without the need to export/import the model. Moreover, the source and receivers can be modeled as points referenced in Grasshopper, allowing the user to easily set and manage a great number of points. The Grasshopper version of Pachyderm does not include edge diffraction model. The surfaces of virtual model with different acoustic properties need to be set in different layers. The material properties (i.e., sound absorption and scattering coefficients) are assigned to each layer in the model using the Pachyderm interface in Rhino. The surfaces of the model are either referenced or modeled in Grasshopper. The acoustic properties of the materials are assigned to the surfaces by recalling the Rhino layer in which they have been specified. The sound absorption and sound scattering coefficients of the surfaces are set in the Pachyderm interface in Rhino, by detailing a value for each octave band in the frequency range from 63 to 8000 Hz. The sound absorption

coefficients can be saved by the user, while the sound scattering ones cannot be saved and needs to be inserted by the operator for each layer/material.

An acoustic model was set in order to reproduce the measurement conditions (microphone and source positions) and the acoustic properties of the materials applied to the surfaces of the courtyard. The virtual model of the courtyard is shown in Figure 55.

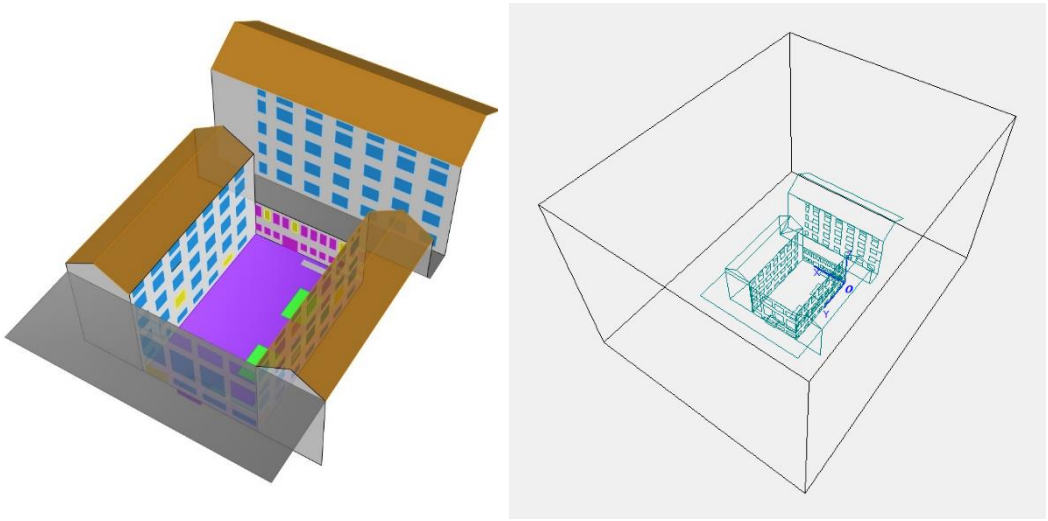

Figure 55. Screenshot of the virtual model of the courtyard in Rhinoceros/Pachyderm (left) and Odeon (right).

The calibration was performed by comparing the mean of the measured T_{20} at the courtyard level and in the outdoor positions over the façade with the corresponding average obtained through simulation. In order to calibrate the acoustic simulations based on the field measurement, as a first step, sound absorption coefficients found in literature databases and scientific articles [444,465,466] were assigned to the surfaces of the virtual model. The scattering properties were initially set as either "low scattering" (LS) or "medium scattering" (MS) according to the roughness of the surface, based on a visual investigation by the authors. However, given the different sensitiveness and methods to quantify the sound diffusion properties of the virtual surfaces in the simulation tools, this step was carried out separately for the two simulation environments. The sound absorption coefficients used to characterize the surfaces of the model in the two simulation tools are detailed in Table 51 in Appendix 5A; the same table reports the corresponding scattering properties (i.e., LS and MS) that are detailed for the two simulation tools in Table 52 (also in the Appendix 5A). The scattering coefficients used in the two models are different and are based on previous expertise. A test was performed in which the simulations were run using the same scattering coefficients, that evidenced marked discrepancies in the results, highlighting the different sensitivity of the tools to that parameter.

The simulation settings defined for both Odeon and Pachyderm are a transition order (i.e., reflection order after which the simulation switches from image-source method to raytracing) of 2, cut-off time of 5000 ms. The number of rays in Odeon is set at 300000 while in Pachyderm it is automatically defined using the "minimum

convergence" option of the ray-tracing component in Grasshopper. Since only Odeon supports edge diffraction calculation, it was disabled for the intercomparison purposes with Pachyderm. Moreover, given that for all outdoor receiver positions the source-receiver line is unobstructed, the effect of edge diffraction was considered negligible. The weather conditions considered for the simulation are kept as default, i.e., with an air temperature equal to 20°C and a relative humidity of 50%. A screenshot of the Odeon simulation settings is shown in Figure 57, while Figure 56a shows the main simulation algorithm developed in Pachyderm for Grasshopper, with a focus on the simulation setting in Figure 56b.

A sensitivity analysis was initially performed in both tools to understand how the accuracy of the simulated values was influenced by the cut-off time and ray number (for Odeon only). The cut-off time was varied between 5000 ms and 1000 ms and the ray number was varied between 300000 and 100000. While no significant difference in T_{20} and *SPL* values was found, it was nonetheless decided to proceed with a ray number of 300000 and a cut-off time of 5000 ms, given the negligible impact of the different settings on the calculation time.

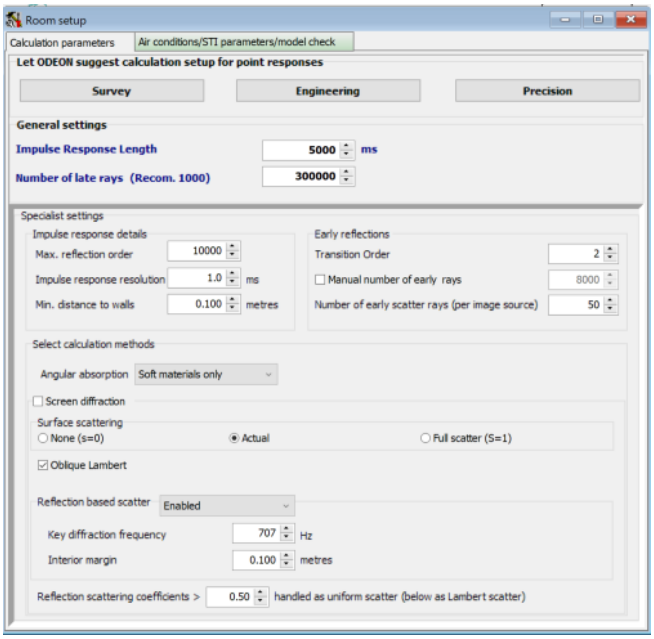

Figure 57. Simulation settings used for Odeon.

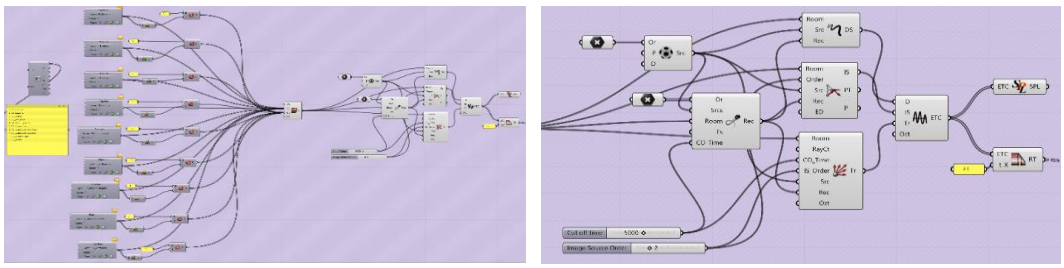

Figure 56. a) main simulation algorithm set in Pachyderm; b) simulation setting used.

The initial model, with material properties assigned based on literature data, was fed to Pachyderm Acoustics and Odeon. Based on the divergence between the simulated and measured T_{20}, the virtual models were calibrated by adjusting the sound absorption and sound scattering coefficients of the materials assigned to the surfaces of the model to fit the measured T_{20}. Starting from the same virtual model with the preliminary acoustic properties, these calibration processes were performed independently for the two simulation tools considered. The adjustments were performed both by weighting the sound absorption/scattering coefficients by a certain factor and by replacing materials with others with similar visual aspects but different acoustic properties.

According to [467] a simulation model is well calibrated when the differences between the simulated and measured values are smaller than the Just Noticeable Difference (JND) values for the considered acoustic parameter, which are defined in ISO 3382-1:2009 Standard [238]. While the JND for reverberation time is set at 5%, however, given the engineering scope of this research, also a 10% agreement between the simulated and measured octave band T_{20} was considered acceptable. A 10% agreement in reverberation time was adopted in [468,469], as considered indicative of a minimum practically important difference. The properties applied to the materials of the virtual model after the calibration are collected in Table 53, Table 54 as concerns sound absorption coefficients and Table 55 with respect to the sound scattering coefficient (see Appendix 5A). It must be noted that, while the simulation tools estimate the acoustic parameters in octave bands in the range 63 to 8000 Hz, the measurement of T_{20} is limited to the octave bands between 125 to 4000 Hz. Therefore, the simulated and measured data are compared in the latter range.

The simulated octave-band T_{20} obtained at the end of the calibration processes for the courtyard and façade receivers using Pachyderm is shown in Figure 58 and in Figure 59 using Odeon. The simulated values reported are calculated as the average of the values obtained at the different courtyard and façade positions. All the presented graphs show the average T_{20} values measured in the same positions used as reference for the calibration, and the ±5% and ±10% thresholds.

As concerns Pachyderm, after the model calibration, the difference between the mean simulated T_{20} and the measured one at the courtyard level is less than 10% in the range 1000 to 4000 Hz and is less than 5%, i.e., the Just Noticeable Difference for reverberation time (JND_{RT}) defined by ISO 3382-1:2009 Standard [238], in the frequency range between 125 Hz and 500 Hz. The difference between the mean simulated and measured T_{20} over the façade is below 10% with the exception of the value at 2000 Hz, for which it is 11%. The T_{20} simulated by Odeon for both courtyard and façade receivers is below or close to the JND_{RT} (±5% threshold) in the range between 250 and 4000 Hz, while its outside the 10% threshold at 125 Hz, with a difference between 18-19%. Overall, these results are considered acceptable and consequently the acoustic model calibrated, considering the engineering scope of the study.

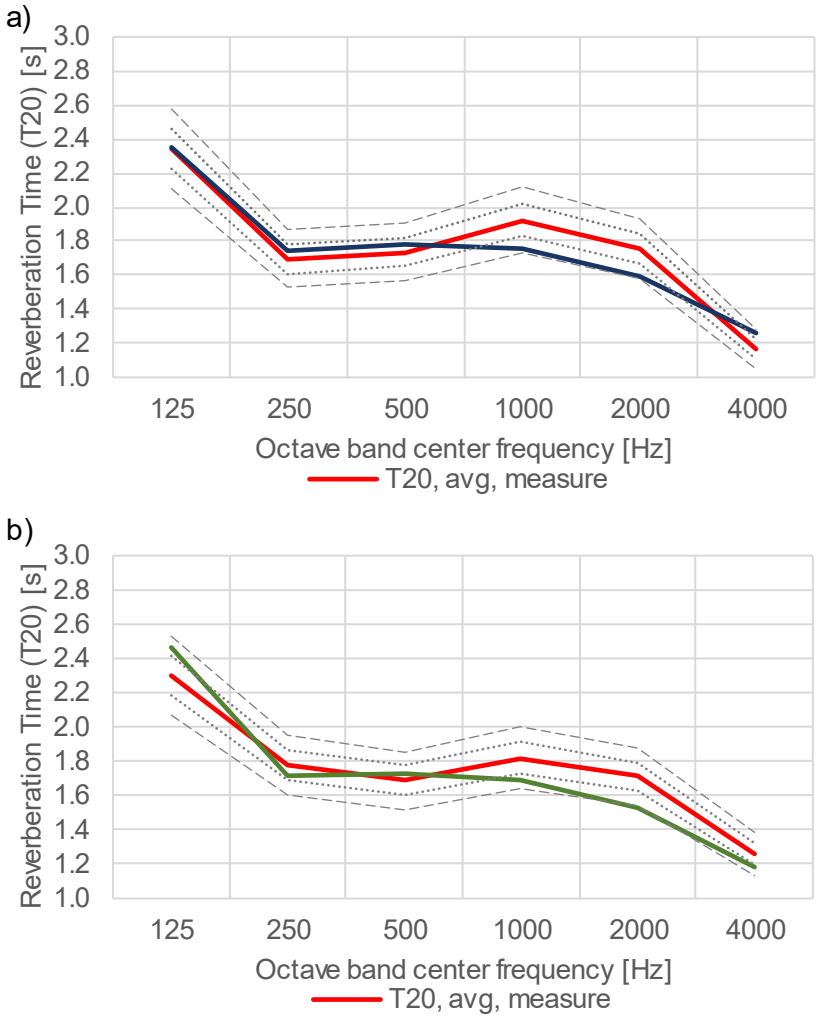

Figure 58. Average of the octave band reverberation time (T_{20}) obtained with Pachyderm after the model calibration a) for the courtyard and b) for the façade receivers. The dotted and dashed lines indicate the ±5% and ±10% thresholds.

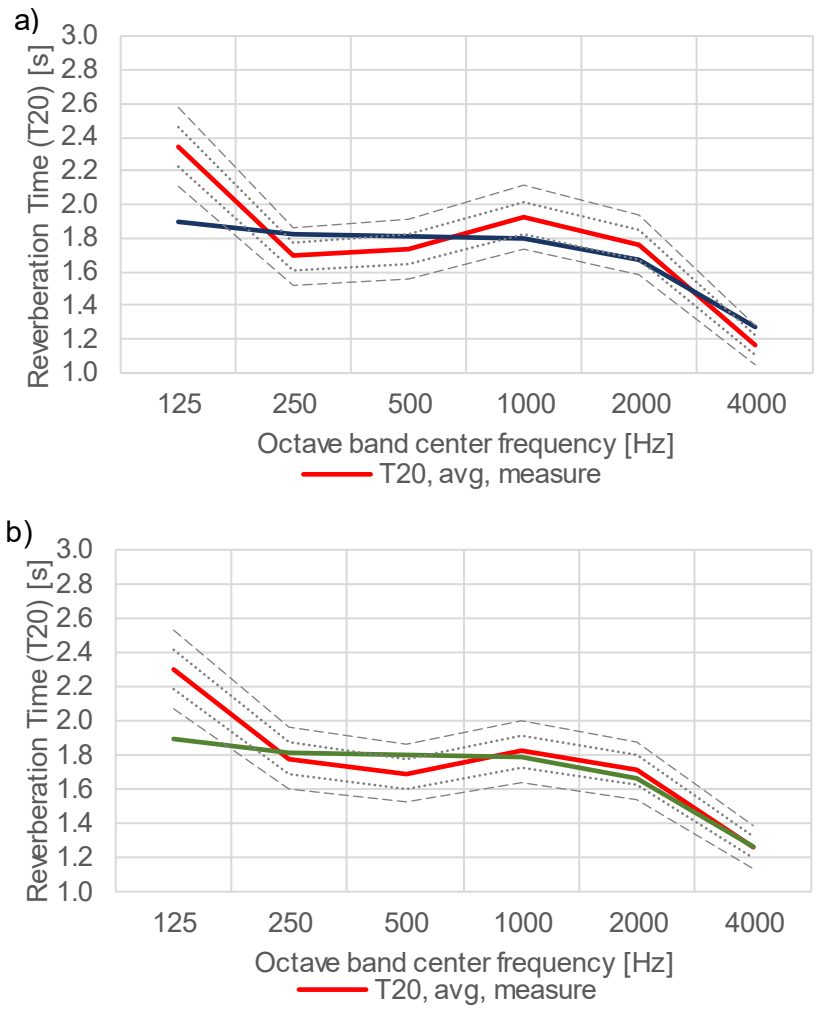

Figure 59. Average of the octave band reverberation time (T_{20}) obtained with Odeon after the model calibration a) for the courtyard receivers and b) for the façade receivers. The dotted and dashed lines indicate the ±5% and ±10% thresholds.

Evaluation of the simulated *SPLs*

Once the models were calibrated, the simulated *SPL* was compared to the measured one in positions G1, G5, G8 and G9 at the courtyard level, and F1, F2, and F3 over the façade.

The comparison was performed considering the overall *SPL* values and, for a more detailed investigation, on the octave-band *SPL* values. Both the overall and the frequency-dependent *SPL*s are referred to the range 125 to 4000 Hz, coherently with the previously described calibration process. The agreement between the overall *SPL* values was assessed calculating the absolute difference between them in each position and as average value for the courtyard/façade positions (this latter value corresponds to the Mean Absolute Error, MAE). The error found for the frequency depended investigation was calculated based on the difference between the measured and simulated *SPL* based on [470], identified in the following as JND Error [-]. The JND Error was calculated following Equation (17).

$$JND\ Error = \frac{\sum_{n=1}^{N_{Freq}} \sum_{i=1}^{N_{Pos}} \frac{\left| SPL_{measured,n,i} - SPL_{simulated,n,i} \right|}{JND_{SPL}}}{N_{Freq} \cdot N_{Pos}} \quad (17)$$

where N_{Freq} is the number of frequency-dependent values considered (in this case the *SPL* values in the different octave bands), N_{Pos} is the number of measurement positions considered and JND_{SPL} is the just noticeable difference for *SPL*, which equals to 1 dB according to ISO 3382-1:2009 Standard [238]. The JND Error compares the average *SPL* difference found for all positions and octave bands values considered to the JND_{SPL} and quantifies how many times the mean difference found is larger than the JND_{SPL}.

The difference found between the simulated and measured *SPL*s are discussed on the basis of the JND_{SPL} and on the 3 dB threshold reported in [471,472] that is associated to a "just perceptible" change in apparent loudness.

5A.4.2. Results and discussion

The results of the evaluations with respect to the overall *SPL*s simulated in the different positions are reported for Pachyderm and Odeon in Table 13. The absolute differences in *SPL* are detailed for each of the considered façade and courtyard positions and as average values of the differences (MAE) for both positions.

Table 13. Evaluation of the overall *SPL* difference found between measurement and simulations.

	SPL difference [dB]							MAE façade [dB]	MAE courtyard [dB]
	F1	F2	F3	G1	G5	G8	G9		
Pachyderm	0.1	0.3	0.5	1.6	1.5	1.9	1.8	0.3	1.7
Odeon	0.4	0.6	0.1	1.4	1.3	1.5	1.6	0.4	1.5

The results highlight that the predicted *SPL*s by Odeon and Pachyderm are close to the measurement, meaning that the tools were able to model the sound energy at the different location with reasonable accuracy. When considering the absolute differences in overall *SPL* found at the specific locations, values inferior to the JND_{SPL} were found for both Odeon and Pachyderm estimations at the façade positions (F1, F2 and F3), while larger differences were found in the courtyard, with values larger than the JND_{SPL}, although in all cases below the 3 dB threshold. This trend can be caused to the presence of elements in the courtyard (e.g., a stack of sand, a water tank and inhomogeneities in the cobblestone paving) that were not included in the simulations and that may have affected the measured *SPL*s in those positions. The MAE found for the façade positions are 0.3 dB and 0.4 dB for Pachyderm and Odeon, respectively, while those for the courtyard positions are 1.7 and 1.5 dB.

The results of the frequency dependent evaluation of the simulated *SPL*, i.e., the calculated JND Errors, are reported in Table 14.

Table 14. Evaluation of the frequency-dependent *SPL* different found between measurement and simulations.

	JND Error for façade positions [-]	JND Error for courtyard positions [-]
Pachyderm	1.6	1.6
Odeon	1.4	1.5

The JND Errors highlight more marked *SPL* differences when considering the octave bands values, that were not evidenced by the comparison of the overall *SPL* values. The JND Errors reported for both simulation tools at the courtyard and façade positions are ~1.5. These results means that mean difference found is on average 1.5 times the JND_{SPL} (i.e., ~1.5 dB), which is considered reasonably acceptable in light of the 3 dB threshold.

For completeness, Table 48 in Appendix 5A includes the octave band and overall *SPL* measured in the different courtyard and façade positions.

It must be however marked that typically geometrical room acoustic models neglect or simplify wave-based phenomena such as diffraction effect, which may have a marked effect in urban settings. Nonetheless, in outdoor scenarios such as the one here considered, i.e., with an unobstructed path between source and receivers, the use of this type of tools was proved reliable.

5A.4.3. Conclusions and further developments

This study investigates the reliability of the use of room acoustic simulation tools to predict outdoor *SPL*s, considering two simulation tools based on geometrical acoustic principles, i.e., Odeon and Pachyderm. A measurement campaign in a courtyard has been carried out to obtain the reverberation time and the sound pressure levels in different outdoor positions at the courtyard level and over the façade of one of the side buildings, at the different floor levels. The virtual models of the courtyard are calibrated based on the measured T_{20}, by adjusting the acoustic properties of the materials in order to minimize the differences between the measured and simulation T_{20} values. The ability to predict *SPL* values in different positions is then assessed on the calibrated acoustic models based on the agreement between the overall *SPLs* and the octave-band center frequency *SPL*s. In summary, a good agreement is found between measured and simulated *SPL*s, with all difference falling below the 3 dB threshold that marks a just perceptible change in apparent loudness. For façade positions, the difference in the overall *SPL* below the JND_{SPL}. These results suggest that Odeon and Pachyderm were able to capture the key acoustic properties of the courtyard and that a good agreement was found between the measured and predicted *SPL*s values in acoustically calibrated model. This outcome suggest that room acoustic tools can be used to reliably estimate *SPL*s values in outdoor scenarios similar to the one considered in this study. It must be however remarked that in the considered scenario the source and receivers' positions are in direct sight and therefore the effect of diffraction, that in other urban scenarios can be relevant, is minor. Therefore, the results of this study can be extended only to urban and acoustic conditions similar to the one here presented.

Further development of this study may include the analysis of different urban settings, the presence of multiple sound sources or linear sound sources. Moreover, the research can be expanded by considering of a wider set of acoustic parameters or by basing the comparison on impulse response analysis, by employing other simulation tools, also including the currently emerging wave-based ones, and through perceptual-based evaluations, which may provide a greater understanding on the human perception under different acoustic scenarios.

5A.5. Design applications

5A.5.1. Effect of façade design variations in a courtyard

This research contribution aims to investigate the noise reduction potential of a retrofit intervention for the façades at the two opposite sides of different urban scenarios, using acoustic simulations. The goal of the design intervention on the buildings is to introduce double skin façade systems, whose outer layer, in its form and material features, is the object of the present study. Staring from concept design idea for the façade design applied to a case-study courtyard, the work aims to analyze the influence of various geometric and material options on the environmental noise level in outdoor positions.

In certain urban scenarios, such as nightlife districts or in touristic areas, the leisure noise generated by people talking in the outdoor public areas (e.g., street, squares, etc.), has a significant impact. Especially in nightlife districts, leisure noise can be considered the predominant noise source during night times [73–76]. In neighborhoods where leisure functions are located at the ground floors of residential buildings, the mitigation of the generated noise is of crucial importance to protect the health and wellbeing of the resident population. Moreover, it is likely that in the near future the relevance of leisure noise would increase, as that of traffic noise is expected to be reduced by electrical vehicles [473,474].

This study investigates the noise reduction potentials of different façade design options in a courtyard, considering the presence of leisure noise in the courtyard itself.

As a first step, the case-study courtyard already presented in § 5A.4 was used to investigate the effectiveness of different geometric and material façade design options at reducing outdoor *SPL*s. Based on the findings of this step, the study is advanced by considering the noise reduction potential of the most performing solution found in other urban scenarios, i.e., a street and an isolated building, in the attempt to assess its effectiveness in a broader variety of settings. To conclude, the effect of a sound absorbing paving is evaluated and compared to the noise reduction potential of the façade design options.

Method

The acoustic simulation were carried out using Pachyderm [243], that was used to predict the variation of outdoor A-weighted Sound Pressure Level (*SPL*) occurring over the façades of the side buildings of the courtyard, as a function of the different design scenarios investigated.

The case-study courtyard

The case-study is an existing courtyard of the Politecnico di Torino in Turin, Italy; the courtyard was described in § 5A.4, and a picture of the courtyard is presented in Figure 60a. At the present state, the buildings facing the courtyard host laboratories and offices of the university and no activity such as bar or restaurant is present, however, the scenario can be considered representative of an urban courtyard hosting the open spaces of restaurants and bars located at the ground floor of residential buildings. The retrofit design proposal is the addition of a wedged double skin to the two opposite building on the longest sides of the courtyard. The two buildings, shown at the two sides of Figure 60a, will be referred to as building A and building B in the following. Figure 60b presents an example of double skin façade design option for the two buildings.

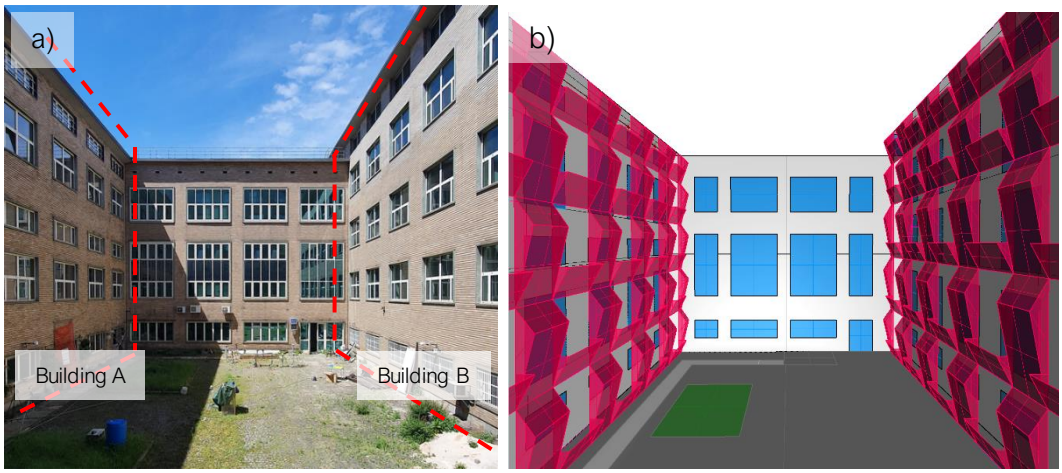

Figure 60. a) Picture of the courtyard adopted as case-study, with the identification of buildings A and B and the position of the double skin (red dashed line); b) parametric model of the double skin to be applied to the side buildings (in red color).

The double skins are meant to create a series of small balconies in place of the windows of the pre-existing building and also to reduce environmental noise over the façades. The present contribution focuses on the ability of the proposed double skin design to lower environmental noise levels in outdoor positions.

Acoustic measurements and model calibration

The acoustic model of the courtyard was calibrated with respect to in-situ measurement of reverberation time (T_{20}) conducted in May 2021. The acoustic properties of the materials in the virtual model were adjusted to ensure a good matching between the simulated and measured reverberation time at the courtyard level and over the façade of the building, as described in § 5A.4. In the calibrated model, the difference between the mean simulated reverberation time and the measured one at the courtyard level and over the building façade is less than 5% in the frequency range between 125 Hz and 500 Hz, and less than or close to 10% in the range 1000 to 4000 Hz.

Acoustic simulation set up

The acoustic simulation was performed using the Grasshopper version of Pachyderm Acoustics (v 2.0.0.2) [243]. The simulation procedure combines image source and raytracing and were performed with transition order 2 and a cut-off time of 5000 ms. The number of rays shot is automatically determined by Pachyderm based on the convergence of the simulated results.

The acoustic parameter used to describe the simulated variation of environmental noise perceived by the people located in the courtyard and in the balconies is the A-weighted *SPL*, which accounts for the frequency-dependent intensity perceived by the human ear. An omnidirectional sound source was positioned at the geometric center of the courtyard, at 1.5 m height from the ground. The source represents a group of people talking in the courtyard, as done in [107]. Its frequency spectrum is based on the ICRA noise [475] and presents an overall sound power level (*SWL*) of 80.0 dB. Table 15 reports the octave-band and global *SWL* of the source.

Table 15. Octave band sound power level of the omnidirectional sound source used to simulate the presence of a group of people talking at the center of the courtyard.

	Octave-band center frequency (Hz)								
	63	125	250	500	1000	2000	4000	8000	overall
SWL [dB]	60.8	65.5	76.6	76.6	64.8	58.1	55.1	46.3	80.0

The sound receivers were initially located in correspondence of the barycenter of the windows of the façade of both buildings A and B, at 2 m from the base-plane of the double skin (that corresponds to a distance of 3 m from the existing façade). Since the courtyard is almost symmetric and the results obtained on the two façades were comparable on a floor basis, for the sake of simplicity, only those of the receivers on building B (see Figure 60) were considered, which are shown in Figure 61.

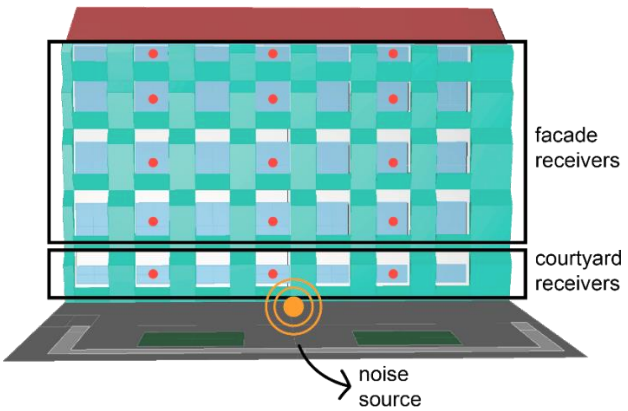

Figure 61. Virtual model of building B showing the position of sound receivers at the courtyard level and over the façade and the position of the sound source

It must be highlighted that even though the results have been collected on building B only, the proposed design variations investigated are applied to both buildings A and B in all the tested scenarios. Three receivers were placed at each of

the 5 floors of the design building. The receivers located at the ground floor of the building, namely courtyard receivers, are used to estimate the variation of A-weighted *SPL* perceived by pedestrians in the courtyard, while that of those located from the 1st to the 4th floors are used to estimate that of dwellers in the balconies.

Form and material variation of the double skin façade design

The proposed double skin has been designed to integrate the creation of new functionalities to the existing building with the reduction of environmental noise levels. It is composed of a pattern of protruding wedges that enables the creation of a series of balconies in place of the pr-existing windows, providing the building users with small private open spaces.

In order to evaluate and optimize the design based on the predicted noise levels, some design alternatives are investigated. While the main design concept of the double skin remains unaltered, the geometric variations inform the inclination of the sides of the wedges and their depth; moreover, the application of sound absorbing materials to different portions of the double skin was tested.

The double skins are applied to the buildings on the longest sides of the case-study courtyard and some slight changes to the existing buildings were implemented to host the double skins. The base plane of the structures is placed at a distance of 1 m from the existing façades, and the double skins are composed of a series of protruding wedges with the inter-floor height and variable depths. While the wedges that covers an opaque portion of the building are complete, those located in correspondence of the windows of the façade present only the lower sides, whose height is fixed at 1.1 m, while the upper portions are absent to create balcony-like elements. The inclined sides of the wedges interact with the sound propagation within the courtyard by diffusing the incoming sound, i.e., redirecting it in different directions, in the attempt to promote the reflection of sound energy outside the courtyard. A parametric model of the two double skin façades was defined in Grasshopper to generate the set of geometric and material design variations to be investigated. Figure 62a shows reference configuration, i.e., a flat double skin with sound reflective finish, along with the geometric variations of the wedges and the corresponding identification codes. Figure 62b provides an overview of all the geometric and material changes applied to the double skin design.

The geometry of the wedges was altered by controlling the wedge depth and the relative tip height, result in different tilting of the wedges' sides (see Figure 62a and "Geometry" section in Figure 62b). The depth of the wedges was varied in all the floors and was either set at 0.3 m, 0.6 m or 0.9 m, respectively identified as d_03, d_06, d_0.9. Moreover, it was also varied according to an increasing/decreasing gradient, i.e., 0.3 m at ground and first floor, 0.6 m at second floor, 0.9 m at third and fourth floor for the increasing gradient option (d_incr), and vice-versa for the decreasing one (d_decr). Besides the depth, also the position of the wedge tip was altered, as it was set at either 25% or 75% of the wedge height, identified in the following as t_25% and t_75%, respectively. This variation results in either greater or smaller angles of inclination of the lower sides of the wedges, and vice-versa for the tilting of the upper

sides. Moreover, it also results in a variation of the area of the lower and upper sides of the wedges.

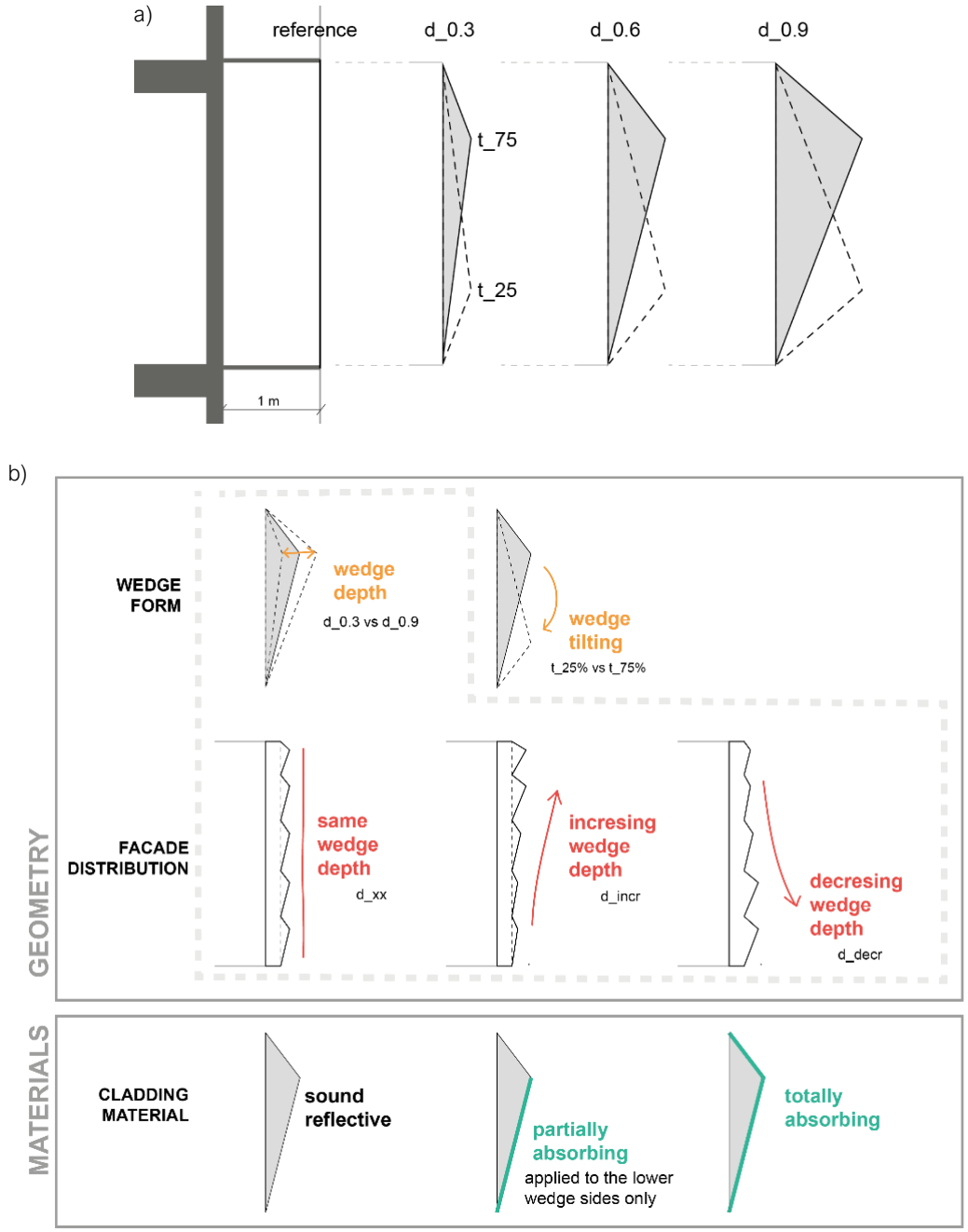

Figure 62. a) section of the reference configuration and examples of geometric variation of the wedges, considering wedge depth and tip position; b) scheme of the geometric and material variations tested, showing the different form variation at the wedge and façade.

It must be noted that the design variations shown in Figure 62 are representative of the wedges located in front of an opaque portions of the façade. Indeed, those located in front of the windows present only the lower wedge sides that work as the balcony parapets; in these cases, the wedge tip position was fixed at 1.1 m, which

corresponds to the height of the balcony parapet, and only wedge depth is varied parametrically.

As regards the material variations (see "Materials" section in b), the tested options include the partial or total replacement of the glass applied to the wedges in the "sound reflective" configuration, with a commercial sound absorbing material suitable for outdoor application, that consists of a perforated metal panels with a porous filling. The sound absorbing material was either used over all the surfaces of the double skin (named "totally absorbing" configuration) or applied to the downward-oriented sides of the wedges while the upper parts were sound reflective (named "partially absorbing"). This has been done in the attempt to better exploit both the sound absorbing and the sound diffusing properties of the façade, by absorbing the sound coming from the courtyard impinging on the lower sides of the wedges and promoting the redirection of the sound towards the sky with the upward oriented sides of the wedges, to reduce sound trapping. Moreover, the partially absorbing configuration may also result in reduced intervention costs and an increase in the durability of the sound absorbing panels, which are partially shielded from the weather elements. The octave-band sound absorption (α) and sound scattering coefficients (s) of the two cladding options are detailed in Table 16.

Table 16. Octave band sound absorption (α) and sound scattering (s) coefficients of the sound reflective and sound absorbing materials used for the double skin façades.

		Octave-band center frequency (Hz)							
		63	125	250	500	1000	2000	4000	8000
Perforated metal (sound absorbing)	α	0.09	0.09	0.14	0.38	0.67	0.85	0.88	0.88
	s	0.03	0.03	0.05	0.05	0.06	0.07	0.10	0.15
Glass (sound reflective)	α	0.15	0.15	0.05	0.03	0.03	0.02	0.02	0.02
	s	0.03	0.03	0.05	0.05	0.06	0.07	0.10	0.15

In total, 30 design configurations of the double skin were evaluated, resulting from 10 geometric variations, each considered with the 3 different acoustic material options. The design configurations are summarized in Figure 63. The noise reduction performance of these configurations was assessed with respect to the reference configuration, i.e., a flat double skin with sound reflective finish.

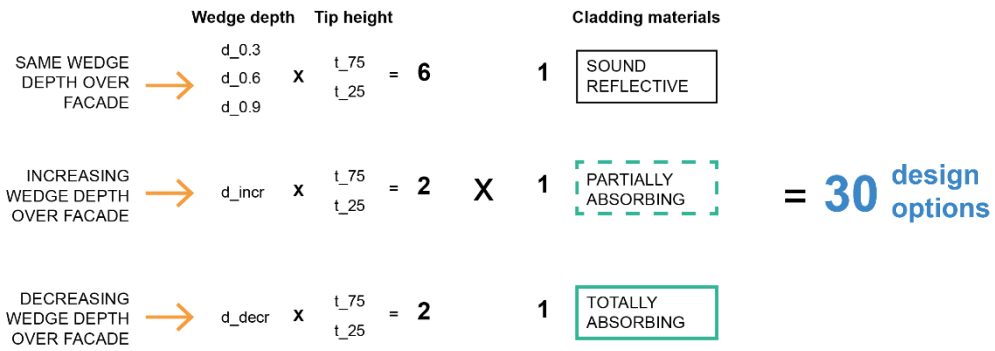

Figure 63. Scheme of the 30 façade configurations tested.

Testing of the design option in different urban configurations

The scope of the research was broadened by testing the most performing configuration found in the previous step in different urban scenarios, to understand the extent to which the findings were generalizable to a wider variety of urban settings.

This study aims to evaluate the ability of the most performing façade strategy to reduce the impact of leisure noise in courtyard and street with various widths. To this aim, the two urban settings were analyzed with three width options, i.e., 10, 20 and 30 m. Figure 64 shows the urban configurations considered, i.e., street and courtyard, with the three width options analyzed.

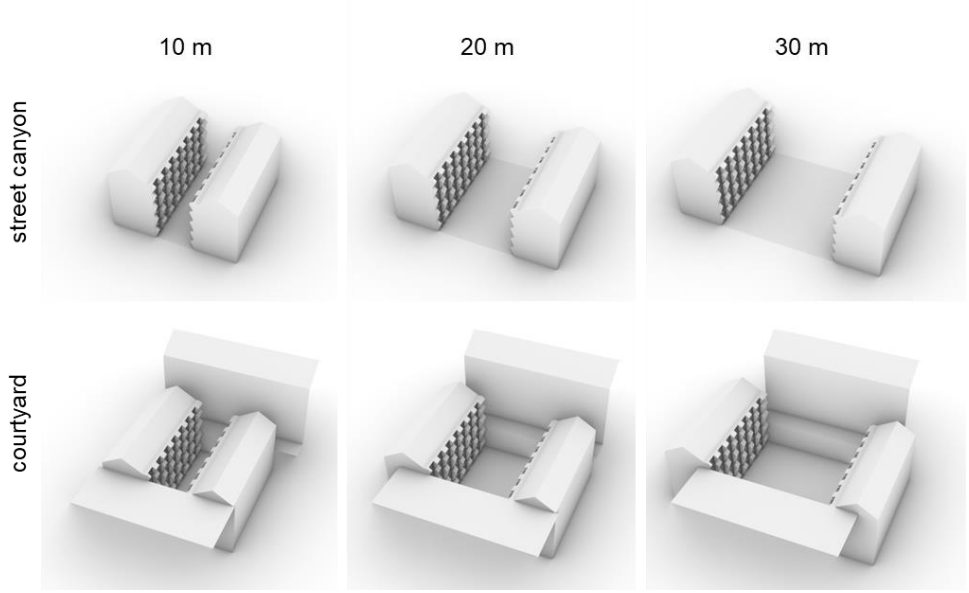

Figure 64. Summary of the urban configurations considered with the 3 width options.

In order to reproduce a street canyon, the basic courtyard configuration was altered by removing the buildings enclosing the shorter sides. The obtained model, despite exhibiting a limited length can be considered representative of a street, as evidenced in [107]. For each urban setting, a reference scenario, with a flat double skin with sound reflective finish applied to the façades at the two opposite sides, is compared to the most effective configuration found at the previous research step. Since the analysis is referred to chatting noise, the sound source position and *SWL* are kept unaltered with respect to the previous section.

Testing of the presence of sound absorbing paving

To conclude, a simulation analysis was performed to assess the contribution provided by the application of low-noise asphalt to the pavement of the case-study courtyard in presence of leisure noise. In this case, the scenario considered the treatment of the courtyard paving with a representative porous asphalt (i.e. void ratio 20%) [476], in combination with the reference configuration of the double skin façade (see). The acoustic coefficients of the asphalt are reported in Table 17.

Table 17. Octave band sound absorption (α) and scattering (s) coefficients of the low-noise asphalt. *unavailable data, assumed equal to measured data in the closest octave band.

		Octave-band center frequency (Hz)							
		63	125	250	500	1000	2000	4000	8000
Low-noise asphalt	α	0.30*	0.30	0.09	0.36	0.36	0.37	0.37*	0.37*
	s	0.03	0.03	0.05	0.05	0.06	0.07	0.1	0.15

Results and discussion

In the following sections, the results of the three research steps are detailed. As previously evidenced, the variation of *SPL* resulting from the design variations of the double skin at the different floors of building A and B was comparable. Therefore, for the sake of simplicity, the results reported in the following refer to the receivers on building B, although the design variation are applied to both façades.

Analysis of the façade design alternatives on environmental noise reduction

The A-weighted *SPL* results collected by the receivers located in outdoor positions over the façade of building B for the different design configurations of the double skin are plotted in Figure 65. The simulated A-weighted *SPL* values for the flat double skin option with sound reflective finish are considered as reference (in red in the graphs). The sound reflective, partially absorbing and totally absorbing material options are shown with a color gradient, from the lighter to the darker green.

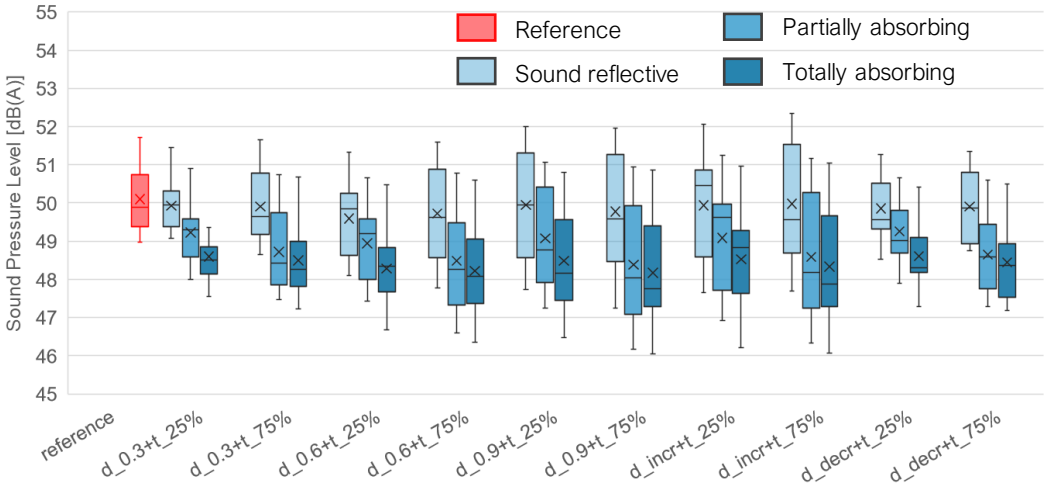

Figure 65. Variation of A-weighted *SPL* over the façade of building B resulting from the different material and geometric configurations tested, in comparison to the reference configuration (in red).

The *SPL*s are reported using boxplots to provide information on the statistic distribution of the simulated A-weighted *SPL*s over the façade. Besides the quartile thresholds, the arithmetic mean values for the façade and courtyard receivers are reported (marked by a cross). The highest values reached by the boxplot can be

considered representative of the closest receivers to the sound source, i.e., 1st floor, while the lower values are those of the receivers located at the highest floors of the building.

The analysis of *SPL* for the different geometric variations with sound reflective finish, which allows to isolate the effect of the geometric options, reports limited *SPL* variation over the façade. The mean value is close to 50 dB(A) for all design options and for the reference configuration, i.e., flat double skin, showing negligible variations i.e., smaller than the JND_{SPL} of 1 dB [238]. While this highlights the minor influence of geometric variation on the mean outdoor *SPL*, it must be noted that the lowest *SPL* values, i.e., the value perceived by the highest floors, vary more markedly based on the geometric configurations. The lowest values of *SPL* seem to decrease for increasing depth of the wedges. Indeed, the configurations that reach the lowest values, i.e., around or inferior to 48 dB(A), are those presenting a depth of 0.6 m or 0.9 m and an increasing wedge depth at the highest floors, i.e., d_0.6+t_25%, d_0.9+t_25%, d_0.9+t_75%, d_incr+t_25%., d_incr+t_75%. This is likely to be due to the more effective noise screening exhibited by the deeper wedges for the receivers at the highest floors. Conversely, the geometric solutions where the wedge depth decreases with increasing floors present *SPL*s comparable to those obtained for the reference configurations and for the options with a wedge depth of 0.3 m. The wedge tip position does not have a noticeable influence on the *SPL* in case of a sound reflective treatment.

When considering the totally absorbing configurations, a noticeable decrease in the mean *SPL* over the façade up to ~1.5 dB is reported with respect to the same configuration with sound reflective materials. This result is coherent with the findings of other studies [17]. When considering the minimum values reached by the *SPL*s, the geometric trends previously observed for the reflective finish are confirmed. The lowest values obtained in case of the sound absorbing treatment are around 46 dB, evidencing a *SPL* reduction of 3 dB with respect to the lowest values reached by the reference configuration.

As concerns to the results obtained by the partially absorbing and totally absorbing configurations, it must be highlighted that the mean, maximum and minimum *SPL*s reported for the two solutions are comparable for almost all configurations (i.e., differences smaller than the JND_{SPL}). This trend is emphasized for the options with the wedge tip at 75% of the height, probably due to the resulting greater area of the inferior sides of the wedges treated with sound absorbing materials.

In order to better focus on the variation of *SPL* at the different building floors, Figure 66 shows the floor-based *SPL* for the different material and geometric configurations. The floor-based *SPL* is shown using histograms quantifying the arithmetic mean of the *SPL* values of the three receivers placed at each floor; for completeness, also the standard deviation is reported.

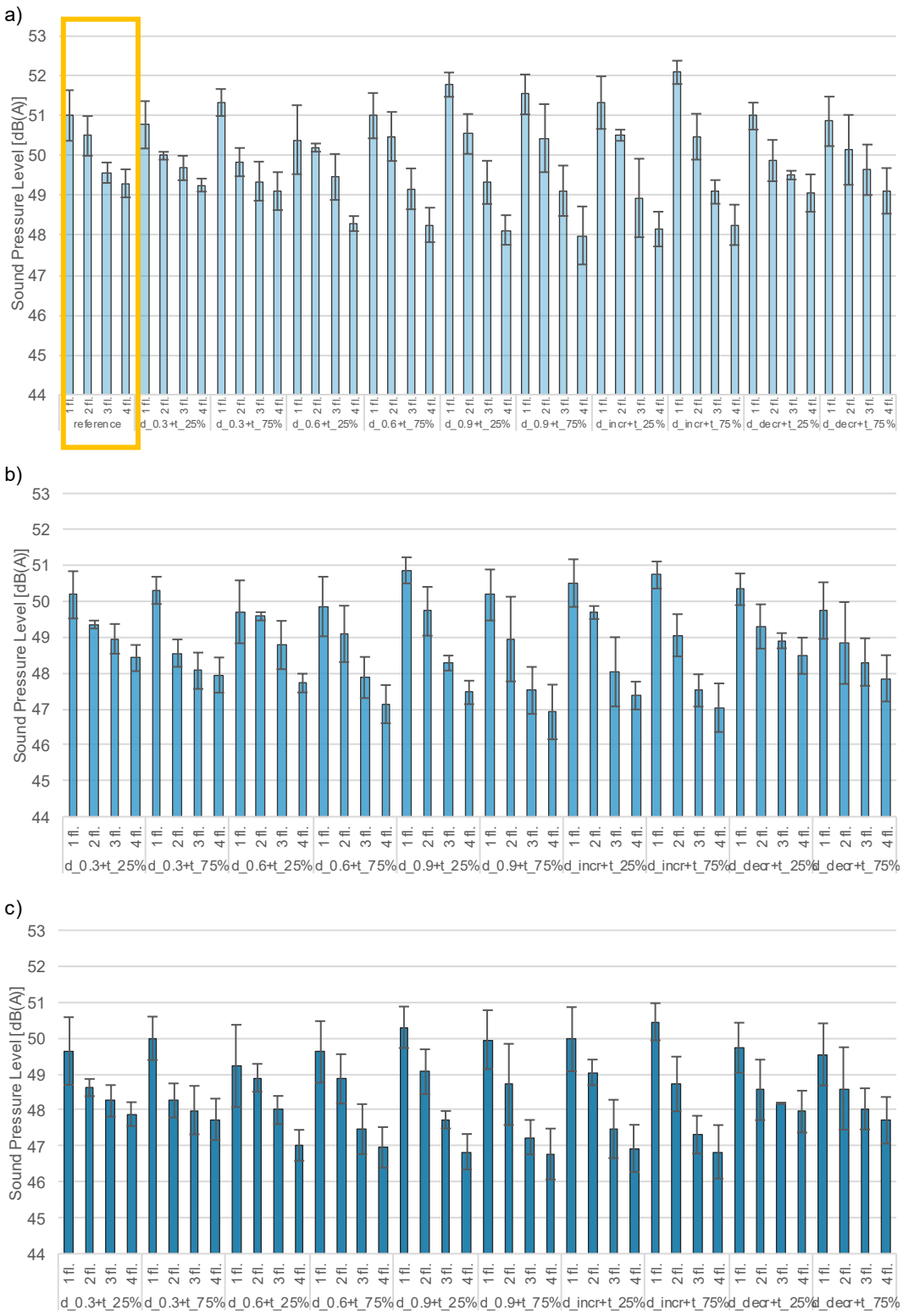

Figure 66. Floor-based variation of SPLs for the different double skin façade variations, for sound reflective (a), partially absorbing (b) and totally absorbing (c) material configurations. The yellow rectangle marks the reference configuration.

The graphs confirm a decreasing SPL trend for increasing floors. The reference configuration (highlighted in yellow in Figure 66) has a mean *SPL* value ranging from 51 dB(A) at the 1st floor to 49.3 dB(A) at the 4th floor of the building. Considering the different geometric options with sound reflective materials, more marked decrease of *SPL* for increasing building floors are reported for the geometric configurations with the greatest wedge depths (0.6 m, 0.9 m or increasing wedge depths), which leads to lower *SPL* values at the 4th floor, as already discussed. Nonetheless, it must be noted that a *SPL* increase of ~1 dB is reported at the 1st floor for the configuration with increasing wedge depths at the tip at 75% of the height. In contrast, the configurations with wedge depths of 0.3 m and decreasing wedge depths result in floor-based *SPL* variations comparable to the reference configuration. The floor-based analysis confirms the effectiveness of the partially absorbing configuration. It results in noticeable floor-based *SPL* reductions (greater than the JND_{SPL}) with respect to the corresponding geometry with sound reflective materials for all the geometric options with the tips at 75% of the wedge height. In the case of the totally absorbing configuration, all the tested geometric options lead to noticeable reductions, whose magnitude is comparable to that reached by the partially absorbing options with the tips at 75% of the height. These geometric configurations are indeed those that better exploit the sound absorbing treatment applied to the downward oriented wedge side in the case of the partially absorbing configuration, especially in case of the 0.9 m wedge depths or the increasing wedge depths. Therefore, d_0.9+t_75% and d_incr+t_75% with a partially absorbing treatment emerge as the most effective design solutions among those tested. They exhibit good noise reduction performance (up to a mean SPL reduction of 2 dB at the 4th floor), while allowing to limit the intervention cost and potentially also to increase the durability of the sound absorbing materials.

The A-weighted *SPL* at the courtyard level (see Figure 67), representing pedestrian positions, is just marginally influenced by the geometric and material variations of the double skin. The maximum, minimum and mean value show a negligible variation for the geometric options tested (differences smaller than 1 dB). The application of sound absorbing materials leads to *SPL* reduction generally inferior or in the order of 1 dB with respect to the reference scenario (slightly greater reductions are reported in comparison with respect to the corresponding geometric option with a sound reflective treatment). As for the receivers over the façade, the difference between the partially absorbing and totally absorbing options is negligible.

Overall, the most effective double skin design configurations are d_0.9+t_75% and d_incr+t_75% with a partially absorbing material configuration, which provide noticeable *SPL* reductions over the façade at all floors of the building, with results comparable to the totally absorbing material treatment.

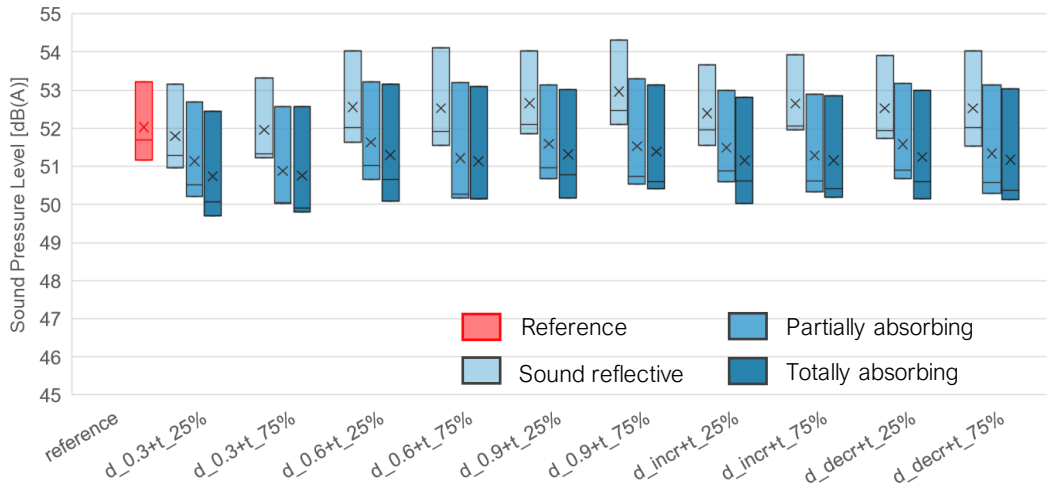

Figure 67. Variation of A-weighted *SPL* for pedestrian receivers (i.e., at the ground level of building B) resulting from the different material and geometric configurations tested, in comparison to the reference one (in red).

Analysis of the effectiveness of the façade option in different urban scenarios

In order to evaluate the effectiveness of the double skin façade design strategies on noise reduction in other urban settings, the design option d_0.9+t_75% with partially absorbing material configuration is chosen, as one of the most performing ones. This configuration exhibits 0.9 m deep wedges, whose tip is placed and 75% of the overall wedge height and the downward oriented edge is treated with sound absorbing material. The façade configuration is shown in Figure 68 when applied to building B.

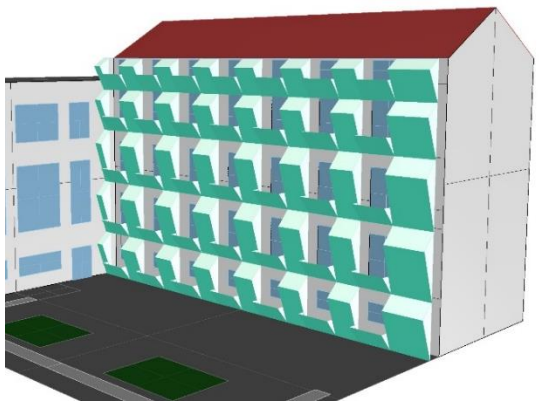

Figure 68. Virtual model of building B with d_0.9+t_75% and the partially absorbing material configuration. Sound absorbing material is shown in dark green.

The predicted *SPL* for the façade receivers for the courtyard and street configurations are shown in Figure 69a for the street configuration and in Figure 69b for the courtyard one. The mean differences in floor-based *SPL* are summarized in Table 18 for the tested urban configurations, also including the pedestrian positions

(not reported in Figure 69). In the results, the *SPL* obtained by the best performing façade option are compared to the reference (flat and sound reflective double skin).

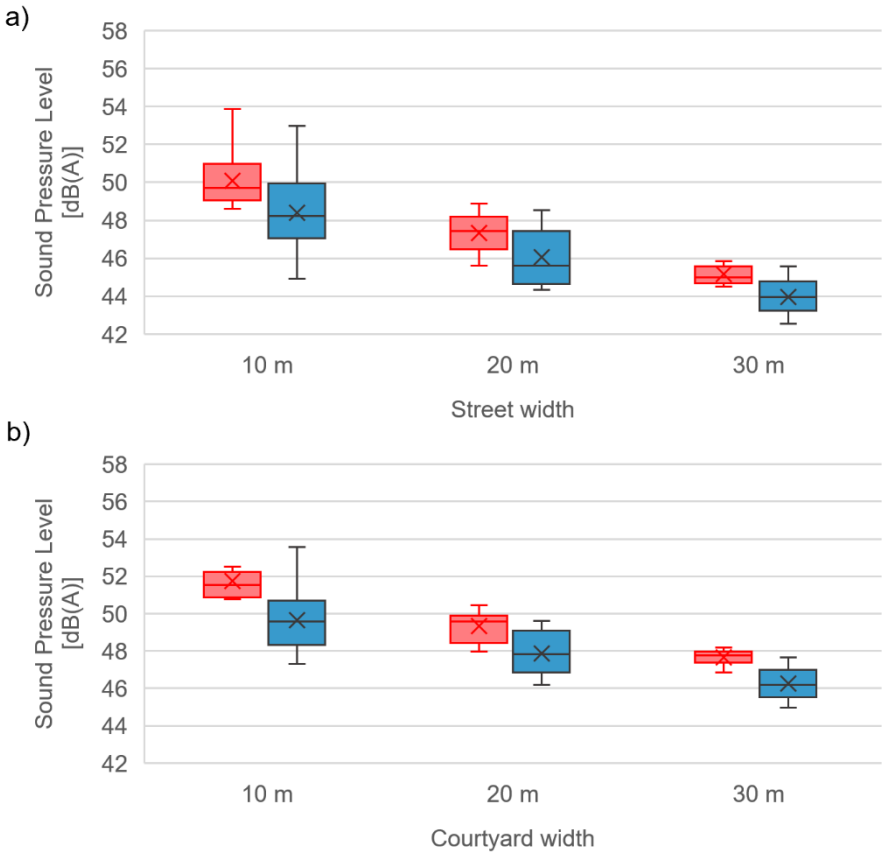

Figure 69. A-weighted *SPL*s over the façade predicted for the street (a) and courtyard (b) as a function of their width.

The *SPL* values are generally greater for the courtyard than for the street, with difference for the reference configurations close to 2 dB. This trend is caused by the sound trapping behavior of the courtyard, that is more enclosed in comparison to the street and cause the emitted energy to be reflected multiple times. The predicted *SPL*s tend to be greater for the narrower courtyard and street configurations, due to the reduced source-receiver distance and for the sound trapping. In the reference configuration (flat with sound reflective materials), the mean *SPL* passes from ~50 dB(A) to ~45 dB(A) for the street and from ~52 dB(A) to ~48 dB(A) for the courtyard, as the width passes from 10 to 30 m. The effectiveness most performing double skin façade option is confirmed in the tested urban configurations. The mean *SPL* is reduced by ~1 dB for the narrower urban configurations, while the *SPL* reduction is less marked for the wider scenarios, suggesting a greater effectiveness for denser urban configurations. The lowest *SPL* values is almost 4 dB lower for the most performing double skin façade design for the narrower configurations.

The floor-based analysis (Table 18) shows that the *SPL* variations tend to be greater for narrower urban configurations and for upper building floors. Noticeable *SPL* reductions are reported from the 1st floor for the 10 m-wide urban scenarios, and

from the 2nd floor for the wider ones. This result is caused by the multiple sound reflections occurring in denser settings, especially for receivers at the highest building floor, that emphasizes the effectiveness of the mitigation provided by sound absorbing façade treatment. The maximum *SPL* reduction, equal to 3 dB, is reported at the 4th floor for the 10 m-wide courtyard. As expected, the *SPL* variation for pedestrians is negligible for all urban scenarios.

Table 18. Mean difference in A-weighted SPLs at the different floors for the urban configurations analyzed. Noticeable reductions are in bold.

	street			courtyard		
	10 m	20 m	30 m	10 m	20 m	30 m
pedestrians	-0.1	0.5	-0.3	-0.4	0.0	0.2
1st floor	**-1.2**	-0.6	-0.5	**-1.5**	-0.7	-0.5
2nd floor	**-1.1**	**-1.4**	**-1.5**	**-1.7**	**-1.7**	**-1.5**
3rd floor	**-1.7**	**-1.4**	**-1.7**	**-2.1**	**-1.4**	**-1.3**
4th floor	**-2.7**	**-1.4**	**-2.0**	**-3.0**	**-1.6**	**-1.6**

Overall, these results highlight that the effectiveness of the considered façade option increases when it is applied to dense urban environments, especially at the highest building floors.

Analysis of the effect of sound absorbing paving on noise reduction

The results of the testing of the application of the low-noise asphalt to the paving of the case-study courtyard are reported in Figure 70.

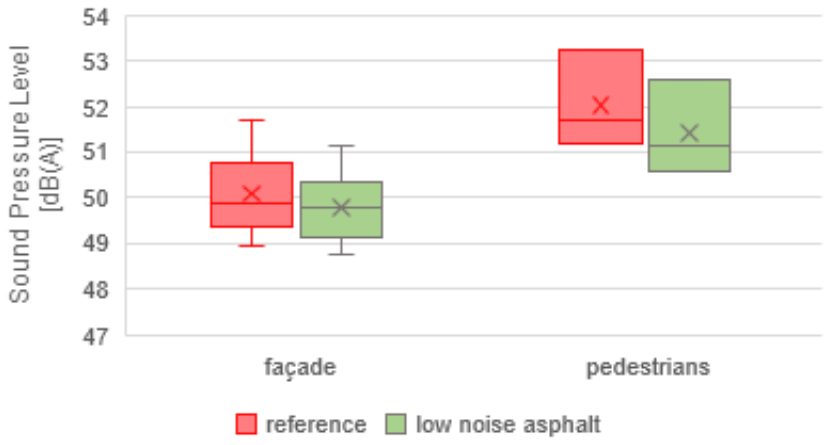

Figure 70. Comparison of the SPLs for façade and courtyard receivers in the reference configuration and with low-noise asphalt applied to the courtyard paving.

The *SPL* variation found are negligible for the façade receivers and those at pedestrian positions, overall evidencing that the application of a sound absorbing asphalt to the courtyard is not effective to mitigate leisure noise. This result is in line with the findings in [107]. This is probably caused to the prevailing role of sound

reflections occurring over building façade of the courtyard with respect to those occurring over its paving, whose dampening doesn't provide significant benefits in terms of acoustic comfort.

Conclusions and further developments

This study has analyzed the variations in A-weighted *SPL* resulting from different design variations of the double skin façade applied to the buildings at the two opposite sides of a courtyard in presence of leisure noise (people talking in the courtyard). In total, 30 design options were tested, combining geometric and material variations. As concerns geometric variations, starting from a preliminary design concept for the double skins, composed of a series of protruding wedges, the variation of the wedge depths and of the tilting angles of their sides in investigated. Moreover, the application of sound absorbing materials to the wedge sides or to the downward oriented side is compared to the base scenario with sound reflective finish materials. The obtained *SPL* are compared to those obtained by the reference double skin (flat and with sound reflective materials) that represent a more conventional design configuration, at the façade and pedestrian positions. The analysis has shown that the geometric variation alone did not result in noticeable *SPL* variations over the façade, while marked *SPL* reductions are reported for the application of sound absorbing materials on the double skin. The greatest *SPL* reductions over the façade are reported at the highest building floors for the configuration with wedge depth of 0.6 or 0.9 m, or increasing wedge depths, combined to the partially absorbing or the totally absorbing material configurations. The reported *SPL* variations at pedestrian positions are generally negligible for the configuration tested.

The double skin façade design option exhibiting 0.9 m deep wedges, whose tip is placed and 75% of the overall wedge height and the partially absorbing configuration (with sound absorbing materials only on the downward oriented wedge sides) can be considered the most effective one at reducing *SPL* over the façades. It leads to a mean façade SPL reduction of ~1.5 dB. To evaluate the sensitivity of the *SPL* variation to the considered urban scenario, this configuration has been compared to the reference one in a street and in a courtyard, with 3 width options from 10 to 30 m. The results show that the effectiveness of the selected double skin design increases for narrower and denser urban settings, especially at the highest building floors, with *SPL* reductions up to 3 dB.

To conclude, the application of a sound absorbing asphalt to the paving of the case-study courtyard has been tested. Since the *SPL* variations reported are negligible in both façade and pedestrian positions, the application of low-noise asphalt result in an ineffective strategy to mitigate leisure noise.

Further investigations may extend the analysis to traffic noise sources, which are generally the prevailing noise source in cities, may include different double skin design options on a floor basis and the use of wave-based acoustic simulations for a detailed investigation of the resulting *SPL* variations in the balconies. Moreover the use of perceptual evaluations through laboratory experiments, such the ones in [77–80], may help gaining a deeper understanding on the perceived impact of the design options.

5A.5.2. A proposal to improve acoustic comfort in Wolfsburg Connect project

The project called “Wolfsburg Connect” by Henning Larsen will create a new mixed-use master plan in the heart of Wolfsburg, Germany. Among the objectives of the project is the creation of a diverse public realm that celebrates human scale, with propriety being given to pedestrians and soft mobility. At the time of writing, the project is under development and the information available is collected from [477,478] and from personal communication with the design team at Henning Larsen, directed by the architect Katrin Bindner.

Wolfsburg Connect is a large new development, with a design area of 91.500 m^2, that will be constructed on an empty area close to the Mittelland Canal, with an additional expansion in the already-built area of the city. The design intervention consists of a series of mixed-use terraced buildings and a taller office building, all connected by a pedestrian area articulated in a series of sub-spaces with different functions; the site plan of the project is shown in Figure 71 [477]. The pedestrian area, which is one of the main cores of the design, consists of a path connecting a series of open courtyards, located at different elevations, culminating in the public space close to the Wolfsburg railway station that also connects to the bridge crossing the Mittelland Canal.

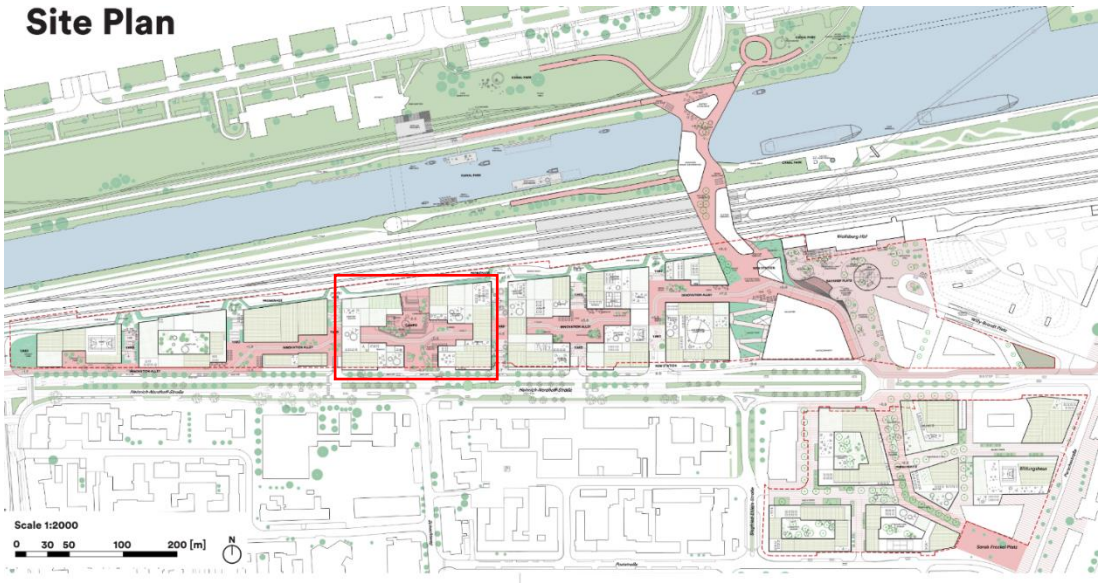

Figure 71. Site plan of Wolfsburg Connect; the portion of the project selected for the acoustic analysis is highlighted in red.

The area of intervention, shown in Figure 72 [477], is challenging from the acoustic point of view, being located between a major vehicular road and a railway, and relatively close to the Volkswagen factory. This has been also reported in the noise immission study on the area [479], which estimates that noise rating levels are between 43 dB(A) and 75 dB(A) during the day, and between 39 dB(A) and 72 dB(A) at nighttime, exceeding the orientation levels defined by the DIN 18005-1:2002-07 Standard [480].

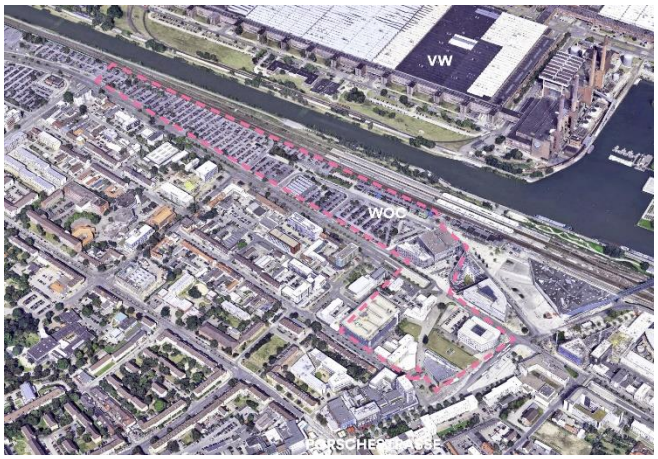

Figure 72. Area of intervention for Wolfsburg Connect.

In light of the importance of the Volkswagen plant in the area, that is the worldwide headquarters of the Volkswagen Group, the design proposal maintains and emphasize the visual connection between the city and the factory, with a series of cutting view corridors across the new development, as seen in Figure 73 [478]. This design choice may however cause the sound emitted by the street and the railway to enter the courtyards, potentially reducing acoustic comfort for dwellers and pedestrians.

Figure 73. Cutting view corridors created to visually connect the city with the VW plant.

In this frame, a simulation study was conducted to better understand how the design of the façades of the project could influence the noise level perceived by building users and pedestrians. In particular, the study predicts the variation of outdoor noise levels achieved with both material variations and shape variations of the façades, considering different glazing ratios. The variation of glazing ratio was here evaluated as it can be dictated by different architectural goals, such as the indoor daylight requirements, which may vary based on the project location.

This study is articulated into three steps:

- as a first one, a parametric investigation of the effect of the application of materials exhibiting either sound absorbing or sound reflective behaviors on the

opaque portions of the façades is conducted, considering 4 possible glazing ratios;
- in the second step, 2 geometric variations of the building extremities that forms the courtyard openings are tested with a sound reflective treatment and compared to the original design solution;
- a third step, in which the most favorable design strategies for the first two steps are combined together to quantify the cumulate effect of the geometric and material design strategies.

While a database of potential façade blocks for Wolfsburg Connect was defined, the façades of the project were not finalized at the time in which this study was carried on. Therefore, the parametric investigation may provide quantitative acoustic performance feedback to orient design decisions related to the façade design and, in general, suggest some indicative guidelines for building façades design in a wider set of scenarios. This data can also increase the awareness of the designers on the acoustic implications of design choices and support an effective coupling of acoustic comfort objectives with architectural quality.

Method

The research is meant to assess the potential sound reductions for building users and pedestrians achievable by architectural design strategies concerning the material applied to the opaque portions of the buildings' façades and form variations for the openings of the courtyard. The methodology followed to set-up the acoustic model and to define the façade design variations are described in the following.

Virtual model and simulation set-up

The study was conducted on a parametric model developed in Grasshopper and using Pachyderm [243], an acoustic simulation tool integrated into Grasshopper based on GA principles, to obtain performance feedback.

The acoustic analysis was carried out on a representative portion of the project, whose virtual model is shown in Figure 74, which consists of four terraced buildings surrounding the courtyard hosting the "Campo". Its localization in the masterplan is highlighted in red in Figure 71. The Campo courtyard occupies a strategic position in the project and has a diverse program that supports the office functions, and stays active in the evenings and weekends, contributing to a vibrant city life.

For completeness, the buildings on the other side of the main road (in light grey color Figure 74) were also modeled to account for potential sound reflections; no significant obstacle is present on the railway side.

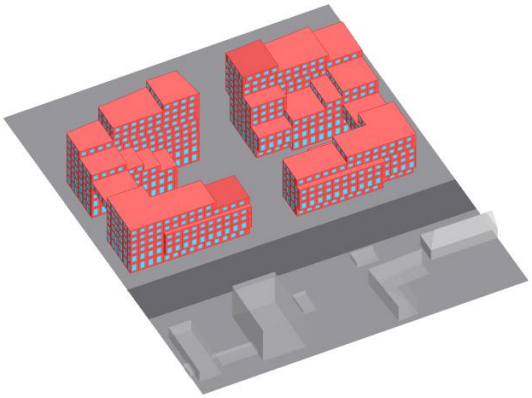

Figure 74. Virtual model of the portion of the project used for the acoustic analyses.

The simulations are performed with a cut-off time of 3000 ms and a transition order of 1. These settings combine result accuracy with short simulation time and were selected as the difference between the floor-averaged SPL results obtained with these settings and the results obtained with transition order 2 and cut-off time 6000 ms were smaller than 1 dB. The number of rays emitted by the source is automatically defined by Pachyderm based on results convergence.

Railway and street noise sources were modeled with a series of point sources, placed at a distance of 10 m and were set in correspondence of the courtyard openings. The sources used to model vehicular traffic (11 sources in total) were placed at a height of 0.3 m and at 1 m from the vehicle center line, towards the receivers, as suggested by Nord2000 [481]. The source is defined according to the normalized traffic noise spectrum of EN 1793-3:1998 Standard [482]. The railway source was modeled with 12 sources, placed at a height of 0.5 m; the source is set according to the normalized spectrum in EN 16272-3-1:2012 [483]. While in reality, the railway tracks are set at a lower elevation (about 5 m lower than the design site), they were modeled with the same elevation of the design area to work around the limitation of Pachyderm that does not account for the diffraction effect. Moreover, the noise generated by the people in the courtyard is considered to account for the noise connected to the new functions planned in the area. Therefore, 7 sources were distributed in the courtyard at a height of 1.5 m. Each source was meant to represent 4 people talking, each set with a sound power level defined as “raised”, according to [484,485].

The sound receivers used to collect data for building users were placed in outdoor positions at 0.5 m from the center of windows, in accordance with DIN 4109-1:2018-01 Standard [486]. In particular, in the virtual model of the courtyard, a point representing a sound receiver was parametrically inserted every 6 windows. The points located in non-representative positions (e.g., those not facing the sources as shielded from them or located beyond their length) were not considered in the simulations. In the end, the actual number of receivers considered in the results is 151 and are located in over the courtyard façade and over the outer façades in correspondence to the modeled sound sources.

To account for pedestrian comfort, 10 additional receivers were distributed in the courtyard at a height of 1.65 m in scattered positions. A scheme of the receivers is shown in Figure 75.

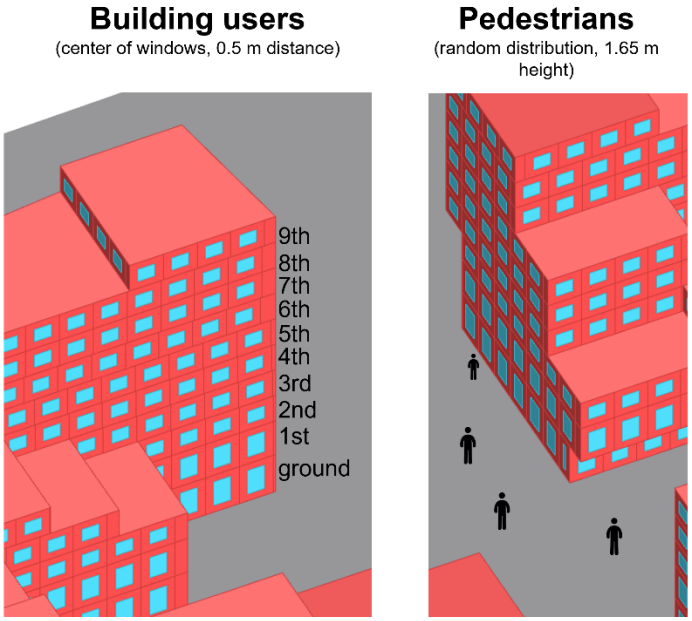

Figure 75. Scheme of the receivers used to assess acoustic comfort of building users and pedestrian.

The sound power level (*SWL*) of the railway and traffic sources was calibrated to ensure that the *SPL* values estimated by the acoustic simulation were coherent with those of the results of the environmental acoustic study provided by the consultants for daytime [479]. Despite the impact of noise on wellbeing is generally greater at night, daytime was here selected as the noise levels due to both the railway and traffic noise were greater, and also considering the functions present in the Campo courtyard. The parameter used for the calibration is the A-weighted *SPL* at the third floor of the building for the façades directly facing the railway and the street; the floor was chosen as it is representative, being located roughly at half the height of the buildings, and since its design is coherent with that included in the acoustic study. The predicted daytime A-weighted *SPL* data estimated by the acoustic consultants for the third floor of the buildings is shown in Figure 76 [479]. To this aim, the *SWL* of the railway and traffic sources was adjusted until the differences between the A-weighted *SPL* for the receivers on the third floor of the building simulated by Pachyderm and that reported in [479] were smaller than 1 dB.

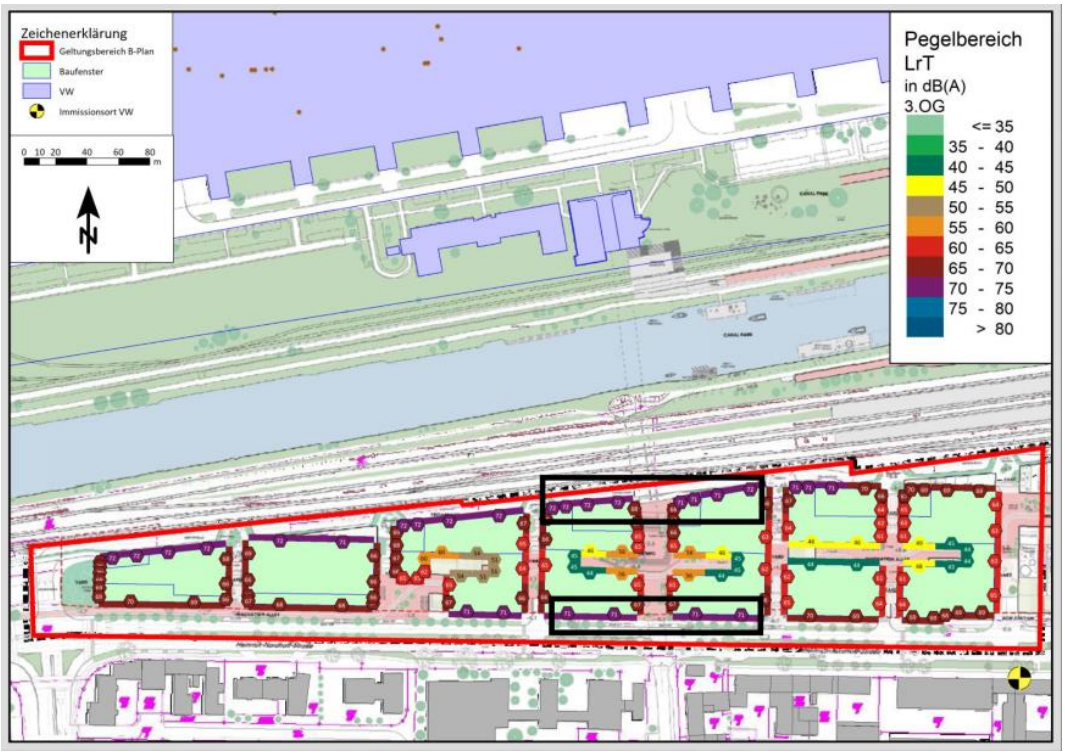

Figure 76. Results of the acoustic study for daytime at the third floor. The data within the black rectangles was used for the calibration of the model.

The calibrated *SWL*s of each point source representing traffic noise, railway noise and talking people is reported in Table 19.

Table 19. Octave band sound power level of the calibrated noise sources.

	Octave-band SWL [dB]								
	63	125	250	500	1000	2000	4000	8000	overall
Talking people	54.0	65.0	75.5	80.9	77.9	69.8	63.3	54.4	83.7
Traffic	80.7	80.7	85.0	88.0	91.3	88.7	83.7	83.7	95.3
Railway	77.0	77.0	83.0	88.7	92.0	93.0	88.7	88.7	97.2

Façade design variations

In the 1st step of the study, the variation of the materials applied to the façades of the Campo courtyard was tested, considering 4 glazing ratios (i.e., 25%, 35%, 45%, and 55%.). The courtyard with the 4 glazing ratios is shown in Figure 77.

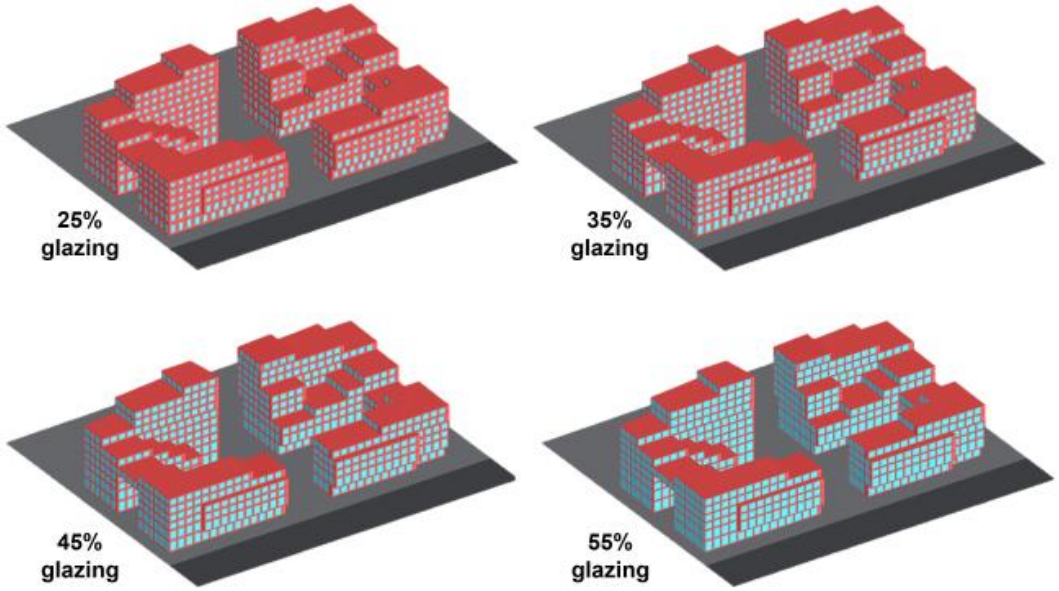

Figure 77. Images of the 3D models of the tested buildings with the four glazing ratios.

To this aim, the buildings were modeled parametrically in Grasshopper and at each floor a window pattern was created by subdividing the façade itself in smaller portions, each with a width of 4 m and by creating a window at the center of each potion. The glazing ratio was parametrized by scaling the edges of these windows from their center points, to ensure a uniform pattern of windows.

The material variations are applied to the opaque portions of the façades and the analysis simulates the effect of two sound absorbing cladding materials with respect to a common façade cladding options with sound reflective properties, used as reference. The material options tested are shown in Figure 78, along with the random-incidence octave-band sound absorption coefficients reported in the product datasheets. The selected sound absorbing cladding materials are commercial products suitable for outdoor applications, i.e., a porous cork-based plaster and slotted acoustic bricks with a fibrous filling in the cavity. They are based on different sound absorbing mechanisms and exhibit different frequency dependent sound absorption coefficients (Figure 78). Porous plaster exhibit broadband sound absorption properties with a weighted sound absorption coefficient (α_w) [158] of 0.75; the α_w of the acoustic bricks is 0.4H and presents a more uneven behavior along the frequency spectrum, with highest values at low frequencies.

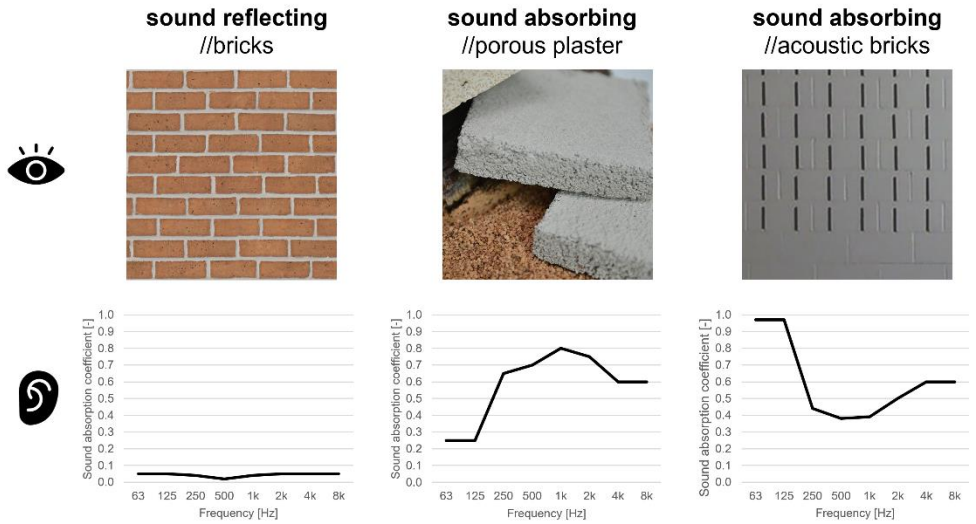

Figure 78. Visual appearance and octave band sound absorption coefficient of the sound reflective (reference) material and of the two sound absorbers. The values at 63 and 8000 Hz (not specified) are assumed equal to those of the nearer octave band.

The results of the 1st simulation step are gathered over all the receivers of the model and considering the three sound sources combined. Moreover, source-specific evaluations are performed to test the SPL variation over the façade portions facing the railway and the courtyard, considering only the railway and courtyard noise, respectively.

The 2nd step of the research aimed to study how the form of the courtyard openings could be modified to promote acoustic comfort in the courtyard by screening the noise coming from the street and the railway. In the tested portion of the project, the courtyard openings are created by the two extremities of the buildings facing the railway and the street. The proposed variations are based on the tilting of these buildings ends, to create either a concave or convex solutions, without compromising the visual connection between the city and the factory. These form variations, shown in Figure 79, are compared to the original design configurations. To isolate the effect of form change, the façades were treated with sound reflective materials with a reference glazing ratio of 25%.

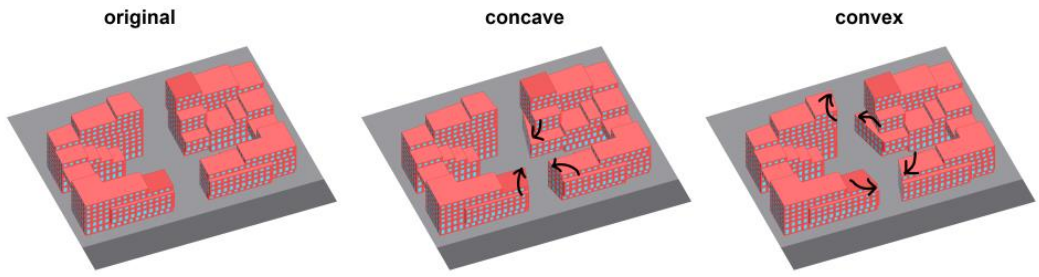

Figure 79. Form variations of the courtyard openings.

In the 3rd step of the research, the most performing design strategies found in the previous analysis related to form and material changes are combined together to assess the maximum benefit achievable with architectural design.

Evaluation of the acoustic comfort of building users and pedestrians

In order to quantify the acoustic comfort at the receivers' positions, the A-weighted *SPL* was estimated for each of the tested design variations.

Different analyses were performed depending on the scenario under investigation, involving either all or only part of the sound sources and receivers.

The effect of the design variations is reported as *SPL* difference between the tested scenario and the same geometric scenario with sound reflective materials (1st step) or with respect to the original geometric configuration with sound reflective materials (2nd and 3rd steps). The analysis of the 1st step was carried out on the *SPL* at all the receivers' positions in presence of all sources. In addition, some specific analyses are performed to evaluate the effect of the façade options considering a specific sound source only (i.e., railway or leisure noise) with respect to the sound receivers facing the considered source (i.e., the building façades oriented towards the railway, or those facing the courtyard). These latter analyses can also provide some general insights on the achievable the *SPL* reductions in generic and conventional scenarios, such a pedestrian courtyard or a building façade facing a street. Since Pachyderm neglects diffraction, the above-mentioned analyses are defined to reduce the potential impact of this limitation over *SPL* results.

In the 2nd simulation step, the *SPL* variation within the courtyard is tested considering the noise emitted by the vehicular traffic and the railway. Since Pachyderm does not account for diffraction, the results obtained may be affected by this limitation, leading to overestimated reductions. Nonetheless, this effect can be considered relatively limited given the great number of sound reflections occurring in the courtyard with a sound reflective façade materials, and can still provide useful indications to architectural designers.

Differently, in the 3rd step, the *SPL* variation within the courtyard generated by traffic and railway noise is assessed in combination with a sound absorbing material. In line with the previous observation, this step may be more affected by the absence of diffraction in the simulation model. While the outcome of this analysis should be interpreted with caution, they are nonetheless reported and discussed in the Results section, in light of the methodological aim of the work.

All the above reported analyses are performed on a floor basis, by calculating the difference between the energetic averages of the *SPL*s at each floor for all sound source contributions with respect to the reference configuration, i.e., the façade with the same glazing ratio and sound reflective materials.

Additionally, a more detailed analysis is performed using SPSS to evaluate the frequency distribution of *SPL*s for the most performing solutions found in the 1st and 2nd steps of the study with respect to the corresponding reference ones.

The difference found between the simulated *SPL*s are discussed on the basis of the JND_{SPL} of 1 dB [238] and on the 3 dB threshold reported in [471,472] that is associated to a "just perceptible" change in apparent loudness.

Results

The difference in mean *SPL*s at the different floors of the buildings and for pedestrians for the 1st step of the study are reported in Table 20. The results evidence

that the porous plaster is linked to the greatest *SPL* reductions, and that lower glazing ratios provide the greatest benefits, as a consequence of the greater façade area treated with sound absorbing materials. The most performing solution combines porous plaster with a 25% glazing ratio and provides *SPL* reductions greater than the JND_{SPL} for façade receivers above the 2nd floor and for pedestrians. The greatest *SPL* reduction, equal to 1.9 dB, is found at the 5th floor of the building.

Table 20. Mean *SPL* difference [dB] found for the two sound absorbing options combined to the glazing ratio variation with respect to the same configuration with sound reflective materials. Noticeable SPL difference are in bold.

	Porous Plaster				Acoustic bricks			
	25%	35%	45%	55%	25%	35%	45%	55%
9th floor	**-1.5**	-0.8	-0.8	-0.5	-0.9	-0.5	-0.4	-0.4
8th floor	**-1.4**	**-1.0**	-0.7	-0.5	**-1.0**	-0.6	-0.5	-0.4
7th floor	**-1.2**	-0.8	-0.6	-0.5	-0.7	-0.5	-0.5	-0.4
6th floor	**-1.1**	-0.9	-0.8	-0.6	-0.7	-0.6	-0.5	-0.4
5th floor	**-1.9**	**-1.0**	-0.9	-0.6	**-1.4**	-0.6	-0.6	-0.4
4th floor	**-1.2**	**-1.0**	-0.8	-0.7	-0.8	-0.6	-0.5	-0.5
3rd floor	**-1.1**	-0.8	-0.6	-0.5	-0.7	-0.5	-0.4	-0.3
2nd floor	**-1.0**	-0.7	-0.6	-0.5	-0.7	-0.5	-0.4	-0.3
1st floor	-0.6	-0.6	-0.5	-0.4	-0.5	-0.4	-0.3	-0.3
ground fl.	-0.7	-0.6	-0.4	-0.3	-0.5	-0.3	-0.3	-0.2
pedestrians	**-1.4**	**-1.3**	**-1.0**	-0.9	**-1.0**	-0.8	-0.6	-0.6

Based on the above analysis, the most favorable design options exhibit a glazing ratio of 25% with porous plaster applied to the opaque façade portions. The frequency distribution of the *SPL* results of the reference configuration (25% glazing ratio + sound reflective bricks) and of the most favorable one are shown in Figure 80 and Figure 81, respectively.

The graph seems to suggest a two-modal distribution of the *SPL* values, with to frequency peaks around two different values. This behavior is likely to be associated to receivers directly facing the railway and vehicular traffic noise sources (peak at highest *SPL* values) and the receivers facing the courtyard or pedestrian receivers (peak at lower *SPL* values). The graph highlight that the most performing façade configurations result in a shift in the mean *SPL*, that varies from 65 dB(A) in the reference configuration to 62.5 dB(A) in the most performing one.

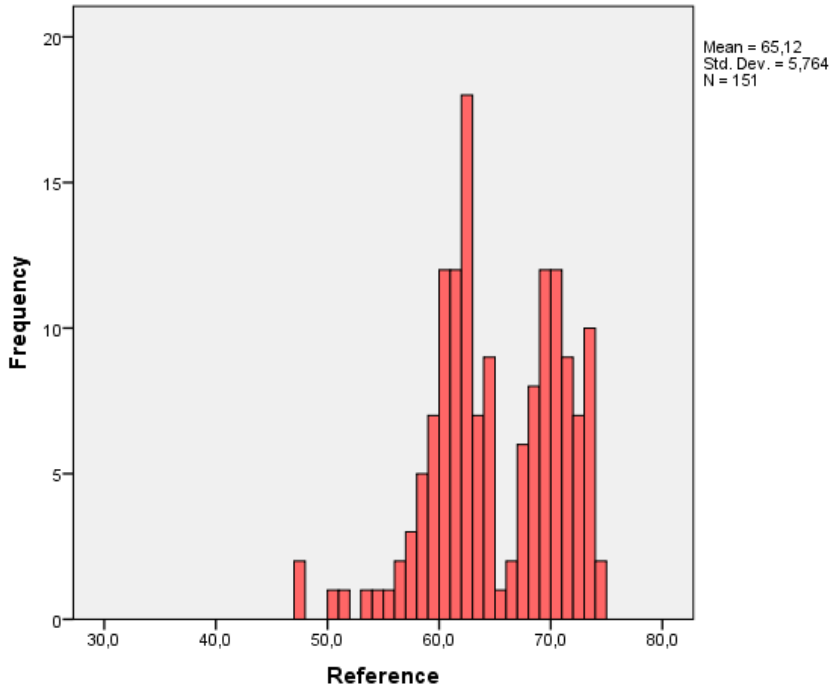

Figure 80. Frequency distribution of the *SPL* [dB(A)] found for the façade option with a glazing ratio of 25% and sound reflective bricks.

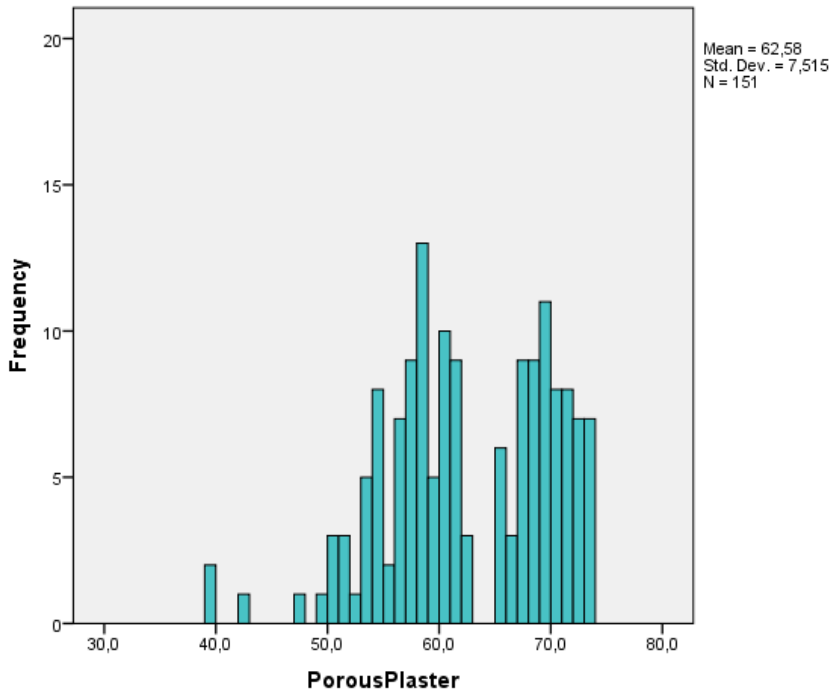

Figure 81. Frequency distribution of the *SPL* [dB(A)] found for the façade option with a glazing ratio of 25% and porous plaster.

In addition, two source-receiver specific analyses were performed, focusing on the railway noise mitigation achieved towards the railway and on the leisure noise reduction obtained within the courtyard i.e., for the receivers on the façades at the sides of the courtyard and for pedestrian receivers. Both analyses are only related to

the application of porous plaster which, based on previous findings, resulted the most favorable material option among those tested. The results of the analysis focusing on leisure noise are collected in Table 21, while those related to railway noise in Table 22. As concerns the analysis on leisure noise, noticeable *SPL* reductions are reported with porous plaster at all floors for the majority of the glazing ratio options. The only exceptions occur at the lower floors and top floor for the glazing ratio of 55%. The greatest *SPL* reductions are reported for the 25% glazing ratio, from the 5th to the 7th floor of the building, with reductions equal or greater than 3 dB. This promising result are linked to the enclosed form of the courtyard, that emphasize the role played by sound reflections, and consequently, by their attenuation by sound absorbing materials. The *SPL* reductions over the façades tend to diminish for greater glazing ratios, while for all the glazing ratios the greatest reductions are observed from the 5th to the 7th floor. The *SPL* reduction for pedestrian receivers follow the same trend of façade receivers, with greater *SPL* reduction for lower glazing ratios, although with a more limited magnitude. Overall, the solutions provide *SPL* reductions for pedestrians close to the JND_{SPL}, ranging from 1.3 dB to 0.9 dB, for glazing ratio of 25% and 55%, respectively.

Table 21. Difference in mean *SPL* [dB] for courtyard receivers and leisure noise at the different building floors and for pedestrians. Noticeable *SPL* difference are in bold.

	Porous Plaster			
	25%	35%	45%	55%
9th floor	**-1.6**	**-1.7**	**-1.2**	-0.6
8th floor	**-2.5**	**-2.5**	**-1.9**	**-1.5**
7th floor	**-3.0**	**-2.8**	**-2.0**	**-1.7**
6th floor	**-3.3**	**-2.4**	**-2.3**	**-1.7**
5th floor	**-3.0**	**-2.6**	**-2.3**	**-1.9**
4th floor	**-2.5**	**-2.1**	**-1.8**	**-1.5**
3rd floor	**-2.4**	**-2.0**	**-1.8**	**-1.6**
2nd floor	**-2.0**	**-1.6**	**-1.4**	**-1.1**
1st floor	**-1.5**	**-1.3**	**-1.1**	-0.9
ground fl.	**-1.4**	**-1.2**	**-1.0**	-0.9
pedestrians	**-1.3**	**-1.2**	**-1.0**	-0.9

When considering railway noise, the *SPL* reduction observed over the façade oriented towards the railway are more limited than the one reported for the courtyard, given the minor role played by sound reflections in this context (see Table 22).

Noticeable *SPL* reductions are only reported above the 7th floor of the building for the application of porous plaster combined to a glazing ratio of 25%. Overall, the application of porous plaster on the façade results in limited benefits when considering a single building facing the noise source, with *SPL* reductions slightly above the JND_{SPL} reached only at the upper building floors with the lower glazing ratio (25%).

Table 22. Difference in mean *SPL* [dB] for receivers of the façade oriented towards the railway and railway noise at the different building floors. Noticeable *SPL* difference are in bold.

	Porous Plaster			
	25%	35%	45%	55%
9th floor	**-1.4**	-0.7	-0.6	-0.4
8th floor	**-1.4**	-0.8	-0.4	-0.4
7th floor	**-1.1**	-0.7	-0.5	-0.4
6th floor	-0.7	-0.5	-0.5	-0.3
5th floor	-0.7	-0.5	-0.6	-0.3
4th floor	-0.7	-0.5	-0.4	-0.3
3rd floor	-0.6	-0.4	-0.3	-0.2
2nd floor	-0.5	-0.3	-0.3	-0.2
1st floor	-0.4	-0.4	-0.3	-0.2
ground fl.	-0.5	-0.4	-0.3	-0.2

The results of the 2nd step of the study, testing slight form variations for the building edges at the sides of the courtyard openings are shown in Table 23.

Table 23. Difference in mean S*PL* [dB] for the convex and concave configurations found within the courtyard for the different façade floors and pedestrians. Noticeable *SPL* difference are in bold.

	Concave	Convex
9th floor	-0.4	-0.5
8th floor	-0.6	0.5
7th floor	-0.6	0.2
6th floor	-0.3	**-8.8**
5th floor	-0.8	**-1.9**
4th floor	**-1.6**	**-3.2**
3rd floor	**-1.3**	0.2
2nd floor	-0.7	**-3.6**
1st floor	**-1.0**	**-2.5**
Ground fl.	**-1.2**	**-1.3**
pedestrians	**-1.0**	**-2.0**

The results are referred to the receivers of the courtyard (over the façades facing the courtyard and for pedestrian receivers) and to the noise emitted by the railway and the vehicular traffic. Leisure noise is not considered in this case, as the variation of building edge form is suggested to reduce the impact of railway / vehicular traffic within the courtyard. *SPL* variations compare the concave and convex building edge configurations with the original one (all with a glazing ratio of 25% and sound reflective material), used as reference. While both the concave and convex configurations seem to provide noticeable *SPL* reductions, those observed for convex option are the greatest, with reaching values greater than 3 dB, with a peak reduction of almost 9 dB at the 6th floor. It must be however remarked that the observed reductions may be

affected by the limitation of the simulation tool, that neglects diffraction. Indeed, while the enclosed shaped of the courtyard promote sound reflections, the predicted *SPL* may be underestimated, especially in proximity of terraces and protrusions. Nonetheless, the results suggest that the improvement of the screening effect provide by the building edges at the courtyard openings is a promising strategy to mitigate the impact of traffic and railway noise within the courtyard.

The frequency distributions of the *SPL* values obtained for the pedestrian and over the façade facing the courtyard for the reference and convex configurations are shown in Figure 82 and Figure 83, respectively. As expected, the graph highlights a shift in the predicted *SPL* toward lower values, leading to a variation in mean *SPL* from ~54.5 dB(A) to ~52 dB(A).

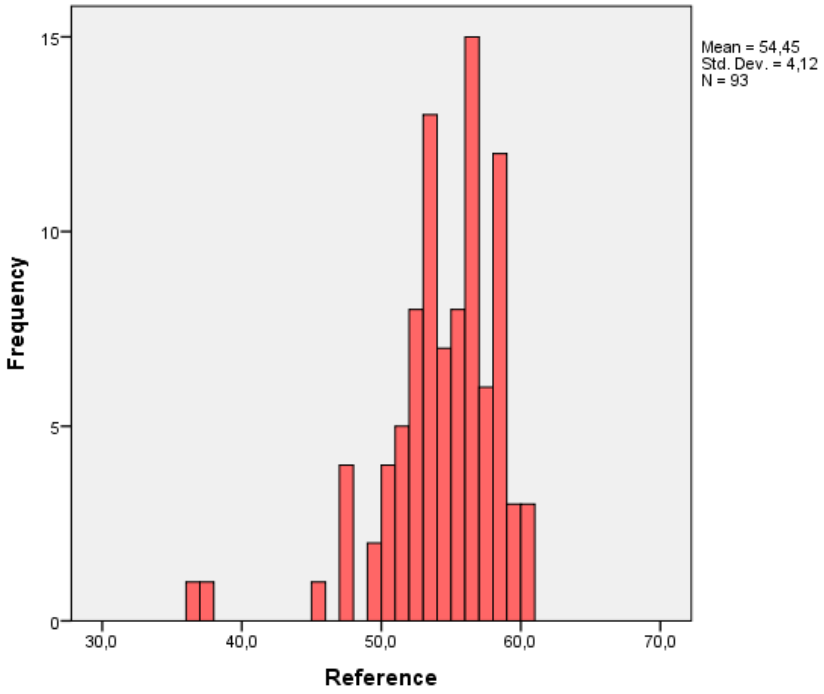

Figure 82. Frequency distribution of the *SPL* [dB(A)] of courtyard receivers found for the reference configuration, with the original form.

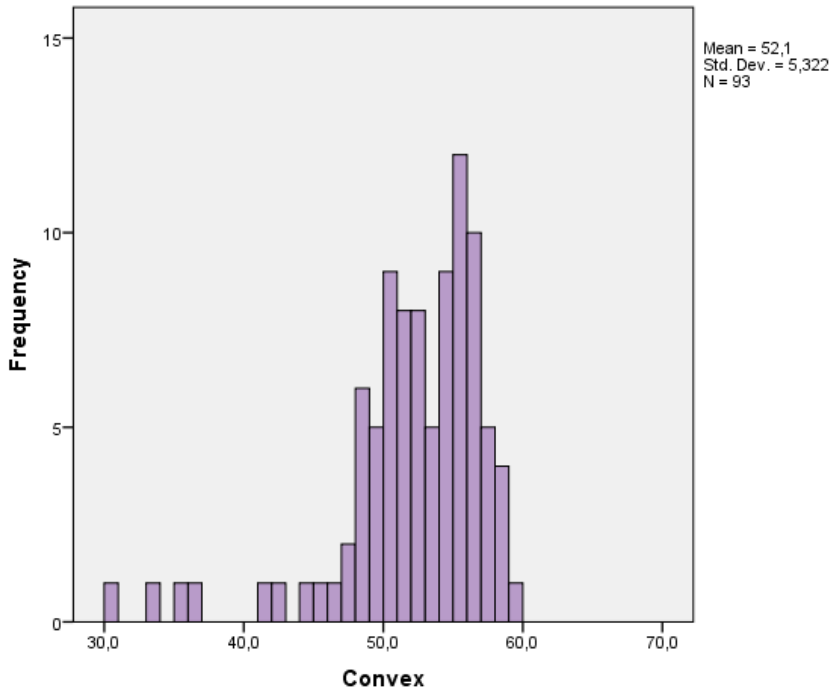

Figure 83. Frequency distribution of the *SPL* [dB(A)] of courtyard receivers found for the convex configuration.

Table 24 collects the *SPL* differences found for the 3rd study step, when the most performing material and form variations previously found (i.e., porous plaster, 25% glazing ratio and convex building edge configuration) are combined.

Table 24. Difference in mean *SPL* [dB] for the convex building edges in combination with porous plaster and a 25% glazing ratio at the different façade floors and pedestrians. Noticeable *SPL* difference are in bold.

	Convex
9th floor	-2.0
8th floor	-1.0
7th floor	-0.7
6th floor	-13.7
5th floor	-3.5
4th floor	-5.2
3rd floor	-1.4
2nd floor	-5.9
1st floor	-4.6
Ground fl.	-2.6
pedestrians	-3.3

The *SPL* trend over the façade is coherent with that observed in Table 23, although the magnitude of the *SPL* reduction is greater, as a consequence of the dampening of sound reflections provide by the application of porous plaster. A performance-wise selection of the materials and geometric properties of the project resulted in the largest noise reduction, emphasizing the potential benefits provided by

the inclusion of performance aspects during design processes. Nonetheless, as previously noted, *SPL* reduction may be overestimated by the lack of diffraction modeling. While these results can provide some indications, more advanced analysis are needed to quantify *SPL* variation with greater accuracy.

Conclusions

This study has investigated the environmental noise mitigation provided by a series of design modifications applied to a portion of Wolfsburg Connect project by Henning Larsen. The focus of the investigation is a pedestrian courtyard located within a railway and a vehicular traffic road, considered a representative portion of the project. The study has investigated how façade materials and minor form changes of the side building could reduce the sound pressure level over the façade and for pedestrians. To this aim, the railway and vehicular traffic noise sources were calibrated to closely represent the actual acoustic conditions in the area, and the leisure noise generated by people within the courtyard was included. In the first step of the research, the application of two sound absorbing materials to the opaque façade portions was compared to the application of sound reflective materials, considering 4 glazing ratios. This step evidenced the greatest SPL reduction provided by the broadband sound absorber and that such reductions increase for lower glazing ratios. The second step evaluated two slight form modifications for the building edges at the courtyard opening in the attempt to increase their screening effect with respect to the receivers within the courtyard. The last research step combined the most favorable design options identified at the previous step to evaluate how a performance driven selection of the material and form of the building façade could improve acoustic comfort in the area.

Further investigations may include the use of GA based simulation tools with diffraction modeling or wave-based tools to allow to accurately estimate screening effect and to provide a detailed accounting of the localized effect of façade design features (e.g., terraces, balconies, parapets, etc.). The work can be expanded by considering a wider number of acoustic parameters or by the use of perceptual evaluations, such as those in [77–80], which may represent an interesting development of the study.

Acknowledgements

The author thanks Giuseppe Vannelli for the precious support during the measurement campaign in § 5A.4. The author is grateful for the support provided by Katrin Bindner, Mikkel Esrup Steenberg, Jakob Strømann-Andersen and Alvaro Villanueva for the analysis of Wolfsburg Connect project by Henning Larsen (§ 5A.5.2).

Chapter 5B

Outdoor thermal comfort: evaluation of the accuracy of ENVI-met predictions

Objective	Evaluating the prediction reliability of ENVI-met close to a dark-colored façade under extremely hot conditions, with a focus on T_{mrt} and T_s. The study compares predictions with in-situ measured observations.
Outcome	Limited agreement is found between measured and simulated T_{mrt}, with marked underestimation, evidencing also an underestimation of façade surface temperature
Highlights	• Underestimations of T_{mrt} and T_s were reported in this study, for all simulation methods tested; $T_{s,f}$ are underestimated also for a light colored wall, although to a minor extent. • The approximation of the outer wall layer result in greater accuracy of the $T_{s,f,}$ and of T_{mrt}. • Full forcing was reported to improve the result's accuracy $T_{a,}$ but not that of T_{mrt} and T_s. • The underestimations of T_{mrt} and T_s result in underestimated PET values, that does not capture the actual thermal stress conditions in their full extent.

5B.1. Overview and research goals

This Chapter focuses on the prediction reliability of ENVI-met, by comparing the simulation results with in-situ measured data, with a focus on T_{mrt}. While in Chapter 4B a qualitative comparison between the T_{mrt} models implemented in different simulation tools was presented, this Chapter offers a quantitative accounting of the prediction accuracy of ENVI-met, which can be considered the most employed and comprehensive simulation tool among those presented.

In the framework of urban overheating and climate change ENVI-met can be used to predict outdoor thermal comfort conditions and to identify adaptation strategies at the urban scale. Based on the predicted environmental variables, thermal comfort indices can be calculated to describe the human thermal sensation in different design scenarios. Given the crucial role played T_{mrt} in this framework [26,328,346,348,487], accurate estimations of such parameter are essential to provide reliable data to inform decision making processes and optimize design proposals. Given the contribution of emitted longwave radiation on T_{mrt} in surrounding locations, a correct accounting of the outer surface temperature of urban facets is also important.

The validation study presented in this Chapter focuses on the prediction reliability of ENVI-met with respect to T_{mrt}, air temperature and surface temperatures of of surrounding building elements, by comparing the tool's prediction with measured data in a challenging urban scenario with extremely hot weather conditions.

5B.2. Introduction

ENVI-met is in continuous development, and new versions of the tools have been released recently, in an attempt to overcome some of the tool's known limitations. The possibility to employ the indexed view sphere (IVS), introduced in version 4, allows for the accounting of the material properties surrounding the calculation points through ray tracing. This feature is expected to increase T_{mrt} accuracy, overcoming the simplification of previous versions based on domain-wide mean material properties (see § 4B.5.1 in Chapter 4B). Moreover, from version 4, thermal mass and inertia of building elements is included in the calculation. The latest release at the time of writing, version 5, is a fundamental renewal of ENVI-met, with enables to calculate T_{mrt} based on the radiation in the six directions, following the integral radiation measurement (IRM) approach [26,370]. This feature replaces the previously implemented two-directional approach, potentially increasing the accuracy of the results. In addition to these advancements, previous studies have identified methodological strategies to improve results accuracy, such as allowing for model initialization by running longer simulations, using local weather data as forcing conditions, and forcing the model with detailed measured weather conditions, i.e., using "full-forcing" (FF) instead of the most commonly employed "simple forcing" (SF) [355,369,488–490].

Several research studies have attempted to assess the reliability of ENVI-met estimations in a range of different scenarios, by comparing the simulation results with measured data. A metanalysis published in 2018 [347] aimed to shed light on the

capability of ENVI-met to provide accurate predictions based on the previously published validation studies. The analysis reports a wide number of contributions studies on air temperature (T_a) validation and a relatively limited number of studies focusing on T_{mrt}, despite T_a exhibits less spatial variability in urban areas and is reported to have a limited impact on thermal stress with respect to T_{mrt} [3]. Based on the collected T_{mrt} validation studies, ENVI-met predictions are considered reasonably accurate [347]. In addition, as also highlighted [347], only a very limited number of studies have evaluated the surface temperatures (T_s) of urban facets, some of which reporting good agreement between simulated and measured façade or ground T_s [374,491,492], while some others finding underestimations for ground or façade T_s [355,493].

In light of the continuous development of ENVI-met, a brief overview of some more recent T_{mrt} validation studies is reported. A systematic investigation [355] performed with ENVI-met (v 4.4.2, using SF, without IVS) found noticeable differences between predicted T_{mrt} values and those obtained with IRM in Szeged (Hungary). This study has also investigated the ground surface temperature, evidencing marked underestimation. The research in [348] evaluates the reliability of T_{mrt} simulations by ENVI-met under extreme hot conditions in Arizona (USA). The study was conducted by comparing ENVI-met (v 4.3, using SF, without IVS) results with T_{mrt} data measured with the globe thermometer and with IRM in different positions and periods of the year. The results of the study evidenced a poor agreement between the simulation and the measured results. In [366], observation of T_{mrt} in a courtyard in Seville, (Spain) which were obtained with globe thermometer method, were compared with the one simulated by ENVI-met (v 4.4.5, using SF, without IVS) finding a promising agreement between measured and simulated data. The study in [368] evaluate the difference in T_{mrt} measured with the globe thermometer and modelled with ENVI-met v 4.4.5 (with SF, without IVS) finding overestimation in T_{mrt} values during daytime in summer. Another study, carried out during summer in Hong Kong with ENVI-met v 5 with IVS and FF, found good agreement between measured and simulated T_{mrt} values [370]. A systematic analysis in [369] tested different simulation approaches using ENVI-met v 4.4.6 with respect to IRM-measured T_{mrt} in various locations in Hong Kong during summertime, evidencing the tool's capability to provide accurate predictions based on the simulations settings.

As it can be noticed, the presented validation studies report a complex picture, with wide variations in the model's accuracy as a result of different simulation scenarios, model settings, periods of the year and measurement methods. Overall, the validation studies referred to T_{mrt}, are often a) referred to previous versions of the software, which present major differences from the current one (version 5), and/or performed without enabling IVS mode and with SF, b) carried out during relatively mild weather conditions, c) not including the monitoring of T_s of building elements, which influences longwave radiation exchanges and T_{mrt}, or d) employ as reference T_{mrt} values obtained with globe thermometer, whose application in outdoor settings is reported to be questionable [26,328,346,351–354]

The research described in this Chapter contributes to filling the existing research gap by comparing the measured environmental parameter affecting outdoor thermal

comfort and the simulated ones during an extreme hot day in Turin (Italy), in proximity of a building façade. The selected case-study, i.e., a dark-colored façade facing south with almost no obstructions, can be considered a challenging scenario for simulations, given the major role played by both shortwave and longwave radiative fluxes. The simulation was performed with the most recent release of ENVI-met at the time of writing, i.e., v 5, with IVS mode enabled, and by testing different simulation approaches, involving SF and FF and two distinct wall models. All the environmental parameters influencing outdoor thermal comfort were monitored, with a specific focus on T_{mrt} and the outer surface temperature (T_s) of the façade wall and paving. T_{mrt}, as already pointed out, is the environmental parameter with the greatest influence on outdoor thermal comfort, while T_s influence the longwave exchanges between the body and the façade, which in turn affect T_{mrt}. A model intercomparison allowed to broaden the evaluation of the predicted T_s, considering a light-colored façade. In addition, the difference between T_{mrt} obtained with the globe-thermometer and following the IRM technique is assessed and the influence of the distance to the façade to the obtained T_{mrt} is evaluated.

In summary, the objectives of this research are:

- The comparison of T_{mrt} results obtained by the globe thermometer with respect to those determined following the simplified IRM method and the evaluation of the extent to which T_{mrt} varies at two different distances from a south oriented façade.
- The evaluation of the reliability of ENVI-met (v 5, with IVS) predictions, in a challenging scenario, i.e., in proximity of a dark-colored building and under extreme hot weather conditions. The study evaluates the prediction reliability for T_a, T_{mrt} and outer T_s of surrounding building elements. To this aim, four different modeling approaches were tested, with different forcing methods for the boundary conditions and different approximations of the façade wall stratigraphy. The analysis include the study of the directional radiative fluxes, an evaluation of $T_{s,f}$ accuracy for a light-colored façade wall and investigates the impact of the predicted T_a and T_{mrt} on the calculate PET values.

5B.3. Different approaches to determine T_{mrt} in outdoor settings

The two main methods used to determine T_{mrt} in outdoor settings are the integral radiation measurement (IRM) (also known as six-direction radiation measurement) and based on the use of a globe thermometer.

There is good agreement in the scientific community that the IRM is the most accurate method to determine T_{mrt} outdoors [26,328,346,351–354]. Despite the increased accuracy, IRM approach is more expensive and complex to carry out in practice than the globe thermometer. The globe thermometer is a rather simple and cheap instrument, whose outdoor application exhibits a series of drawbacks that reduce its measurement accuracy. According to [26], the main limitations are linked to a) the spherical shape of the globe thermometer, which is not representative for a

human body in a standing position, as it is often the case of people in outdoor spaces, and result in an underestimation of the lateral contributions; b) the black color of standard globe thermometers leads to an overestimation of the absorbed shortwave radiation; c) the long response time of the globe thermometer is not suitable to account for the rapid variation of environmental variables occurring in outdoor settings.

Given the practical advantages of globe thermometer measurement, past research studies have attempted to address some of the mentioned limitations of the globe thermometer by employing smaller or grey ones [328,351], or by developing correction models [353,494].

Comparisons of the data acquired with the two measurement techniques are presented in [328,351,353,494]. The two measuring methos to determine T_{mrt} are briefly described in the following.

The use of the globe thermometer is considered the simplest and cheapest method to obtain T_{mrt} [26,332]. The method is described in ISO 7726:2001 Standard [337] and is based on the measure of the globe temperature T_g. The globe thermometer, which was originally intended for indoor measurement and was only extended for outdoor application at a later time, is (in its standard version) a flat black-painted hollow copper sphere (diameter is 150 mm, thickness is 0.4 mm) with a thermometer bulb at the center which measures the globe temperature T_g [°C] [26,328]. T_g at equilibrium results from the heat exchange processes through radiation and convection, so the T_g represents the weighted average of the T_a and T_{mrt} [26]. T_{mrt} [°C] can be therefore calculated using the following Equation (18) :

$$T_{mrt} = \sqrt[4]{\left(T_g + 273.15\right)^4 + \frac{h_{Cg}}{\varepsilon \cdot d_g^{0.4}} \cdot \left(T_g - T_a\right)} - 273.15 \quad [°C] \tag{18}$$

where ε is the emissivity of the black sphere, assumed to be equal to 0.95 [26], d_g [m] is the diameter of the sphere (i.e., 0.15 m) and h_{Cg} [W/m^{2}K] is the globe's convection coefficient. The parameter h_{Cg} is wind dependent and can be calculated with Equation (19) [337]:

$$h_{Cg} = 1.1 \cdot 10^8 \cdot w^{0.6} \quad [\mathrm{W/m^2K}] \tag{19}$$

The IRM approach is described in VDI 3787 [336] and was originally proposed by Höppe [350]. It is based on the simultaneous measurement of the shortwave (i.e., solar) and longwave (i.e., thermal infrared) irradiances (or radiant flux densities), identified as K_i and L_i, respectively, for 6 orthogonal directions (i.e., south, north, east, west, up, down) to obtain the mean radiant flux density S_{Str}. The method requires the use of net radiometers able to independently measure shortwave and longwave irradiances. A net radiometer is composed of 2 pyranometers, measuring shortwave radiation, and 2 pyrgeometers, measuring longwave one, each of which is installed on the two sides of the instrument, thus measuring the K_i and L_i in opposite directions.

The original IRM method requires the use of three net radiometers oriented in three orthogonal directions. A simplified version of the IRM, which was employed during the measured campaign presented in this Chapter, is based on the use of a single net radiometer that is manually rotated 3 times to allow for acquisitions in the 6 orthogonal directions. According to this method, the 3 acquisitions have to be performed within 10 minutes measurement window. This simplified procedure is suggested in VDI 3787 [336] and described in [332,356], and was applied in previous micrometeorological studies [353,356].

The mean values of the shortwave and longwave irradiances measured in the 6 directions, respectively K_i and L_i [W/m^2], is used to calculate the mean radiant flux density S_{Str} [W/m^2] absorbed by the body, that is determined following Equation (20):

$$S_{Str} = \sum_{i=1}^{6} W_i(\alpha_k \cdot K_i + \alpha_l \cdot L_i) \quad [\mathrm{W/m^2}] \tag{20}$$

where W_i are the weighting factors corresponding to the direction of measurement, which accounts for human body shape (i.e., seated or standing); a_k is the absorption coefficient of the clothed human body for shortwave radiation, which is assumed equal to 0.7; a_l is the absorption coefficient of the clothed human body for shortwave radiation, which is assumed equal to 0.97 [26,328].

The W_i values accounts for the view factors between a person and the surrounding surfaces, and they vary based on the human body shape (i.e., seated or standing), which is approximated to a squared prism [495]. W_i values are also defined for a sphere, where all directions weight the same, and can be used for comparison with the measurement with the globe thermometer. Table 25 collects the weighting factors values [328,336,350], for a seated and standing body position and for the sphere.

Table 25. Standard weighting factors (Wi) for lateral and vertical directions.

	Lateral directions (i.e., east, west, south, north)	Vertical directions (i.e., upward, downward)
Standing person	0.220	0.06
Seated person	0.185	0.13
Sphere	0.167	0.167

Based on T_{mrt} definition, i.e., the temperature of fictive isothermal enclosure that behaves as a perfect black body emitter and cause the same amount of radiative exchange with the human body as the actual environment, T_{mrt} [°C] can be calculated as in Equation (21):

$$T_{mrt} = \sqrt[4]{\frac{S_{Str}}{\varepsilon_p \cdot \sigma}} - 273.15 \quad [°C] \tag{21}$$

where ε_p is the emissivity of the human body ($\varepsilon_p = \alpha_l$ according to Kirchhoff's law), and σ is the Stefan-Boltzmann constant ($\sigma = 5.67 \cdot 10^{-8}$ W/m^{2}K^4).

5B.4. Method

The procedure followed to carry out the micrometeorological measurement campaign and the performance simulation in the case-study scenario are described respectively in the sections 5B.4.2 and 5B.4.3.

5B.4.1. The urban and architectural context

The measurement campaign was carried out close to a south-oriented façade of a classroom building at Politecnico di Torino, in Turin (Italy), which was used as a case-study. The selected building façade is dark-colored and remains almost always sunlit during the central hours of the day, given the little presence of shading elements in its proximity. These features, in combination with extreme hot conditions, make it a challenging scenario to test the modeling capability of microclimatic simulation tools, especially related to the accounting of shortwave and longwave fluxes. The case-study building and measurement site are shown in Figure 84.

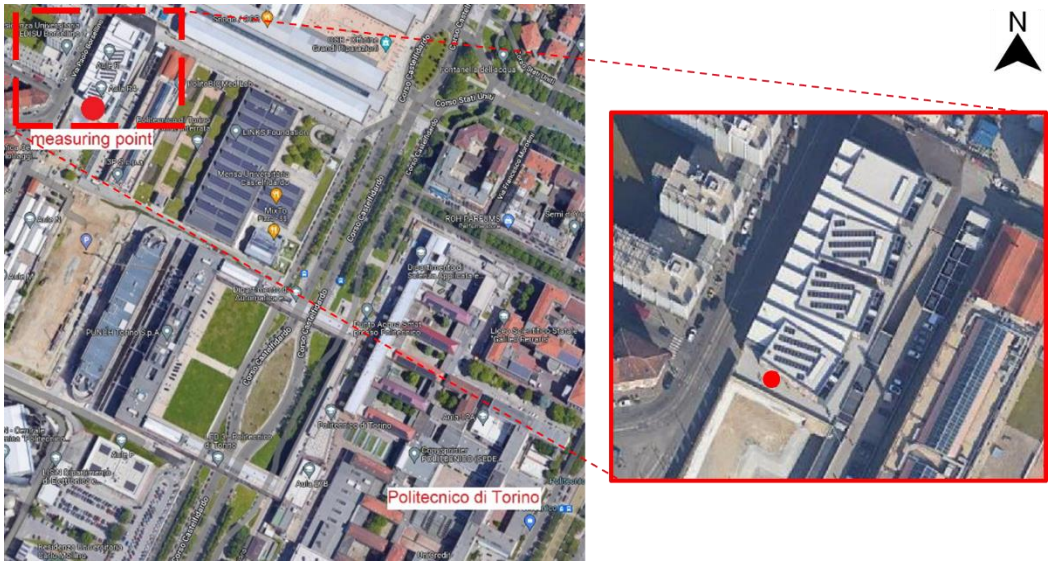

Figure 84. Satellite view of the measurement location with respect to Politecnico di Torino main campus (left); detailed view on the case-study building and surrounding context (right).

The classroom building is a historical industrial building that was recently retrofitted, by maintaining part of the original fronts. The measurement campaign was carried out close to a newly built front of the building, which exhibit south-west orientation (34° from North) and faces a pedestrian area with a stone paving. The building has a height of 13.7 m, and its south oriented façade is composed of two parts: a mainly opaque portion in different brown shades, presenting only small windows, and a small stepped back glazed portion.

The measurement campaign was carried out in a central position in front of the opaque portion of the building. It has a width of 21.8 m and presents a dark brown basement, while the upper part of the façade is characterized by an irregular pattern of rectangular blocks in different brown shades. The design prospect of the south-west façade in its entireness, provided by "Building and Logistics Department" (EDILOG) of Politecnico di Torino, is shown in Figure 85.

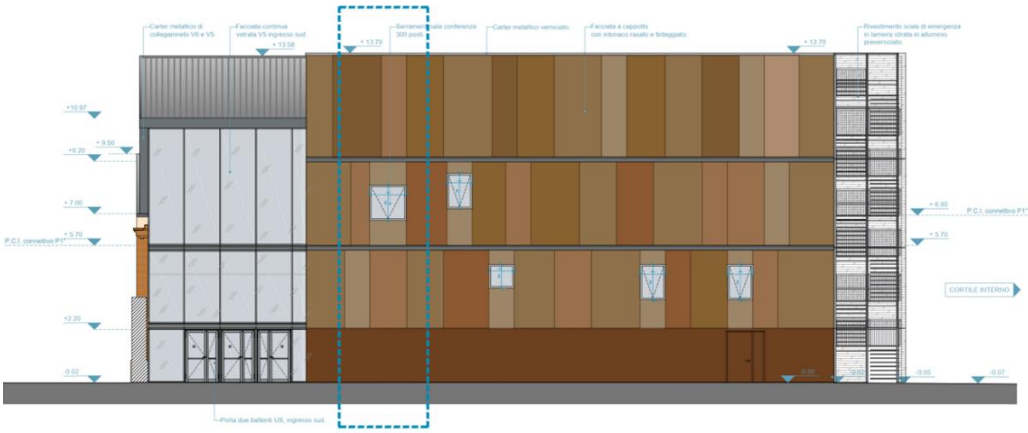

Figure 85. Architectural prospect of the south-east oriented façade of the classroom building

Since only early-stage construction site was present south to the façade during the measurement campaign, no major obstructions were present, and the building façade was sunlit for the central hours of the day.

5B.4.2. The micrometeorological measurement campaign

The climatic context

The measurement campaign was conducted on July,18 2022, a hot summer day with a clear sky with almost no wind. At that time, Turin and Piedmont region were subject to extreme weather conditions. According to a report by Regional Agency for Environmental Protection (ARPA Piemonte), July 2022 was the third hottest July on record, with a positive thermal anomaly in T_a of 3.4°C with respect to the mean value during 1971-2000 [496]. The same report highlights a heat wave between 14 and 26 July, i.e., in the period in which the measurement campaign was conducted, where the mean value of the maximum T_a reported in the Po Valley area, where Turin is located, was constantly above 32°C.

The measurement campaign

The micrometeorological measurement campaign aimed to collect information on thermal comfort conditions in proximity of the building façade, with three main goals:

a) Evaluating the accuracy of T_{mrt} measures obtained with the globe thermometer with respect to those obtained with IRM, used as reference;
b) Assess the extent to which the distance to the façade wall influence T_{mrt};

c) Gathering data to evaluate the accuracy of ENVI-met predictions, related to micrometeorological parameters and nearby surface temperatures.

The measurement campaign covered the central hours of the day, lasting from 10:30 to 20:00. During this timeframe, the environmental variables influencing human thermal comfort in outdoor settings, i.e., air temperature (T_a), relative humidity (RH), air velocity (w), and mean radiant temperature (T_{mrt}) were monitored; in the case of T_{mrt}, two different measurement approaches were followed. The Testo 480 measuring instrument was used to acquire data also on T_a and w through Testo thermal probe (model 0635 1024), while the RH was measured using Testo comfort probe (model 0628 0143). The globe temperature (T_g), used to calculated T_{mrt}, was measured with a standard black globe thermometer (Testo 0602 0743). The measured data was acquired for the entire duration of the measurement campaign, with a time step of 1 minute. The calculation of the T_{mrt}, identified in the following as T_{mrt} *sphere (globe)* was performed based on the measured T_g and T_a while, for the sake of simplicity, the moving average of w (over 3 minutes) was used to determine h_{Cg} and reduce the fluctuation of T_{mrt} values (see Equations (18) and (19)).

In addition to the globe thermometer, T_{mrt} was determined according the simplified IRM approach [336]. The T_{mrt} values obtained are calculated for a sphere and for a standing person (see weighting factors Table 25 in § 5B.3), identified respectively as T_{mrt} *sphere (IRM)* and T_{mrt} *standing (IRM).* A single 4-component net radiometer (model CNR4 by Kipp & Zonen) was used. The net radiometer was connected to a datalogger (DataTaker DT85) that acquired data every 5 s; this instrumentation was used to determine T_{mrt} every 30 minutes, from 10:30 to 20:00, alternating two measurement positions.

The measurement equipment is shown in Figure 86, while the technical details of the instrumentation used to measure the meteorological variables are summarized in Table 26.

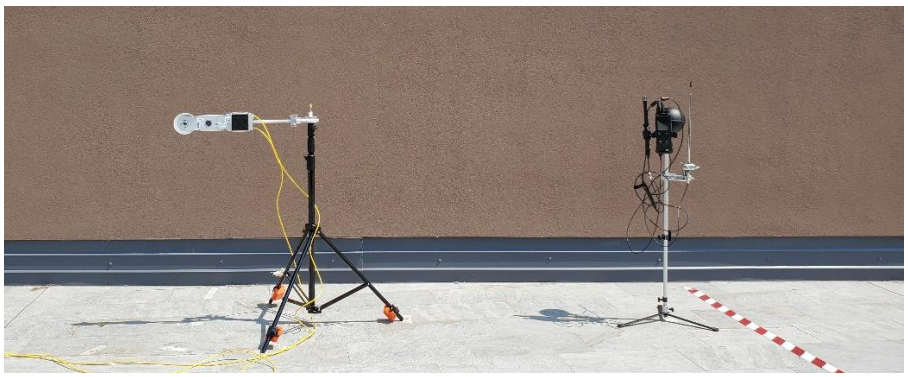

Figure 86. Picture of the measurement equipment, consisting of a single net radiometer (left) and the Testo 480 measuring instrument with the connected sensors (right).

Table 26. Measured meteorological variables, time step between acquisitions and corresponding measuring instrument.

Measured variable	Instrument	Measurement range	Accuracy
Air temperature T_a [°C]	Testo 0635 1024	-20 to +70°C	±0.5°C
Wind speed w [m/s]	Testo 0635 1024	0 to +20.00 m/s	±(0.03 m/s, ± 5% of meas. val.)
Relative humidity RH [%]	Testo 0628 0143	0 to 100 %	±(1.8 %RH+0.7% of meas. val.) ±0.03 %RH/K (based on 25 °C)
Globe temperature T_g [°C]	Testo 0602 0743	0 to +120 °C	Class 1
Shortwave and longwave flux density in the six directions S_{Str} [W/m^2]	Kipp & Zonen CNR4	0 to 2000 W/m^2	Spectrally Flat Class C (Second Class)

As the simplified IRM procedure [332,336] requires, the 3 acquisitions have to be completed within 10 minutes. Therefore, during the measurement campaign, the radiometer was manually rotated after 3 minutes of data acquisition. Considering the time needed to manipulate the instrument, this ensured that the 10 minutes measurement window was respected. The acquisitions related to the first 20 s after each rotation, which corresponds to the response time of the instrument, were removed. Considering the sampling of 5 s, this procedure led to about 32 acquisitions for each orthogonal direction. These values were arithmetically averaged to obtain L_i and K_i in the 6 directions. Given the aim to compare the T_{mrt} measured with this procedure to that obtained using the globe thermometer and the one simulated by ENVI-met, the T_{mrt} was calculated for a sphere, i.e., T_{mrt} *sphere (IRM)*, for the comparison with the T_{mrt} based on T_g, and of the standing person, i.e., T_{mrt} *standing (IRM)*, for comparison with ENVI-met (see Table 25).

The 6 orthogonal orientations of the net radiometers were determined considering the façade as reference north, i.e.., data referred to “north” (and “south”) is taken with the sensors towards (and away from) the façade, and the other directions are orthogonal to this.

In order to ensure that all radiative fluxes densities measured were relative to a single point, the instrument was rotated in the 3 orthogonal directions around the measurement point, which corresponded to the midpoint between the sensors. The three radiometer orientations with respect to the measuring positions that are used in the proposed procedure are shown in Figure 87. Starting from the orientation in Figure 87a, the instrument was rotated by 90° around the axis of the support (see Figure 87b), and then the instrument and tripod were moved and rotated along the vertical axis by 90°, as shown in Figure 87c.

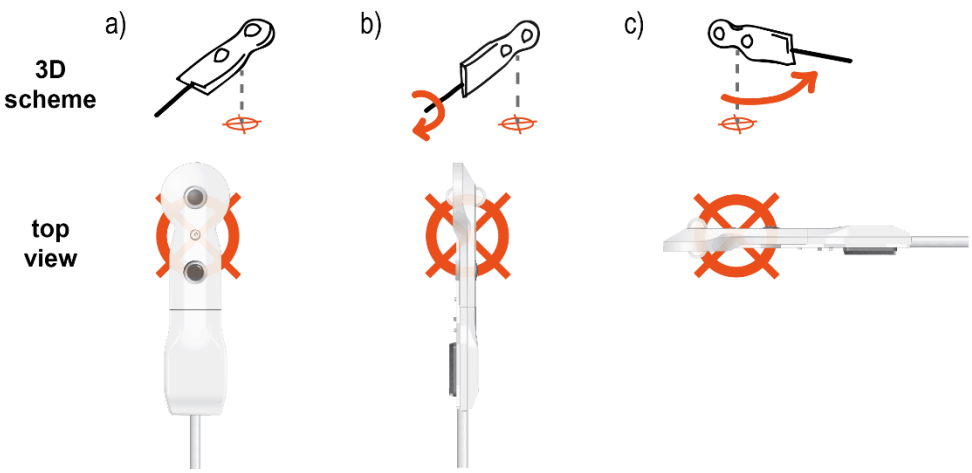

Figure 87. Example of the net radiometer (seen as both 3D schemes and from top view) with respect to the measurement point (orange mark) in a) upward/downward, b) east-west, c) south-north orientations.

This presents a novelty in the approach, as in the original IRM procedure, which is carried out using 3 net radiometers in parallel, the sensors are fixed to a single tripod and displaced from its center [328]. While this minimizes the risk of reciprocal shading on the instruments, it leads to spatially shifted acquisitions, which are therefore not directly referred to a single point in space. Also the simplified procedure carried out in [356], was performed by rotating the instrumentation without moving the tripod, with the sensors positions displaced from the tripod, in coherent way to the original version of the IRM. In the measurement here presented, given the absence of shading effect, it was considered preferable to have more spatially punctual acquisitions. This is also considered more consistent with the simulation output of ENVI-met, which provides data for the center point for each grid cell, and with T_{mrt} *sphere (globe)* values.

The measurement point of the Testo 480 instrument and connected sensors is located at a central position of the façade at a distance of 0.75 m from it.

Since T_{mrt} values exhibit a significant spatial variation [3], one of the research goal was to investigate the extent to which T_{mrt} varies at different distance from the building façade. To this aim, in the case of the simplified IRM, acquisitions were performed at two different distances from the façade: one comparable to that of Testo 480, i.e., at 0.75 from the façade in a central position, were measurements were taken every hour from 11:00 to 20:00, and one at 2.25 m from the façade, with acquisitions every hour from 10:30 to 19:30. For the sake of clarity, the point at 0.75 m from the façade will be identified as “Position 1” (P1) and that at 2.25 m as “Position 2” (P2). All the measurement sensors were kept at 1.1 m height from the ground, which represents the place of the weighting center of the standing human body [26,328].

Figure 88 shows the net radiometer in P1 and P2, i.e., at 0.75 m and 2.25 m from the façade. Please notice that the net radiometer orientations shown in Figure 88 corresponds to that shown in Figure 87b (left image in Figure 88) and Figure 87a (right image).

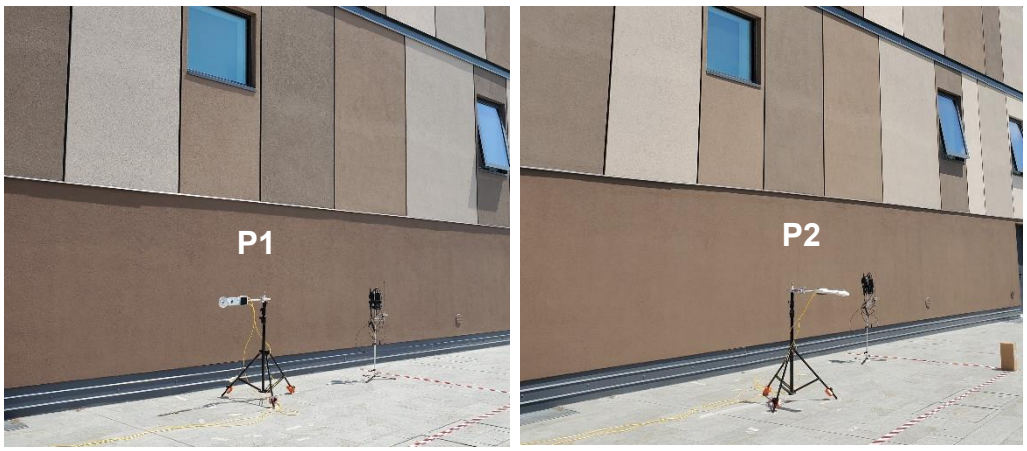

Figure 88. Picture of the net radiometer in Position 1 from the façade (right) and in Position 2 (left).

Table 27 summarizes the measuring time step and positions for each environmental variable monitored.

Table 27. Details on the measuring time step and positions of the monitored environmental variables.

Measured variable	Time step	Distance from façade
Air temperature T_a [°C]	60 s	0.75 m (P1)
Wind speed w [m/s]	60 s	0.75 m (P1)
Relative humidity RH [%]	60 s	0.75 m (P1)
Globe temperature T_g [°C]	60 s	0.75 m (P1)
Shortwave and longwave flux density in the six directions S_{Str} [W/m^2]	30 min. *	0.75 m (P1) 2.25 m (P2)

*Overall measurement duration of ~10 min., with 5 s sampling

In order to provide an overall description of the human body thermal sensation, the Physiological Equivalent Temperature (PET) [°C] was calculated from the measured environmental parameters using RayMan tool [419]. The PET index is defined in [45] as "air temperature at which the heat balance of the human body is maintained with core and skin temperature equal to those under the conditions being assessed"; a detailed description of PET, among the other thermal indices, is present in [32]. Being the spatial variation of T_a, RH and w more reduced than T_{mrt}, PET was calculated using T_a, RH and w obtained in P1. The calculation was performed for a standard person, i.e., for a 35-year-old man, with the following parameters: height = 1.75 m; weight = 75 kg; static clothing insulation = 0.9 clo; work metabolism = 80 W.

In addition to these environmental variables directly influencing thermal comfort, the surface temperature of the façade ($T_{s,f}$) was monitored using a calibrated T-type thermocouple, linked to the previously described datalogger (time step of 5 s). The calibration of the thermocouple was performed to reduce the measurement error below ± 0.3°C in the range between 0 and 60 °C (as described in Chapter 3B, section 3B.3.2), in accordance to ASTM E220-19 Standard [202]. For this sake, the temperatures measured by the thermocouple were compared to those measured by

a PT100 Platinum Resistance Thermometer, used as reference, at around three temperatures, i.e., 0 °C, 30 °C and 60 °C. Linear correction values were extrapolated and used to adjust the values measured by the thermocouple. The thermocouple was installed over the façade basement and screened using a layer of aluminum tape covered by an additional layer of paper tape in a color alike that of the surrounding wall. Three aluminum tape markers were used to identify thermocouple location and to ease the estimation of the reflected temperature for the thermal image analysis. A picture of the installed thermocouple is shown in Figure 89.

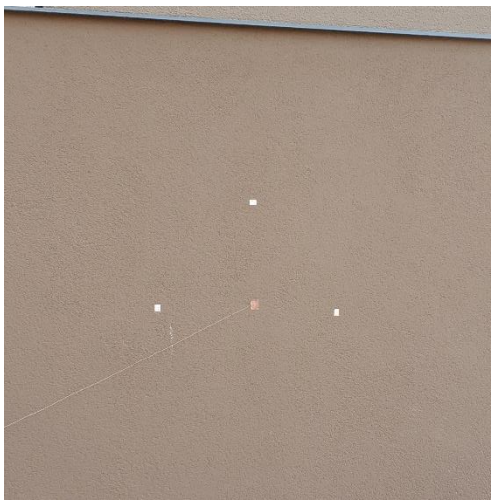

Figure 89. Picture of the installed thermocouples used to the monitor $T_{s,f.}$ (at center). The three surrounding makers are used to ease the identification of the sensor in the thermal images.

Thermal images were taken every 30 minutes using an infrared (IR) camera (model: Testo 882), in parallel to the T_{mrt} acquisitions with the IRM. From these thermal images, the surface temperature of the paving $(T_{s,p})$ could be determined, using the measured $T_{s,f.}$ as a reference. The emissivity was set at 0.9, which correspond to the emissivity of most conventional construction materials, and the reflected temperature was set based on that observed in correspondence of the aluminum tape markers. The other variables needed to the thermal images analysis are based on the in situ measured data.

Furthermore, a set of measurements was conducted to characterize the solar reflectance the surfaces of the building façade and paving, in view of the performance simulation. To this aim, the solar reflectance of the façade basement ($\rho_{sol,fb}$) and of the paving ($\rho_{sol,p}$) was measured using the two pyranometers installed at the sides of the net-radiometer. The solar reflectance was calculated as the ratio of the shortwave irradiance measured by the sensor oriented towards the measured surface, i.e., which is reflected by it, to that measured by the opposite sensors, i.e., the one incident on the surface. The instrument was kept parallel to the measured surface, at ~30 cm from it. These two measures were carried out while ensuring that the shadow cast by the instrument itself on the tested surface was negligible. Pictures taken during the measurement of the solar reflectance of the façade basement are shown in Figure 90.

Figure 90. Pictures of the measurement of the $\rho_{sol,fb}$.

Given the pattern of the upper part of the façade, which exhibits different brown shades (see Figure 85 and Figure 88), also these portions of the façade were characterized to obtain reliable input for the simulations. In this case, the visible reflectance coefficient (ρ_v) of the 4 brown shades was measured using a portable spectrophotometer (Minolta CM600d), in addition to the measurement of the ρ_v of the plaster of the façade basement. For each portion, three measurements were taken to account for potential color inhomogeneities. The spectral values of these measurement were averaged together and weighted with the normalized relative spectral distribution of global solar radiation, following the procedure in ISO 9050:2003 Standard [204]. For each façade portion, ρ_v was calculated by averaging all these values together. Since the façade portions present different colors, they were assumed to have different visible reflectance, and an equal reflectance in the remaining parts of the solar spectrum (NIR and UV). Based on the measured visible and solar reflectance values of the façade basement, the reflectance referred to the in the NIR and UV ranges could be estimated, considering the ASTM G173-03 [497] subdivision of the solar spectrum reported for air mass 1.5 direct normal and circumsolar irradiance and a clear sky. The ρ_{sol} of the 4 brown shades on the upper part of the building was then obtained based on the calculated reflectance in the UV and NIR ranges and the measured ρ_v in the four portions of the upper façade.

5B.4.3. ENVI-met simulation set-up

Four methods were followed to set-up the simulation in ENVI-met, combining two different ways to define the environmental forcing conditions and the façade wall stratigraphy:

- *Simple Forcing* + *Wall A* (SF+WA): the forcing conditions are set using hourly weather data through “simple forcing” (SF) mode and a user-weighted standard solar irradiance profile and a single value for wind speed and direction + the façade wall stratigraphy is modelled in a detailed way, identified as “Wall A” (WA);

- *Simple Forcing + Wall* B (SF+WB): the forcing conditions are set through SF (in accordance to the previous method) + the façade wall stratigraphy is simplified, i.e., "Wall B" (WB);
- *Full Forcing + Wall A* (FF+WA): the forcing conditions are using detailed data every 30 minutes through full forcing (FF) + Wall A is used to model the façade wall stratigraphy;
- *Full Forcing + Wall B* (FF+WB): the forcing conditions are set though FF (in accordance to the previous method) + Wall B is used to model the façade wall stratigraphy.

The environmental forcing conditions are based on local weather data, as recommended in [488]. The first two methods, which employ "Simple Forcing", are more simplified and require routinely measured data to set the boundary conditions. On the contrary, those employing "Full Forcing" have a more detailed definition of the boundary conditions and require weather data, such as diffuse and direct solar irradiances, that are generally of limited availability to practitioners. The two modeling methods used to describe the façade wall stratigraphy are based on a detailed accounting of the wall layer (within the limitation of ENVI-met's modeling) in the case of "Wall A", while involve a simplification of the outer layer using weighted properties, i.e., "Wall B", proposed in an attempt to improve the model accuracy.

The simulation approaches related to the virtual model (i.e., Wall A and B) and forcing conditions, i.e., SF and FF, are described separately in the following.

The virtual model

ENVI-met [498] v. 5.0.3 was used to simulate the measurement scenario. The software can simulate complex 3D environments approximated according to an orthogonal 3D grid, where the cell dimensions and number can be set by the user.

The case-study building and its surrounding context were modelled using 72x72x25 grids, with a grid cell size of 1.5x1.5x1.5 m. Therefore, the model domain is 108x108 m with a height of 67.5 m. Moreover, 7 nesting grids were set to minimize edge effects. A telescoping factor of 10% was applied above the height of 14 m. The lowest grid cells were split along their height into 5 smaller cells, to allow for a finer resolution at pedestrian locations. The virtual model is generated by taking as reference the case-study façade, which was modelled parallel to the grids (i.e., as perfectly south facing) to make its surface planar. In order to account for its actual orientation, the model rotation out of grid north was set to 34°. The virtual model used for the simulations is shown in Figure 91 along with the area in which the measurements were carried out.

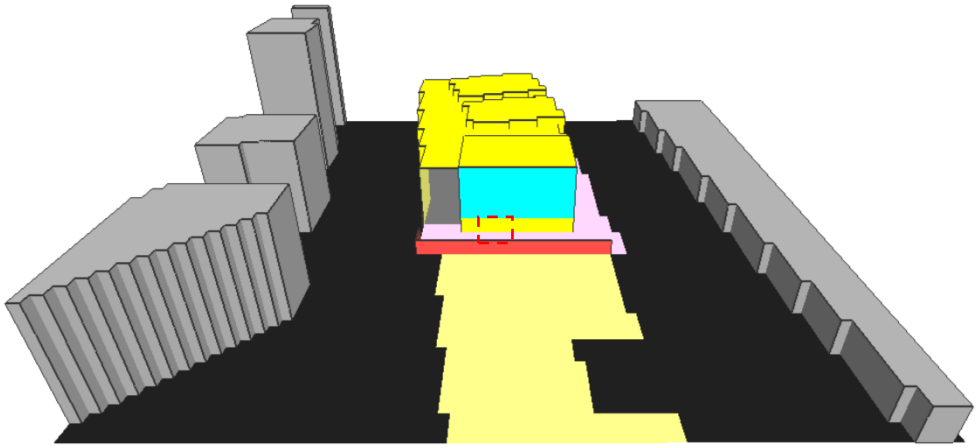

Figure 91. 3D view of the virtual model used for the simulations; the red rectangle identified the location of the measurement campaign.

The case-study building façade was modeled considering the measured and calculated ρ_{sol} of its compositing portions, i.e., basement and upper part, described in § 5B.4.2. For the basement, the measured solar reflectance ($\rho_{sol,fb}$) was used, while the upper part, given the relatively low model resolution, was modeled as homogeneous, with solar reflectance equal to the mean of the calculated solar reflectance weighted by the areas of the differently colored blocks. The windows of the façades were omitted in the model, being them small in comparison to the grid dimensions and located at a much greater height than the measurement location.

The soil profile used to model the pavement of the surrounding pedestrian area (colored in pink in Figure 91) is based on the ENVI-met pre-set material “Dark Granit Pavement", whose solar reflectance is altered to account for the measured $\rho_{sol,p}$ of the pavement, that is equal to 0.33. The remaining parts of the domain are treated with “Asphalt Road”, for the road parts in black color, and with “Sandy Soil” for the construction site, in yellow color.

Only the immediate surroundings of the case-study building were modeled in detail. The buildings of the context were modeled as volumes, and a standard wall and roof material was applied to them (i.e., “Default wall – moderate insulation”). In order to account for the wooden fence used to delimit the construction site in front of the case-study façade, a vertical “single wall” with a height of 3 m was used.

In ENVI-met, building façade walls are represented by thermodynamical models consisting of 7 calculation nodes, which enables the modelling of 3 layers, whose thickness can be defined by the user. A detailed description of the 7-nodes wall model can be found in [374,491]. A given material (either pre-set or customized by the user) materials has to be assigned to each of the three layers. The properties of each layer are defined by the layer thickness t [m], and by the solar absorptance a_{sol} [-], solar reflectance ρ_{sol} [-], emissivity ε [-], specific heat capacity c [J/kgK], thermal conductivity λ [W/mK] and density δ [kg/m^3] of the assigned material. As previously mentioned, the façade walls were modelled in a detailed way (Wall A) or in a simplified way (Wall B), that are described in the following.

Wall A - Detailed façade wall modeling

For the detailed modeling of the façade wall, i.e., Wall A, the actual stratigraphy of the opaque portions of the façade has been reproduced in ENVI-met, within the 3-layer constraint of the software. The actual façade is made of a double brick wall and has an external thermal insulation composite system (ETICS), for an overall thickness of 55.5 cm. Its detailed stratigraphy, provided by the EDILOG Department of the University, is shown Figure 92.

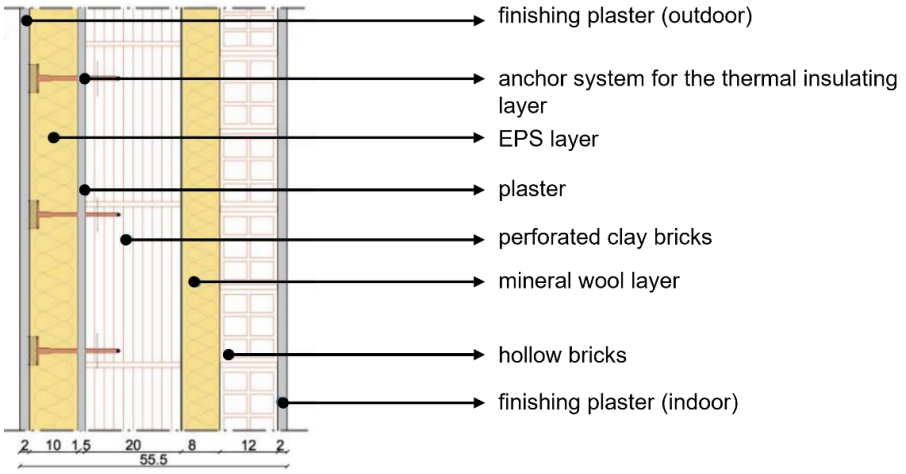

Figure 92. Detailed stratigraphy of the opaque façade portion, with functional layers and thicknesses [cm].

To model Wall A, the wall stratigraphy in Figure 92 was simplified to 3 layers. The outer 2 layers, i.e., a plaster layer and expanded polystyrene (EPS) layer, were modeled in detail for the simulation, while the remaining layers were approximated using a fictive inner layer. This was done to prioritize an accurate modeling of the outermost layers, which are the ones affecting outdoor microclimatic conditions the most, as done in [499]. The approximated inner layer exhibits the overall thickness of the composing layers, and its properties are defined as the weighted average of the properties of its composing layers. The 3 layer-wall stratigraphy used to model the façade wall is detailed in Figure 93.

Except for ρ_{sol}, the material properties are based on literature data or technical specifications. The details and properties of the composing layers are collected in Table 28 and numbered from outside to inside; the outer plaster layer (1) varies from the basement façade to its upper part, to account for the measured or calculated ρ_{sol} (see § 5B.4.2).

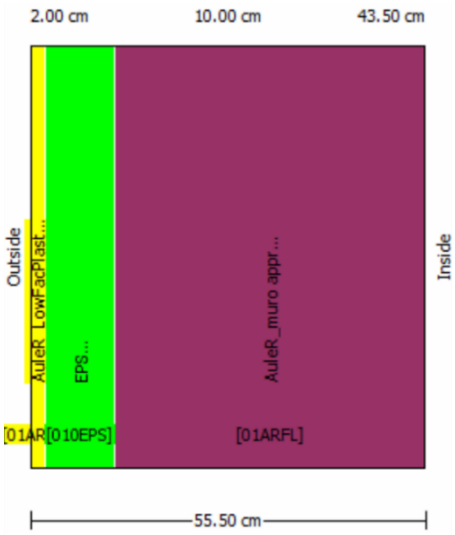

Figure 93. Screenshot of ENVI-met interface showing the wall stratigraphy used for Wall A.

Table 28. Details and properties of the layers used for Wall A (the detailed façade model). The numeration of the layer starts from the outermost one.

	t [m]	a_{sol} [-]	ρ_{sol} [-]	ε [-]	c [J/kgK]	λ [W/mK]	δ [kg/m^3]	Refs.
Plaster, basement (1)	0.02	0.83	0.17	0.9	850	0.54	1400	[500]
Plaster, upper façade (1)	0.02	0.77	0.23	0.9	850	0.54	1400	[500]
EPS (2)	0.1	0.5	0.5	0.6	1300	0.035	30	[501–504]
Approximated layer (3)	0.435	0.5	0.5	0.86	949	0.23	848	[505–507]

Wall B - Simplified façade wall modeling

In the simplified façade modeling, the façade wall stratigraphy was further simplified. This test was done to investigate the effect of wall modeling on $T_{s,f}$ and to evaluate if such approach was able to increase the accuracy of the simulated $T_{s,f}$. A single layer was used to model the outer part of the façade, comprising the EPS layer and the plaster layer, while two layers of the same material were used to model the interior part of the façade. The layers composing the interior part are assigned with the properties described in Table 28 for "Approximated layer". The outer part was modeled using an equivalent layer, having the ε, ρ_{sol} and a_{sol} of the plaster and a c, δ and λ calculated as the weighted average of those of the original EPS and plaster layer. This modeling approach was done in the attempt to provide the equivalent layer with the material properties of the plaster, i.e., the outermost layer of the actual stratigraphy and of the detailed façade modeling, that mainly influence the outer surface temperature, while using the weighted average of the EPS + plaster layer for the remaining properties, which primarily affect the heat transfer through the wall. An image of the wall stratigraphy is shown in Figure 94, while the detailed information on the composing layers is collected in Table 29.

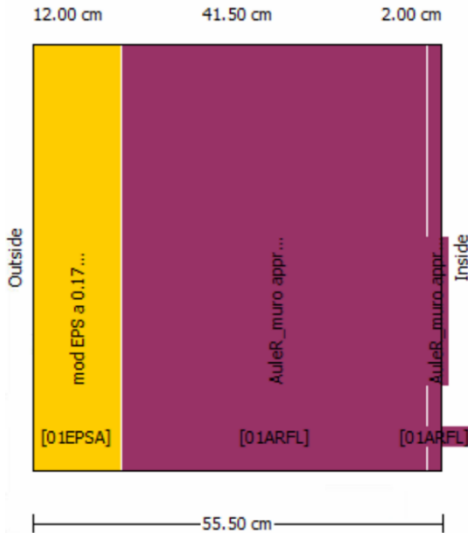

Figure 94. Screenshot of ENVI-met interface showing the wall stratigraphy used for Wall B.

Table 29. Details and properties of the layers used for Wall B (the simplified façade model). The numeration of the layer starts from the outermost one.

	t [m]	a_{sol} [-]	ρ_{sol} [-]	ε [-]	c [J/kgK]	λ [W/mK]	δ [kg/m^3]	Refs.
Plaster + EPS, basement (1)	0.12	0.83	0.17	0.9	1225	0.119	258	[500–504]
Plaster + EPS, upper façade (1)	0.12	0.77	0.23	0.9	1225	0.119	258	[500–504]
Approximated layer (2 + 3)	0.435	0.5	0.5	0.86	949	0.23	848	[505–507]

The simulation settings and environmental boundary conditions

As concerns the simulation settings, the IVS module was enabled (finer resolution up to a height of 14 m), to have a detailed estimation of the radiative heat transfer [370,373], and T_{mrt} was calculated using the six-directional approach [370], with the default human projection factors based on VDI 3787 [336].

To allow for model initialization, the simulation was run for 48 h starting on the previous day (July 17th) at 00:00 and simulation results were extracted from the last 24 h, i.e. July 18th [489]. The output interval was set to 30 minutes. As a preliminary test, a 72 h simulation was run as done in [489], however, since no significant difference was found between the main environmental parameters (i.e., T_{mrt}, T_a) obtained in the second and last 24 hours of simulation, the duration of the simulation was set to 48 h to reduce computation time.

As mentioned previously, the forcing conditions for the simulation were defined based on local weather data, according to two methods, i.e., SF and FF.

Simple forcing (SF)

When SF mode was employed, the environmental boundary conditions related to relative humidity *(RH)*, air temperature *(T_a)*, solar irradiance and wind speed (*w*) and direction, were defined in a simplified way using hourly data (for *RH* and T_a), single values (for wind speed and direction) and weighting factors (for solar irradiance). The forcing conditions are set according to the data measured by the weather station of Politecnico di Torino located on building at ~350 m from the measurement location. Despite the simulation is run for 48 h, the data required for simple forcing is related to a single day. Therefore, the simulation was run for 48 h, by repeating the boundary conditions defined for July 18, as done in [355].

The value of *w*, T_a and *RH* conditions measured by the weather station are shown in Figure 95.

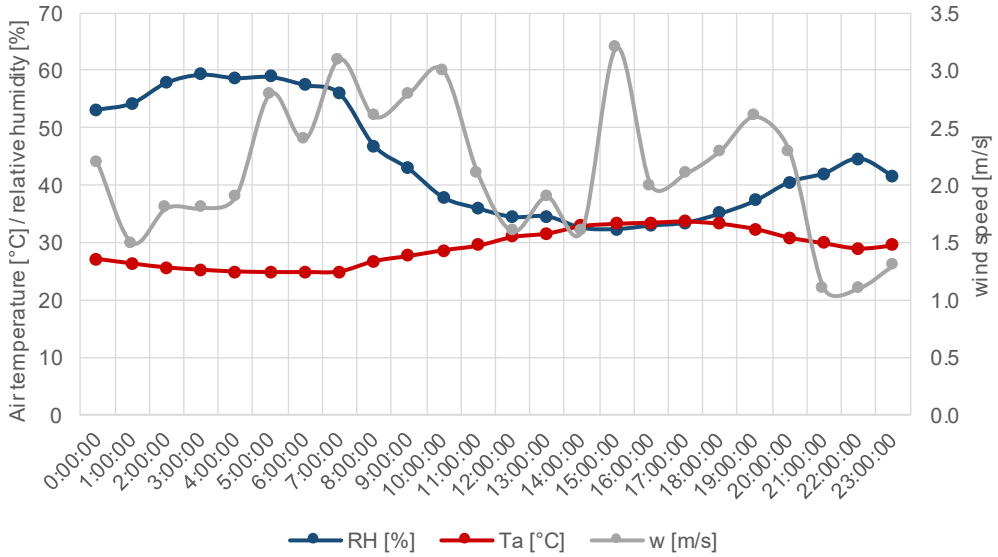

Figure 95. Boundary conditions measured on an hourly basis by the weather station.

The boundary conditions were manually set with hourly data for the T_a [°C] and *RH* [%], while wind speed *w* [m/s] and direction [°] were defined respectively considering the average *w* value from 10:00 to 20:00 and with the prevalent wind direction (rounded to 5°) in the same time frame. The pre-set global irradiance profile in ENVI-met was corrected with an adjustment factor to minimize its difference to the global irradiance measured by the Politecnico weather station. The single values used to define these boundary conditions are detailed in Table 30.

Table 30. Single values used to set the environmental boundary conditions for the simulation.

w [m/s]	wind direction [° from North]	adj. factor for solar irradiance [-]
2.2	45	0.81

Full forcing (FF)

For the FF mode, a greater amount of data on the environmental conditions is required. More specifically, the input data are related to T_a [K], *RH* [%], *w* [m/s], wind direction [°], direct normal solar irradiance, diffuse solar irradiance and downward infrared (longwave) irradiances [W/m^2]. The above-described data need to be detailed for every 30 minutes during the simulation timeframe and uploaded as .csv file on the Forcing Manager. With the exception of the downward longwave irradiance, which irradiance was left to ENVI-met to calculate (by inputting 0 values), all the data was obtained from the Politecnico weather station and is referred to 10 m above ground. Since the simulation was run for 48 h, the data required was detailed for July 17th and July 18th; the input data is plotted in Figure 96.

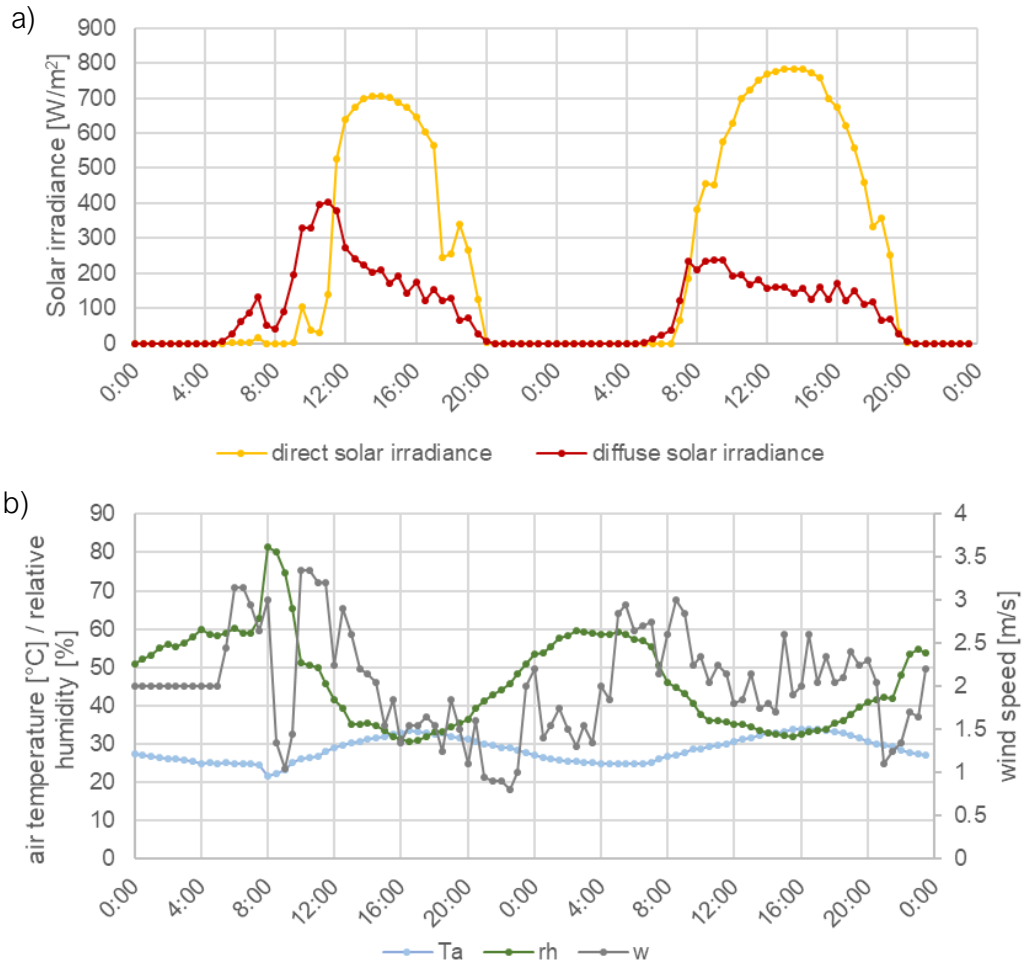

Figure 96. Graphs showing the data required to set the full forcing mode for July 17th and 18th, related to a) direct normal and diffuse solar irradiances, b) T_a, *RH* and *w*.

To avoid model instability, a larger number of nesting grids, i.e., 10, and z grids, i.e., 30, was used in the virtual model, with respect to what previously described. For the same reason, some corrections were made on the forcing data: for the first few simulation hours *w* was set at 2 m/s and the wind direction was calculated as the moving average over four original wind directions, corresponding to 2 h, to avoid large angle variations. The computation time of FF simulations, given the more detailed

forcing condition and the model domain adjustments, was almost twice as much that of SF simulations. This may obstacle the practical implementation of this approach in the professional field, which often requires shorter computation time.

5B.4.4. Evaluation of the simulated surface temperature with different façade solar reflectance

As an additional step, the reliability of $T_{s,f}$, considering a high solar reflectance of the wall itself, was assessed by model intercomparison. The analysis aims to broaden the $T_{s,f}$ validation, which is referred to a dark colored façade (i.e., with low solar reflectance), by evaluating the predicted results in case of a light-colored façade, i.e., with high solar reflectance. Indeed, climate sensitive design strategies often involve the use of "high-albedo" materials, and a correct accounting of the surface temperatures is crucial to estimate their effect on the microclimate.

WUFI v6.2 [508] was used to predict the $T_{s,f}$ used as reference to evaluate the accuracy of ENVI-met predictions. WUFI is a validated simulation tool that models heat and moisture transport in walls and other multi-layer building components exposed to natural weather. As a first step, a simulation referred to the actual façade basement ($\rho_{sol,fb}$ = 0.17) was run to check results agreement with observed $T_{s,f}$, then another the simulation was run high-albedo façade, with a $\rho_{sol,fb}$ of 0.8. The façade was modelled in WUFI in accordance to Wall A, which is the most detailed modelling allowed by ENVI-met (see Table 28), and a south orientation of the wall was assumed. To allow for model stabilization, the simulation in WUFI was started 24 h before the beginning of the measurement campaign, and simulation data was obtained every 30 minutes. The hourly boundary conditions related to T_a, *RH, w* and were set according to the in-situ measured data for the time span corresponding to the measurement campaign. The remaining data (i.e., that needed for the model stabilization) and the direct beam and diffuse solar irradiances were based on the data of the weather station of Politecnico di Torino.

5B.4.5. Simulation outcome and model validation

The simulation outcome related to the selected environmental variables (T_a, T_{mrt}) was extracted for each measurement position at 1.05 m from the ground, that is close to the weight center of the human body of 1.1 m [26,328] and correspond to the height of the sensors during the measurement campaign. The T_s of the wall and paving ($T_{s,f}$ and $T_{s,p}$) were extracted in correspondence to the measurement location.

In addition, PET index was determined to describe the perceived thermal sensation. The calculation is performed in the attempt to isolate the effect on calculated PET values of the environmental variables affecting thermal comfort the most, i.e., T_a, T_{mrt} [509], which are the ones that have been validated in this study. Therefore, the indices were calculated based on the simulated T_a and T_{mrt} values, and with in-situ measured data for the remaining variables (*RH* and *w)*, similarly to the approach followed in [355]. PET indices were calculated using RayMan Pro (v 3.1

beta) [419] for a standard person, i.e., with the same characteristics reported in § 5B.4.2.

For a more detailed analysis on T_{mrt} and T_s predictions, the measured directional radiative components (K_i and L_i) were compared to the simulated ones.

As concerns the model validations, the accuracy of ENVI-met predictions was evaluated for the most relevant environmental variables affecting thermal comfort, i.e., T_a and T_{mrt}, [509], for $T_{s,f}$ and $T_{s,p}$, and for the directional radiative fluxes (K_i and L_i).

In this research, the agreement between measured and simulated environmental parameters is evaluated based on the number of observation (N), the calculation of R^2, MAE, MAPE and RMSE. Moreover, the simulation error in correspondence to the maximum observed values, named "peak error", is reported for completeness.

R^2 is a correlation metrics, ranging between 0 and 1, that can be used to evaluate how close the data are to the fitted regression line and indicates the proportion of the variance in the dependent variable (measured data) that can be explained by the predicted data. The MAE is calculated as the mean difference between the predicted values and the measured values. Additionally, also the mean absolute percentage error (MAPE) has been calculated, which is based on MAE but is expressed as percentage with respect to the reference values. The RMSE quantifies the standard deviation of the difference between the predicted and the measured values; its value is more sensitive to large errors than MAE. The reliability of the model is the greatest for $R^2 \rightarrow 1$, MAE $\rightarrow 0$, MAPE $\rightarrow 0$ and RMSE $\rightarrow 0$.

The above-described statistical parameters can be calculated from the model predicted (P) and observed (O), and the number of observation (N), according to the following Equations (22)-(25):

$$R^2 = 1 - \frac{\sum_{i=1}^{N}(P_i - O_i)^2}{\sum_{i=1}^{N}(|O_i - O_{mean}|)^2} \quad (22)$$

$$MAE = \frac{1}{N}\sum_{i=1}^{N}|\hat{P}_i - O_i| \quad (23)$$

$$MAPE = \frac{1}{N}\sum_{i=1}^{N}\left|\frac{\hat{P}_i - O_i}{O_i}\right| \quad (24)$$

$$RMSE = \sqrt[2]{\frac{1}{N}\sum_{i=1}^{N}(P_i - O_i)^2} \quad (25)$$

These statistical parameters have also been used to evaluate the agreement between T_{mrt} *sphere (globe)* and both T_{mrt} *standing (IRM)* and T_{mrt} *sphere (IRM)*.

5B.5. Results

5B.5.1. The microclimatic measurement

The measured T_a [°C], *RH* [%], *w* [m/s] at 0.75 m distance from the case-study façade are plotted in the graph in Figure 97. As it can be noticed, T_a was constantly above 30°C during the measurement, with maximum values at 37°C, the wind speed was rarely above 1 m/s and there were dry conditions (*RH* below 30% during the hottest hours of the day).

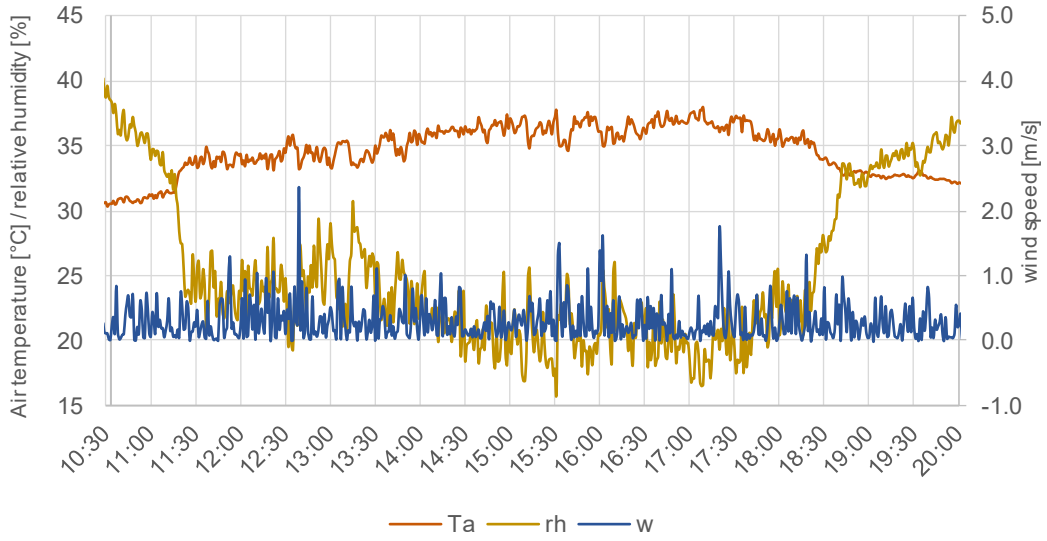

Figure 97. Environmental variables measured at 0.75 m from the façade.

The T_{mrt} values obtained with the IRM, given its greater accuracy over the globe thermometer method [26,328,346,351–354], are here considered as a reference to a) estimate the agreement between the two approaches by comparing T_{mrt} *sphere (IRM)* and T_{mrt} *sphere (globe)* obtained at 0.75 m from the façade, and b) assess the reliability of the use globe thermometer for biometeorological purposes by comparing T_{mrt} *standing (globe)* to T_{mrt} *sphere (IRM)*.

In addition, the influence of the façade distance on T_{mrt} can be evaluated by comparing the trends of T_{mrt} *standing (IRM)* obtained at 0.75 m and 2.25 m from it.

The results are here discussed with respect to the accuracy range of ±5°C suggested by ISO 7726:1998 Standard [337] for measuring instrumentation in case of thermal stress conditions and that was employed in past validation studies [348,355].

Difference between the mean radiant temperatures obtained with globe thermometer and IRM

The graph in Figure 98 collects the T_{mrt} values obtained during the measurement campaign at 0.75 m (in P1) from the building façade.

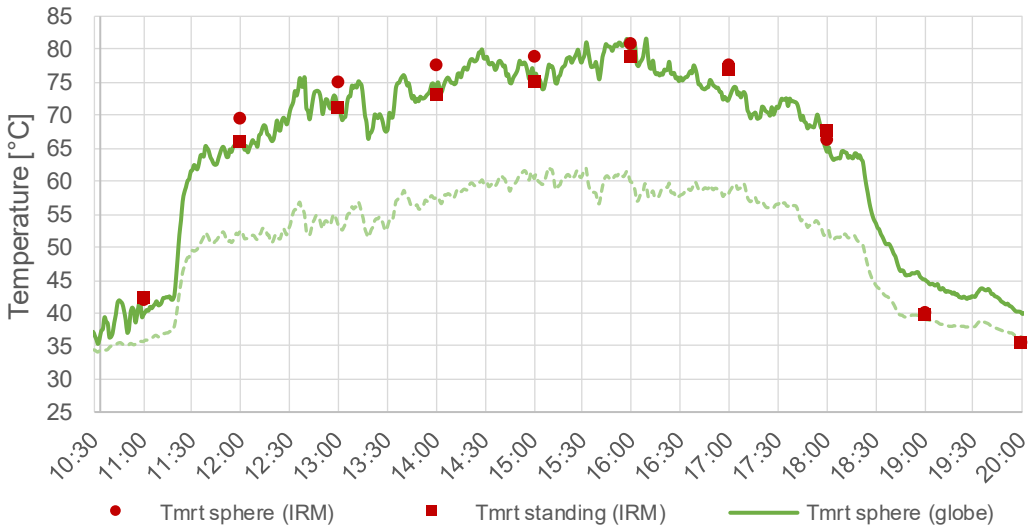

Figure 98. Measured T_g and T_{mrt} determined using the globe thermometer and with IRM at 0.75 m from the building façade.

The graph allows to compare the T_{mrt} determined from T_g [°C] (also plotted in the graph) with the globe thermometer i.e., T_{mrt} *sphere (globe)*, and following IRM, which are referred to a standing person, i.e., T_{mrt} *standing (IRM)*, and to a sphere, i.e., T_{mrt} *sphere (IRM)*.

T_{mrt} *standing (IRM)* accounts for the shape of a standing person, for which lateral radiative contributions are dominant, while for the calculation of T_{mrt} *sphere (IRM)* all radiative contributions have equal weight. This difference can be noticed from the T_{mrt} *standing (IRM)* and T_{mrt} *sphere (IRM)* comparison, as the latter is greater than T_{mrt} *standing (IRM)* during the peak hours of the day (from 11:00 to 17:00), given the high solar altitude and the greater upward W_i for T_{mrt} *sphere (IRM)* (see Table 25).

The trend of T_{mrt} *sphere (globe)* is generally coherent with those of both T_{mrt} *sphere (IRM)* and T_{mrt} *standing (IRM)* during daytime. After 18:00, T_{mrt} *sphere (globe)* exhibit greater values than both T_{mrt} sphere (IRM) and T_{mrt} standing (IRM), similarly to the results reported in [328].

The agreement between T_{mrt} measured with IRM, i.e., T_{mrt} *sphere (IRM) and* T_{mrt} *sphere (IRM)* and with the globe thermometer, i.e., T_{mrt} *sphere (globe)* was evaluated considering for the latter parameter the average the observed values in the ~10 min time windows of the IRM measurement (at 0.75 m from the façade).

The graph in Figure 99a shows a scatterplot of T_{mrt} *sphere (globe)* and T_{mrt} *sphere (IRM)*, while in Figure 99b T_{mrt} *sphere (globe)* values are plotted against T_{mrt} *sphere (IRM)*. The first comparison allows to estimate the coherency between the two measurement methods, while the second to investigate how reliable T_{mrt} *sphere (globe)* is for biometeorological measurements, which are normally referred to a standing human body.

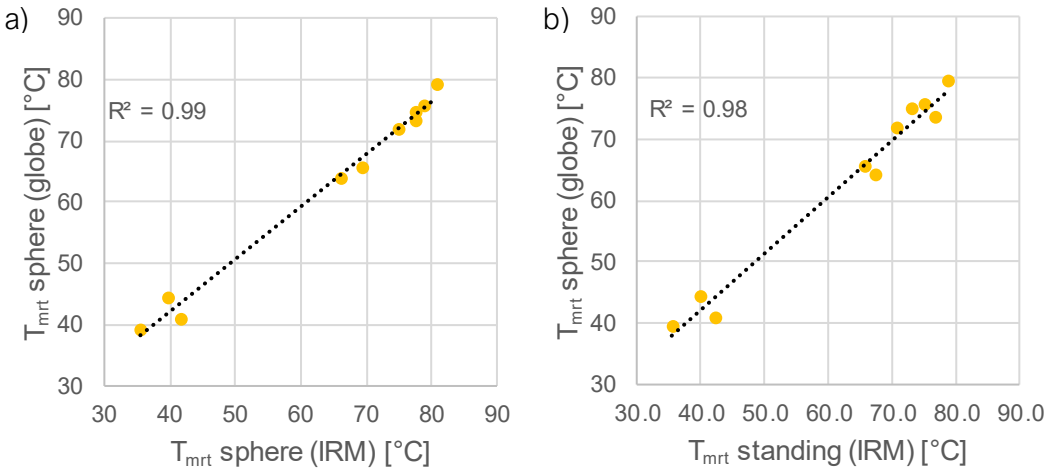

Figure 99. Scatterplots of the determined a) T_{mrt} *sphere (IRM)* versus T_{mrt} *sphere (globe)* and *b)* T_{mrt} *standing (IRM)* versus T_{mrt} *sphere (globe).*

Table 31 collects the statistical parameters used to evaluate the agreement between T_{mrt} *sphere (globe)* and T_{mrt} *sphere (IRM)* and between T_{mrt} *sphere (globe)* and T_{mrt} *standing (IRM).*

Table 31. Statistical parameters calculated to evaluate the agreement between T_{mrt} sphere (IRM) and T_{mrt} sphere (globe).

	N	R^2	MAE	MAPE	RMSE
T_{mrt} *sphere (IRM)* vs T_{mrt} *sphere (globe)*	10	0.99	3.05	0.05	3.24
T_{mrt} *standing (IRM)* vs T_{mrt} *sphere (globe)*	10	0.98	2.07	0.04	2.53

The RMSE values are within the ±5°C suggested by ISO 7726:1998 Standard [337] for thermal stress conditions, evidencing a good agreement between the values. Overall, this result evidences a good matching, without allowing to highlight the expected disagreement between the two T_{mrt} measures reported in previous studies [26,328,346,351–354]. Nonetheless, these results should be taken with caution, given the very limited amount of data used for the comparison and the fluctuation of T_{mrt} *sphere (globe)* values, which could reduce the representativeness of the data selected for the comparison. Another potential source of error is the uncertainly of the T_a values used for the calculation of T_{mrt}, whose measurement error was estimated within ±0.5°C, and may affect the accuracy T_{mrt} *sphere (globe)*. More extensive measurement campaigns are needed to better shed light on the agreement between the two measurement approaches.

Effect of façade distance on mean radiant temperature

The graph in Figure 100 shows the T_{mrt} values for a standing person obtained with IRM in P1 and P2, i.e., at either 0.75 m from the façade and at 2.25 m from it. As it can be noticed from the graph, the two T_{mrt} trends are similar during the hottest hours

of the day, with slightly higher values at the position closer to the façade during the central hours of the day. These slight differences, which are likely to be caused by the greatest influence in P1 of the longwave irradiance emitted by the façade, are however in the ±5°C and therefore not considered significant.

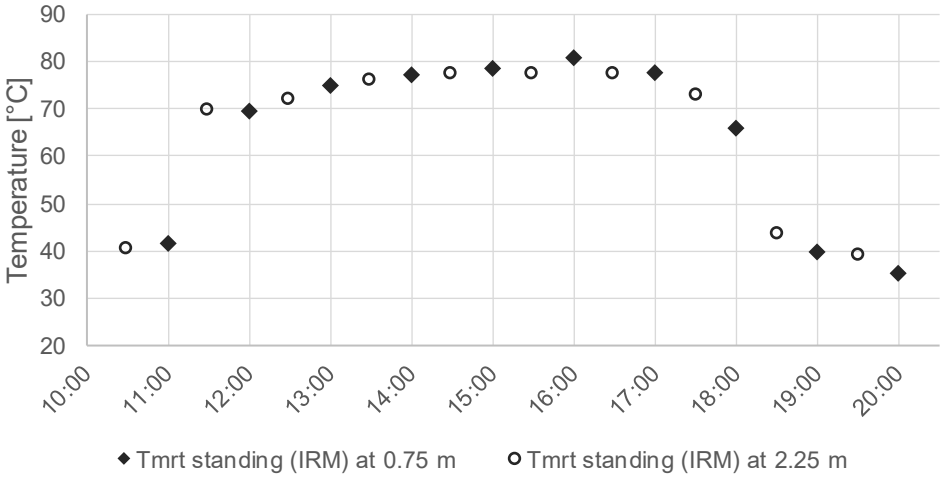

Figure 100. T_{mrt} measured with IRM in P1 and P2.

5B.5.2. The microclimatic simulation results

Validation of air temperature

The variation of measured and simulated air temperature (T_a) over time in P1 is shown in Figure 101, while Figure 102 collects the scatterplots of the measured and simulated T_a with the four simulation methods and

Table 32 reports the calculated statistical parameters used to quantify the model's accuracy and the peak errors. A summary of the peak errors for all the tested variables is shown in Figure 126 in Appendix 5B. Methods SF+WA and SF+WB underestimate Ta, on the central hours of the day, with no significant difference between the two methods, while FF+WA and FF+WB generally overestimate T_a, after 14:00, with no significant difference between the two methods.

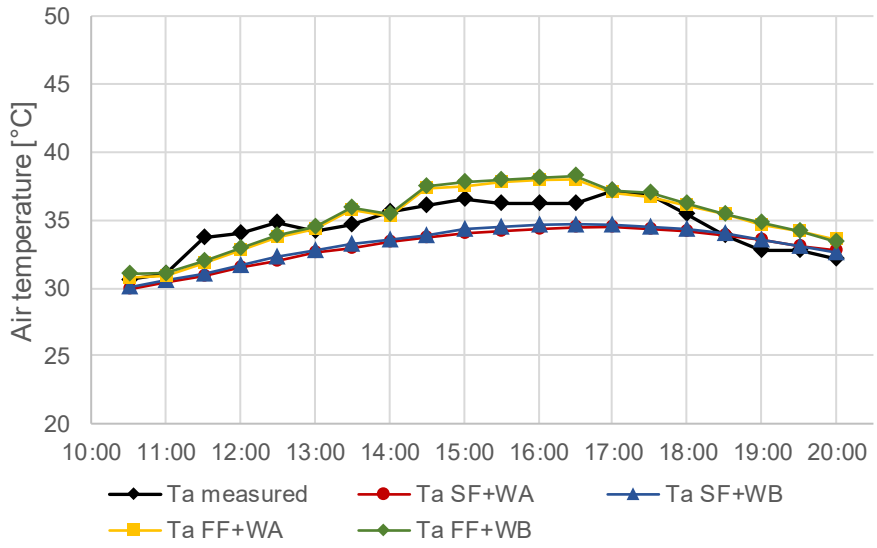

Figure 101. Comparison between measured T_a trends in P1

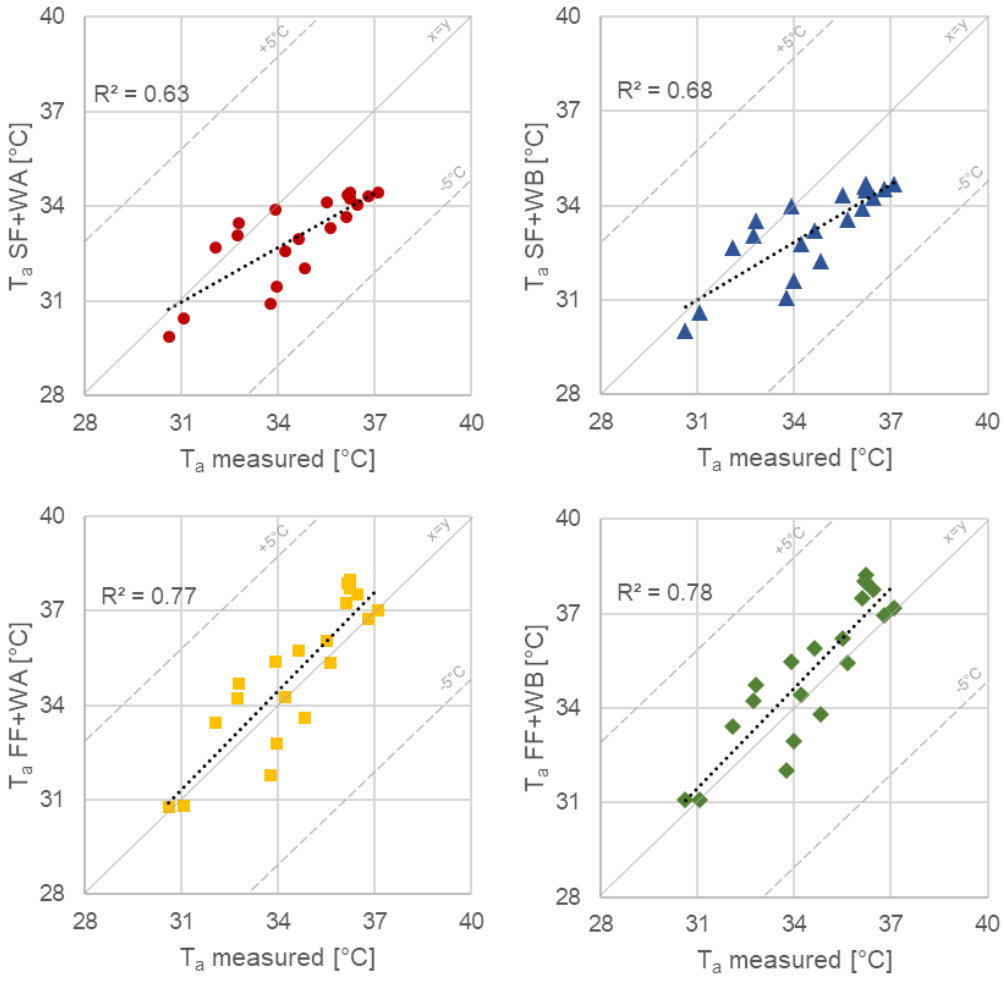

Figure 102. Scatterplots of the measured T_a and the simulated one in P1, with the four simulation methods.

Table 32. Statistical evaluation metrics and peak error of the simulated T_a.

	N	R^2	MAE	MAPE	RMSE	Peak Err.
T_a *SF+WA*	20	0.63	1.69	0.05	1.90	-2.67
T_a *SF+WB*	20	0.68	1.52	0.04	1.72	-2.44
T_a *FF+WA*	20	0.77	1.02	0.03	1.20	-0.09
T_a *FF+WB*	20	0.78	1.08	0.03	1.27	0.07

The calculated R^2 is between 0.63 and 0.78, the MAE found is between 1.02 and 1.69 °C and the RMSE is between 1.20 and 1.90 °C, depending on the simulation methods. These values are quite in line with the median MAE for T_a reported in [347] and with the statistical parameters found in [366]. According to the evaluation metrics, FF+WA and FF+WB methods lead to the least T_a divergence with measured data. This result suggest that FF leads to more accurate T_a estimations than SF. Conversely, SF+WA reports the greatest RMSE and MAE errors, resulting in the lowest agreement.

It has to be however highlighted that the outcome of this T_a evaluation may be influenced by the uncertainty related to measured T_a values used as reference, as previously discussed. Therefore, further investigations are needed to better shed light on the accuracy of the predictions for T_a.

Validation of mean radiant temperature

The graph in Figure 103 plots the variation of measured T_{mrt} values over time, and of the corresponding simulated values obtained with the four simulation methods. The measured T_{mrt} values are referred to both P1 and P2 in light on the negligible difference found between the T_{mrt} values at the two distances from the façade (see § 5B.5.1). Figure 104 shows the scatterplots of simulated and measured T_{mrt} values, while the peak error and calculated statistical metrics to describe the model error are collected in Table 33 (see Figure 126 in Appendix 5B for the peak error summary).

The graphs reports that the simulated T_{mrt} is generally underestimated by ENVI-met. More specifically, all methods result in T_{mrt} trends quite coherent with the measured one, although systematically underestimated, with greater underestimations for simulation methods featuring WA, i.e., WS+WA and FF+WA. Only at 18:30 and 20:00 all methods report a T_{mrt} overestimation, with the former one is probably caused by an incorrect accounting of the time in which the measurement location becomes shaded, linked to the geometric approximation of the virtual model.

The simulation methods resulting in the least agreement is SF+WA (RMSE = 10.09 °C, peak error = -6.98 °C), while the greatest agreement is reported for simulation methods with WB, i.e., SF+WB and FF+WB (RMSE between 8.36–8.46 °C, and peak errors between 10–11 °C). These findings suggest that the simplified model for façade wall, i.e., WB, helps increasing T_{mrt} accuracy, while the use of FF was not reported to meaningfully increase T_{mrt} results accuracy in the case under consideration.

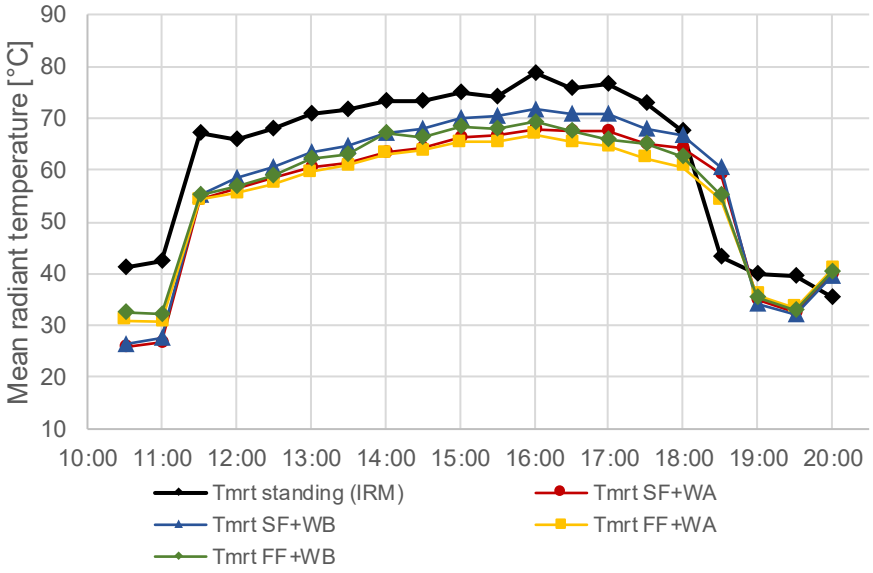

Figure 103. Comparison between measured and simulated T_{mrt} trends

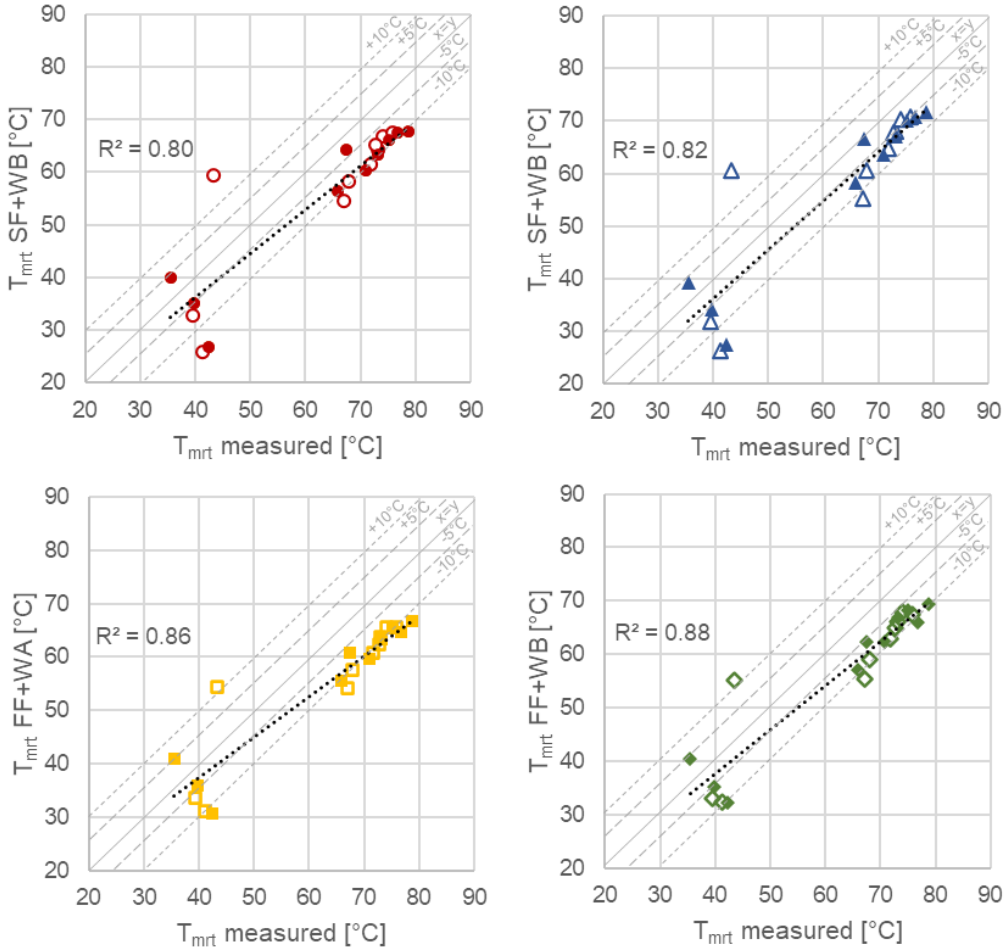

Figure 104. Scatterplots of the measured T_{mrt} and the simulated one with the four methods. White and colored indicators refer to P1 and P2, respectively.

Table 33. Statistical evaluation metrics and error at peak of the simulated T_{mrt}.

	N	R^2	MAE	MAPE	RMSE	Peak Err.
T_{mrt} *SF+WA*	20	0.80	9.50	0.16	10.09	-10.93
T_{mrt} *SF+WB*	20	0.82	7.44	0.14	8.46	-6.98
T_{mrt} *FF+WA*	20	0.86	9.71	0.16	9.98	-11.97
T_{mrt} *FF+WB*	20	0.88	8.09	0.14	8.36	-9.41

The evaluation metrics for the simulated T_{mrt} found are within the range of the errors reported in [347], although generally above the median value reported for R^2, MAE and RMSE. The validation results in [355] (referred to a previous ENVI-met release, with the two directional T_{mrt} model and without IVS, see Chapter 4B) reported T_{mrt} underestimation in the location comparable to those of this measurement campaign (i.e., unobstructed site close to south oriented façade identified as P3 in [355]). Nonetheless, the errors found in this campaign are greater than those found in more recent studies, such as [369,370], which were however carried out in different conditions than the one here considered. Overall, all the tested simulation methods led to modeling errors exceeding the accuracy range of ±5°C suggested by ISO 7726:1998 Standard [337] for thermal stress conditions.

Being T_{mrt} the most relevant environmental variable affecting outdoor thermal comfort, this limited agreement highlight that ENVI-met v5.0.3, despite the recent advancements, still failed at correctly estimate T_{mrt} in the tested scenario under extremely hot conditions.

Validation of façade and paving surface temperatures

In order to better understand the reported T_{mrt} divergence, this section focuses on the T_s estimation of the façade wall and paving.

Figure 105 shows the variation of the measured and simulated outer surface temperature of the façade basement $(T_{s,f})$ over time. Figure 106 shows the scatterplots of simulated and measured $T_{s,f}$ and Table 34 the statistical parameters and peak errors (the latter are also summarized in Figure 126 in Appendix 5B).

The graph shows that the simulated $T_{s,f}$ is underestimated by all methods, with the best agreement found for simulations with Wall B. The $T_{s,f}$ trends reported for FF+WA and SF+WA are similar to one another. This similarity, although less marked, is reported also for SF+WB and FF+WB, although FF+WB reported lower $T_{s,f}$ values than SF+WB during the central hours of the day, leading to a reduced agreement with measured data. Among the method tested, SF+WB leads to the most reduced $T_{s,f}$ errors.

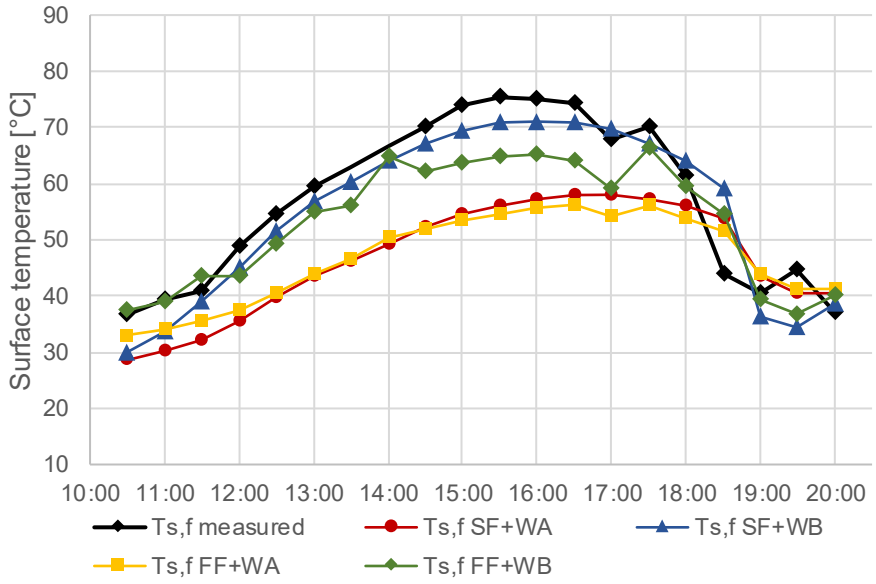

Figure 105. Comparison between measured and simulated $T_{s,f}$ trends. The two missing data in $T_{s,f}$ measured are due to a measurement issue.

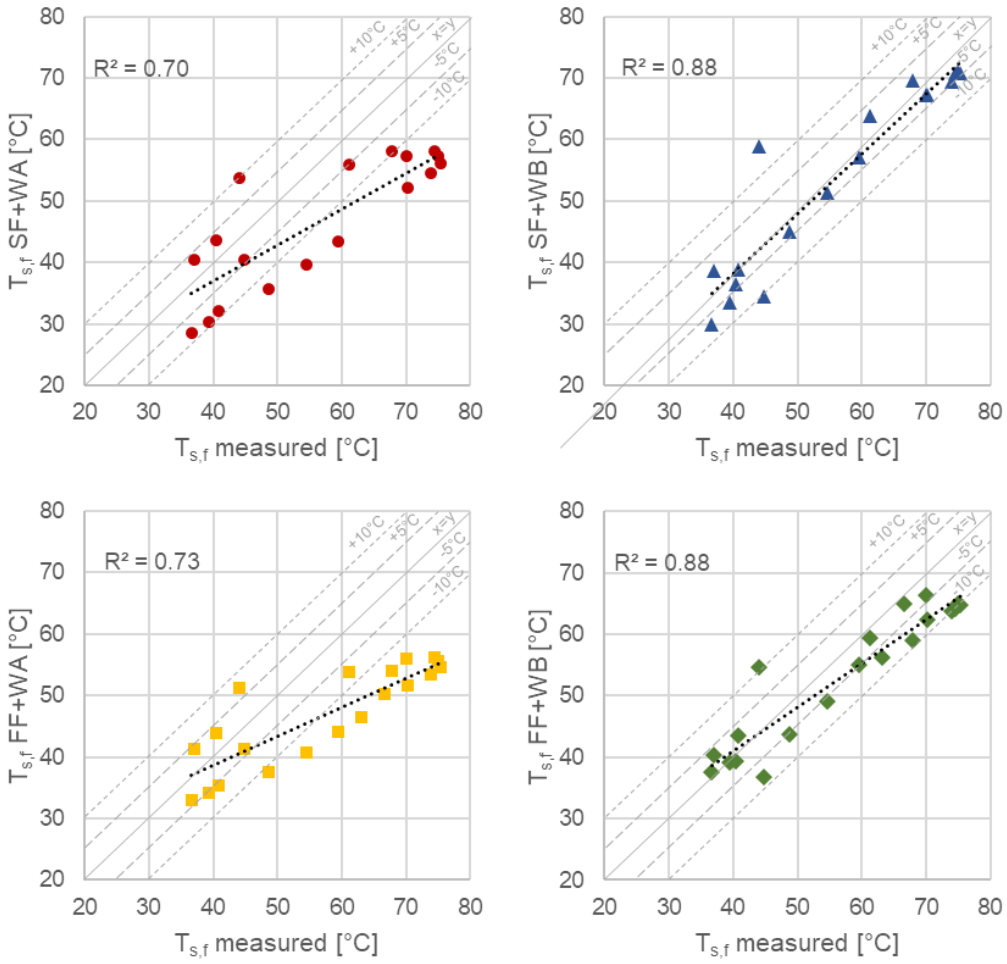

Figure 106. Scatterplots of the measured $T_{s,f}$ and the simulated ones the four simulation methods.

Table 34. Statistical evaluation metrics and error at peak of the simulated $T_{s,f}$.

	N	R^2	MAE	MAPE	RMSE	Peak Err.
$T_{s,f}$*SF+WA*	18	0.68	11.63	0.20	12.81	-19.17
$T_{s,f}$*SF+WB*	18	0.89	4.53	0.09	5.57	-4.61
$T_{s,f}$*FF+WA*	18	0.73	11.46	0.19	13.06	-20.75
$T_{s,f}$*FF+WB*	18	0.88	5.84	0.10	6.88	-10.71

As it can be noticed, SF+WA and FF+WA leads to a marked underestimation of $T_{s,f}$ before 18:00 (RMSE around 13°C and peak errors beyond -19 °C). Method SF+WB, where the approximated wall model, lead to the most reliable $T_{s,f}$ data among the testes methods (RMSE = 5.57°C, peak error = -4.61 °C), although still underestimated. The $T_{s,f}$ agreement found for method FF+WB, while being better than that of SF+WA and FF+WA, is inferior to that of SF+WB (RMSE = 6.88 °C, peak error = - 10.71 °C). Nonetheless, method FF+WB better captures sudden variations in T_{sf}, such as the one reported at 17:00. At 18:30 a $T_{s,f}$, overestimation is reported for all methods, probably caused by the shading error previously reported.

The variation of the observed and simulated $T_{s,p}$ in correspondence of P2 are shown in Figure 107. Given the limited role of radiation exchanges in the vertical directions (see Table 25), for the sake of brevity, only the statistical evaluation and peak errors are reported (see Table 35).

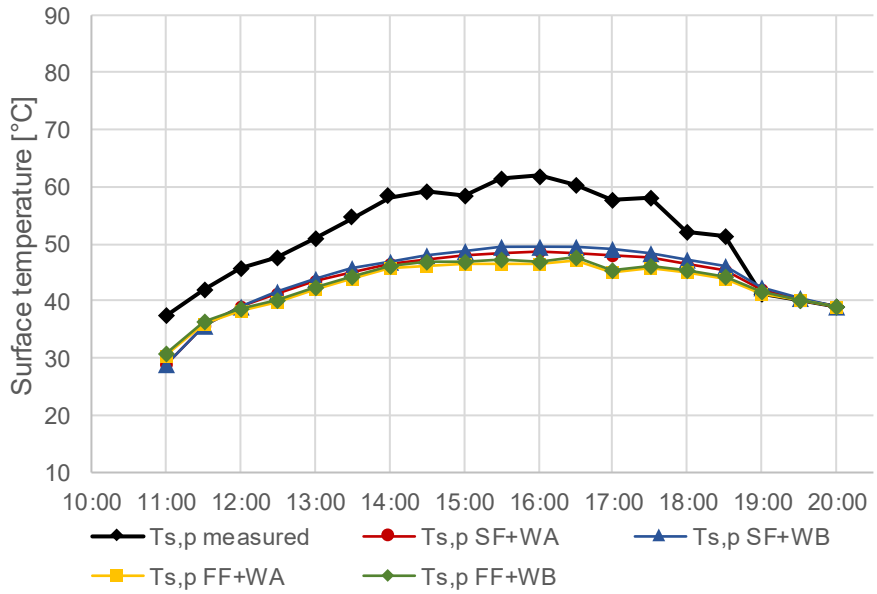

Figure 107. Comparison between measured and simulated $T_{s,p}$ trends.

The results evidence marked underestimation of $T_{s,p}$, which are slightly more reduced for simulation methods with SF with respect to those with FF. Slight variations are reported between WA and WB, probably caused by the simulated radiative exchanges between the façade wall and paving surfaces. Some previous studies have investigated the accuracy of T_s predictions. Underestimated $T_{s,p}$ have been reported

in [355], with deviations greater than 10 °C. As concerns $T_{s,f}$, the validation in [493] found limited underestimations, while good agreement is found between the measured and simulated façade surface temperatures in the validation studies in [374,491], as well as in [492] for paving surface temperatures. Nonetheless, the study in [374,491] was performed in a markedly different scenario and with milder conditions with respect to the ones of the analysis here presented: an uninsulated white façade located in Holzkirchen (Germany), resulting in much lower surface temperatures than the ones observed in this study.

Table 35. Statistical evaluation metrics and error at peak of the simulated $T_{s,p}$.

	N	R^2	MAE	MAPE	RMSE	Peak Err.
$T_{s,p}$ *SF+WA*	19	0.80	7.90	0.15	8.87	-9.55
$T_{s,p}$ *SF+WB*	19	0.81	7.44	0.14	8.32	-8.70
$T_{s,p}$ *FF+WA*	19	0.80	8.93	0.16	10.10	-12.61
$T_{s,p}$ *FF+WB*	19	0.81	8.55	0.16	9.67	-12.18

To conclude, this section reports the results of the evaluation of the accuracy of $T_{s,f}$ simulated by ENVI-met, in the case of a façade with a high solar reflectance value, i.e., 0.8, to broaden the analysis to light-colored façades.

Figure 108 reports the $T_{s,f}$ trends as measured and as modeled by WUFI (for $\rho_{sol,b}$ = 0.17). This preliminary step was performed to evaluate the matching between the measured data and the predictions of WUFI.

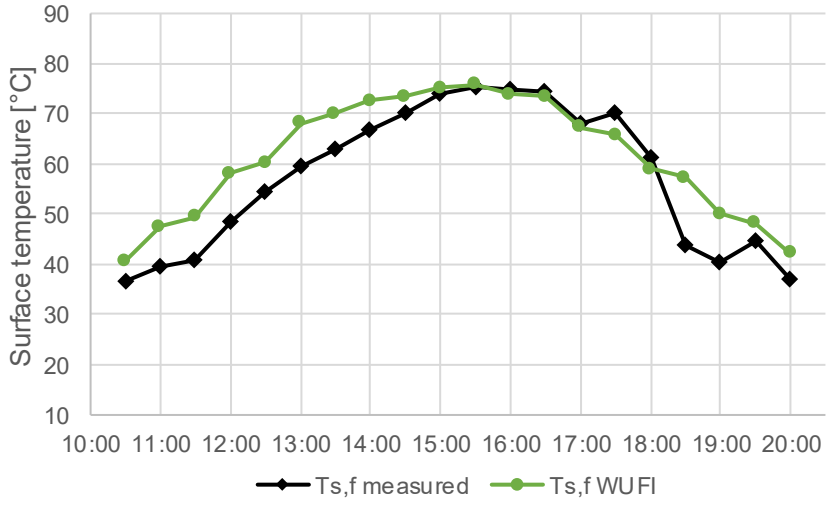

Figure 108. Comparison between the measured $T_{s,f}$ and that estimated by WUFI.

The graph highlight a good agreement of the maximum $T_{s,f}$ reached, corresponding to the time frame between 15:00 and 17:00, while the deviation during the rest of the day are likely to be caused by the non-perfect south orientation of the actual façade and by the presence of obstruction, that are neglected in WUFI.

The $T_{s,f}$ simulated by WUFI for a $\rho_{sol,fb}$ = 0.8 was compared to the one simulated by ENVI-met, as shown in Figure 109. The evaluation of the result agreement is limited to the time window between 15:00 and 17:00 (see the dashed rectangle in Figure 109), which exhibits the greatest agreement with the measured data in the actual scenario. The evaluation metrics are reported in Table 36; since the evaluation is referred to the greatest $T_{s,f}$ values and to a very limited number of data, R^2 and the peak error are not reported.

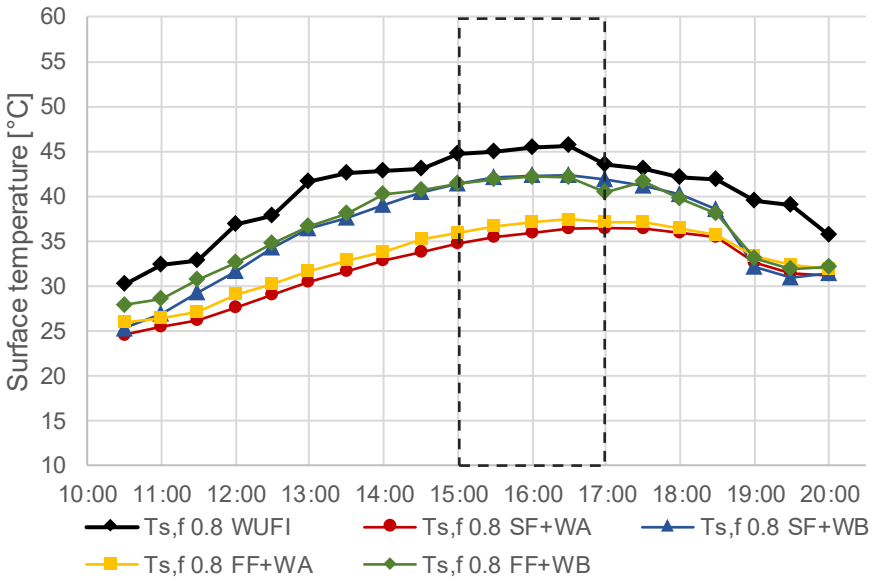

Figure 109. $T_{s,f}$ trends simulated by WUFI and ENVI-met for a $\rho_{sol,fb}$ = 0.8.

Table 36. Statistical evaluation metrics and error at peak of the simulated $T_{s,f}$ for $\rho_{sol,fb}$ = 0.8.

	N	MAE	MAPE	RMSE
$T_{s,f}$*SF+WA*	5	9.09	0.20	9.14
$T_{s,f}$*SF+WB*	5	2.90	0.06	2.96
$T_{s,f}$*FF+WA*	5	8.00	0.18	8.03
$T_{s,f}$*FF+WB*	5	3.29	0.07	3.29

As expected, a high solar reflectance value of the façade results in much lower $T_{s,f}$ than the one previously reported: the maximum $T_{s,f}$ for $\rho_{sol,fb}$ = 0.8 is 45 °C compared to the 75 °C reached by the actual façade. The results highlight that $T_{s,f}$ is underestimated my ENVI-met also in case of a "high-albedo" façade, with larger underestimations for Wall A (RMSE from 8 to 9 °C) and reduced one for Wall B (RMSE = ~3 °C). Compared to the actual façade ($\rho_{sol,fb}$ = 0.17), the magnitude of the errors is in this case reduced, coherently with the reduced $T_{s,f}$ observed for $\rho_{sol,fb}$ = 0.8.

The analysis here presented aims to shed light on how the forcing conditions and wall modeling influence the $T_{s,f}$ by ENVI-met, considering a dark colored façade (actual condition with $\rho_{sol,fb}$ = 0.17) and a light colored one ($\rho_{sol,fb}$ = 0.8). As regards

biometeorological purposes, a correct accounting of the T_s is crucial to correctly estimate the longwave radiative exchanges between the considered surface and the human body, which contribute to T_{mrt}.

Nonetheless, the environmental parameters influencing outdoor thermal comfort are numerous and interconnected, as are those influencing surface temperature. Indeed, several modeling aspects influence the estimated T_s, and go beyond those here accounted, i.e., the forcing conditions and the wall model. Among these aspects, the amount of shortwave radiation being reflected/absorbed by the surface determines $T_{s,f}$ to a great extent, while also influencing T_{mrt} and outdoor thermal comfort. Therefore, a correct accounting of T_s, despite being essential to outdoor thermal comfort estimation, should be contextualized among the other many influencing factors to understand the overall impact on outdoor thermal comfort.

Validation of directional radiative contributions

The six-directional calculation of T_{mrt} in ENVI-met allows to investigate the radiative contributions in the different orientations. Therefore, in this section the measured and simulated directional shortwave and longwave irradiances are compared to better shed light on the predictions of T_{mrt}, $T_{s,f}$ and $T_{s,p}$.

The measured and simulated directional longwave irradiances (L) are reported in graphs in Figure 110 for P1 and in Figure 111 for P2. L values provide an indication on the T_s of the surrounding elements "seen" by the sensors in the different directions (considering that most construction materials have ε = ~0.9).

Regardless the position, the simulated L are underestimated to different extents, depending on the direction considered. The greatest underestimation is reported for L_{north}, especially for simulation method with WA, consistently with the $T_{s,f}$ underestimation already discussed. The underestimation of L_{down} can be linked to the observed $T_{s,p}$ underestimation, while that of L_{south} may be caused by the presence of the "Single Wall" in its view, whose simplified modelling neglects the emitted longwave radiation, which can be one of the source of underestimation also for L_{east}, L_{west}. The other longwave irradiances, i.e., L_{east}, L_{west} and L_{up}, exhibit less marked underestimations, especially in the case of simulation methods with FF, which include a more detailed description of the forcing conditions. Moreover, the good matching found for L_{up} suggests that the atmospheric infrared radiation was satisfactorily modelled by ENVI-met, especially for the simulation with FF.

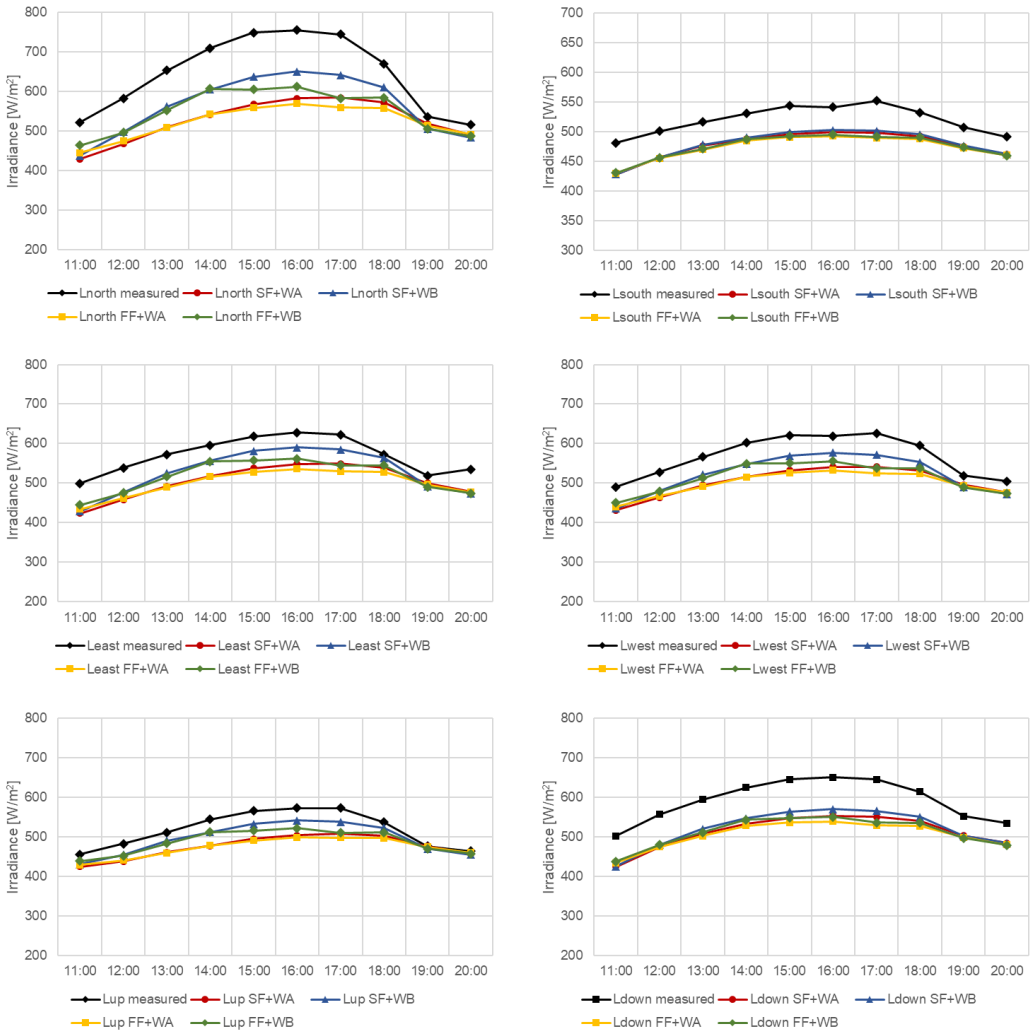

Figure 110. Measured and simulated longwave irradiances in the six directions in P1.

ENVI-met outputs for the shortwave irradiances (K) in the six directions are referred to the reflected fraction only and therefore are generally not comparable to the measured directional shortwave irradiances [370], which include also direct and diffuse solar irradiances. Nonetheless, the measured and simulated, K_{north} and K_{down}, that refer to the orientation towards the façade and the paving, can be considered comparable to each other in P1. Indeed, the proximity of the sensor to the two surfaces and the negligible sky view factor, makes in these orientations the influence of direct and diffuse radiation minor with respect to the reflected shortwave radiation. The same can be considered valid in P2 for K_{down} but not for K_{north}, given the greater distance from the façade that makes the measured K_{north} more affected by direct and diffuse irradiances. Based on these considerations, the graphs in Figure 112 plot K_{north} and K_{down} in P1, while only K_{down} is reported for P2 (see Figure 113).

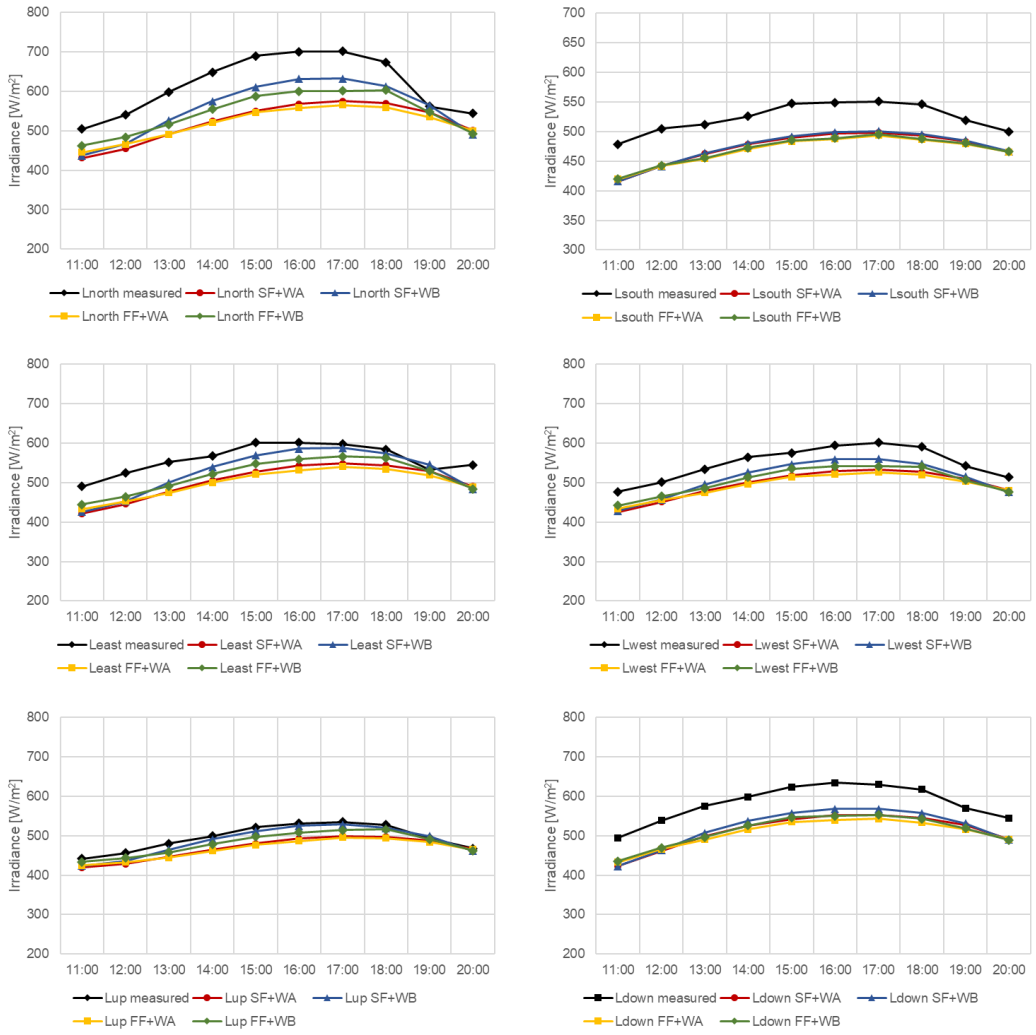

Figure 111. Measured and simulated longwave irradiances in the six directions in P2.

The results evidence that the simulated K_{north} (i.e., reflected by the building façade) are equally overestimated for the four simulation methods. As concerns K_{down}, an overall good agreement with measured data is reported, with only slight overestimations. The simulated shortwave irradiance obtained with the FF are comparable to those obtained with SF, despite SF is based on a predefined global solar irradiance profile to be weighted and FF requires a separated definition of the direct and diffuse components, with a higher temporal resolution. This seems to suggest that the decomposition of global irradiance in the direct/diffuse component performed in SF matches the one observed.

As expected, no difference is found between simulations with WA and WB, since while the forcing conditions were different between SF and FF, while ρ_{sol} of the paving and façade wall was unaltered between WA and WB.

The overestimation of the reflected solar radiation from the façade direction suggest a corresponding underestimation of the solar radiation being absorbed by the façade, which is expected to be among the cause (if not the primary one) of the $T_{s,f}$ underestimation previously evidenced. It must be therefore here highlighted that, if this issue related to shortwave radiation will be addressed in future ENVI-met version,

the validity of the indication related to wall modelling (i.e., Wall A and B) influence of $T_{s,f}$ accuracy need to be reassessed.

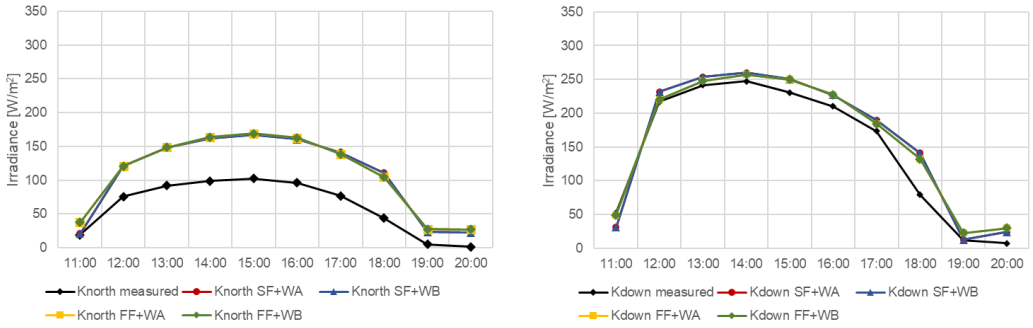

Figure 112. Measured and simulated shortwave irradiances in P1.

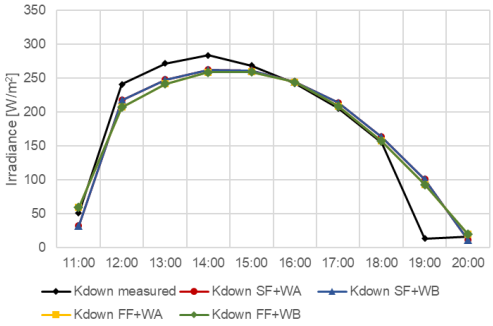

Figure 113. Measured and simulated shortwave irradiances in P2.

For a more detailed accounting of the agreement between simulated and measured directional irradiances, the calculated statistical parameters for SF+WA, SF+WB, FF+WA and FF+WB are reported in Table 56, Table 57, Table 58, Table 59, respectively, in Appendix 5B.

Outdoor thermal comfort assessment

The graph in Figure 114 shows the calculated PET trends in P1, along with the indication of the thermal perception corresponding to the PET ranges, as defined in [510]. The PET used as reference is based on in-situ measured data, while those referred to the simulation methods are based on the simulated T_a, T_{mrt}. (see § 5B.4.5).

All the PET trends are well above the threshold of the "very hot" thermal sensation, which corresponds to extreme heat stress, for most part of the day, i.e., from 11:30 to 18:00 (or 18:30 in the case of simulated PET).

As it can be noticed, the reference PET trend is generally greater than the one based on simulated data, with difference up to ~8 °C. This is likely caused by the T_{mrt} underestimation, which is reflected in the PET values. Indeed, PET values present a strong sensitivity to T_{mrt}, especially in sunlit locations, and past studies have evidenced a linear relationship between the two parameters [346,487].

The analysis in [355] similarly found that the PET values calculated based on ENVI-met simulation outcome were underestimated, with divergences (for the most comparable location) quite in line with those found here.

Overall, this results evidence that the underestimations in T_{mrt} values impact to a noticeable extent the calculated PET values, highlighting that in the case under consideration ENVI-met predictions failed at capturing the actual thermal stress conditions observed in the area during the measurement campaign.

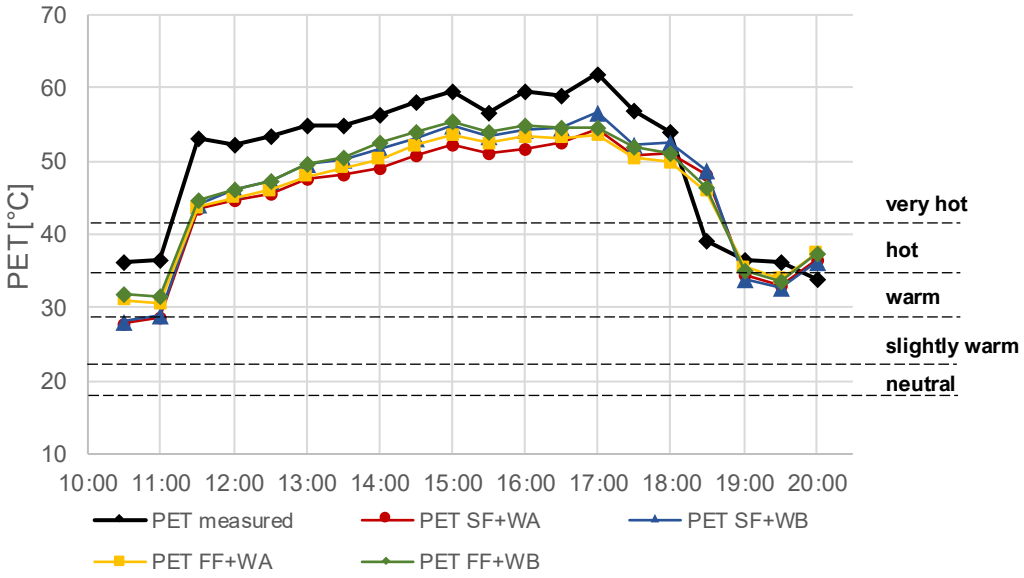

Figure 114. PET trends calculated from measured and simulated environmental parameters.

5B.6. Conclusions and further work

In this Chapter, a validation study was performed to evaluate ENVI-met ability to correctly predict T_a and T_{mrt} close to a dark-colored façade under extreme hot weather conditions. The contribution compares the result obtained by ENVI-met (v5.0.3) following four modeling approaches with in-situ measured data and analyses their impact on PET. The study includes the evaluation the façade and paving T_s and the directional radiative fluxes, and a model intercomparison to evaluate T_s reliability also for a light-colored façade. Additionally, the study compares the T_{mrt} results obtained with the globe thermometer and IRM and evaluates the sensitivity of T_{mrt} to the distance to the façade.

In this study no marked differences were found between T_{mrt} values obtained with IRM and globe thermometer, although further investigations are needed, considering a larger number of observations. The T_{mrt} values at the two distances from the façade, i.e., 0.75 and 2.25 m resulted comparable to each other.

ENVI-met simulations were found to underestimate T_{mrt}, $T_{s,f}$, $T_{s,p}$ and the directional longwave fluxes (L), while overestimations were found for the reflected shortwave irradiances (K). The simulation run using full forcing (FF) reported improved accuracy for T_a, although no improvement was reported in this analysis for T_{mrt} and T_s, for which simple forcing resulted in greater agreement. The T_{mrt} and T_s agreement was found to increase for the approximate wall model (Wall B) compared to the detailed one (Wall A) with no effect on T_a. $T_{s,f}$ underestimations were found also for a light colored façade,

although their magnitude was limited in comparison to those reported for the dark colored façade.

Overall, the results suggest that ENVI-met was not able to correctly predict T_{mrt} in the considered scenarios, evidencing marked underestimations that impacted the predictions of the thermal sensation (PET values).

The study presented in this Chapter is referred to an urban scenario in absence of vegetation. This work can be extended by evaluating ENVI-met's ability to predict the effect of greening (e.g., trees, green walls), which are among the most effective strategies to improve outdoor microclimatic conditions. Moreover, further investigations may include longer measurement campaigns with larger numbers of observations, the considerations of various urban scenarios and milder weather conditions, the measurement of downwelling infrared radiation to set the forcing conditions, and the use of new ENVI-met releases, given the continuous development of the tool.

Acknowledgements

The author is grateful to Stefano Fantucci and Giorgia Autretto for the precious contribution during the measurement campaign and guidance in the results analysis, and to Gabriele Piccablotto, Pierpaolo Nuzzo and Leonardo Catalano for their support.

5B.7. Chapter Nomenclature

a_k	Absorption coefficient of the human body for shortwave radiation (IRM)	[-]
a_l	Absorption coefficient of the human body for longwave radiation (IRM)	[-]
a_{sol}	Absorption coefficient for shortwave radiation	[-]
c	Specific heat capacity	[J/kgK]
h_{cg}	Convection coefficient of the globe thermometer	[W/m^{2}K]
K_i	Shortwave irradiance in direction i	[W/m^2]
L_i	Longwave irradiance in direction i	[W/m^2]
RH	Relative humidity	[%]
S_{str}	Radiation flux density	[W/m^2]
t	Thickness	[m]
T_a	Air temperature	[°C] [K]
T_g	Globe temperature	[°C]
T_s	Surface temperature	[°C]
T_{mrt}	Mean radiant temperature	[°C]
$T_{s,f}$	Outer surface temperature of façade	[°C]
$T_{s,p}$	Outer surface temperature of paving	[°C]
w	Wind speed	[m/s]
W_i	Weighting factors for direction (IRM)	[°C]
δ	Density	[kg/m^3]
ε	Emissivity	[-]
ε_p	Emissivity of the human body	[-]
λ	Thermal conductivity	[W/mK]
ρ_{sol}	Solar reflectance	[-]
$\rho_{sol,fb}$	Solar reflectance of façade basement	[-]
$\rho_{sol,p}$	Solar reflectance of paving	[-]
ρ_v	Visible reflectance	[-]
σ	Stefan-Boltzmann constant	[W/m^{2}K^4]

Chapter 6

Parametric study on acoustic and thermal comfort in different urban scenarios

Objective	To test the effect of green wall application in different urban settings on both acoustic and thermal comfort conditions
Outcome	8 urban settings were tested, each considered with 4 green wall configurations and a reference scenario, with conventional materials were used (sound reflective and with a light or dark appearance)
Highlights	• Greater *SPL* are reported in denser urban settings. Nonetheless, in such scenarios *SPL* reductions provided by green wall applications are the greatest. Green walls can reduce *SPL*s in their proximity, although in dense scenarios reductions are reported also over the untreated building on the opposite side of the road. • The corner is the least thermally comfortable scenario, combining reduced wind speed with limited shade. The courtyard and the street are the most comfortable urbans settings for pedestrians. • The analysis highlights a complex and potentially conflicting interrelation between acoustic and thermal comfort goals, evidencing the importance of a combined consideration of the two aspects.

6.1. Overview and motivation

This Chapter presents a parametric investigation of outdoor acoustic and thermal comfort in different urban scenarios, where the effectiveness of green walls on improving outdoor conditions is evaluated.

Green walls are reported to jointly reduce environmental noise levels and improve outdoor thermal comfort in urban areas. They are flexible solutions that can be implemented in both newly built scenarios and in existing ones, as retrofit interventions. While acoustic and thermal aspects were considered in an independent way in the previous Chapters, the study in this Chapter presents an attempt at a combined approach where the two realms are jointly evaluated. The goal is to provide a preliminary understanding of the urban scenarios in which green walls can provide sensible improvements to outdoor comfort conditions, evidencing also potential agreements or conflicts between acoustic and thermal goals. The importance of a multidisciplinary approach to comfort evaluation has been highlighted in several studies related to indoor [511,512] and outdoor [513,514] environments. The study presented in this Chapter can be considered a preliminary simulative investigation on the effectiveness of green wall application with respect to outdoor acoustic and thermal comfort. The tested scenarios range from an isolated building to an urban courtyard, and each is considered with different dimensions, to provide the reader with a set of urban configurations large enough to gain some understanding of green wall effectiveness in a wide variety of scenarios.

While the original analysis was performed by combining different form and material configurations of the urban fabric as concerns both acoustic and thermal comfort, in light of the findings of the validation study in Chapter 5B, only the results of the form variations are analyzed for thermal comfort aspects.

The content of this Chapter has been partly included in "*Parametric study on outdoor acoustic and thermal comfort in different urban scenarios",* submitted for presentation at IC2UHI 2023 Conference, authored by Elena Badino, Louena Shtrepi, Arianna Astolfi and Valentina Serra.

A part of the research contribution in this Chapter and Appendix 6 was conceptualized and partially developed during the visiting period at Henning Larsen (Copenhagen, Denmark).

6.2. Introduction

Cities are complex environments composed of a wide variety of urban settings, from open areas such as squares to dense urban scenarios, such as narrow streets, each of which with its own form, dimensions, and material specifications. Given the distinct character of these spaces, it is considered important to evaluate how the effectiveness of certain design strategies to improve outdoor comfort conditions are affected by the urban settings in which they are applied.

Among the various strategies that can be implemented in cities, green walls are reported to combine benefits with respect to both acoustic and thermal comfort aspects. Green walls can be applied to new and existing buildings, making them flexible solutions that can be implemented in already defined urban environments.

Green walls refer to systems that enable the greening of a vertical surface [515]. They can be divided in “green façades” and “living walls”, where the former refer to the use of climbing plants that grows against a wall, while the latter refer to modular or continuous growth along the wall surface (i.e. pre-vegetated sheets attached to wall or frame) [515,516]. Compared to green façades, living walls require some essential materials such as supporting elements, growing substrate and irrigation system to maintain various plants; on the other hand, living walls usually perform better than green façades owing to pre-cultivated plants and transferability. Comprehensive reviews on green walls are presented in [515,516].

The integration of greenery systems to buildings in cities can potentially increase the quality of urban environments from different standpoints, among which are the reduction of environmental noise, the mitigation of microclimatic conditions and the increase of the energy efficiency of buildings [51,515,517]. Moreover, the presence of greenery has a beneficial psychological impact on urban dwellers, enhances the visual aesthetics of the cities, and raises real estate prices [51,516,518].

Plants absorb solar radiation to develop their biological functions. Since the evapotranspiration process cools both the plant foliage and the ambient air around them, it can lead to milder microclimatic conditions in its proximity during the hot season [517,518]. Indeed, greenery systems for roofs and walls are considered to be one of the most appropriate sustainable solutions to mitigate the urban heat island (UHI) [516]. Moreover, green walls and roof contribute to a reduction of heat gain and losses of the building envelope by screening the exterior wall from direct solar radiation and wind, and increasing the overall thermal insulation of the envelope [517]. In addition, vertical greenery systems can mitigate noise pollution and improve acoustic comfort conditions in both outdoor and indoor settings thanks to their sound absorbing properties and by increasing the wall’s sound insulation [466,519,520].

According to [51], the UHI mitigation potential of greening systems is influenced by the following variables: a) climatic conditions (solar radiation, outdoor air temperature and humidity, wind and precipitation); b) radiative properties (surface‘s reflectance and emissivity); c) thermal properties (thermal capacity and thermal transmittance); e) and hydrological variables (latent heat loss through evaporation by plants and soil). In [58,59] the effects of green walls on outdoor thermal comfort were tested. In [59] a reduction of 2°C in T_{mrt} was measured in front of a green façade in comparison to a light-colored bare wall. According to the simulation study in [58], outdoor thermal comfort can be locally improved by green walls, while their effect is negligible at more than 3 m of distance. The study also reports that the greatest benefits for pedestrian’s thermal comfort are provided by the lowest portion of the green wall (i.e., 4 m), while above this height the influence is significantly reduced. In [521] measurement in a scaled mock-up of building and streets found an air temperature variation up to 5°C inside the building and up to 1°C outside the building, considering a street canyon with a green wall on one street side. In [522] a marked

difference in exterior surface temperature was observed, with the green wall reporting a value up 23 °C lower than a reference wall during a sunny summer day.

With respect to acoustics, vegetation can reduce sound levels by means of four mechanisms: a) sound scattering by plant elements, b) sound absorption by vegetation (leaves and soil), c) ground effect [523]. According to [519,524], most previous studies have mostly focused on horizontal greening (ground and roof), while relatively scarce attention has been given to vertical one.

Green wall elements have been investigated with respect to their sound absorption [466,519,520,524] and sound insulating performance [519,524]. A systematic analysis was performed in [466] using the reverberation chamber to assess the contribution of different factors on the sound absorbing and sound scattering coefficients of vegetation (soil depth, soil moisture content, vegetation coverage), showing that the greatest contribution on sound absorption is provided by the soil layer, while the presence of greening further increase sound absorption, especially at higher frequencies. The measurement campaigns in [520,522,524] confirm this trend, evidencing the excellent sound absorption performance of soil layer and greening.

The noise reduction potential of sound absorbing materials applied on urban facets has been object of several previous studies [17,107,122], making green wall promising solutions to contribute to environmental noise mitigation. It must be however highlighted that, ultimately, the acoustic performance of green walls can be comparable to those of conventional sound absorbing materials. Despite this type of materials are conventionally developed for indoor applications, some solutions suitable for outdoor application are available on the market. A database of materials suitable for outdoor use is reported in Appendix 6, along with the octave band and weighted sound absorption coefficients [158]. The database was developed during the visiting period at Henning Larsen in the attempt to collect information of different material options suitable for outdoor application and support designers in their selection. Although not comprehensive, the database collects some conventional building construction materials, that typically exhibit sound reflective properties, and commercial sound absorbers, in the attempt to collect some potential material solutions and ease the performance comparison among them. While the sound absorbing performance of the collected materials are diverse and may differ significantly from that of the green wall analyzed in the following, the analysis reported in this Chapter can still provide some general indications on the effectiveness of sound absorbing façade treatment in different urban scenarios.

Given the multisensory nature of comfort and the complex interrelationships among various sensory stimuli [511,512,525], the study of the effect of certain design strategies on multiple comfort aspects can be considered of interest, although further investigations are needed to assess the resulting overall comfort conditions.

The objective of this study is to assess the effect of green walls on outdoor thermal and acoustic comfort conditions. In light of their multifaceted performance, green walls can be considered a very promising solution to improve microclimatic conditions in summertime and reduce environmental noise levels in cities. The effectiveness of

their application is investigated, considering different urban settings and green wall configurations, to evidence the scenarios in which such strategies can lead to the greatest benefits in terms of outdoor acoustic and thermal comfort conditions and to evidence potential discordances between the considered performance goals emerging from certain design strategies.

6.3. Method

The outdoor acoustic and thermal comfort conditions are simulated for a set of urban scenarios, where living walls are applied in different configurations over the building façades. The method followed to define the pool of urban settings, and to set-up the performance simulations are detailed in the following.

6.3.1. The urban settings

In order to investigate the effectiveness of the application of green walls to improve outdoor acoustic and thermal comfort, a parametric investigation was performed, in which green walls were tested in different urban settings, considered representative of typical European cities. The configurations considered, combining different green wall configurations applied to eight urban settings are summarized in Figure 115.

In the study the application of green walls is considered for in an isolated building (IB), a corner (CR), a street canyon (ST) and a courtyard (CY), considering the above-mentioned scenarios with different widths (i.e., 10 m or 20 m). The width of the building is set at 30 m and their height at 20 m, corresponding to 6 floors above ground. Besides the different urban settings, different green wall configurations were investigated for each urban setting. The green wall was applied to the entirety of both building façades (T) and of one façade only (O), and either on the ground floor (L) or upper floors (U) of both façades. All these material configurations were compared to a reference one (R), where the façades of the buildings have a conventional finishing solution. From the acoustic point of view, the reference material behaves as a sound reflective surface, i.e., as most of conventional construction materials. From the microclimatic point of view, the reference material is plaster (i.e., a high emissivity surface) and two solar reflectance options are tested, representing a light and a dark colored appearance.

To provide a realistic accounting of actual urban environments, the virtual model exhibits a regular pattern of windows (shown in Figure 116), which is omitted for simplicity in the scheme in Figure 115.

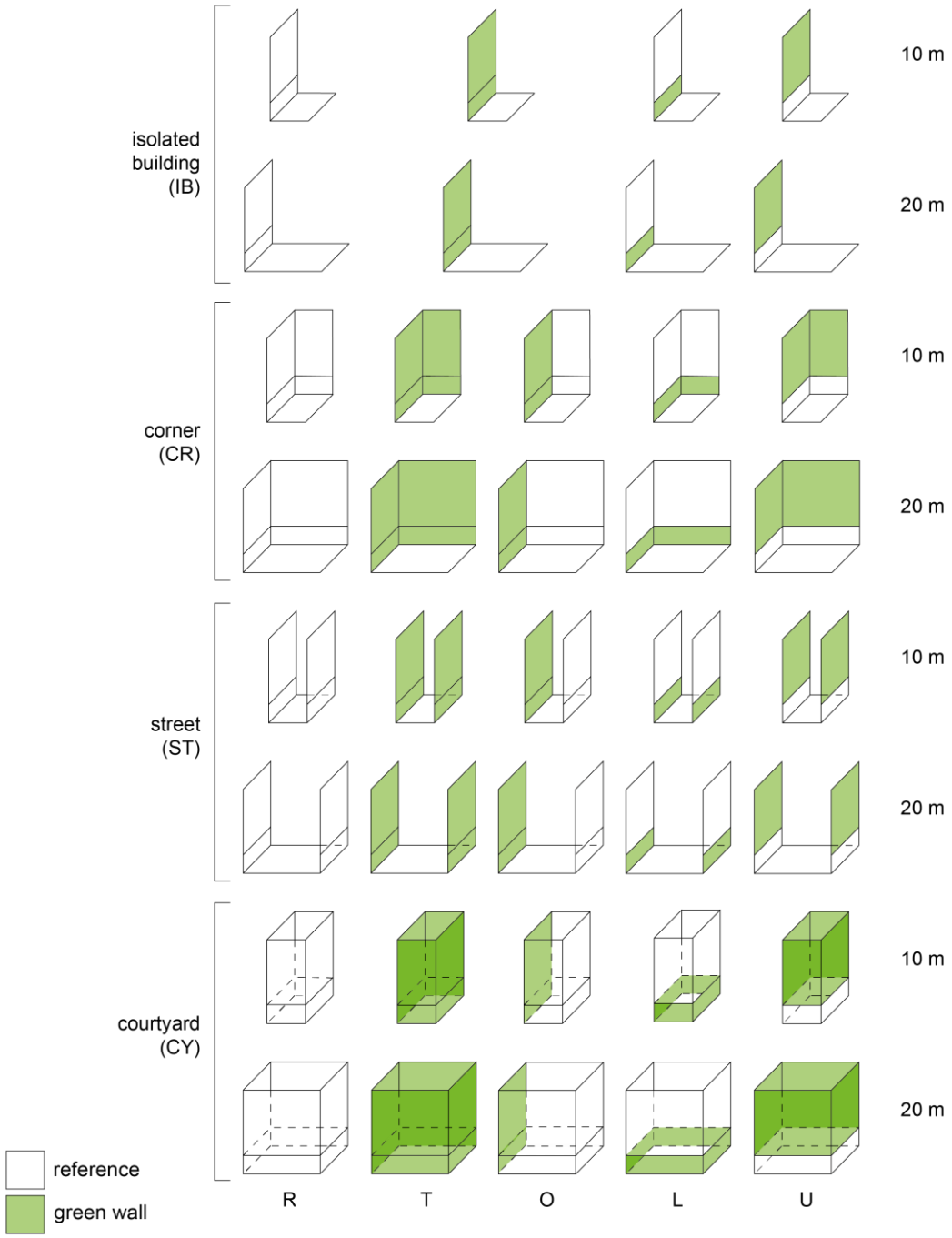

Figure 115. Scheme of the urban settings tested with the various material configuration. The identification codes of the urban settings and material configurations are also provided.

6.3.2. The acoustic simulation set-up

The acoustic simulations were run with Pachyderm v 2.0.0.2, with a transition order (TO) of 2, the number of rays automatically set by the tool based on results convergence and a cut-off time of 2000 ms. A preliminary sensitivity test was performed to select the simulations settings, by changing the TO and cut-off time, finding negligible differences with TO equals to 2 and a cut-off time of 3000 ms.

Three omnidirectional point sources were used to represent vehicular traffic noise, that is the most relevant noise source in urban areas [72,73]. The sound sources were set 10 m apart at a height of 0.3 m above the ground [481], along the street centerline. Each source was set according to the normalized traffic noise spectrum of EN 1793-3:1998 Standard [482] with a sound power level (*SWL*) of 75.7 dB. The octave band *SWL* for each point source is detailed in Table 37.

Table 37. Octave band sound power level of the vehicular noise sources

	Octave-band *SWL* [dB]								
	63	125	250	500	1000	2000	4000	8000	overall
Vehicular traffic	60.7	60.7	65	68	71.3	68.7	63.7	63.7	75.7

Based on the limited length of the urban configurations tested, the receivers are set at its center to minimize the edge effect. The same approach was followed in [107], where a sensitivity test on *SPL* variation as a function of street length is reported. The receivers were set at a central position over the façades of the two opposite buildings, one for each floor, located at the barycenter of the windows at 2 m distance from the façade plane. For clarity, an example of the virtual model (referred to the ST configuration with a width of 20 m) with sound sources and receivers' position is shown in Figure 116.

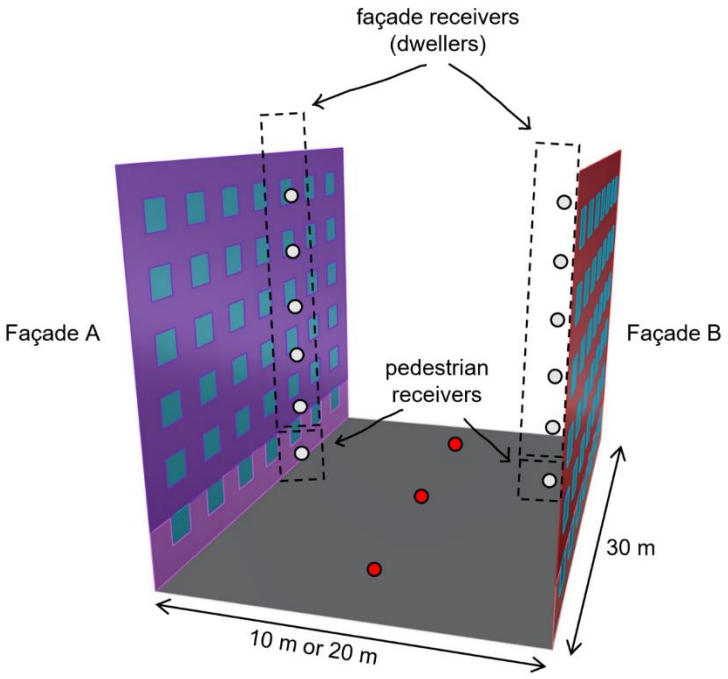

Figure 116. Example of virtual model of the urban setting with the positions of the sound sources (red dots) and sound receivers (white dots). The proposed virtual model is ST20 (20 m-wide street)

A preliminary test was run by comparing the sound pressure level (*SPL*) results of 3 receivers on each floor (located in the correspondence of the 3 central windows)

with those obtained by the central window only; since the results were negligible, only the central receiver was considered. For simplicity the two façades are identified as "Façade A" and "Façade B" (see Figure 116). In the material configuration O, where the green wall is applied to a façade only, it is applied to Façade A. The receivers located at the ground floor of both buildings are used to gather data on pedestrians' comfort, while those from the 1st to the 5th floor of the buildings to describe the comfort conditions of dwellers or building users, and are considered separately for the two façades.

The acoustic properties of the green wall are defined according literature resources for a 10 cm thick substrate [520], and those of the reference are referred to a standard brickwork [465]. The octave-band sound absorption coefficients (α) and sound scattering coefficients (s) of the bricks and green wall and are detailed in Table 38. The acoustic properties of the remaining urban surfaces, i.e., the street paving and the windows (respectively referred to rough concrete and double glazing) are taken from the material database in [444].

Table 38. Octave band sound absorption coefficient and sound scattering coefficient [-] of the brickwork and green wall. *unavailable data, assumed equal to measured data in the closest octave band.

		Octave-band center frequency [Hz]							
		63	125	250	500	1000	2000	4000	8000
Green wall	α	0.39*	0.39	0.90	1.00	1.00	1.00	1.00	1.00*
	s	0.05	0.05	0.05	0.05	0.05	0.08	0.20	0.40
Reference material	α	0.05*	0.05	0.04	0.02	0.04	0.05	0.05	0.05*
	s	0.05	0.05	0.05	0.05	0.06	0.07	0.10	0.15

While the analysis is performed considering the above-mentioned materials, it must be aware that ultimately the green wall performs as a "generic" highly performing broadband sound absorber and the brickwork as a sound reflective material (as most construction materials). Therefore, the trends of *SPL* variations reported for the green wall can also provide indications on other types of sound absorbing materials suitable for outdoor application with similar acoustic properties (porous concrete, etc.).

The acoustic parameter used to quantify acoustic comfort is the A-weighted *SPL* [dB(A)], which accounts for the frequency-dependent sensitivity of human ear. The analysis was conducted considering the *SPL* variation over the façade, considered indicative of acoustic comfort for dwellers, and at the ground floor, i.e., for pedestrians, separately. As concerns façade values, the analysis is performed on a floor basis and with respect to the average *SPL* variation found over the façades. For each urban setting, the *SPL* variation was evaluated with respect to the reference scenario with sound reflective façade materials.

The difference found between the simulated *SPL*s are discussed on the basis of the JND_{SPL}, which equals to 1 dB according to ISO 3382-1:2009 Standard [238], and on the 3 dB threshold reported in [471,472] that is associated to a "just perceptible" change in apparent loudness.

6.3.3. The microclimatic simulation set-up

The microclimatic simulations were performed with ENVI-met version 5.0.2. The calculations were carried out for July,11 2021, considered a typical summer day in Turin with a clear sky. The boundary conditions data was gathered from the meteorological station of the Regional Agency for Environmental Protection (ARPA Piemonte) in Via della Consolata, which is in Turin city center.

The forcing conditions were set using simple forcing (hourly data for air temperature and relative humidity and single values for wind speed and direction, see Chapter 5B for further details). The hourly variation of air temperature (T_a), relative humidity (RH) and wind speed (w) measured by the weather station are shown in Figure 117. The single value used to set the wind speed, wind direction and global solar irradiance are shown in Table 39.

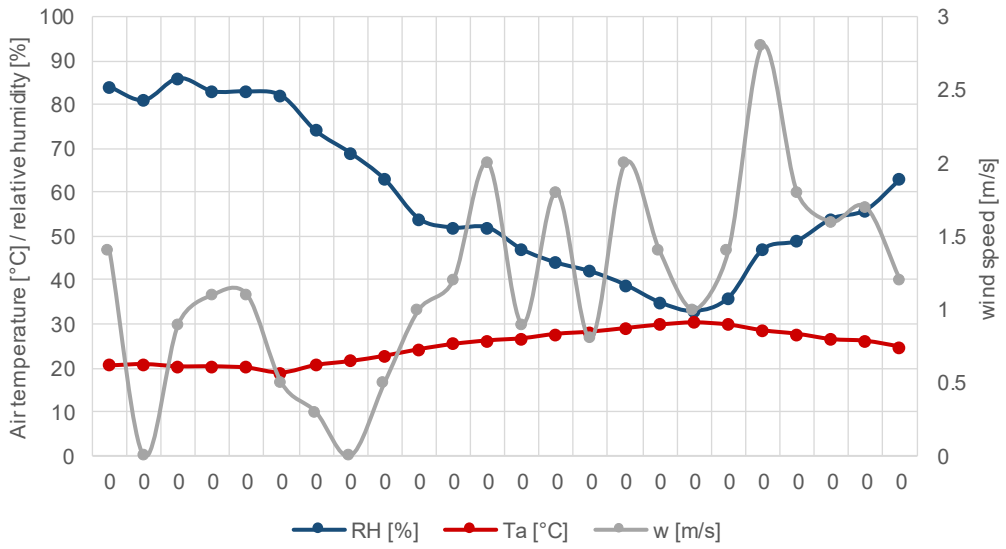

Figure 117. Boundary conditions measured on an hourly basis by the weather station.

Table 39. Single values used to set the environmental boundary conditions for the simulation.

w [m/s]	wind direction [° from North]	adj. factor for solar irradiance [-]
1.18	114	0.89

In line with the approach applied in Chapter 5B, the simulations were run for 48 h to allow for model initialization, with simulation results gathered in the last 24 h. The IVS mode was enabled to allow for site-specific radiative exchange modeling, with finer resolution up to 20 m. The calculation of mean radiant temperature (T_{mrt}) was performed following the six-directional approach (see Chapter 5B).

The model domain is composed of 1.6x1.6x2 m cells, with the lowest ones subdivided into 5 sub-cells along the z-direction to have a greater resolution at pedestrian level. A telescoping factor of 10% was applied above the height of 21 m. The model domain is composed of 25 (or 35 cells for the courtyard) x 30 cells on the xy plane and 22 cells in the z direction. Six nesting grids were set around the model domain to minimize the edge effect.

For the purpose of the analysis, the configurations are set with Façade A set as perfectly south oriented. An example of the virtual model in ENVI-met (the 20 m wide street with material configuration U) is shown in Figure 118.

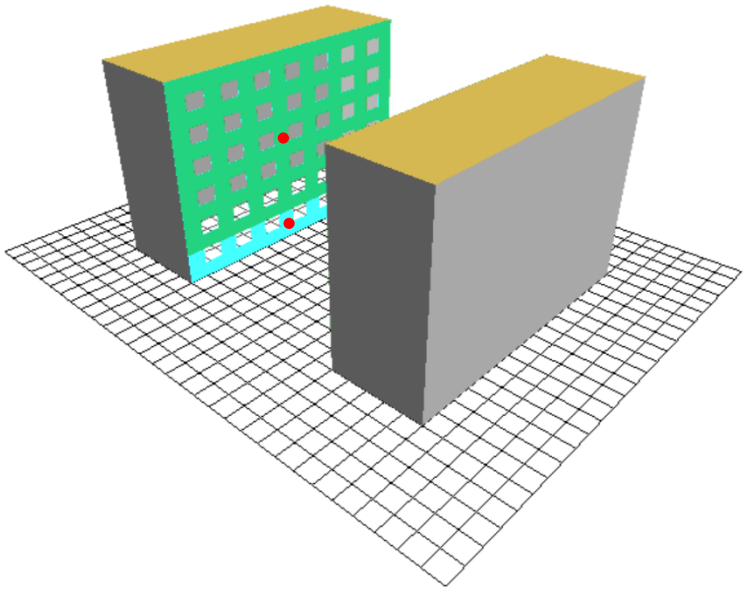

Figure 118. Screenshot of the virtual model in ENVI-met. The example is referred to ST_20m_U configuration (the 20 m-wide street with green wall on the upper portion of the façades). The red dots mark the calculation positions.

The material properties of the green wall and reference wall material are based on the pre-set default materials in ENVI-met material database named “Default wall - moderate insulation” (0100MI) and “green + mixed substrate” (01NADS), whose stratigraphy is shown in Figure 119.

The reference wall was considered with a solar reflectance of either 0.3 or 0.7 of the outer layer, identified as R03 and R07, respectively, to account for dark and light colored appearances of the façade wall. Therefore, the overall number of simulated scenarios is 68, resulting from the combination of the urban settings with the different material configurations (for the isolated building, one configuration was tested, being the scenario invariant with respect to its width).

The paving material is set according to the default material “Concrete Pavement Gray” (0100PG) and that of the windows according to “Heat protection windows (one air layer)” (0100GH).

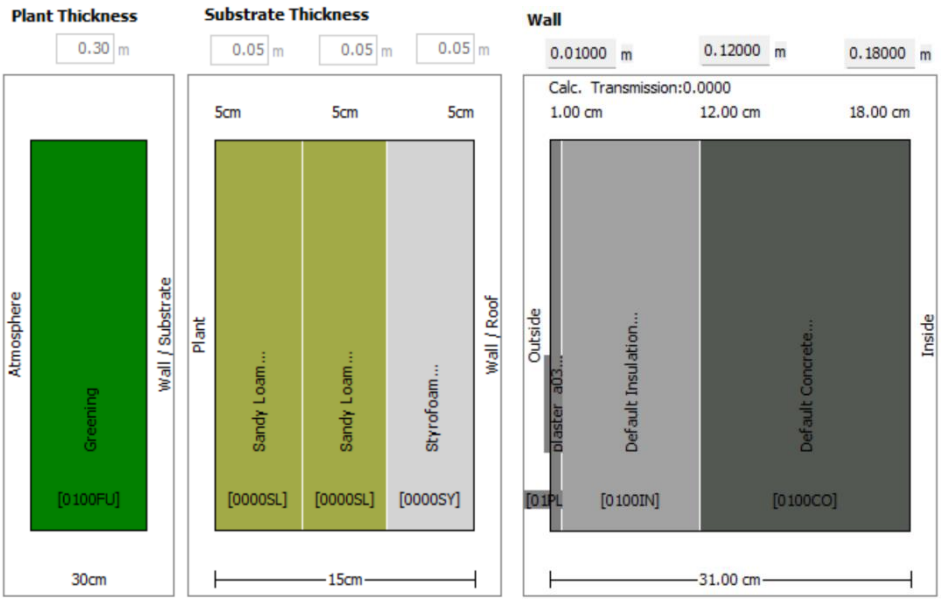

Figure 119. Screenshot of the ENVI-met interface with the stratigraphy of the green wall and reference wall.

Two calculation point positions are defined, one for pedestrian comfort and one for comfort conditions in the façade (see Figure 118). This latter position can provide some indication for small balconies (despite the balconies are not modelled in ENVI-met). Both calculation points are located close to the south facing façade i.e. Façade A, at a distance of 0.8 m from it, and are at either 1.1 m from the ground [26,328] or in a central position over the façade (4th floor). The calculation points are only referred to the south facing façade as it sunlit during the day and is the most critical one with respect to thermal stress conditions (the opposite one is shaded during the central hours of the day).

The thermal comfort conditions were described using the Physiological Equivalent Temperature (PET) and the T_{mrt}, which is the most important environmental variable affecting outdoor thermal comfort [26,328,346,348,487]. The PET calculation is performed using BIO-met for a standard person, i.e., for a 35-year-old man, with the following parameters: height = 1.75 m; weight = 75 kg; static clothing insulation = 0.9 clo; work metabolism = 80 W.

As a preliminary step, a sensibility test was run to define how much the modeled urban scenario's dimensions influenced the predicted outdoor thermal comfort conditions. Indeed, given the number of urban scenarios to be simulated and the computational time required for each of them, it was crucial to define the model dimensions to ensure accurate simulation results at a reasonable computation time.

The sensitivity analysis was performed on the street canyon configuration with a width of 20 m (ST_20) which was considered the most critical urban scenario where to assess the edge effects on the simulation results. The comparison was performed with respect to the PET value and the T_{mrt} predicted in a central position close to the south-facing façade at a height of 1.1 m from the ground. Two simulations were performed, one with a street length of 30 m, and one of 90 m. All the simulation settings were kept constant in the two tested conditions. The difference between the

simulated values was quantified as the mean and peak values of the absolute difference between the predicted hourly T_{mrt} and PET values between 6:00 and 20:00. The PET exhibited a mean difference of 0.4 °C and a peak difference of 2.6 °C at 8:00; the T_{mrt} values exhibited a mean difference of 1.5 °C and a peak difference of 6.3 °C at 8:00. The mean absolute difference values let suggest that the result difference is negligible over the day, as it is inferior to 1°C for the PET and to 5°C for the T_{mrt}, as defined by the ISO 7726:1998 Standard [337] for thermal stress conditions [348,355]. Conversely, the peak differences in PET and T_{mrt} reported at 8:00 exceed the proposed thresholds. Nonetheless, the importance of thermal stress conditions in early morning is generally limited, as the most challenging conditions occur during the central hours of the day, which reported a good agreement between the simulation results (the mean absolute difference between 11:00 and 17:00 is 0.2 °C for PET and 1.5 °C for T_{mrt}). Based on these considerations, the 30 m long urban configurations were considered accurate enough.

***NB** The results of the validation study presented in Chapter 5B have evidenced an insufficient ability of ENVI-met to capture the longwave and shortwave radiation from the building façade. This limitation is likely to hamper the reliability of results on the microclimatic effect of material changes. For instance, the variation of solar reflectance of the façade influences the amount of shortwave radiation being reflected by it, and, as a consequence of the variation of solar radiation absorbed by it, also the amount of longwave radiation emitted by the element itself. The research study in Chapter 5B reported an underestimation of emitted longwave radiation (following an underestimation of façade surface temperature) and, at the same time, an overestimation of the shortwave radiation reflected by it. Consequently, the ability of ENVI-met to predict the effect of material variations is considered questionable at current times, and further evaluations are needed to better understand its reliability. Therefore, while this study was originally performed considering both form and material changes of the urban scenarios, only the results of form changes are presented and discussed in § 6.4. In particular, in light of the good agreement found between simulated and measured T_{mrt} in the validation studies in [370,374,491], which are referred to a light-colored façade, R07 material variation, exhibiting a solar reflectance of 0.7 is considered.

6.4. Results

6.4.1. Acoustic simulation results

The results of the acoustic simulations are reported separately for the different urbans settings considered.

Table 40 collects the A-weighted *SPL* simulated over the façade of the buildings (detailing the floor-based value and average value) and at pedestrian level. In order to isolate the effect of the different urban settings on the predicted *SPL*, the urban

settings are considered with the reference (R) material configuration, i.e., with sound reflective materials.

The *SPL*s are greater for the narrower scenarios (10 m wide) and decrease at higher building floors, as a consequence of the reduced source-receiver distance. The *SPL* on Façade A and B are comparable on a floor basis for specular scenarios. For scenarios of the same width, the *SPL* increases for denser urban settings (i.e., from the isolated building to the courtyard), as a consequence of the greater number of sound reflections occurring in more enclosed spaces. Overall, the greatest *SPL*s are reported at pedestrian positions, with a maximum value of 63.2 dB(A) for the 10 m-wide courtyard (CY). The maximum *SPL* value over the façade, equal to 58.9 dB(A) is reported at the 1st building floor for the same urban setting.

Table 40. A-weighted *SPL* [dB(A)] simulated over the façade and at pedestrian level for the different urban settings and the reference (R) material configuration.

		10 m				20 m			
		IB	CR	ST	CY	IB	CR	ST	CY
Façade A	5th floor	50.2	51.4	53.2	57.1	49.6	50.9	51.0	55.0
	4th floor	51.5	52.5	54.0	57.5	49.6	50.8	51.1	55.0
	3rd floor	52.4	53.2	54.6	57.8	50.6	51.6	51.8	55.3
	2nd floor	53.6	54.3	55.1	58.1	51.7	52.5	52.6	55.7
	1st floor	55.5	56.0	56.4	58.9	52.8	53.4	53.2	56.0
	average	53.0	53.8	54.8	57.9	51.1	51.9	52.0	55.4
Façade B	5th floor	-	-	53.2	57.1	-	-	51.0	55.0
	4th floor	-	-	54.0	57.5	-	-	51.1	54.9
	3rd floor	-	-	54.6	57.8	-	-	51.8	55.3
	2nd floor	-	-	55.1	58.1	-	-	52.6	55.7
	1st floor	-	-	56.4	58.9	-	-	53.2	56.0
	average	-	-	54.8	57.9	-	-	52.0	55.4
pedestrians		61.5	61.7	61.5	63.2	56.6	57.2	56.9	59.4

The differences in A-weighted *SPL* found for the various green wall configurations in case of the isolated building (IB) with 10 and 20 m widths are collected in Table 41.

In this urban setting there is no Façade B, and the material configuration T is equivalent to O; therefore, the corresponding results are omitted from the table. Moreover, the different widths only affect the distance from the source to receivers on Façade A. As concerns façade receivers, noticeable *SPL* reductions (greater than JND_{SPL}) are reported for both widths at all floors for material configurations T (green wall over the entire building façade) and U (green wall from 1st to 5th floor). The façade mean *SPL* reduction for both material configurations are 2 dB for the width of 10 m and 2.6 dB for the 20 m one. For a given width, T and U material configurations results in comparable *SPL* variations on a floor-basis. The magnitude of the *SPL* reduction reported for T and U configurations increases along building height for the 10 m-wide configuration and appear to decrease for the 20 m-wide one (with the exception of the 1st floor), with maximum reductions of ~3.1 dB. Therefore, the maximum reduction predicted is comparable to the 3 dB threshold. The material configuration L (green

wall on the ground floor of the façade) results in no *SPL* variations. Negligible *SPL* variations at pedestrian receivers are reported for all tested scenarios.

Table 41. Difference in *SPL* [dB] found at the different floors of the two façades and at pedestrians' position for the isolated building (IB) with 10 and 20 m widths. Noticeable reductions are in bold.

		IB 10				IB 20			
		T	O	L	U	T	O	L	U
Façade A	5th floor	**-2.2**	-	0.0	**-2.1**	**-1.5**	-	0.0	**-1.5**
	4th floor	**-2.3**	-	0.0	**-2.3**	**-1.9**	-	0.0	**-1.9**
	3rd floor	**-1.4**	-	0.0	**-1.4**	**-3.1**	-	0.0	**-3.0**
	2nd floor	**-1.5**	-	0.0	**-1.4**	**-2.9**	-	0.0	**-2.9**
	1st floor	**-2.7**	-	0.0	**-2.7**	**-2.5**	-	0.0	**-2.5**
	average	**-2.0**	-	0.0	**-2.0**	**-2.6**	-	0.0	**-2.4**
pedestrians		-0.7	-	-0.6	0.0	-0.9	-	-0.9	0.0

Table 42 collects the *SPL* differences for the corner (CR) scenario with the 10 and 20 m widths. Since there is no Façade B, the corresponding results are not reported. The width variation here affects the distance from the source (as in the case of the isolated building) and the length of the façade on the shorter side of the corner. The *SPL* reductions found for the corner scenario are greater than those found for the isolated building.

Table 42. Difference in *SPL* [dB] found at the different floors of the two façades and at pedestrians' position for the corner (CR) with 10 and 20 m widths. Noticeable reductions are in bold.

		CR 10				CR 20			
		T	O	L	U	T	O	L	U
Façade A	5th floor	**-2.8**	**-2.1**	0.0	**-2.7**	**-2.1**	**-1.4**	0.0	**-2.1**
	4th floor	**-3.2**	**-2.2**	0.0	**-3.1**	**-3.0**	**-1.9**	-0.1	**-2.9**
	3rd floor	**-2.0**	**-1.4**	-0.1	**-1.8**	**-3.7**	**-3.0**	-0.2	**-3.4**
	2nd floor	**-2.0**	**-1.5**	-0.2	**-1.7**	**-3.7**	**-2.9**	-0.3	**-3.2**
	1st floor	**-3.0**	**-2.7**	-0.3	**-2.7**	**-2.9**	**-2.5**	-0.4	**-2.5**
	average	**-2.6**	**-2.0**	-0.1	**-2.4**	**-3.1**	**-2.3**	-0.2	**-2.8**
pedestrians		-0.9	-0.7	-0.9	0.0	**-1.5**	-0.9	**-1.4**	-0.1

Noticeable *SPL* reductions are found for façade receivers at all building floors, for both the 10 m and 20 m configurations, except for material configuration L. The configuration T results in the greatest reductions, reporting up to 3.2 dB and up to 3.7 dB of reduction for the 10 and 20 m wide corners, respectively, that are above the 3 dB threshold. For a given corner width, the *SPL* reduction over the façade observed for material configuration T and U are comparable, as previously noted. The façade mean *SPL* reduction is between 2.6 and 3.1 dB for T material configurations, between 2.4 and 2.8 dB fou U, and between 2.0 and 2.3 dB for O configurations for the 10 m and 20 m wide corners, respectively. Noticeable *SPL* variations for pedestrians are only reported for 20 m wide corner, in case of T and L material configurations, with

reductions of ~1.5 dB. both of which exhibiting the green wall close to pedestrian receivers. The same configurations results in almost noticeable *SPL* reduction at pedestrian position for the 10 m wide corner. Overall, the material configuration L is the only one resulting not effective for the façade receivers, reporting *SPL* reductions below the JND_{SPL} in all cases.

The *SPL* reductions for the street (ST) configurations with the two widths are summarized in Table 43.

Table 43. Difference in *SPL* [dB] found at the different floors of the two façades and at pedestrians' position for the street (ST) with 10 and 20 m widths. Noticeable reductions are in bold.

		ST 10				ST 20			
		T	O	L	U	T	O	L	U
Façade A	5th floor	**-5.0**	**-3.1**	-0.4	**-4.9**	**-2.7**	**-2.0**	-0.1	**-2.6**
	4th floor	**-4.0**	**-3.1**	-0.4	**-3.9**	**-2.9**	**-2.3**	-0.2	**-2.9**
	3rd floor	**-3.5**	**-2.0**	-0.4	**-3.4**	**-4.2**	**-2.6**	-0.2	**-4.1**
	2nd floor	**-2.8**	**-1.9**	-0.8	**-2.4**	**-3.3**	**-2.5**	-0.5	**-2.8**
	1st floor	**-3.1**	**-2.3**	**-1.2**	**-2.3**	**-2.8**	**-2.2**	-0.7	**-2.2**
	average	**-3.7**	**-2.5**	-0.6	**-3.4**	**-3.2**	**-2.3**	-0.3	**-2.9**
Façade B	5th floor	**-4.9**	**-1.8**	-0.4	**-4.9**	**-2.7**	-0.9	-0.1	**-2.6**
	4th floor	**-4.1**	**-1.8**	-0.4	**-4.0**	**-2.9**	**-1.0**	-0.2	**-2.9**
	3rd floor	**-3.5**	**-2.0**	-0.5	**-3.4**	**-4.2**	**-1.2**	-0.2	**-4.1**
	2nd floor	**-2.9**	**-1.3**	-0.9	**-2.4**	**-3.4**	-0.7	-0.5	**-2.8**
	1st floor	**-3.1**	**-1.1**	**-1.2**	**-2.3**	**-2.8**	-0.7	-0.7	**-2.2**
	average	**-3.7**	**-1.6**	-0.6	**-3.4**	**-3.2**	**-0.9**	-0.3	**-2.9**
pedestrians		**-1.6**	**-1.0**	**-1.5**	-0.1	**-1.9**	**-1.0**	**-1.8**	-0.1

In this case the *SPL* reductions are greater than the ones previously reported. Noticeable reductions are reported for almost all façade floors and at pedestrian positions. The ineffectiveness of material configuration L at reducing *SPL* over the façades is confirmed also for the street scenario. Noticeable reductions of *SPL* are reported at pedestrian positions for all the material configurations except for the U one, where green wall is only applied to the upper façade portion. The *SPL* reductions are comparable between Façade A and B on a floor basis, as the scenarios are specular, apart from material configuration O, where only Façade A is treated. The mean façade reductions are 3.7 and 3.4 dB for T and U material configurations for the 10 m wide street and 3.2 and 2.9 dB for the same configuration for the 20 m wide street, i.e., with values close or greater than the 3 dB threshold. The maximum noise reduction, equal to 5.0 dB, is reported at the top building floor for the 10 m wide street and material configuration T. The reduction found for material configuration O are greater on Façade A, but noticeable reductions are reported also on Façade B in the 10 m wide street. This suggests that the application of a green wall/sound absorbing façade materials can improve acoustic comfort also in nearby buildings, as already highlighted in [107], especially in denser urban settings. Noticeable *SPL* reductions for pedestrians are reported for all configurations exhibiting green wall over the ground

floor of the buildings (T, O, L), with values up to 1.6 dB for T and L configurations in the 10 m wide street, and up to 1.9 dB for the 20 m wide one. Configuration O reaches 1 dB of reduction in pedestrian positions for both street widths.

Table 44 collects the *SPL* difference for the 10 and 20 m wide courtyard (CY) scenarios. The *SPL* reductions are greater than the ones previously reported, with noticeable reductions in all façade positions for all material configurations. Therefore, also in this case, noticeable reductions are reported on Façade B when only Façade A is treated (material configuration O). Noticeable *SPL* reductions are reported at pedestrian positions with the exception of material configuration U in the 20 m-wide courtyard. The most performing material configuration is T, in coherence with what previously evidenced. The average *SPL* reduction found over the façades for material configuration T are up to 6.5 dB (for the 10 m wide courtyard with material configuration T). The *SPL* variations are comparable for Façade A and Façade B on a floor-basis, as evidenced in the street scenarios. The peak *SPL* reduction, equal to 7.7 dB is reported at the highest building floor for material configuration T applied to the 10 m-wide courtyard. The *SPL* reductions for pedestrians are greater in the wider courtyard (above 4 dB) than in the narrower one (~3 dB), as in the case of the street.

Table 44. Difference in *SPL* [dB] found at the different floors of the two façades and at pedestrians' position for the courtyard (CY) with 10 and 20 m widths. Noticeable reductions are in bold.

		CY 10				CY 20			
		T	O	L	U	T	O	L	U
Façade A	5th floor	-7.7	-4.1	-1.5	-7.4	-5.7	-2.9	-1.1	-5.7
	4th floor	-7.4	-4.3	-1.7	-7.1	-6.6	-3.1	-1.3	-6.4
	3rd floor	-6.3	-3.3	-2.1	-5.7	-7.0	-3.4	-1.7	-6.4
	2nd floor	-5.7	-3.3	-2.8	-4.6	-6.3	-3.4	-2.4	-4.7
	1st floor	-5.3	-3.5	-3.0	-3.8	-5.2	-2.9	-2.8	-3.7
	average	-6.4	-3.7	-2.2	-5.7	-6.2	-3.1	-1.9	-5.4
Façade B	5th floor	-7.7	-3.2	-1.6	-7.4	-5.7	-2.1	-1.1	-5.5
	4th floor	-7.5	-2.9	-1.8	-7.1	-6.6	-1.9	-1.3	-6.4
	3rd floor	-6.4	-3.4	-2.1	-5.8	-7.1	-2.5	-1.7	-6.4
	2nd floor	-5.6	-2.7	-2.7	-4.5	-6.2	-1.8	-2.4	-4.8
	1st floor	-5.3	-2.3	-3.0	-3.9	-5.2	-1.8	-2.9	-3.7
	average	-6.5	-2.9	-2.2	-5.7	-6.2	-2.0	-1.9	-5.4
pedestrians		-3.2	-2.0	-3.0	-0.4	-4.4	-2.0	-4.1	-0.4

The main findings are that the green wall application is the more effective the more reverberant is the urban space considered. In general, the noise reduction observed over the façade are greater than the one found at pedestrian positions, making green wall often ineffective for pedestrian comfort in least dense urban scenarios. The noise reduction generally occurs close to the green wall, meaning that to increase acoustic comfort for pedestrians the green wall needs to be installed (also) at the ground floor, and vice versa a green wall on the upper floors is required to increase acoustic comfort for dwellers. Moreover, in the case of the application of the

green wall to one façade only, noticeable noise reductions are reported also on the opposite building, suggesting that the benefits provided by the green wall can be perceived also in close-by buildings. The maximum noise reduction, equal to 7.7 dB, is reported in the narrower courtyard with the green wall applied to all the façades.

6.4.2. Microclimatic simulation results

The hourly variation of PET and T_{mrt} values for the different urban is reported in Figure 120 and Figure 121 for pedestrian position, and in Figure 122 and Figure 123 as concerns façade position. For convenience, the average and peak PET and T_{mrt} values are summarized in Table 45 and Table 46 for façade ad pedestrian positions, along with the duration of direct solar radiation in those positions. As previously mentioned, all the data reported refers to the material configuration R07, i.e., a reference façade wall with a solar reflectance of 0.7.

The PET and T_{mrt} trends in Figure 120 and Figure 121 refer to pedestrian position and show that the greatest PET values are reported for corner with peak value of 62.7 °C (average PET 40.3 °C) for the 20 m wide one and of 57.6 °C (average PET 37.8 °C) for the 10 m wide one. The lowest peak PET values are reported by the street (ST), with a difference between peak values greater than 10 °C with respect to the corner configuration of the same width. The T_{mrt} trends show that the greatest peak values are reported for the 20 m wide options and for the 10 m ones having no or limited building elements that screen the calculation point from direct solar radiation, leading to values ~77 °C at pedestrian position.

Therefore, the 20 m wide scenarios, and the 10 m wide CR and IB scenarios are associated to different peak PET values, despite comparable peak T_{mrt} values. This is caused by the lower wind speed exhibited by the corner due to the shielding effect provided by the corner side in the prevailing wind direction, which results in increased PET values. Similarly, while the peak T_{mrt} of the street (ST) and courtyard (CY) are quite similar, the PET trends are different, with lower values for the street, due to the greater wind speed that promotes thermal comfort.

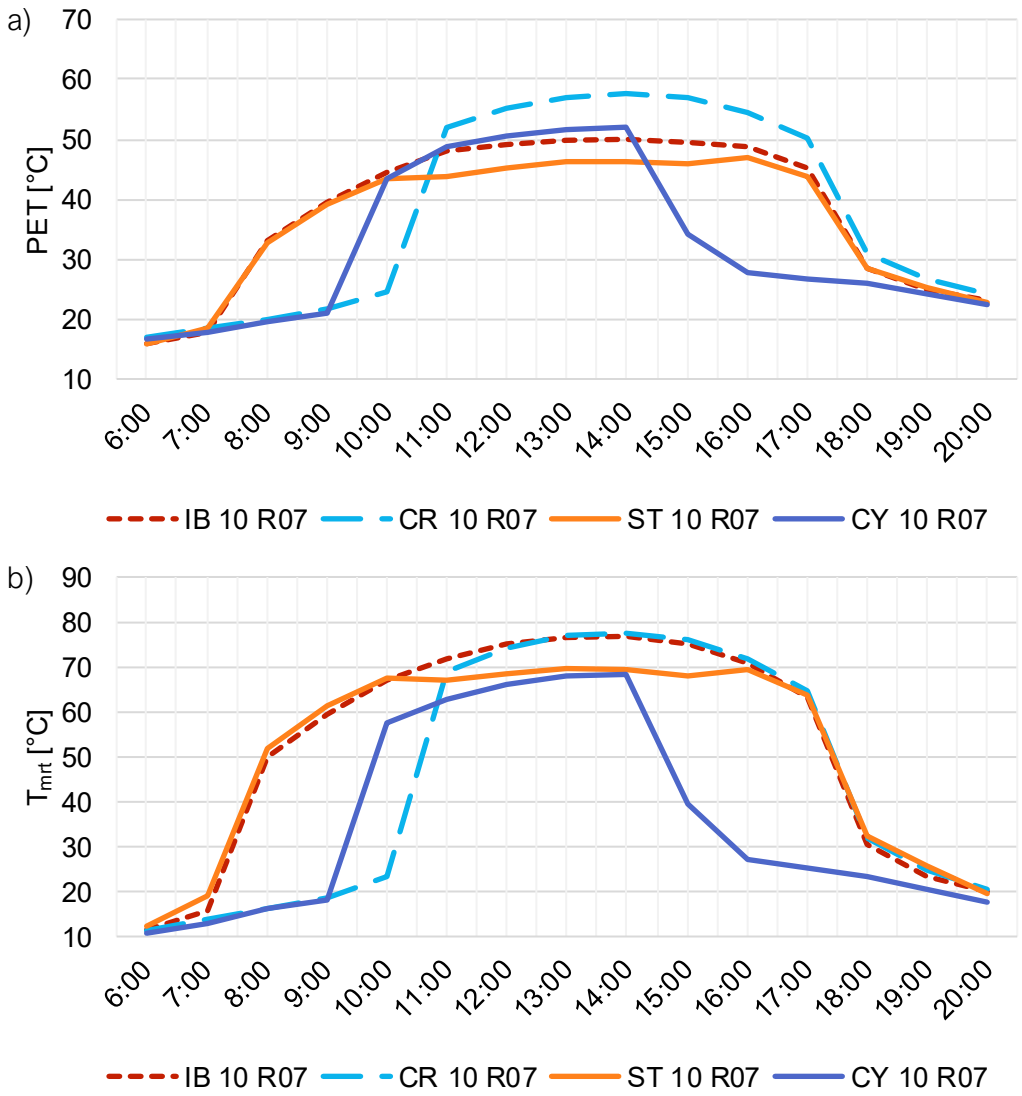

Figure 120. Hourly variation of (a) PET and (b) T_{mrt} in the pedestrian position for the different urban settings with a width of 10 m.

Overall, the thermal conditions for pedestrians exhibit greatest PET values for the 20 m wide corner, with values greater than the 10 m-wide corner for the effect of the more marked wind shielding. The narrower scenarios ST and CY result in more comfortable thermal conditions with respect to the corresponding wider ones. These scenarios present buildings south (and also on the sides) to the calculation point and the effect of their widths on wind speed it not considered the main factor affecting thermal conditions. On one hand these elements screen the calculation position from direct solar radiation, on the other hand they may generate a radiative trapping phenomenon, limiting the longwave radiative exchanges with the sky. Overall, the T_{mrt} results suggest that the screening effect overweight the increased longwave radiation in the tested scenarios.

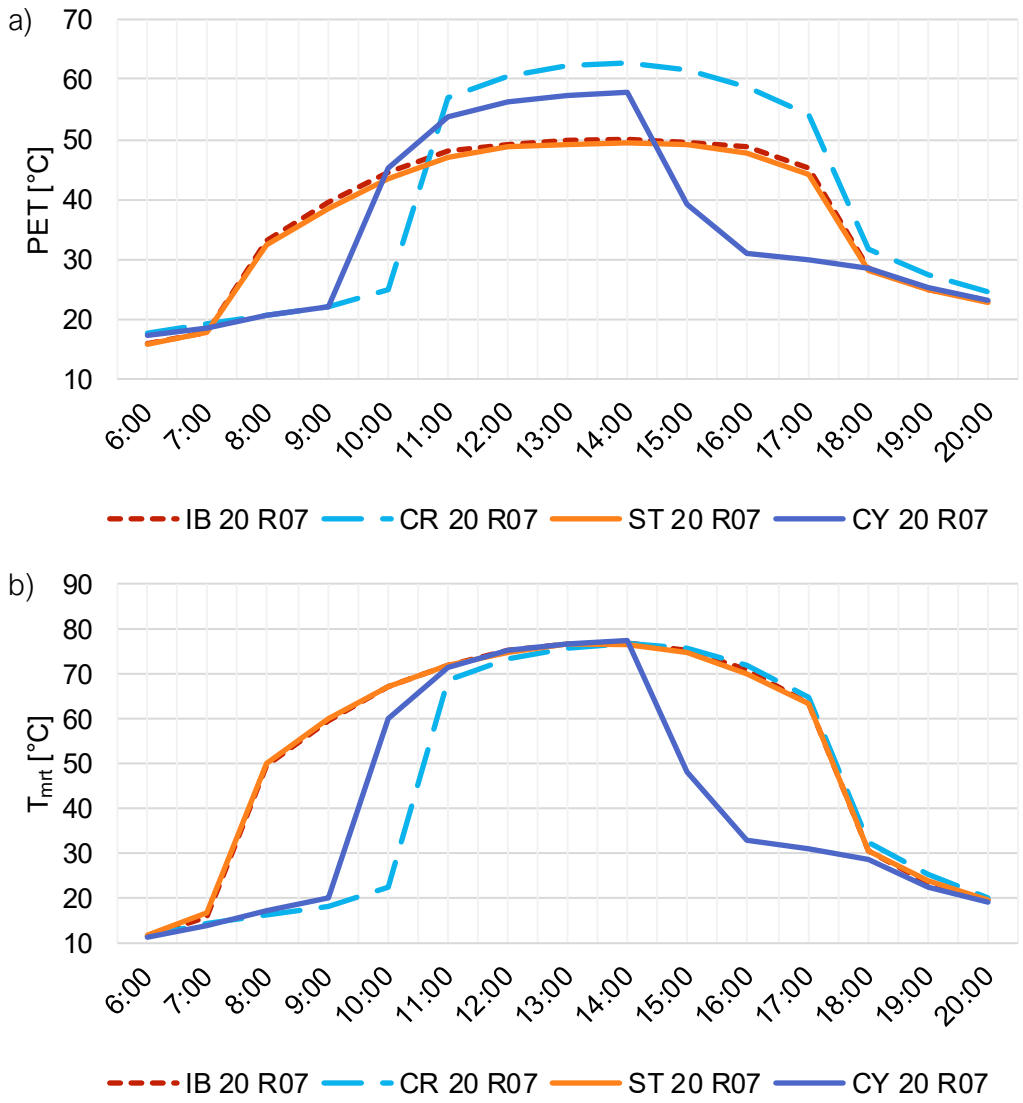

Figure 121. Hourly variation of (a) PET and (b) T_{mrt} in the pedestrian position for the different urban settings with a width of 20 m.

The results in Figure 122 and Figure 123, referred to the façade position, show lower PET and T_{mrt} trends with respect to those found at pedestrian position. This is probably caused by the greater sky view factor and consequent reduced radiative exchanges with surrounding urban facets, which result in lower T_{mrt} at the façade position, combined with the greatest wind speed.

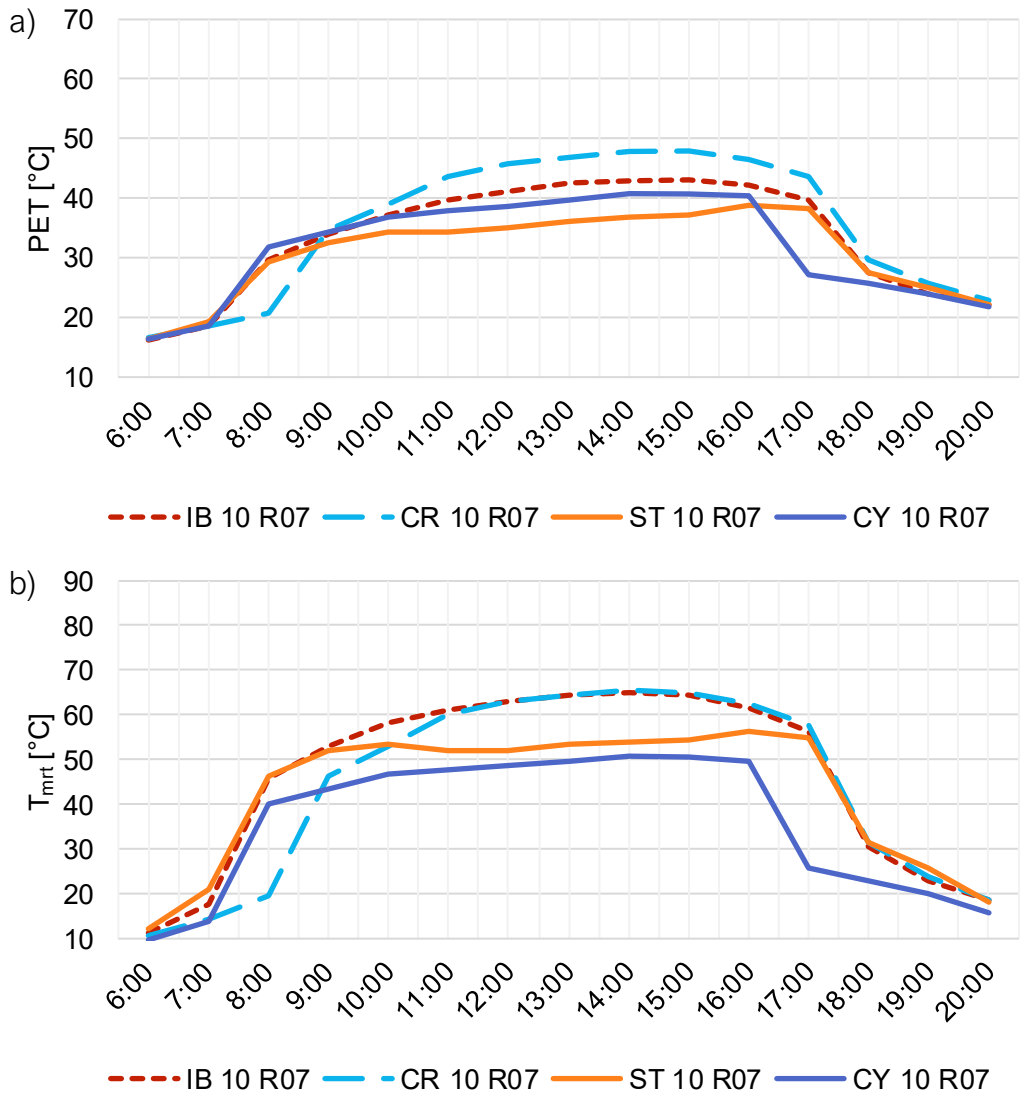

Figure 122. Hourly variation of (a) PET and (b) T_{mrt} in the façade position for the different urban settings with a width of 10 m.

As previously noted, the greatest thermal stress is experienced in the 20 m wide corner (CR) urban setting, with PET values up to 48.1 °C. The T_{mrt} trend of CR is similar to that of the isolated building (IB), which however leads to lower PET values, due to the shielding effect of the corner. The street (ST) is the configuration with the lowest PET trend, despite the configuration with the lowest T_{mrt} value is the courtyard one, for the shielding effect. As previously noted, the T_{mrt} and PET trends are similar for the two widths in case of IB and CR, and the differences found between the narrower or wider CR configuration found at the façade position are lower than those reported at the pedestrian one. Differences are found for ST and CY with the 10 m and 20 m widths, with lower PET and T_{mrt} values for the narrower scenarios, similarly to what previously reported for pedestrians.

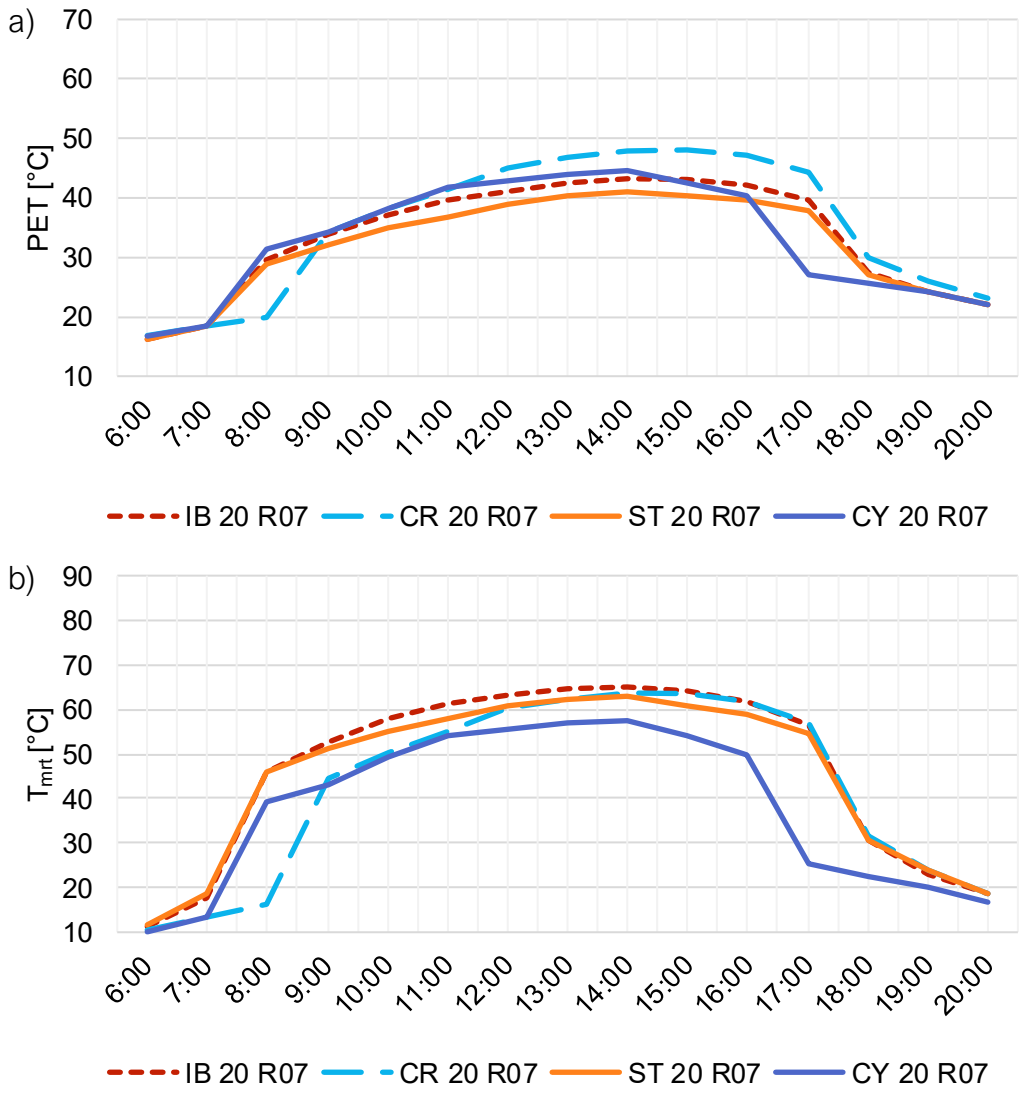

Figure 123. Hourly variation of (a) PET and (b) T_{mrt} in the façade position for the different urban settings with a width of 20 m.

The average and peak PET and T_{mrt} values at pedestrian position (see Table 45) confirm the previous findings. The corner (CR) leads to the least comfortable conditions for both widths (greatest average and peak PET), while the most comfortable conditions are found for the courtyard (CY), reporting the lowest average PET, and the street (ST), reporting the lowest peak value of PET. The T_{mrt} values are on average the greatest for the isolated building and the lowest for the courtyard. Direct solar radiation is present at pedestrian position for 10 h in case of an unobstructed scenarios, such as the isolated building (IB), and this is reduced to 5 h for the courtyard, which has an enclosed shape that screens the calculation points from solar radiation for several hours.

Table 45. Average and peak PET and T_{mrt} values at pedestrian position. The hours when the peak occurs are in parentheses.

		10 m				20 m			
		IB	CR	ST	CY	IB	CR	ST	CY
PET [°C]	average	37.8	37.8	36.6	32.2	37.8	40.3	37.2	35.1
	peak	50.0 (14)	57.6 (14)	46.4 (14)	52.0 (14)	50.0 (14)	62.7 (14)	49.4 (14)	57.8 (14)
T_{mrt} [°C]	average	52.5	44.8	51.0	35.6	52.5	44.4	52.4	40.3
	peak	76.8 (14)	77.5 (14)	69.6 (14)	68.3 (14)	76.8 (14)	76.7 (14)	76.4 (14)	77.4 (14)
Direct solar radiation		10 h (8-17)	7 h (11-17)	10 h (8-17)	5 h (10-14)	10 h (8-17)	7 h (11-17)	10 h (8-17)	5 h (10-14)

Similar trends are reported at the façade position (see Table 46), with worst thermal comfort condition for the corner (CR). The best conditions are found in this case for the street (ST), which exhibits the lowest average and peak PET values. The greatest average T_{mrt} values are exhibited by the isolated building (IB), and the lowest ones by the courtyard (CY). In general, as previously noted, the PET and T_{mrt} values over the façade are lower than in case of the pedestrian position, while the duration of direct solar radiation is greater (between 9 and 10 h), given the reduced screening provided by surrounding buildings in the calculation point at the 4th floor above ground.

Table 46. Average and peak PET and T_{mrt} values in the façade position. The hours when the peak occurs are in parentheses.

		10 m				20 m			
		IB	CR	ST	CY	IB	CR	ST	CY
PET [°C]	average	33.4	35.3	30.9	31.7	33.4	35.2	31.9	32.9
	peak	43.1 (14-15)	47.8 (15)	38.4 (17)	40.7 (15-16)	43.1 (14-15)	48.1 (15)	41.0 (14)	44.6 (14)
T_{mrt} [°C]	average	33.4	43.8	42.5	35.7	33.8	42.2	44.9	37.8
	peak	65.0 (14)	65.6 (14)	56.4 (16)	50.8 (14)	65.0 (14)	63.5 (14-15)	62.9 (14)	57.5 (14)
Direct solar radiation		10 h (8-17)	9 h (9-17)	10 h (8-17)	9 h (8-16)	10 h (8-17)	9 h (9-17)	10 h (8-17)	9 h (8-16)

6.4.3. Some combined considerations

The potentially complex interrelation between outdoor acoustic and thermal comfort goals emerges from this study. While the effect of green wall on thermal comfort conditions could not be accounted, the influence of the different urban scenarios on acoustic and thermal comfort conditions suffice to provide some illustrative data to support these considerations.

The isolated building, while being associated to the lowest noise levels, presents critical thermal conditions due to the absence of shading. The corner scenario, which from the acoustic point of view is associated to relatively low *SPL* values that are quite comparable to the street ones, when considering thermal aspects results in markedly lower comfort conditions than the street, due to wind shielding. Another example is the courtyard, which is associated to the greatest noise levels as a result of the

elevated number of sound reflections occurring in that space. The same scenario nonetheless leads to the most comfortable thermal conditions for pedestrians (lowest average PET), being it shaded for a significant fraction of the day. This suggests that the presence of surrounding buildings defining the enclosed space of the courtyard play a dual role, i.e., are beneficial for shading and detrimental for the sound reflections occurring over them. While the courtyard exhibits the greatest noise levels, at the same time, it is associated to the greatest *SPL* reductions in case of a green wall. Indeed, the great number of sound reflections occurring emphasize the effectiveness of the sound absorption properties of the green wall. Therefore, such design strategy can be effective to lower noise levels and also further improve the thermal comfort conditions in such spaces.

This study let suggest how a combined consideration of acoustic and thermal comfort goals is important to better shed light on the two realms at the same time. The two performance objectives are indeed different in nature as they rely on diverse physical phenomena and therefore a given scenario that can be beneficial for one of them is not necessarily favorable for the other performance objective. Therefore, a holistic approach to façade design is endorsed to control the overall performance and prevent undesirable consequences of design intervention resulting from overlooked performance aspects during design processes.

6.5. Conclusions

This study investigates the effectiveness of green walls applied in different configurations to a variety of urban settings at improving outdoor acoustic and thermal comfort conditions for pedestrians and dwellers. Green walls belonging to the “living wall” category present excellent sound absorbing properties and can mitigate microclimatic conditions in their surroundings. The urban settings in this contribution are representative of typical European cities and present different degrees of urban density, ranging from an isolated building to a courtyard, each considered with two different widths. The green wall is applied to the building to either all façades, to a single façade, and only to the upper/lower portion of the façades. The analysis focuses on comfort conditions at pedestrian positions and over the façade and considers the variation of A-weighted SPL to quantify acoustic comfort and of PET and T_{mrt} to evaluate thermal comfort.

As concerns acoustic comfort, the results highlight that denser urban environments lead to greater SPL values, and that the SPL reduction obtained by the application of green walls are greater in denser contexts, which being more reverberant better exploit the mitigation provided by sound absorbing materials. The SPL reductions are mainly observed in position close to the green wall and reaches 7.7 dB of reduction at the 5^{th} floor in case of the 10 m wide courtyard. Moreover, the application of a green wall to a façade only is able to improve acoustic comfort also on the opposite façade, that is untreated. Improved conditions at pedestrian locations are only reported in dense urban settings (street, courtyard and some configurations of the corner), when the green wall is applied (also) in the lower façade portion (no improvements for pedestrians are reported for green wall on the upper façade portion.

Based on the findings of Chapter 5B, the analysis on thermal comfort is limited to the comparison between the conditions found in the different urban settings, without considering the effect of the green wall. The greatest PET values for pedestrians are reported for the corner configuration, where there is very limited shading by surrounding constructions and the main wind direction is shielded. The most comfortable conditions for pedestrians (when considering the peak PET values) are reported for the street, where there is shading, and the wind speed is relatively elevated. The effect of different widths can impact the wind shielding effect and the shading from solar radiation, making narrower scenarios more comfortable in the case of the courtyard and street configurations, and less comfortable in case of the corner one. The thermal comfort conditions over the façade are milder than the ones for pedestrians and follow the same trends.

Overall, the study suggests that complex pictures, where thermal comfort and acoustic comfort objectives may diverge for a given scenario, highlighting the importance of a holistic approach to provide a broad understanding of the performance implications of the considered design choices.

This preliminary study can be integrated by including the effect of materials and green wall on thermal comfort conditions, once the reliability of the tool could be proven. Moreover, further investigations are needed to define a comprehensive database that can inform the definition of design ground rules to support practitioners in the selection of effective strategies to improve acoustic and thermal comfort in urban open areas. The analysis could include a wider variety of material options (e.g., NIR-reflective paints, thermochromic coatings, sound diffusive materials), different cardinal orientations and climatic conditions, and different types of noise sources (e.g., aircraft, railway or leisure noise). Moreover, the use of an integrated simulation approach, where acoustics and thermal performance are evaluated within the same program interface should be explored to ease the process and endorse the application of such approach among practitioners. In this framework, also the use of a multi-disciplinary assessment of outdoor comfort conditions is envisaged. Examples of this approach are presented in [511,512] for indoor spaces and in [513,514] for outdoor ones, and highlight the importance of a multi-domain approach to gain an holistic understanding of human comfort.

Acknowledgements

The author is grateful for the support provided by Martha Lewis and Jakob Strømann-Andersen from Henning Larsen for the development of the study presented in this Chapter.

Chapter 7

Conclusions

7.1. Final remarks

The contributions presented in the previous Chapters revolve around the themes of outdoor thermal and acoustic comfort, with the aim to explore and suggest strategies to include such aspects during design processes, with a focus on the role of building façades. As introduced in § 1, the thesis work aimed at meeting three main research goals, ranging from methodologies for the material characterization, to identification and evaluation of performance simulation tools to support decision making processes. Moreover, the application of simulation tools to analyze façade design alternatives in idealized scenarios and actual case-studies is presented, to investigate the opportunities and limits of such approach. All these research steps were carried out in parallel for the acoustic and thermal realms, following the same methodological approach that ranged from the material scale to the urban microscale. All the presented Chapters, although interconnected, have been individually structured to provide conclusions within the scope of the Chapters themselves, which are here summarized for clarity.

After an introductive overview on the themes of outdoor thermal and acoustic comfort (**Chapter 2**), the actual research contributions of the thesis are presented. The research studies in Chapter 3A and 3B have allowed to focus on the characterization of innovative materials that can be applied as outer layer of façade walls. **Chapter 3A** has focused on different porous concrete panels, varying in concrete mix design, thickness, and mounting conditions. Such materials are suitable for outdoor applications and their use of building façade can locally reduce environmental noise levels. The Chapter has highlighted how the mounting conditions of porous concrete panels can markedly impact on their sound absorbing performance, and that layered solutions can combine practical advantages to performance comparable to that of single-layered solutions of equivalent thickness. The research on innovative façade materials related to the thermal realm is presented in **Chapter 3B**, where panels coated with thermochromic paint, which exhibit dynamic optical properties varying as a function of surface temperature, are investigated. Dynamic materials can be considered the future of building material solutions, and thermochromic ones are expected to reduce energy demand for both heating and cooling, by modulating the heat flow through the building envelope. The research contribution aims to suggest experimental procedures for the characterization of the dynamic performance of thermochromic materials in the laboratory and in outdoor conditions, and focuses also on the impact of photodegradation on their switching properties. After these research studies, the thesis moves to the urban microscale. The following two Chapters, i.e., Chapter 4A and 4B, focus on some of the issue revolving around the use of simulation tools to gather performance feedback during design phases. **Chapter 4A** focused on the application of performance-based design in acoustics, which is still little employed in practice. Data was gathered on a set of built case-studies to highlight the digital workflows followed, the simulation tools used and to evidence the main advantages of such approach as well as some of the challenges that seems to limit its practical implementation. **Chapter 4B** focuses on the mean radiant temperature, whose reliable estimation is crucial to effectively orient design decisions and is greatly

affected by radiative exchanges with vertical surfaces, such as façades. The prediction of this parameter in urban environments is however challenging and the simulation tools generally apply simplifications and assumption in the calculation that are often not clearly stated. The Chapter compares the mean radiant temperature models of common simulation tools to highlight the radiative components included and the main assumptions applied, to support users in the identification of suitable simulation tools and in the interpretation of the simulation outcome. The thesis work proceeds with **Chapter 5A**, presenting an evaluation of the use of geometrical room acoustic simulation tools for sound pressure level estimation in outdoor settings and a set of design applications. The evaluation study, which is based on an outdoor measurement campaign, has allowed to evidence how the outdoor sound pressure levels predictions of Odeon and Pachyderm can be considered reliable, endorsing the use of these tools to assess noise level variations resulting from different façade design options. Following these findings, two application studies are presented, one focusing on a proposal for a façade retrofit intervention in a courtyard, and one focusing on a representative portion of Wolfsburg Connect project by Henning Larsen. Both applications illustrate how different design alternatives could be acoustically tested during the design processes to optimize the form and material properties to lower noise levels, with minor design variations that do not alter the main design concept. The most widely used microclimatic simulation tool, i.e., ENVI-met, is evaluated in **Chapter 5B**, by comparing the main variables affecting thermal comfort in a challenging urban scenario under extremely hot conditions. The validation study evidenced that ENVI-met was not able to correctly predict the measured environmental parameters, with a series of limitations that are considered to hamper the tool's ability to compare design scenarios with respect to thermal comfort conditions, especially in case of material variations. In light of this outcome, while **Chapter 6** presents a parametric investigation on green wall effect on both thermal and acoustic conditions in a set of urban scenarios, the results related to thermal comfort conditions are limited to urban form variations. The investigation was performed using Pachyderm and ENVI-met to analyze the influence of green walls on the comfort conditions, considering eight urban settings, each of which tested with five façade configurations. The study evidences the role played by sound reflections in urban settings, highlighting how denser urban scenarios lead to marked increases in noise levels and in a greater effectiveness of the sound absorbing treatment. From the thermal comfort standpoint, the importance of shading and wind shielding emerges, with greater comfort for pedestrians in the street and courtyard and the greatest thermal stress in corner-like urban configurations. Although limited, the importance of a combined evaluation of acoustic and thermal comfort conditions emerges from the study. Indeed, the two performance goals often conflict with each other and therefore overall effective solutions can be reached only by gaining awareness on both performance aspects during design processes.

The main contribution of this thesis is to increase the knowledge on simulation approaches to estimate and improve outdoor thermal and acoustic comfort conditions by means of façade design choices and methodologies to assess the performance of innovative materials that are expected to influence, and potentially benefit, outdoor

comfort conditions. This theme represents a novelty, since few works in scientific literature are focused on the multifaceted impact of these architectural elements on surrounding conditions. The inclusion performance objective related to outdoor comfort during design processes can make building façades work also as public infrastructures, able to mitigate comfort conditions in their surroundings. Acting on building façade is a viable strategy not only in new urban developments but also in already built contexts, given the several retrofit interventions that are carried out on the building envelopes for energy efficiency purposes or maintenance. Indeed, these actions can also represent valid opportunities to locally improve comfort conditions, thus contributing to the liveability of present and future cities, and to the improvement of health and well-being in urban areas.

7.2. Further work

The theme encompassed by the Ph.D. research activity are wide and multifaceted. The exploratory work has highlighted some of potentialities and limitations of the currently available approaches to estimate performance and to orient design decisions consequently. The work can be considered a starting point for future research on outdoor thermal and acoustic comfort and can be extended following several research lines. For instance, further investigations at the level of materials can be explored, with different types of materials (e.g., perforated acoustic panels, 3D printed materials, acoustic metamaterials, green walls, NIR-reflective materials, etc.). Other ways to continue the research include the evaluation of other simulation tools with respect to measured data, which in case of acoustic ones could include wave-based tools, and the use of a wider variety of urban scenarios and weather conditions for the measurement campaigns. Moreover, the work can be expanded by investigating the effect of façade design strategies on both outdoor and indoor spaces. Another future development of the presented work could focus on perceptual evaluations, by assessing the combined effect of thermal and acoustic conditions (and potentially also other ones) on the overall perception of comfort. The comparison of the collected subjective evaluations to objective ones may contribute to a deeper understanding of outdoor comfort themes. To conclude, the development of an integrated simulation approach for acoustic and thermal comfort aspects is another ambitious research theme, which can ease and promote the use of performance-based design among practitioners.

References

[1] United Nations, Department of Economic and Social Affairs, Population Division, World Population Prospects 2019: Highlights (ST/ESA/SER.A/423), 2019.

[2] United Nations Population Fund, ed., State of World Population: Unleashing the potential of urban growth, UNFPA, New York, NY, 2007.

[3] T.R. Oke, G. Mills, A. Christen, J.A. Voogt, Urban Climates, Cambridge University Press, Cambridge, 2017. https://doi.org/10.1017/9781139016476.

[4] T. Stocker, D. Qin, eds., Climate change 2013: the physical science basis, International Panel on Climate Change, 2013.

[5] World Health Organization, Quantitative risk assessment of the effects of climate change on selected causes of death, 2030s and 2050s, World Health Organization, 2014. https://apps.who.int/iris/handle/10665/134014 (accessed September 21, 2020).

[6] F. Thomas, C.E. Sabel, K. Morton, R. Hiscock, M.H. Depledge, Extended impacts of climate change on health and wellbeing, Environ. Sci. Policy. 44 (2014) 271–278. https://doi.org/10.1016/j.envsci.2014.08.011.

[7] M. Santamouris, F. Fiorito, On the impact of modified urban albedo on ambient temperature and heat related mortality, Sol. Energy. 216 (2021) 493–507. https://doi.org/10.1016/j.solener.2021.01.031.

[8] O. Andrews, C. Le Quéré, T. Kjellstrom, B. Lemke, A. Haines, Implications for workability and survivability in populations exposed to extreme heat under climate change: a modelling study, Lancet Planet. Health. 2 (2018) e540–e547. https://doi.org/10.1016/S2542-5196(18)30240-7.

[9] T.R. Oke, Boundary layer climates, Second edition, 1987. https://doi.org/10.1017/CBO9781107415324.004.

[10] D. Mauree, E. Naboni, S. Coccolo, A.T.D. Perera, V.M. Nik, J.-L. Scartezzini, A review of assessment methods for the urban environment and its energy sustainability to guarantee climate adaptation of future cities, Renew. Sustain. Energy Rev. 112 (2019) 733–746. https://doi.org/10.1016/j.rser.2019.06.005.

[11] B.J. van Ruijven, E. De Cian, I. Sue Wing, Amplification of future energy demand growth due to climate change, Nat. Commun. 10 (2019) 2762. https://doi.org/10.1038/s41467-019-10399-3.

[12] World Health Organization, Environmental noise guidelines for the European Region, World Health Organization, Copenhagen, Denmark, 2018. http://www.euro.who.int/__data/assets/pdf_file/0008/383921/noise-guidelines-eng.pdf?ua=1 (accessed July 15, 2020).

[13] A. Magrini, A. Lisot, A simplified model to evaluate noise reduction interventions in the urban environment, Build. Acoust. 23 (2016) 36–46. https://doi.org/10.1177/1351010X16637527.

[14] Acoustics Ventilation And Overheating: Residential Design Guide, Association of Noise Consultants, Northallerton, NJ, USA, 2020.

[15] D. Lai, W. Liu, T. Gan, K. Liu, Q. Chen, A review of mitigating strategies to improve the thermal environment and thermal comfort in urban outdoor spaces, Sci. Total Environ. 661 (2019) 337–353. https://doi.org/10.1016/j.scitotenv.2019.01.062.

[16] E. Jamei, P. Rajagopalan, M. Seyedmahmoudian, Y. Jamei, Review on the impact of urban geometry and pedestrian level greening on outdoor thermal comfort, Renew. Sustain. Energy Rev. 54 (2016) 1002–1017. https://doi.org/10.1016/j.rser.2015.10.104.

[17] W. Yang, J.Y. Jeon, Design strategies and elements of building envelope for urban acoustic environment, Build. Environ. 182 (2020).

https://doi.org/10.1016/j.buildenv.2020.107121.

[18] A. Balderrama, J. Kang, A. Prieto, A. Luna-Navarro, D. Arztmann, U. Knaack, Effects of Façades on Urban Acoustic Environment and Soundscape: A Systematic Review, Sustainability. 14 (2022) 9670. https://doi.org/10.3390/su14159670.

[19] R. Aghamolaei, M.M. Azizi, B. Aminzadeh, J. O'Donnell, A comprehensive review of outdoor thermal comfort in urban areas: Effective parameters and approaches, Energy Environ. (2022) 0958305X2211161. https://doi.org/10.1177/0958305X221116176.

[20] S. Alves, L. Estévez-Mauriz, F. Aletta, G.M. Echevarria-Sanchez, V. Puyana Romero, Towards the integration of urban sound planning in urban development processes : the study of four test sites within the SONORUS project, Noise Mapp. 2 (2015) 57–85. https://doi.org/10.1515/noise-2015-0005.

[21] E. Naboni, A. Milella, R. Vadalà, F. Fiorito, On the localised climate change mitigation potential of building facades, Energy Build. 224 (2020). https://doi.org/10.1016/j.enbuild.2020.110284.

[22] J. Strømann-Andersen, P.A. Sattrup, The urban canyon and building energy use: Urban density versus daylight and passive solar gains, Energy Build. 43 (2011) 2011–2020. https://doi.org/10.1016/j.enbuild.2011.04.007.

[23] D. Sung, A New Look at Building Facades as Infrastructure, Engineering. 2 (2016) 63–68. https://doi.org/10.1016/J.ENG.2016.01.008.

[24] E. Naboni, F. Fiorito, Architecture as an outdoor and indoor climate giver, in: Regenarative Des. Digit. Pract. Handb. Built Environ., Eurac Research, 2019.

[25] H. Lee, H. Mayer, Thermal comfort of pedestrians in an urban street canyon is affected by increasing albedo of building walls, Int. J. Biometeorol. 62 (2018) 1199–1209. https://doi.org/10.1007/s00484-018-1523-5.

[26] N. Kántor, J. Unger, The most problematic variable in the course of human-biometeorological comfort assessment — the mean radiant temperature, Open Geosci. 3 (2011). https://doi.org/10.2478/s13533-011-0010-x.

[27] X. Shi, Performance-based and performance-driven architectural design and optimization, Front. Archit. Civ. Eng. China. 4 (2010) 512–518. https://doi.org/10.1007/s11709-010-0090-6.

[28] R. Oxman, Performance-Based Design: Current Practices and Research Issues, Int. J. Archit. Comput. 6 (2008) 1–17. https://doi.org/10.1260/147807708784640090.

[29] B.C. Paulson Jr., Designing to Reduce Construction Costs, J. Constr. Div. 102 (1976) 587–592. https://doi.org/10.1080/19397030902947041.

[30] S. Lu, X. Yan, W. Xu, Y. Chen, J. Liu, Improving auditorium designs with rapid feedback by integrating parametric models and acoustic simulation, Build. Simul. 9 (2016) 235–250. https://doi.org/10.1007/s12273-015-0268-x.

[31] P. Höppe, Different aspects of assessing indoor and outdoor thermal comfort, Energy Build. 34 (2002) 661–665. https://doi.org/10.1016/S0378-7788(02)00017-8.

[32] S. Coccolo, J. Kämpf, J.-L. Scartezzini, D. Pearlmutter, Outdoor human comfort and thermal stress: A comprehensive review on models and standards, Urban Clim. 18 (2016) 33–57. https://doi.org/10.1016/j.uclim.2016.08.004.

[33] O. Potchter, P. Cohen, T.-P. Lin, A. Matzarakis, Outdoor human thermal perception in various climates: A comprehensive review of approaches, methods and quantification, Sci. Total Environ. 631–632 (2018) 390–406. https://doi.org/10.1016/j.scitotenv.2018.02.276.

[34] T.J. Cox, P. D'Antonio, Acoustic absorbers and diffusers: theory, design and application, 3rd ed., Taylor & Francis, Abingdon-on-Thames, Oxfordshire United Kingdom, 2017.

[35] HOSANNA Project, Novel Solutions for Quieter and Grener Cities, 2013.

[36] W. Kropp, J. Forssén, L. Estévez-Mauriz, eds., Urban sound planning: the SONORUS

project, Chalmers University of Technology, Division of Applied Acoustics, Gothenburg, Sweden, 2016.

[37] J. Zacharias, T. Stathopoulos, H. Wu, Spatial Behavior in San Francisco's Plazas: The Effects of Microclimate, Other People, and Environmental Design, Environ. Behav. 36 (2004) 638–658. https://doi.org/10.1177/0013916503262545.

[38] L. Chen, E. Ng, Outdoor thermal comfort and outdoor activities: A review of research in the past decade, Cities. 29 (2012) 118–125. https://doi.org/10.1016/j.cities.2011.08.006.

[39] S.W. Kim, R.D. Brown, Pedestrians' behavior based on outdoor thermal comfort and micro-scale thermal environments, Austin, TX, Sci. Total Environ. 808 (2022) 152143. https://doi.org/10.1016/j.scitotenv.2021.152143.

[40] ANSI/ASHRAE 55-2017, Thermal Environmental Conditions for Human Occupancy, Atlanta, USA, 2017.

[41] B. Givoni, M. Noguchi, H. Saaroni, O. Pochter, Y. Yaacov, N. Feller, S. Becker, Outdoor comfort research issues, Energy Build. 35 (2003) 77–86. https://doi.org/10.1016/S0378-7788(02)00082-8.

[42] M. Nikolopoulou, K. Steemers, Thermal comfort and psychological adaptation as a guide for designing urban spaces, Energy Build. (2003).

[43] P. Ole Fanger, Thermal comfort. Analysis and applications in environmental engineering., Cph. Dan. Tech. Press. (1970).

[44] S. Coccolo, J. Kämpf, J.L. Scartezzini, D. Pearlmutter, Outdoor human comfort and thermal stress: A comprehensive review on models and standards, Urban Clim. 18 (2016) 33–57. https://doi.org/10.1016/j.uclim.2016.08.004.

[45] P. Höppe, The physiological equivalent temperature - a universal index for the biometeorological assessment of the thermal environment, Int. J. Biometeorol. 43 (1999) 71–75. https://doi.org/10.1007/s004840050118.

[46] E. Jamei, P. Rajagopalan, M. Seyedmahmoudian, Y. Jamei, Review on the impact of urban geometry and pedestrian level greening on outdoor thermal comfort, Renew. Sustain. Energy Rev. 54 (2016) 1002–1017. https://doi.org/10.1016/j.rser.2015.10.104.

[47] I. Kousis, A.L. Pisello, For the mitigation of urban heat island and urban noise island: two simultaneous sides of urban discomfort, Environ. Res. Lett. 15 (2020) 103004. https://doi.org/10.1088/1748-9326/abaa0d.

[48] M. Santamouris, Using cool pavements as a mitigation strategy to fight urban heat island—A review of the actual developments, Renew. Sustain. Energy Rev. 26 (2013) 224–240. https://doi.org/10.1016/j.rser.2013.05.047.

[49] J. Wang, Q. Meng, K. Tan, L. Zhang, Y. Zhang, Experimental investigation on the influence of evaporative cooling of permeable pavements on outdoor thermal environment, Build. Environ. 140 (2018) 184–193. https://doi.org/10.1016/j.buildenv.2018.05.033.

[50] G.-E. Kyriakodis, M. Santamouris, Using reflective pavements to mitigate urban heat island in warm climates - Results from a large scale urban mitigation project, Urban Clim. 24 (2018) 326–339. https://doi.org/10.1016/j.uclim.2017.02.002.

[51] M. Santamouris, Cooling the cities – A review of reflective and green roof mitigation technologies to fight heat island and improve comfort in urban environments, Sol. Energy. 103 (2014) 682–703. https://doi.org/10.1016/j.solener.2012.07.003.

[52] M. Hendel, Which pavement structures are best suited to limiting the UHI effect? A laboratory-scale study of Parisian pavement structures, Build. Environ. (2018) 14.

[53] E. Naboni, L. Ofria, E. Danzo, A Parametric Workflow to Conceive Facades as Indoor and Outdoor Climate Givers, (n.d.) 8.

[54] K. Fabbri, J. Gaspari, S. Bartoletti, E. Antonini, Effect of facade reflectance on outdoor

microclimate: An Italian case study, Sustain. Cities Soc. 54 (2020) 101984. https://doi.org/10.1016/j.scs.2019.101984.

[55] H. Lee, H. Mayer, Thermal comfort of pedestrians in an urban street canyon is affected by increasing albedo of building walls, Int. J. Biometeorol. 62 (2018) 1199–1209. https://doi.org/10.1007/s00484-018-1523-5.

[56] L. Mauri, G. Battista, E. de Lieto Vollaro, R. de Lieto Vollaro, Retroreflective materials for building's façades: Experimental characterization and numerical simulations, Sol. Energy. 171 (2018) 150–156. https://doi.org/10.1016/j.solener.2018.06.073.

[57] F. Rosso, I. Golasi, V.L. Castaldo, C. Piselli, A.L. Pisello, F. Salata, M. Ferrero, F. Cotana, A. de Lieto Vollaro, On the impact of innovative materials on outdoor thermal comfort of pedestrians in historical urban canyons, Renew. Energy. 118 (2018) 825–839. https://doi.org/10.1016/j.renene.2017.11.074.

[58] J.A. Acero, E.J.Y. Koh, X. Li, L.A. Ruefenacht, G. Pignatta, L.K. Norford, Thermal impact of the orientation and height of vertical greenery on pedestrians in a tropical area, Build. Simul. 12 (2019) 973–984. https://doi.org/10.1007/s12273-019-0537-1.

[59] B. Jänicke, F. Meier, M.-T. Hoelscher, D. Scherer, Evaluating the Effects of Façade Greening on Human Bioclimate in a Complex Urban Environment, Adv. Meteorol. 2015 (2015) 1–15. https://doi.org/10.1155/2015/747259.

[60] H. Takebayashi, High-Reflectance Technology on Building Façades: Installation Guidelines for Pedestrian Comfort, Sustainability. 8 (2016) 785. https://doi.org/10.3390/su8080785.

[61] E. Erell, D. Pearlmutter, D. Boneh, P.B. Kutiel, Effect of high-albedo materials on pedestrian heat stress in urban street canyons, Urban Clim. 10 (2014) 367–386. https://doi.org/10.1016/j.uclim.2013.10.005.

[62] A. Middel, V.K. Turner, F.A. Schneider, Y. Zhang, M. Stiller, Solar reflective pavements—A policy panacea to heat mitigation?, Environ. Res. Lett. 15 (2020) 064016. https://doi.org/10.1088/1748-9326/ab87d4.

[63] A. Chatzidimitriou, S. Yannas, Microclimate development in open urban spaces: The influence of form and materials, Energy Build. 108 (2015) 156–174. https://doi.org/10.1016/j.enbuild.2015.08.048.

[64] S. Garshasbi, M. Santamouris, Using advanced thermochromic technologies in the built environment: Recent development and potential to decrease the energy consumption and fight urban overheating, Sol. Energy Mater. Sol. Cells. 191 (2019) 21–32. https://doi.org/10.1016/j.solmat.2018.10.023.

[65] M. Zinzi, S. Agnoli, G. Ulpiani, B. Mattoni, On the potential of switching cool roofs to optimize the thermal response of residential buildings in the Mediterranean region, Energy Build. 233 (2021) 110698. https://doi.org/10.1016/j.enbuild.2020.110698.

[66] G. de Roo, Environmental planning and the compact city a dutch perspective, Stud. Environ. Sci. 72 (1998) 1027–1042. https://doi.org/10.1016/S0166-1116(98)80061-7.

[67] I. Douglas, Urban sounds and smells. The noisy, aromatic city, in: Cities Environ. Hist., I.B. Tauris, London, United Kingdom, 2013.

[68] European Union, Decision No 1386/2013/EU of the European Parliament and of the Council of 20 November 2013 on a General Union Environment Action Programme to 2020 "Living well, within the limits of our planet," Off. J. Eur. Union. (2013) 171–200. https://doi.org/10.2779/57220.

[69] World Health Organization, Environmental Noise Guidelines for the European Region, (2018) 160. https://doi.org/10.3390/ijerph14080873.

[70] S. Secchi, A. Astolfi, G. Calosso, D. Casini, G. Cellai, F. Scamoni, C. Scrosati, L. Shtrepi, Effect of outdoor noise and façade sound insulation on indoor acoustic environment of Italian schools, Appl. Acoust. 126 (2017) 120–130. https://doi.org/10.1016/j.apacoust.2017.05.023.

[71] European Commission, Assessment and management of environmental noise (EU Directive), Off. J. Eur. Communities. (2002) 12–25. https://doi.org/10.1016/j.jclepro.2010.02.014.

[72] European Environmental Agency, Noise in Europe 2014, 2014. https://doi.org/10.2800/763331.

[73] M. Jesús, M.D. Fernández, I. Flindell, A.J. Torija, J.A. Ballesteros, Estimating leisure noise in Spanish cities, 86 (2014) 17–24. https://doi.org/10.1016/j.apacoust.2014.04.019.

[74] Arpa Piemonte, Valutazione dell'inquinamento da rumore in ambiente esterno, Torino, Italy, 2018.

[75] E. Ottoz, L. Rizzi, F. Nastasi, Recreational noise: Impact and costs for annoyed residents in Milan and Turin, Appl. Acoust. 133 (2018) 173–181. https://doi.org/10.1016/j.apacoust.2017.12.021.

[76] J. Ballesteros Garrifo, A.J. Torija, M.D. Fernández, J.A. Ballesteros, Differences Between Road Traffic and Leisure Noise in Urban Areas . Developing a Model for Automatic Identification, ACTA Acust. United Acust. 102 (2016) 35–44. https://doi.org/10.3813/AAA.918922.

[77] A. Taghipour, S. Athari, A. Gisladottir, T. Sievers, K. Eggenschwiler, Room Acoustical Parameters as Predictors of Acoustic Comfort in Outdoor Spaces of Housing Complexes, Front. Psychol. 11 (2020) 344. https://doi.org/10.3389/fpsyg.2020.00344.

[78] C. Calleri, L. Shtrepi, A. Armando, A. Astolfi, Evaluation of the influence of building façade design on the acoustic characteristics and auditory perception of urban spaces, Build. Acoust. 25 (2018) 77–95. https://doi.org/10.1177/1351010X18757353.

[79] K. Eggenschwiler, K. Heutschi, A. Taghipour, R. Pieren, A. Gisladottir, B. Schäffer, Urban design of inner courtyards and road traffic noise: Influence of façade characteristics and building orientation on perceived noise annoyance, Build. Environ. 224 (2022) 109526. https://doi.org/10.1016/j.buildenv.2022.109526.

[80] A. Taghipour, T. Sievers, K. Eggenschwiler, Acoustic Comfort in Virtual Inner Yards with Various Building Facades, Int. J. Environ. Res. Public. Health. 16 (2019) 249. https://doi.org/10.3390/ijerph16020249.

[81] J. Kang, Soundscape in city and built environment: current developments and design potentials, City Built Environ. 1 (2023) 1. https://doi.org/10.1007/s44213-022-00005-6.

[82] ISO 12913-1:2014, Acoustics - Soundscape -Part 1: Definition and conceptual framework, International Organization for Standardization, Geneva, Switzerland, 2014.

[83] A. Radicchi, P. Cevikayak Yelmi, A. Chung, P. Jordan, S. Stewart, A. Tsaligopoulos, L. McCunn, M. Grant, Sound and the healthy city, Cities Health. 5 (2021) 1–13. https://doi.org/10.1080/23748834.2020.1821980.

[84] European Commission, Science for Environment Policy (2017) Noise abatement approaches. Future Brief 17, (2017) 28. https://doi.org/10.2779/016648.

[85] J. Krimm, Acoustically effective facade, A+BE | Architecture and the Built Environment, 2018.

[86] J. Picaut, T. Le Pollès, P. L'Heremite, V. Gary, Experimental study of sound propagation in a street, Appl. Acoust. 66 (2005) 149–173. https://doi.org/10.1016/j.apacoust.2004.07.014.

[87] K.K. lu, K.M. Li, The propagation of sound in narrow street canyons., J. Acoust. Soc. Am. 112 (2002) 537–550. https://doi.org/10.1121/1.1492821.

[88] G.M. Echevarria Sanchez, T. Van Renterghem, P. Thomas, D. Botteldooren, The effect of street canyon design on traffic noise exposure along roads, Build. Environ. 97 (2016) 96–110. https://doi.org/10.1016/j.buildenv.2015.11.033.

[89] H. Onaga, J.H. Rindel, Acoustic characteristics of urban streets in relation to scattering caused by building facades, Appl. Acoust. 68 (2007) 310–325. https://doi.org/10.1016/j.apacoust.2006.01.010.

[90] M. Hornikx, J. Forssén, Noise abatement schemes for shielded canyons, Appl. Acoust. 70 (2009) 267–283. https://doi.org/10.1016/j.apacoust.2008.04.002.

[91] T. Van Renterghem, M. Hornikx, J. Forssen, D. Botteldooren, The potential of building envelope greening to achieve quietness, Build. Environ. 61 (2013) 34–44. https://doi.org/10.1016/j.buildenv.2012.12.001.

[92] J. Kang, Numerical modelling of the sound fields in urban streets with diffusely reflecting boundaries, J. Sound Vib. 258 (2002) 793–813. https://doi.org/10.1006/jsvi.2002.5150.

[93] J. Kang, Sound propagation in street canyons : Comparison between diffusely and geometrically reflecting boundaries, J. Acoust. Soc. Am. 107 (2000) 1394–1404. https://doi.org/10.1121/1.428580.

[94] A. Can, N. Fortin, J. Picaut, Accounting for the effect of diffuse reflections and fittings within street canyons, on the sound propagation predicted by ray tracing codes, Appl. Acoust. 96 (2015) 83–93. https://doi.org/10.1016/j.apacoust.2015.03.013.

[95] K. Heutschi, A simple method to evaluate the increase of traffic noise emission level due to buildings, for a long straight street, Appl. Acoust. 44 (1995) 259–274. https://doi.org/10.1016/0003-682X(94)00027-S.

[96] M.R. Ismail, D.J. Oldham, A scale model investigation of sound reflection from building façades, Appl. Acoust. 66 (2005) 123–147. https://doi.org/10.1016/j.apacoust.2004.07.007.

[97] H.H. El Dien, P. Woloszyn, The acoustical influence of balcony depth and parapet form: Experiments and simulations, Appl. Acoust. 66 (2005) 533–551. https://doi.org/10.1016/j.apacoust.2004.09.004.

[98] D.N. May, Freeway noise and high-rise balconies, J. Acoust. Soc. Am. 65 (1979) 699–704. https://doi.org/10.1121/1.382482.

[99] S.K. Tang, C.Y. Ho, T.Y. Tso, Insertion losses of balconies on a building façade and the underlying wave interactions, J. Acoust. Soc. Am. 136 (2014) 213–225. https://doi.org/10.1121/1.4883379.

[100] S.K. Tang, Noise screening effects of balconies on a building facade, J. Acoust. Soc. Am. 118 (2005) 213–221. https://doi.org/10.1121/1.1931887.

[101] Y.G. Tong, S.K. Tang, M.K.L. Yeung, Full scale model investigation on the acoustical protection of a balcony-like façade device (L), J. Acoust. Soc. Am. 130 (2011) 673–676. https://doi.org/10.1121/1.3598430.

[102] P.J. Lee, Y.H. Kim, J.Y. Jeon, K.D. Song, Effects of apartment building façade and balcony design on the reduction of exterior noise, Build. Environ. 42 (2007) 3517–3528. https://doi.org/10.1016/j.buildenv.2006.10.044.

[103] D.J. Oldham, E.A. Mohsen, The acoustical performance of self-protecting buildings, J. Sound Vib. 65 (1979) 557–581. https://doi.org/10.1016/0022-460X(79)90903-9.

[104] W. Kropp, J. Bérillon, A Theoretical Model to Consider the Influence of Absorbing Surfaces Inside the Cavity of Balconies, Acta Acust. United Acust. 86 (2000) 485–494.

[105] D.C. Hothersall, K.V. Horoshenkov, S.E. Mercy, Numerical modelling of the sound field near a tall building with balconies near a road, J. Sound Vib. 198 (1996) 507–515. https://doi.org/10.1006/jsvi.1996.0584.

[106] H. Hossam El Dien, P. Woloszyn, Prediction of the sound field into high-rise building facades due to its balcony ceiling form, Appl. Acoust. 65 (2004) 431–440. https://doi.org/10.1016/j.apacoust.2003.11.002.

[107] E. Badino, R. Manca, L. Shtrepi, C. Calleri, A. Astolfi, Effect of façade shape and acoustic cladding on reduction of leisure noise levels in a street canyon, Build. Environ.

157 (2019) 242–256. https://doi.org/10.1016/j.buildenv.2019.04.039.

[108] P.J. Lee, Y.H. Kim, J.Y. Jeon, K.D. Song, Effects of apartment building façade and balcony design on the reduction of exterior noise, Build. Environ. 42 (2007) 3517–3528. https://doi.org/10.1016/j.buildenv.2006.10.044.

[109] X. Wang, D. Mao, W. Yu, Z. Jiang, Acoustic performance of balconies having inhomogeneous ceiling surfaces on a roadside building facade, Build. Environ. 93 (2015) 1–8. https://doi.org/10.1016/j.buildenv.2015.06.027.

[110] X. Wang, W. Yu, X. Zhu, Z. Jiang, D. Mao, Effects of ceiling phase gradients on the acoustic environment on roadside balconies, J. Acoust. Soc. Am. 141 (2017) EL146–EL152. https://doi.org/10.1121/1.4976192.

[111] T. Crippa, E. Dagnini, G. Davies, H. Rees, Façade Engineering and Soundscape, in: Bern, Switzerland, n.d.

[112] S.K. Tang, C.Y. Ho, T.Y. Tso, Insertion losses of balconies on a building façade and the underlying wave interactions, J. Acoust. Soc. Am. 136 (2014) 213–225. https://doi.org/10.1121/1.4883379.

[113] G.M. Echevarría Sánchez, S. Alves, D. Botteldooren, Urban Sound Planning: An Essential Component in Urbanism and Landscape Architecture, in: F. Aletta, J. Xiao (Eds.), Percept.-Driven Approaches Urban Assess. Des., IGI Global, Hershey, PA, 2018: pp. 1–22. https://doi.org/10.4018/978-1-5225-3637-6.ch001.

[114] L. Shtrepi, A. Astolfi, E. Badino, G. Volpatti, D. Zampini, More Than Just Concrete: Acoustically Efficient Porous Concrete with Different Aggregate Shape and Gradation, Appl. Sci. 11 (2021) 4835. https://doi.org/10.3390/app11114835.

[115] L. Shtrepi, A. Astolfi, E. Badino, G. Volpatti, D. Zampini, Acoustically efficient concrete: acoustic absorption coefficient of porous concrete with different aggregate size, (2020) 4 pages. https://doi.org/10.48465/FA.2020.0721.

[116] K. Monkova, M. Vasina, P.P. Monka, D. Kozak, J. Vanca, Effect of the Pore Shape and Size of 3D-Printed Open-Porous ABS Materials on Sound Absorption Performance, Materials. 13 (2020) 4474. https://doi.org/10.3390/ma13204474.

[117] C. Jiang, D. Moreau, C. Doolan, Acoustic Absorption of Porous Materials Produced by Additive Manufacturing with Varying Geometries, (2017).

[118] C. Arenas, C. Leiva, L.F. Vilches, H. Cifuentes, Use of co-combustion bottom ash to design an acoustic absorbing material for highway noise barriers, Waste Manag. 33 (2013) 2316–2321. https://doi.org/10.1016/j.wasman.2013.07.008.

[119] C. Quintaliani, F. Merli, C.V. Fiorini, M. Corradi, E. Speranzini, C. Buratti, Vegetal Fiber Additives in Mortars: Experimental Characterization of Thermal and Acoustic Properties, Sustainability. 14 (2022) 1260. https://doi.org/10.3390/su14031260.

[120] N. Flores Medina, D. Flores-Medina, F. Hernández-Olivares, Influence of fibers partially coated with rubber from tire recycling as aggregate on the acoustical properties of rubberized concrete, Constr. Build. Mater. 129 (2016) 25–36. https://doi.org/10.1016/j.conbuildmat.2016.11.007.

[121] F. Merli, E. Belloni, C. Buratti, Eco-Sustainable Wood Waste Panels for Building Applications: Influence of Different Species and Assembling Techniques on Thermal, Acoustic, and Environmental Performance, Buildings. 11 (2021) 361. https://doi.org/10.3390/buildings11080361.

[122] G.M. Echevarria Sanchez, T. Van Renterghem, P. Thomas, D. Botteldooren, The effect of street canyon design on traffic noise exposure along roads, Build. Environ. 97 (2016) 96–110. https://doi.org/10.1016/j.buildenv.2015.11.033.

[123] T. Adams, Sound Materials, Frame Publisher, Amsterdam, Netherlands, 2016.

[124] N. Neithalath, J. Weiss, J. Olek, Characterizing Enhanced Porosity Concrete using electrical impedance to predict acoustic and hydraulic performance, Cem. Concr. Res. 36 (2006) 2074–2085. https://doi.org/10.1016/j.cemconres.2006.09.001.

[125] A. Ibrahim, E. Mahmoud, M. Yamin, V.C. Patibandla, Experimental study on Portland cement pervious concrete mechanical and hydrological properties, Constr. Build. Mater. 50 (2014) 524–529. https://doi.org/10.1016/j.conbuildmat.2013.09.022.

[126] M. Scholz, P. Grabowiecki, Review of permeable pavement systems, Build. Environ. 42 (2007) 3830–3836. https://doi.org/10.1016/j.buildenv.2006.11.016.

[127] C. Zhao, P. Wang, L. Wang, D. Liu, Reducing Railway Noise with Porous Sound-Absorbing Concrete Slabs, Adv. Mater. Sci. Eng. 2014 (2014) 1–11. https://doi.org/10.1155/2014/206549.

[128] C. Arenas, L.F. Vilches, H. Cifuentes, C. Leiva, J. Vale, C. Fernández-Pereira, Development of Acoustic Barriers Mainly Composed of Co-Combustion Bottom Ash, in: World Coal Ash WOCA Conf., Denver, CO, United States, 2011.

[129] ACI Committee 522-10, Report on Pervious Concrete, American Concrete Institute, Farmington Hills, MI, United States, 2010.

[130] M. Kovác, A. Sicáková, Pervious Concrete as a Sustainable Solution for Pavementsin Urban Areas, in: Procedings 10th Int. Conf. Environ. Eng., VGTU Technika, Vilnius Gediminas Technical University, Lithuania, 2017. https://doi.org/10.3846/enviro.2017.031.

[131] S.H. Kosmatka, M.L. Wilson, Design and Control of Concrete Mixtures, 15th ed, Portland Cement Association, Skokie, Illinois, USA, 2011.

[132] T.S. Tie, K.H. Mo, A. Putra, S.C. Loo, U.J. Alengaram, T.-C. Ling, Sound absorption performance of modified concrete: A review, J. Build. Eng. 30 (2020) 101219. https://doi.org/10.1016/j.jobe.2020.101219.

[133] P. Sukontasukkul, Use of crumb rubber to improve thermal and sound properties of pre-cast concrete panel, Constr. Build. Mater. 23 (2009) 1084–1092. https://doi.org/10.1016/j.conbuildmat.2008.05.021.

[134] C. Ngohpok, V. Sata, T. Satiennam, P. Klungboonkrong, P. Chindaprasirt, Mechanical Properties, Thermal Conductivity, and Sound Absorption of Pervious Concrete Containing Recycled Concrete and Bottom Ash Aggregates, KSCE J. Civ. Eng. 22 (2018) 1369–1376. https://doi.org/10.1007/s12205-017-0144-6.

[135] S.B. Park, D.S. Seo, J. Lee, Studies on the sound absorption characteristics of porous concrete based on the content of recycled aggregate and target void ratio, Cem. Concr. Res. 35 (2005) 1846–1854. https://doi.org/10.1016/j.cemconres.2004.12.009.

[136] E. Gourlay, Effect of water content on the acoustical and thermal properties of hemp concretes, Constr. Build. Mater. (2017) 11.

[137] P. Glé, E. Gourdon, L. Arnaud, Acoustical properties of materials made of vegetable particles with several scales of porosity, Appl. Acoust. 72 (2011) 249–259. https://doi.org/10.1016/j.apacoust.2010.11.003.

[138] H.K. Kim, H.K. Lee, Acoustic absorption modeling of porous concrete considering the gradation and shape of aggregates and void ratio, J. Sound Vib. 329 (2010) 866–879. https://doi.org/10.1016/j.conbuildmat.2017.09.161.

[139] N. Neithalath, J. Weiss, J. Olek, Acoustic performance and damping behavior of cellulose-cement composites, Cem. Concr. Compos. 26 (2004) 359–370. https://doi.org/10.1016/S0958-9465(03)00020-9.

[140] V. Tiwari, A. Shukla, A. Bose, Acoustic properties of cenosphere reinforced cement and asphalt concrete, Appl. Acoust. (2004) 13.

[141] A. Marolf, N. Neithalath, E. Sell, K. Wegner, J. Weiss, J. Olek, Influence of aggregate size and gradation on acoustic absorption of enhanced porosity concrete, ACI Mater. J. 101 (2004) 82–91.

[142] H.K. Kim, H.K. Lee, Influence of cement flow and aggregate type on the mechanical and acoustic characteristics of porous concrete, Appl. Acoust. (2010) 9. https://doi.org/10.1016/j.apacoust.2010.02.001.

[143] N. Neithalath, J. Weiss, J. Olek, Improving the acoustic absorption of enhanced porosity concrete with fiber reinforcement, in: K. Kovler, J. Marchand, S. Mindess, J. Weiss (Eds.), Int. RILEM Symp. Concr. Sci. Eng. Tribute Arnon Bentur, Evanston, IL, United States, 2004.

[144] H. Kim, J. Hong, S. Pyo, Acoustic characteristics of sound absorbable high performance concrete, Appl. Acoust. 138 (2018) 171–178. https://doi.org/10.1016/j.apacoust.2018.04.002.

[145] N. Neithalath, Development and characterization of acoustically efficient cementitious materials, PhD Thesis, Purdue University, 2004.

[146] ISO 354:2003, Acoustics - Measurement of sound absorption in a reverberation room, International Organization for Standardization, Geneva, Switzerland, 2003.

[147] ISO 17497-1:2004, Acoustics - Sound-scattering properties of surfaces. Part 1: Measurement of the random-incidence scattering coefficient in a reverberation room, International Organization for Standardization, Geneva, Switzerland, 2004.

[148] L. Shtrepi, A. Astolfi, G. D'Antonio, G. Vannelli, G. Barbato, S. Mauro, A. Prato, Accuracy of the random-incidence scattering coefficient measurement, Appl. Acoust. 106 (2016) 23–35. https://doi.org/10.1016/j.apacoust.2015.12.021.

[149] L. Shtrepi, A. Prato, Towards a sustainable approach for sound absorption assessment of building materials: Validation of small-scale reverberation room measurements, Appl. Acoust. 165 (2020) 107304. https://doi.org/10.1016/j.apacoust.2020.107304.

[150] Institute of Technical Acoustics at RWTH Aachen University, ITA-Toolbox for MATLAB®, (n.d.).

[151] ISO 9613-1:1993, Acoustics - Attenuation of sound during propagation outdoors. Part 1: Calculation of the absorption of sound by the atmosphere, International Organization for Standardization, Geneva, Switzerland, 1993.

[152] T.W. Bartel, Effect of absorber geometry on apparent absorption coefficients as measured in a reverberation chamber, J. Acoust. Soc. Am. 69 (1981) 1065–1074. https://doi.org/10.1121/1.385685.

[153] T.F.W. Embleton, Absorption Coefficients of Surfaces Calculated from Decaying Sound Fields, J. Acoust. Soc. Jpn. E. 50 (1971). https://doi.org/10.1121/1.1912704.

[154] C. Scrosati, Towards more reliable measurements of sound absorption coefficient in reverberation rooms: An Inter-Laboratory Test, Appl. Acoust. (2020) 19.

[155] D.-Y. Maa, Microperforated-Panel Wideband Absorbers, Noise Control Eng. J. 29 (1987) 77–84. https://doi.org/10.3397/1.2827694.

[156] S. Kephalopoulos, M. Paviotti, F. Anfosso-Lédée, Common noise assessment methods in Europe (CNOSSOS-EU), Publications Office of the European Union, Luxembourg, 2012. https://data.europa.eu/doi/10.2788/31776 (accessed April 9, 2021).

[157] C. Calleri, A. Astolfi, L. Shtrepi, A. Prato, A. Schiavi, D. Zampini, G. Volpatti, Characterization of the sound insulation properties of a two-layers lightweight concrete innovative façade, Appl. Acoust. 145 (2019) 267–277. https://doi.org/10.1016/j.apacoust.2018.10.003.

[158] ISO 11654:1997, Acoustics - Sound absorbers for use in buildings – Rating of sound absorption, International Organization for Standardization, Geneva, Switzerland, 1997.

[159] H. Onaga, J.H. Rindel, Acoustic characteristics of urban streets in relation to scattering caused by building facades, Appl. Acoust. (2007) 16.

[160] J. Picaut, D. Scouarnec, Using Acoustic Diffusors to Reduce Noise in Urban Areas, Acta Acust. United Acust. 95 (2009) 653–668. https://doi.org/10.3813/AAA.918194.

[161] M. Vorländer, Auralization: Fundamentals of Acoustics, Modelling, Simulation, Algorithms and Acoustic Virtual Reality, Springer Science+Business Media LLC, Berlin, Germany, 2008.

[162] ISO 17497-2:2012, Acoustics - Sound-scattering properties of surfaces. Part 2:

Measurement of the directional diffusion coefficient in a free field, International Organization for Standardization, Geneva, Switzerland, 2012.

[163] L. Shtrepi, Diffusive surface design guidelines, in: 8th Congr. Alps Adria Acoust. Assoc., 2018.

[164] L. Shtrepi, Advances in diffusive surface design using 3D architectural parametric modelling programs, in: Proc. 23rd Int. Congr. Acoust., 2019: pp. 2289–2296.

[165] D. Bradley, A. Sharma, J. Adelgren, Assessing the effectiveness of geometrically modified pyramidal diffusers: Scattering coefficient measurements, Proc. Meet. Acoust. 20 (2014). https://doi.org/10.1121/1.4862776.

[166] F.M. Lin, P.Y. Hong, C.Y. Lee, An experimental investigation into the sound-scattering performance of wooden diffusers with different structures, Appl. Acoust. 71 (2010) 68–78. https://doi.org/10.1016/j.apacoust.2009.06.005.

[167] Y.H. Kim, H.S. Jang, J.Y. Jeon, Characterizing diffusive surfaces using scattering and diffusion coefficients, Appl. Acoust. 72 (2011) 899–905. https://doi.org/10.1016/j.apacoust.2011.05.006.

[168] Y. Tsuchiya, H. Lee, T. Sakuma, Scale model measurement of the scattering coefficients of rib/block structure walls, AIJ J. Technol. Des. 19 (2013) 175–178. https://doi.org/10.3130/aijt.19.175.

[169] Y.J. Choi, Effects of periodic type diffusers on classroom acoustics, Appl. Acoust. 74 (2013) 694–707. https://doi.org/10.1016/j.apacoust.2012.11.010.

[170] H. Lee, Y. Tsuchiya, T. Sakuma, Acoustic scattering characteristics of Penrose-tiling-type diffusers, Appl. Acoust. 130 (2018) 168–176. https://doi.org/10.1016/j.apacoust.2017.08.022.

[171] J.Y. Jeon, S.C. Lee, M. Vorländer, Development of scattering surfaces for concert halls, Appl. Acoust. 65 (2004) 341–355. https://doi.org/10.1016/j.apacoust.2003.11.001.

[172] I. Schmich-Yamane, M. Malgrange, C. Rougier, How absorptive can a diffuser be to accurately measure random incidence scattering coefficients?, Proc. Meet. Acoust. 19 (2013). https://doi.org/10.1121/1.4798985.

[173] T. Sakuma, H. Lee, Recent Topics in Acoustic Scattering Coefficient Determination for Wall Surfaces, Build. Acoust. 21 (2014).

[174] L. De Geetere, G. Vermeir, Investigations on real-scale experiments for the measurement of the ISO scattering coefficient in the reverberation room, in: Proc. Forum Acoust., Sevilla, Spain, 2002.

[175] C. Bibby, M. Hodgson, Characterization and improvement of absorption and scattering by profiled architectural surfaces without specialized test facilities, Appl. Acoust. 72 (2011) 889–898. https://doi.org/10.1016/j.apacoust.2011.05.003.

[176] T.J. Cox, Room acoustics diffusers: Pyramids and wedges, 24th Int. Congr. Sound Vib. ICSV 2017. (2017).

[177] E. Badino, G. Autretto, S. Fantucci, M. Zinzi, V. Serra, Laboratory and In-situ assessment of thermochromic coatings for building application: Testing on dynamic properties and photodegradation, in: COBEE 2022, Montreal, Canada, 2022.

[178] M. Santamouris, Minimizing Energy Consumption, Energy Poverty and Global and Local Climate Change in the Built Environment: Innovating to Zero, 1st ed., Elsevier, 2019. https://doi.org/10.1016/C2016-0-01024-0.

[179] F. Favoino, L. Giovannini, A. Pellegrino, V. Serra, Building performance of thermochromic glazing, in: Eco-Effic. Mater. Reducing Cool. Needs Build. Constr., Elsevier, 2021: pp. 401–437. https://doi.org/10.1016/B978-0-12-820791-8.00017-1.

[180] M. Santamouris, A. Synnefa, T. Karlessi, Using advanced cool materials in the urban built environment to mitigate heat islands and improve thermal comfort conditions, Sol. Energy. 85 (2011) 3085–3102. https://doi.org/10.1016/j.solener.2010.12.023.

[181] B. Park, M. Krarti, Energy performance analysis of variable reflectivity envelope systems for commercial buildings, Energy Build. 124 (2016) 88–98. https://doi.org/10.1016/j.enbuild.2016.04.070.

[182] V. Granadeiro, M. Almeida, T. Souto, V. Leal, J. Machado, A. Mendes, Thermochromic Paints on External Surfaces: Impact Assessment for a Residential Building through Thermal and Energy Simulation, Energies. 13 (2020) 1912. https://doi.org/10.3390/en13081912.

[183] J. Roxon, Urban heat island impact on state residential energy cost and CO2 emissions in the United States, Urban Clim. (2020) 10.

[184] M. Zinzi, E. Carnielo, B. Mattoni, On the relation between urban climate and energy performance of buildings. A three-years experience in Rome, Italy, Appl. Energy. 221 (2018) 148–160. https://doi.org/10.1016/j.apenergy.2018.03.192.

[185] Z. Yuxuan, Z. Yunyun, Y. Jianrong, Z. Xiaoqiang, Energy saving performance of thermochromic coatings with different colors for buildings, Energy Build. 215 (2020) 109920. https://doi.org/10.1016/j.enbuild.2020.109920.

[186] A. Seeboth, D. Lötzsch, R. Ruhmann, O. Muehling, Thermochromic Polymers—Function by Design, Chem. Rev. 114 (2014) 3037–3068. https://doi.org/10.1021/cr400462e.

[187] S. Zheng, Y. Xu, Q. Shen, H. Yang, Preparation of thermochromic coatings and their energy saving analysis, Sol. Energy. 112 (2015) 263–271. https://doi.org/10.1016/j.solener.2014.09.049.

[188] T. Karlessi, M. Santamouris, K. Apostolakis, A. Synnefa, I. Livada, Development and testing of thermochromic coatings for buildings and urban structures, Sol. Energy. 83 (2009) 538–551. https://doi.org/10.1016/j.solener.2008.10.005.

[189] Y. Ma, B. Zhu, K. Wu, Preparation of reversible thermochromic building coatings and their properties, J. Coat. Technol. 72 (2000) 67–71. https://doi.org/10.1007/BF02720527.

[190] J. Hu, X. (Bill) Yu, Innovative thermochromic asphalt coating: characterisation and thermal performance, Road Mater. Pavement Des. 17 (2016) 187–202. https://doi.org/10.1080/14680629.2015.1068215.

[191] J. Hu, X. Yu, Performance evaluation of solar-responsive asphalt mixture with thermochromic materials and nano-TiO2 scatterers, Constr. Build. Mater. 247 (2020) 118605. https://doi.org/10.1016/j.conbuildmat.2020.118605.

[192] T. Karlessi, M. Santamouris, Improving the performance of thermochromic coatings with the use of UV and optical filters tested under accelerated aging conditions, Int. J. Low-Carbon Technol. 10 (2015) 45–61. https://doi.org/10.1093/ijlct/ctt027.

[193] M. Calovi, F. Russo, S. Rossi, Esthetic performance of thermochromic pigments in cataphoretic and sprayed coatings for outdoor applications, J. Appl. Polym. Sci. 138 (2021) 50622. https://doi.org/10.1002/app.50622.

[194] J. Mutanen, T. Jaaskelainen, J.P.S. Parkkinen, Thermochromism of fluorescent colors, Color Res. Appl. 30 (2005) 163–171. https://doi.org/10.1002/col.20104.

[195] S.K. Goswami, T.S. Kim, E. Oh, Optical properties and effect of carrier tunnelling in CdSe colloidal quantum dots: A comparative study with different ligands, AIP Adv. (2012).

[196] S.F. Wuister, A. van Houselt, C. de Mello Donegá, D. Vanmaekelbergh, A. Meijerink, Temperature Antiquenching of the Luminescence from Capped CdSe Quantum Dots, Angew. Chem. Int. Ed. 43 (2004) 3029–3033. https://doi.org/10.1002/anie.200353532.

[197] S.F. Wuister, C. de M. Donega, A. Meijerink, Luminescence Temperature Antiquenching of Water-Soluble CdTe Quantum Dots: Role of the Solvent, (2004).

[198] W. Caseri, Color switching in nanocomposites comprising inorganic nanoparticles dispersed in a polymer matrix, J. Mater. Chem. 20 (2010) 5582.

https://doi.org/10.1039/b926280f.

[199] L. Hu, Stabilization of 2D assemblies of silver nanoparticles by spin-coating polymers, Appl. Surf. Sci. (2015).

[200] D. Josephson, A. Stein, Tuning Color and Chroma of Opal and Inverse Opal Structures, in: Responsive Photonic Nanostructures Smart Nanoscale Opt. Mater., The Royal Society of Chemistry, 2013: pp. 63–90. https://doi.org/10.1039/9781849737760-00063.

[201] Z.-Z. Gu, S. Kubo, W. Qian, Y. Einaga, D.A. Tryk, A. Fujishima, O. Sato, Varying the Optical Stop Band of a Three-Dimensional Photonic Crystal by Refractive Index Control, Langmuir. 17 (2001) 6751–6753. https://doi.org/10.1021/la0110186.

[202] ASTM E220-19, Standard Test Method for Calibration of Thermocouples By Comparison Techniques, ASTM International, West Conshohocken, PA, United States, 2019. https://www.astm.org/e0220-19.html.

[203] Hukseflux, Measuring albedo of finite samples, 2007.

[204] ISO 9050.2003, Glass in building - Determination of light transmittance, solar direct transmittance, total solar energy transmittance, ultraviolet transmittance and related glazing factors, International Organization for Standardization, Geneva, Switzerland, 2003.

[205] ISO 11664-4:2019, Colorimetry - Part 4: CIE 1976 L*a*b* colour space, International Organization for Standardization, Geneva, Switzerland, 2019.

[206] ISO 6946:2017, Building components and building elements - Thermal resistance and thermal transmittance - Calculation methods, International Organization for Standardization, Geneva, Switzerland, 2017.

[207] L. Giovannini, F. Favoino, A. Pellegrino, V.R.M. Lo Verso, V. Serra, M. Zinzi, Thermochromic glazing performance: From component experimental characterisation to whole building performance evaluation, Appl. Energy. 251 (2019) 113335. https://doi.org/10.1016/j.apenergy.2019.113335.

[208] E. Badino, L. Shtrepi, A. Astolfi, Acoustic Performance-Based Design: A Brief Overview of the Opportunities and Limits in Current Practice, Acoustics. 2 (2020) 246–278. https://doi.org/10.3390/acoustics2020016.

[209] X. Shi, Performance-based and performance-driven architectural design and optimization, Front. Archit. Civ. Eng. China. 4 (2010) 512–518. https://doi.org/10.1007/s11709-010-0090-6.

[210] X. Shi, W. Yang, Performance-driven architectural design and optimization technique from a perspective of architects, Autom. Constr. 32 (2013) 125–135. https://doi.org/10.1016/j.autcon.2013.01.015.

[211] M. Turrin, P. Von Buelow, R. Stouffs, Design explorations of performance driven geometry in architectural design using parametric modeling and genetic algorithms, Adv. Eng. Inform. 25 (2011) 656–675. https://doi.org/10.1016/j.aei.2011.07.009.

[212] Y.J. Grobman, R. Ron, Digital Form Finding, in: 29th ECAADe, Ljubljana, Slovenia, 2011: pp. 107–115. https://doi.org/10.1007/SpringerReference_168556.

[213] Y.T. Chong, C.H. Chen, K.F. Leong, A heuristic-based approach to conceptual design, Res. Eng. Des. 20 (2009) 97–116.

[214] J. Wang, Improved engineering design concept selection using fuzzy sets, 3052 (2010). https://doi.org/10.1080/09511920110034996.

[215] T. Méndez Echenagucia, A. Capozzoli, Y. Cascone, M. Sassone, The early design stage of a building envelope: Multi-objective search through heating, cooling and lighting energy performance analysis, Appl. Energy. 154 (2015) 577–591. https://doi.org/10.1016/j.apenergy.2015.04.090.

[216] S. Lu, X. Yan, J. Li, W. Xu, The influence of shape design on the acoustic performance of concert halls from the viewpoint of acoustic potential of shapes, Acta Acust. United

Acust. 102 (2016) 1027–1044. https://doi.org/10.3813/AAA.919017.

[217] S. Marble, Digital Workflows in Architecture: Design–Assembly–Industry, Birkhauser, Basel, Switzerland, 2012.

[218] T. Méndez Echenagucia, Computational Search in Architectural Design, PhD Thesis, PhD Thesis, Polytechnic University of Turin, Turin, Italy, 2013.

[219] D. Reinhardt, W.L. Martens, L. Miranda, Acoustic Consequences of Performative Structures - Modelling dependencies between spatial formation and acoustic behaviour, in: Digit. Phys. Proc. 30th ECAADe Conf., 2012: pp. 577–586.

[220] R. Becker, Fundamentals of performance-based building design, Build. Simul. 1 (2008) 356–371. https://doi.org/10.1007/s12273-008-8527-8.

[221] M. Hensel, Performance-Oriented Architecture: Rethinking Architectural Design and the Built Environment, 2013. https://doi.org/10.1002/9781118640630.

[222] B. Kolarevic, A. Malkawi, Performative Architecture: Beyond Instrumentality, 2005. https://doi.org/10.1111/j.1531-314X.2006.00068_1.x.

[223] D. Holzer, Design exploration supported by digital tool ecologies, Autom. Constr. 72 (2016) 3–8. https://doi.org/10.1016/j.autcon.2016.07.003.

[224] M.B. Jensen, Robotic Fabrication of Acoustic Geometries - an explorative and creative design process within an educational context, Archi DOCT. 6 (2019) 1–116.

[225] R. Oxman, Performance-Based Design: Current Practices and Research Issues, Int. J. Archit. Comput. 6 (2008) 1–17. https://doi.org/10.1260/147807708784640090.

[226] R. Oxman, Theory and design in the first digital age, Des. Stud. 27 (2006) 229–265. https://doi.org/10.1016/j.destud.2005.11.002.

[227] D. Rutten, Grasshopper, (n.d.). http://www.grasshopper3d.com/ (accessed March 18, 2020).

[228] Rhinoceros, (n.d.). http://www.rhino3d.com/ (accessed March 18, 2020).

[229] GenerativeComponents, (n.d.). https://www.bentley.com/en/products/product-line/modeling-and-visualization-software/generativecomponents (accessed March 18, 2020).

[230] F. Flager, J. Haymaker, A comparison of multidisciplinary design, analysis and optimization processes in the building construction and aerospace industries, 24th W78 Conf. Bringing ITC Knowl. Work. (2007) 625–630. https://doi.org/10.2340/16501977-0278.

[231] D. Rutten, Galapagos, (n.d.). http://www.grasshopper3d.com/group/galapagos (accessed March 18, 2020).

[232] R. Vierlinger, Octopus, (n.d.). http://www.food4rhino.com/app/octopus (accessed March 18, 2020).

[233] M. Tang, J. Anderson, A. Aksamija, M. Hodge, Performace-based Generative Design: An investigation of the parametric nature of architecture, Proc. 100th ACSA Annu. Conf. Digit. Aptit. 2 (2012) 1–8.

[234] A. Bassuet, Computational and Optimization Design in Geometric Acoustics, (2013) 1–10.

[235] T. Takenaka, A. Okabe, A Computational Method for Integrating Parametric Origami Design and Acoustic Engineering, Comput. Performance–Proceedings 31st Int. Conf. Educ. Res. Comput. Aided Archit. Des. Eur. ECAADe 31. 2 (2013) 289–296.

[236] S. Di Blasio, L. Shtrepi, G.E. Puglisi, A. Astolfi, A cross-sectional survey on the impact of irrelevant speech noise on annoyance, mental health and well-being, performance and occupants' behavior in shared and open-plan offices, Int. J. Environ. Res. Public. Health. 16 (2019). https://doi.org/10.3390/ijerph16020280.

[237] J. Reinten, P.E. Braat-Eggen, M. Hornikx, H.S.M. Kort, A. Kohlrausch, The indoor sound environment and human task performance: A literature review on the role of

room acoustics, Build. Environ. 123 (2017) 315–332. https://doi.org/10.1016/j.buildenv.2017.07.005.

[238] ISO 3382-1:2009, Acoustics - Measurement of room acoustic parameters. Part 1: Performance spaces, International Organization for Standardization, Geneva, Switzerland, 2009.

[239] L. Shtrepi, A. Astolfi, G. D'Antonio, M. Guski, Objective and perceptual evaluation of distance-dependent scattered sound effects in a small variable-acoustics hall, J. Acoust. Soc. Am. 140 (2016) 3651–3662. https://doi.org/10.1121/1.4966267.

[240] E. Bo, A. Astolfi, A. Pellegrino, D. Pelegrin-Garcia, G.E. Puglisi, L. Shtrepi, M. Rychtarikova, The modern use of ancient theatres related to acoustic and lighting requirements: Stage design guidelines for the Greek theatre of Syracuse, Energy Build. 95 (2015) 106–115. https://doi.org/10.1016/j.enbuild.2014.12.037.

[241] Odeon, (n.d.). http://odeon.dk/ (accessed March 18, 2020).

[242] CATT-Acoustic, (n.d.). https://www.catt.se/ (accessed March 18, 2020).

[243] A. Van der Harten, Pachyderm Acoustics, (n.d.). https://www.orase.org/resources (accessed March 14, 2022).

[244] T. Lokki, A. Southern, S. Siltanen, L. Savioja, Acoustics of epidaurus - Studies with room acoustics modelling methods, Acta Acust. United Acust. 99 (2013) 40–47. https://doi.org/10.3813/AAA.918586.

[245] L. Shtrepi, B. Hamilton, A. Astolfi, M. Masoero, Preliminary results of scattering surface modeling and perceptual aspects in wave-based acoustic simulations, in: 23rd Int. Congr. Acoust., Aachen, Germany, 2019: pp. 5990–5993. https://doi.org/DOI:10.18154/RWTH-CONV-239276.

[246] D.D. Orazio, G. Fratoni, A. Rovigatti, B. Hamilton, Numerical simulations of Italian opera houses using geometrical and wave-based acoustics methods, in: 23rd Int. Congr. Acoust., Aachen, Germany, 2019: pp. 5994–5996.

[247] K. Negendahl, Building performance simulation in the early design stage: An introduction to integrated dynamic models, Autom. Constr. 54 (2015) 39–53. https://doi.org/10.1016/j.autcon.2015.03.002.

[248] G. Mirra, E. Pignatelli, S. Di Rosario, An automated design methodology for acoustic shells in outdoor concerts, in: Proc. Euronoise, Crete, Greece, 2018: pp. 2123–2130.

[249] B. Peters, Parametric Acoustic Surfaces, Assoc. Comput. Aided Des. Archit. (2007) 174–181.

[250] B. Peters, Integrating Acoustic Analysis in the Architectural Design Process using Parametric Modeling, Forum Acusticum. (2011) 1589–1594.

[251] T. Wortmann, B. Tunçer, Differentiating parametric design: Digital workflows in contemporary architecture and construction, Des. Stud. 52 (2017) 173–197. https://doi.org/10.1016/j.destud.2017.05.004.

[252] Scopus, (n.d.). https://www.scopus.com (accessed March 18, 2020).

[253] Research Gate, (n.d.). https://www.researchgate.net/ (accessed March 18, 2020).

[254] Alias System Corporation, Autodesk, Autodesk Maya, (n.d.). https://www.autodesk.com/products/maya/overview.

[255] C. Day, H. Marshall, T. Scelo, J. Valentine, P. Exton, The Philharmonie de Paris - Acoustic design and commissioning, in: Proc. Acoust. 2016 - Second Australas. Acoust. Soc. Conf., Brisbane, Australia, 2016: pp. 1–15.

[256] J. McGar, The Acoustic Feats of the World's Costliest Concert Hall, (2015). https://sourceable.net/acoustic-feats-worlds-costliest-concert-hall/ (accessed March 18, 2020).

[257] Philharmonie de Paris, (n.d.). http://www.nagata.co.jp/e{_}sakuhin/factsheets/PdP.pdf (accessed March 18, 2020).

[258] H. Marshall, Implementing the acoustical concept for the Philharmonie de Paris, Grande Salle, in: Proc. Inst. Acoust., Paris, France, 2015: pp. 118–127.

[259] E. Kahle, T. Wulfrank, Y. Jurkiewicz, N. Faillet, Philharmonie de Paris - The Acoustic Brief, in: Proc. Inst. Acoust., Paris, France, 2015: pp. 105–110.

[260] T. Scelo, Integration of acoustics in parametric architectural design, Acoust. Aust. 43 (2015) 59–67. https://doi.org/10.1007/s40857-015-0014-7.

[261] Philharmonie de Paris - Information Sheet, (n.d.). http://www.kahleacoustics.com/en/ref/philharmonie.html{\#} (accessed March 18, 2020).

[262] N. Khan, An algorithm designed a Hamburg concert hall's interior, creating the ideal acoustic experience, (2017). https://qz.com/894929/an-algorithm-designed-a-hamburg-concert-halls-interior-creating-the-ideal-acoustic-experience/ (accessed March 18, 2020).

[263] Elbphilharmonie Hamburg Grosser Saal, (n.d.). http://www.nagata.co.jp/e{_}sakuhin/factsheets/Elbphilharmonie.pdf (accessed March 18, 2020).

[264] E. Stinson, What happens when algorithms design a concert hall? The stunning Elbphilharmonie, (2017). https://www.wired.com/2017/01/happens-algorithms-design-concert-hall-stunning-elbphilharmonie/ (accessed March 18, 2020).

[265] K. Oguchi, Highlights of Room Acoustics and Sound Isolation Design, (2017). http://www.nagata.co.jp/e{_}news/news1702-e.html (accessed March 18, 2020).

[266] Architectural Details: Herzog & de Meuron's Spectacular Elbphilharmonie, (2016). https://architizer.com/blog/architectural-details-herzog-de-meuron-elbphilharmonie/. (accessed March 18, 2020).

[267] E. Mommertz, E. Kahle, The Bochum Concert Hall - The challenge of small concert halls for large orchestras on low budget, in: Proc. Inst. Acoust., Cardiff, United Kingdom, 2018: pp. 174–181.

[268] Anneliese Brost Musikforum Ruhr, (n.d.). https://www.architonic.com/en/project/bez-kock-architekten-anneliese-brost-musikforum-ruhr/5106249 (accessed March 18, 2020).

[269] Musikzentrum Bochum - Information Sheet, (n.d.). http://www.khale.be/en/ref/bochum.html{\#} (accessed March 18, 2020).

[270] Y. Nishiyama, Miura folding: Applying Origami to space exploration, Int. J. Pure Appl. Math. 79 (2012) 269–279.

[271] Ureshino Cultural Center / 2014, (n.d.). http://www.suep.jp/Ureshino{_}cultural{_}center/text{_}inE.html (accessed March 18, 2020).

[272] @Last Software, Google, SketchUp, (n.d.). https://www.sketchup.com/.

[273] Autodesk Revit, (n.d.). http://www.autodesk.com/revit.

[274] R. Garber, Workflows: Expanding Architecture's Territory in the Design and Delivery of Buildings., John Wiley & Sons, Hoboken, NJ, 2017.

[275] Theatroacoustic System for University of Iowa Concert Hall, (n.d.). https://lmnarchitects.com/case-study/theatroacoustic-system-concert-hall (accessed March 18, 2020).

[276] J. Cornachio, Behind the Building: Voxman Music Building by LMN Architects, (n.d.). https://architizer.com/blog/practice/materials/behind-voxman-music-building/ (accessed March 18, 2020).

[277] Y. Jurkiewicz, T. Wulfrank, E. Kahle, Architectural shape and early acoustic efficiency in concert halls (L), J. Acoust. Soc. Am. 132 (2012) 1253–1256. https://doi.org/10.1121/1.4740493.

[278] Y. Jurkiewicz, H. Moller, T. Wulfrank, J. Wang, E. Kahle, Acoustic optimization of

curved architecture in practice : the new Straight Cultural Arts Center in Fuzhou, in: Proc. ISRA 2019, Amsterdam, Netherlands, 2019: pp. 401–408.

[279] T. Wulfrank, Y. Jurkiewicz, E. Kahle, Design-Focused Acoustic Analysis of Curved Geometries using a Differential Raytracing Technique, 21 (2014) 87–96.

[280] J.Ó. García Gòmez, E. Kahle, T. Wulfrank, Shaping concert halls, in: Proc. EuroRegio, Porto, Portugal, 2016.

[281] CATIA, (n.d.). http://www.3ds.com/products-services/catia/.

[282] Square One Research, Autodesk, Ecotect Analysis, (n.d.). https://www.autodesk.com/education/free-software/ecotect-analysis.

[283] J. Minutillo, When the Whole Is Greater Than the Sum of Its Parts, (2009). https://continuingeducation.bnpmedia.com/courses/areditorial/when-the-whole-is-greater-than-the-sum-of-its-parts/ (accessed March 18, 2020).

[284] The Conga Room / Belzberg Architects, (2011). http://www.archdaily.com/160584/the-conga-room-belzberg-architects (accessed March 18, 2020).

[285] Conga Room at LA Live, (n.d.). http://belzbergarchitects.com/project/conga-room/ (accessed March 18, 2020).

[286] The Conga Room, Los Angeles, (n.d.). http://www.designcurial.com/projects/the{_}conga{_}room{_}los{_}angeles (accessed March 18, 2020).

[287] Dynamo, (n.d.). http://dynamobim.org/.

[288] D. Fang, Shells for the senses: the multidisciplinary success of Stage by the Sea, (2016). https://formfindinglab.wordpress.com/2016/09/21/shells-for-the-senses-the-multidisciplinary-success-of-stage-by-the-sea/ (accessed March 18, 2020).

[289] J. Flanagan, Acoustic Shells, Shotcrete. (2015) 16–19. https://shotcrete.org/wp-content/uploads/2020/01/2015Win{_}Flanagan-International.pdf (accessed April 28, 2020).

[290] A. Griffiths, Shell-shaped shelter by Flanagan Lawrence built on Littlehampton seafront, (2014). https://www.dezeen.com/2014/07/22/flanagan-lawrence-acoustic-shells-shelter-stage-littlehampton/ (accessed March 18, 2020).

[291] Flanagan Lawrence – Acoustic Shells, (n.d.). https://theplan.it/eng/webzine/the-plan-award-2015/acoustic-shells{\#}sthash.XmPPnnkv.dpbs (accessed March 18, 2020).

[292] Acoustic Shells, (n.d.). http://flanaganlawrence.com/project/acoustic-shells/ (accessed March 18, 2020).

[293] Soundforms, (n.d.). https://www.flanaganlawrence.com/soundforms (accessed March 18, 2020).

[294] The Park's Bandstand - A built environment story, (n.d.). http://www.beyond2012.org.uk/sounforms-the-parks-bandstand/ (accessed March 18, 2020).

[295] P. Bavister, Soundforms, (n.d.) 405–421. https://www.academia.edu/6385238/The{_}design{_}development{_}and{_}fabrication{_}of{_}a{_}11{_}scale{_}mobile{_}acoustic{_}performance{_}shell{_}prototype (accessed April 28, 2020).

[296] W. Boning, A. Acoustics, A. Bassuet, T. Rise, G. Shell, A Room Without Walls: Optimizing an Outdoor Music Shell To Maintain Views and Maximize, 37 (2014) 332–341.

[297] I.W. Foged, A. Pasold, M. Brath, Acoustic Environments: Applying Evolutionary Algorithms for Sound Based Morphogenesis, Digit. Phys. Proc. 30th ECAADe Conf. (2012) 347–353.

[298] A. Furuto, Acoustic Environments / AREA and Electrotexture Lab, (2011). https://www.archdaily.com/170078/acoustic-environments-area-and-electrotexture-

lab (accessed March 18, 2020).

[299] I.W. Foged, A. Pasold, M.B. Jensen, Evolution of an Instrumental Architecture, ECAADe2014 - Fusion - Proc. 32nd ECAADe Conf. 2 (2014) 365–372.

[300] D. Piker, Kangaroo, (n.d.). http://kangaroo3d.com/.

[301] Resonant Chamber, (n.d.). http://www.rvtr.com/projects/resonant-chamber (accessed March 18, 2020).

[302] L. Anderson, Origami In Stereo: Welcome To The Sound Cloud!, (n.d.). https://architizer.com/blog/resonant-chamber-rvtr/ (accessed March 18, 2020).

[303] J. Filipetti, rvtr: resonant chamber origami architectural acoustic panels, (n.d.). http://www.designboom.com/technology/rvtr-resonant-chamber-origami-architectural-acoustic-panels/ (accessed March 18, 2020).

[304] L. Grozdanic, Resonant Chamber is an Acoustically Responsive Envelope, (n.d.). http://www.evolo.us/architecture/resonant-chamber-is-an-acoustically-responsive-envelope/ (accessed March 18, 2020).

[305] G. Thün, K. Velikov, C. Ripley, L. Sauvé, W. McGee, Soundspheres: Resonant Chamber, Leonardo. 45 (2012) 348–357. https://doi.org/10.1162/LEON_a_00409.

[306] B. Peters, Acoustic Performance as a Design Driver: Sound Simulation and Parametric Modeling using SmartGeometry, Int. J. Archit. Comput. 8 (2011) 337–358. https://doi.org/10.1260/1478-0771.8.3.337.

[307] B. Peters, The Smithsonian Courtyard Enclosure: A case-study of digital design processes, Acadia 2007. (2007) 74–83.

[308] Smithsonian Institution, (n.d.). http://www.bradypeters.com/smithsonian.html (accessed March 18, 2020).

[309] Smithsonian selects Norman Foster to Design New Atrium for Historic Home of two Museum, (n.d.). https://www.fosterandpartners.com/news/archive/2004/03/smithsonian-selects-norman-foster-to-design-new-atrium-for-historic-home-of-two-museums/ (accessed March 18, 2020).

[310] N. Williams, J. Burry, D. Davis, B. Peters, A. Pena De Leon, M. Burry, FabPod: Designing with temporal flexibility & relationships to mass-customisation, Autom. Constr. 51 (2015) 124–131. https://doi.org/10.1016/j.autcon.2014.12.001.

[311] N. Williams, D. Davis, B. Peters, A. Pena de Leon, J. Burry, M. Burry, Fabpod: an open design-to-fabrication system, in: Proc. 18th Conf. Comput.-Aided Archit. Des. Res. Asia CAADRIA, 2013: pp. 251–260.

[312] J. Burry, N. Williams, J. Cherrey, B. Peters, Fabpod: Universal Digital Workflow , Local Prototype Materialization, in: Proc. CAAD Futur., Shanghai, China, 2013: pp. 176–186.

[313] M. Burry, FabPod, (n.d.). https://mcburry.net/fabpod/ (accessed March 18, 2020).

[314] D. Davis, FabPod, (n.d.). https://www.danieldavis.com/fabpod/ (accessed March 18, 2020).

[315] B. Peters, Integrating acoustic simulation in architectural design workflows: The FabPod meeting room prototype, Simulation. 91 (2015) 787–808. https://doi.org/10.1177/0037549715603480.

[316] K. Wong, Shaped by Number, (2010). http://www.cgw.com/Publications/CGW/2010/Volume-33-Issue-9-October-2010-/Shaped-by-Number.aspx (accessed March 18, 2020).

[317] B. Peters, Complex Surfaces – Sound and Space Defining Surfaces for Architecture, (n.d.). https://kadk.dk/case/complex-surfaces-sound-and-space-defining-surfaces-architecture (accessed March 18, 2020).

[318] Manufacturing Parametric Acoustic Surfaces, (n.d.). http://www.bradypeters.com/smartgeometry-2010.html (accessed March 18, 2020).

[319] B. Peters, M. Tamke, S.A. Nielsen, S. Vestbjerg Andersen, M. Haase, Responsive Acoustic Surfaces, in: Respect. Fragile Places 29th ECAADe Conf. Proc., Ljubljana, Slovenia, 2011: pp. 819–828.

[320] D. Pelegrín-García, Comment on " Increase in voice level and speaker comfort in, 2082 (2017). https://doi.org/10.1121/1.3543940.

[321] Project Distortion II, (n.d.). http://www.bradypeters.com/project-distortion-ii.html (accessed March 18, 2020).

[322] SU2Odeon plugin for SketchUp, (n.d.). https://odeon.dk/downloads/su2odeon/ (accessed March 18, 2020).

[323] Treble, (n.d.). https://www.treble.tech/ (accessed April 26, 2023).

[324] ACOUCOU, (n.d.). https://acoucou.org/ (accessed March 18, 2020).

[325] E. Badino, M. Ferrara, L. Shtrepi, E. Fabrizio, A. Astolfi, V. Serra, Modelling mean radiant temperature in outdoor environments: contrasting the approaches of different simulation tools, J. Phys. Conf. Ser. 2069 (2021) 012186. https://doi.org/10.1088/1742-6596/2069/1/012186.

[326] J. Graham, U. Berardi, G. Turnbull, R. McKaye, Microclimate Analysis as a Design Driver of Architecture, Climate. 8 (2020) 72. https://doi.org/10.3390/cli8060072.

[327] Ata Chokhachian, Daniele Santucci, Thomas Auer, A Human-Centered Approach to Enhance Urban Resilience, Implications and Application to Improve Outdoor Comfort in Dense Urban Spaces, Buildings. 7 (2017) 113. https://doi.org/10.3390/buildings7040113.

[328] S. Thorsson, F. Lindberg, I. Eliasson, B. Holmer, Different methods for estimating the mean radiant temperature in an outdoor urban setting, Int. J. Climatol. 27 (2007) 1983–1993. https://doi.org/10.1002/joc.1537.

[329] F. Ali-Toudert, H. Mayer, Effects of asymmetry, galleries, overhanging façades and vegetation on thermal comfort in urban street canyons, Sol. Energy. 81 (2007) 742–754. https://doi.org/10.1016/j.solener.2006.10.007.

[330] S. Thorsson, J. Rocklöv, J. Konarska, F. Lindberg, B. Holmer, B. Dousset, D. Rayner, Mean radiant temperature – A predictor of heat related mortality, Urban Clim. 10 (2014) 332–345. https://doi.org/10.1016/j.uclim.2014.01.004.

[331] ANSI/ASHRAE Standard 55, Thermal Environmental Conditions for Human Occupancy, (2017) 66.

[332] H. Guo, D. Aviv, M. Loyola, E. Teitelbaum, N. Houchois, F. Meggers, On the understanding of the mean radiant temperature within both the indoor and outdoor environment, a critical review, Renew. Sustain. Energy Rev. 117 (2020) 109207. https://doi.org/10.1016/j.rser.2019.06.014.

[333] P.O. Fanger, Thermal Comfort: Analysis and Applications in Environmental Engineering, McGraw-Hill, New York, New York, United States, 1972.

[334] C. Frenzel, S. Gröger, M. Hiller, W. Kessling, K. Müllner, Simulation of thermal comfort in soccer stadia using TRNSYS 17, in: Proc. Build. Simul. 2011, Sydney, Acustralia, 2011: pp. 972–979.

[335] C.R. Underwood, E.J. Ward, The solar radiation area of man, Ergonomics. (1966). https://doi.org/10.1080/00140136608964361.

[336] VDI 3787-2, Environmental meteorology - Methods for the human biometeorological evaluation of climate and air quality for urban and regional planning at regional level - Part I: Climate, Beuth, Berlin, Germany, 2008.

[337] ISO 7726:1998, Ergonomics of the thermal environment — Instruments for measuring physical quantities, International Organization for Standardization, Geneva, Switzerland, 1998.

[338] R. Perez, R. Seals, J. Michalsky, All-weather model for sky luminance distribution—Preliminary configuration and validation, Sol. Energy. 50 (1993) 235–245.

https://doi.org/10.1016/0038-092X(93)90017-I.

[339] S. CIE, Spitial Distribution of Daylight-CIE Standard General Sky, CIE 0111E. (2003).

[340] Y.A. Çengel, Introduction to Thermodynamics and Heat Transfer, Second Edition, McGraw-Hill, New York, New York, United States, 2008.

[341] D. Aviv, M. Hou, E. Teitelbaum, H. Guo, F. Meggers, Simulating Invisible Light: Adapting Lighting and Geometry Models for Radiant Heat Transfer, in: SimAUD 2020, online, 2020.

[342] M.H. Vorre, R.L. Jensen, J. Le Dréau, Radiation exchange between persons and surfaces for building energy simulations, Energy Build. 101 (2015) 110–121. https://doi.org/10.1016/j.enbuild.2015.05.005.

[343] S. Coccolo, Bioclimatic Design of Sustainable Campuses using Advanced Optimisation Methods, École Polytechnique Fédérale de Lausanne, 2017.

[344] B. Holmer, F. Lindberg, D. Rayner, S. Thorsson, How to transform the standing man from a box to a cylinder – a modified methodology to calculate mean radiant temperature in field studies and models, in: Tolouse, France, 2015.

[345] S. Subramaniam, S. Hoffmann, A Critical Evaluation of Radiance as a Tool for Calculating Radiation View Factors., in: Rome, Italy, n.d.: pp. 1420–1427. https://doi.org/10.26868/25222708.2019.210617.

[346] A. Matzarakis, F. Rutz, H. Mayer, Modelling radiation fluxes in simple and complex environments—application of the RayMan model, Int. J. Biometeorol. 51 (2007) 323–334. https://doi.org/10.1007/s00484-006-0061-8.

[347] S. Tsoka, A. Tsikaloudaki, T. Theodosiou, Analyzing the ENVI-met microclimate model's performance and assessing cool materials and urban vegetation applications–A review, Sustain. Cities Soc. 43 (2018) 55–76. https://doi.org/10.1016/j.scs.2018.08.009.

[348] P.J. Crank, Validation of seasonal mean radiant temperature simulations in hot arid urban climates, Sci. Total Environ. (2020) 13.

[349] C.S. Fong, N. Aghamohammadi, L. Ramakreshnan, N.M. Sulaiman, P. Mohammadi, Holistic recommendations for future outdoor thermal comfort assessment in tropical Southeast Asia: A critical appraisal, Sustain. Cities Soc. 46 (2019) 101428. https://doi.org/10.1016/j.scs.2019.101428.

[350] P. Höppe, Ein neues Verfahren zur Bestimmung der mittleren Strahlungstemperatur in Freien. [A new measurement procedure to obtain the mean radiant temperature outdoors]., Wetter Leben. (1992) 147–151.

[351] E. Johansson, S. Thorsson, R. Emmanuel, E. Krüger, Instruments and methods in outdoor thermal comfort studies – The need for standardization, Urban Clim. 10 (2014) 346–366. https://doi.org/10.1016/j.uclim.2013.12.002.

[352] E.L. Krüger, F.O. Minella, A. Matzarakis, Comparison of different methods of estimating the mean radiant temperature in outdoor thermal comfort studies, Int. J. Biometeorol. 58 (2014) 1727–1737. https://doi.org/10.1007/s00484-013-0777-1.

[353] N. Kántor, A. Kovács, T.-P. Lin, Looking for simple correction functions between the mean radiant temperature from the "standard black globe" and the "six-directional" techniques in Taiwan, Theor. Appl. Climatol. 121 (2015) 99–111. https://doi.org/10.1007/s00704-014-1211-2.

[354] H. Staiger, A. Matzarakis, Accuracy of Mean Radiant Temperature Derived from Active and Passive Radiometry, Atmosphere. 11 (2020) 805. https://doi.org/10.3390/atmos11080805.

[355] C.V. Gál, N. Kántor, Modeling mean radiant temperature in outdoor spaces, A comparative numerical simulation and validation study, Urban Clim. 32 (2020) 100571. https://doi.org/10.1016/j.uclim.2019.100571.

[356] N. Kántor, C.V. Gál, Á. Gulyás, J. Unger, The Impact of Façade Orientation and Woody

Vegetation on Summertime Heat Stress Patterns in a Central European Square: Comparison of Radiation Measurements and Simulations, Adv. Meteorol. 2018 (2018) 1–15. https://doi.org/10.1155/2018/2650642.

[357] E. Naboni, M. Meloni, S. Coccolo, J. Kaempf, J.-L. Scartezzini, An overview of simulation tools for predicting the mean radiant temperature in an outdoor space, Energy Procedia. 122 (2017) 1111–1116. https://doi.org/10.1016/j.egypro.2017.07.471.

[358] B. Jänicke, D. Milošević, S. Manavvi, Review of User-Friendly Models to Improve the Urban Micro-Climate, Atmosphere. 12 (2021) 1291. https://doi.org/10.3390/atmos12101291.

[359] E. Naboni, M. Meloni, C. Mackey, J. Kaempf, The Simulation of Mean Radiant Temperature in Outdoor Conditions: A review of Software Tools Capabilities, (2019) 8.

[360] C.V. Gál, K.A. Nice, Mean radiant temperature modeling outdoors: a comparison of three approaches, in: Boston, Massachusetts, USA, 2020: p. 9.

[361] I. Elwy, Y. Ibrahim, M. Fahmy, M. Mahdy, Outdoor microclimatic validation for hybrid simulation workflow in hot arid climates against ENVI-met and field measurements, Energy Procedia. 153 (2018) 29–34. https://doi.org/10.1016/j.egypro.2018.10.009.

[362] Y.-C. Chen, T.-P. Lin, A. Matzarakis, Comparison of mean radiant temperature from field experiment and modelling: a case study in Freiburg, Germany, Theor. Appl. Climatol. 118 (2014) 535–551. https://doi.org/10.1007/s00704-013-1081-z.

[363] H. Lee, H. Mayer, Validation of the mean radiant temperature simulated by the RayMan software in urban environments, Int. J. Biometeorol. 60 (2016) 1775–1785. https://doi.org/10.1007/s00484-016-1166-3.

[364] J.A. Acero, K. Herranz-Pascual, A comparison of thermal comfort conditions in four urban spaces by means of measurements and modelling techniques, Build. Environ. 93 (2015) 245–257. https://doi.org/10.1016/j.buildenv.2015.06.028.

[365] H. Simon, T. Sinsel, M. Bruse, Advances in Simulating Radiative Transfer in Complex Environments, Appl. Sci. 11 (2021) 5449. https://doi.org/10.3390/app11125449.

[366] V.P. Lopez-Cabeza, S. Alzate-Gaviria, E. Diz-Mellado, C. Rivera-Gomez, C. Galan-Marin, Albedo influence on the microclimate and thermal comfort of courtyards under Mediterranean hot summer climate conditions, Sustain. Cities Soc. 81 (2022) 103872. https://doi.org/10.1016/j.scs.2022.103872.

[367] A. Norouziasas, P. Pilehchi Ha, M. Ahmadi, H.B. Rijal, Evaluation of urban form influence on pedestrians' wind comfort, Build. Environ. 224 (2022) 109522. https://doi.org/10.1016/j.buildenv.2022.109522.

[368] R.A. Elraouf, A. ELMokadem, N. Megahed, O.A. Eleinen, S. Eltarabily, Evaluating urban outdoor thermal comfort: a validation of ENVI-met simulation through field measurement, J. Build. Perform. Simul. 15 (2022) 268–286. https://doi.org/10.1080/19401493.2022.2046165.

[369] W. Ouyang, T. Sinsel, H. Simon, T.E. Morakinyo, H. Liu, E. Ng, Evaluating the thermal-radiative performance of ENVI-met model for green infrastructure typologies: Experience from a subtropical climate, Build. Environ. 207 (2022) 108427. https://doi.org/10.1016/j.buildenv.2021.108427.

[370] T. Sinsel, H. Simon, W. Ouyang, C. dos Santos Gusson, P. Shinzato, M. Bruse, Implementation and evaluation of mean radiant temperature schemes in the microclimate model ENVI-met, Urban Clim. 45 (2022) 101279. https://doi.org/10.1016/j.uclim.2022.101279.

[371] M. Bruse, Die Auswirkungen kleinskaliger Umweltgestaltung auf das Mikroklima [The Impacts Of Small-Scale Environmental modifications on the microclimate], 1999.

[372] S. Huttner, Further development and application of the 3D microclimate simulation ENVI-met, University of Mainz, 2012.

[373] ENVI-met, Advances in simulating radiative transfer in complex environments, (n.d.).

https://www.envi-met.com/wp-content/uploads/2020/11/201119-530_06_201116-CaseStudy_IVS-1-1.pdf (accessed February 25, 2021).

[374] H. Simon, L. Kissel, M. Bruse, Evaluation of ENVI-met's multiple-node model and estimation of indoor climate, in: Edimburgh, United Kingdom, 2017.

[375] J. Fischereit, The simple urban radiation model for estimating mean radiant temperature in idealised street canyons, Urban Clim. 35 (2021) 100694. https://doi.org/10.1016/j.uclim.2020.100694.

[376] Ladybug Tools, (n.d.). https://www.ladybug.tools/ (accessed January 11, 2021).

[377] Y. Ibrahim, T. Kershaw, P. Shepherd, Improvement of the Ladybug-tools microclimate workflow: A verification study, in: Proc. BSO-V 2020, Loughborough, UK, 2020.

[378] G. Evola, V. Costanzo, C. Magrì, G. Margani, L. Marletta, E. Naboni, A novel comprehensive workflow for modelling outdoor thermal comfort and energy demand in urban canyons: Results and critical issues, Energy Build. 216 (2020) 109946. https://doi.org/10.1016/j.enbuild.2020.109946.

[379] C. Mackey, Outdoor Microclimate Map, (n.d.). http://hydrashare.github.io/hydra/viewer?owner=chriswmackey&fork=hydra_2&id=Outdoor_Microclimate_Map&slide=0&scale=1&offset=0,0 (accessed January 7, 2021).

[380] T.-P. Lin, A. Matzarakis, R.-L. Hwang, Shading effect on long-term outdoor thermal comfort, Build. Environ. (2010) 9.

[381] ASHRAE Guideline 14, Measurement of Energy, Demand, and Water Savings, Atlanta, USA, 2014.

[382] E. Arens, T. Hoyt, X. Zhou, L. Huang, H. Zhang, S. Schiavon, Modeling the comfort effects of short-wave solar radiation indoors, Build. Environ. 88 (2015) 3–9. https://doi.org/10.1016/j.buildenv.2014.09.004.

[383] E. Arens, R. Gonzalez, L. Berglund, Thermal Comfort Under an Extended Range of Environmental Conditions, (1986) 11.

[384] C. Mackey, T. Galanos, L. Norford, M.S. Roudsari, P. Architects, Wind, Sun, Surface Temperature, and Heat Island: Critical Variables for High-Resolution Outdoor Thermal Comfort, in: Proc. 15th IBPSA Conf., San Francisco, CA, USA, 2017: p. 9.

[385] Outside Surface Heat Balance, Eng. Ref. — EnergyPlus 87. (n.d.). https://bigladdersoftware.com/epx/docs/8-7/engineering-reference/outside-surface-heat-balance.html.

[386] K. Blazejczyk, MENEX· Man-Environment Heat Exchange Model and its Applications in Bioclimatology, in: Proc. OfThe Fifth Int. Conf. Environ. Ergon., 1992.

[387] C. Mackey, Ladybug Tools for Grasshopper 1.4.0 Release, (2022). https://discourse.ladybug.tools/t/ladybug-tools-for-grasshopper-1-4-0-release/17149.

[388] CitySim Software, (n.d.). https://www.epfl.ch/labs/leso/transfer/software/citysim/ (accessed January 7, 2021).

[389] CitySim Pro, (n.d.). www.citysim.pro (accessed January 7, 2021).

[390] C. Miller, D. Thomas, J. Kämpf, A. Schlueter, Urban and building multiscale co-simulation: case study implementations on two university campuses, J. Build. Perform. Simul. 11 (2018) 309–321. https://doi.org/10.1080/19401493.2017.1354070.

[391] W. Emmanuel, K. Jérôme, A verification of CitySim results using the BESTEST and monitored consumption values, (n.d.) 8.

[392] S. Coccolo, D. Mauree, E. Naboni, J. Kaempf, J.-L. Scartezzini, On the impact of the wind speed on the outdoor human comfort: a sensitivity analysis, Energy Procedia. 122 (2017) 481–486. https://doi.org/10.1016/j.egypro.2017.07.297.

[393] G. Mutani, Coccolo, Silvia, J. Kaempf, M. Bilardo, CitySim Guide: Urban Energy Modelling, CreateSpace Independent Publishing Platform, 2018.

[394] G. Peronato, J.H. Kämpf, E. Rey, M. Andersen, Integrating urban energy simulation in

a parametric environment: a Grasshopper interface for CitySim, in: PLEA 2017, Edimburgh, United Kingdom, 2017: p. 8.

[395] D. Robinson, A. Stone, Solar radiation modelling in the urban context, Sol. Energy. 77 (2004) 295–309. https://doi.org/10.1016/j.solener.2004.05.010.

[396] D. Robinson, F. Haldi, J. Kämpf, P. Leroux, D. Perez, A. Rasheed, U. Wilke, CITYSIM: Comprehensive Micro-Simulation of Resource Flows for Sustainable Urban Planning, (2009) 9.

[397] D. Robinson, A. Stone, A simplified radiosity algorithm for general urban radiation exchange, Build. Serv. Eng. Res. Technol. 26 (2005) 271–284. https://doi.org/10.1191/0143624405bt133oa.

[398] P. Tregenza, Daylighting algorithms, 1993.

[399] J.H. Kämpf, D. Robinson, A simplified thermal model to support analysis of urban resource flows, Energy Build. 39 (2007) 445–453. https://doi.org/10.1016/j.enbuild.2006.09.002.

[400] U. Eicker, A. Dalibard, Photovoltaic–thermal collectors for night radiative cooling of buildings, Sol. Energy. 85 (2011) 1322–1335. https://doi.org/10.1016/j.solener.2011.03.015.

[401] N.A. Kenny, J.S. Warland, R.D. Brown, T.G. Gillespie, Estimating the radiation absorbed by a human, Int. J. Biometeorol. 52 (2008) 491–503. https://doi.org/10.1007/s00484-008-0145-8.

[402] S.A. Klein, TRNSYS 18: A Transient System Simulation Program, (2017). http://sel.me.wisc.edu/trnsys.

[403] H. Guo, M. Ferrara, J. Coleman, M. Loyola, F. Meggers, Simulation and measurement of air temperatures and mean radiant temperatures in a radiantly heated indoor space, Energy. 193 (2020) 116369. https://doi.org/10.1016/j.energy.2019.116369.

[404] J. Aschaber, M. Hiller, R. Weber, TRNSYS17: NEW FEATURES OF THE MULTIZONE BUILDING MODEL, (n.d.) 6.

[405] K. Perini, A. Chokhachian, S. Dong, T. Auer, Modeling and simulating urban outdoor comfort: Coupling ENVI-Met and TRNSYS by grasshopper, Energy Build. 152 (2017) 373–384. https://doi.org/10.1016/j.enbuild.2017.07.061.

[406] A. Chokhachian, K. Perini, S. Dong, T. Auer, How Material Performance of Building Façade Affect Urban Microclimate, in: Powerskin 2017, 2017.

[407] M. Hiller, A. Chokhachian, C. Frenzel, P. Arango, W. Kessling, S. Holst, T. Auer, Annual simulation of outdoor thermal comfort with TRNSYS, in: 2021. https://doi.org/10.26868/25222708.2021.30651.

[408] M. Hiller, J. Aschaber, M. Dillig, Integration of low-e surfaces and shortwave solar radiation into human comfort calculation in TRNSYS 17, in: Proc. BauSIM, Vienna, Austria, 2010.

[409] Multizone Building modeling with Type56 and TRNBuild, (n.d.).

[410] B. Gebhart, Surface temperature calculations in radiant surroundings of arbitrary complexity—for gray, diffuse radiation, Int. J. Heat Mass Transf. 3 (1961) 341–346. https://doi.org/10.1016/0017-9310(61)90048-5.

[411] S.A. Klein, J.A. Duffie, J.C. Mitchell, J.P. Kummer, J.W. Thornton, D.E. Bradley, D.A. Arias, W.A. Beckman, N.A. Duffie, J.E. Braun, TRNSYS 18: Volume 3 - Standard Component Library Overview, 2017.

[412] C. Imbert, S. Bhattacharjee, J. Tencar, Simulation of Urban Microclimate with SOLENE-microclimat - An Outdoor Comfort Case Study, in: Proc. 2018 Symp. Simul. Archit. Urban Des. SimAUD 2018, Society for Modeling and Simulation International (SCS), Delft, Netherlands, 2018. https://doi.org/10.22360/SimAUD.2018.SimAUD.026.

[413] T4SU, (n.d.). https://t4su.wordpress.com/2016/07/11/how-to-test-it/ (accessed April

4, 2023).

[414] M. Musy, L. Malys, B. Morille, C. Inard, The use of SOLENE-microclimat model to assess adaptation strategies at the district scale, Urban Clim. 14 (2015) 213–223. https://doi.org/10.1016/j.uclim.2015.07.004.

[415] B. Morille, SOLENE-microclimate: A Tool to Evaluate Envelopes Efficiency on Energy Consumption at District Scale., Energy Procedia. (2015) 6.

[416] A. Hénon, P.G. Mestayer, J.-P. Lagouarde, J.A. Voogt, An urban neighborhood temperature and energy study from the CAPITOUL experiment with the SOLENE model, Theor. Appl. Climatol. 110 (2012) 177–196. https://doi.org/10.1007/s00704-012-0615-0.

[417] J. Vinet, Contribution à la modélisation thermo-aéraulique du microclimat urbain. Caractérisation de l'impact de l'eau et de la végétation sur les conditions de confort en espaces extérieurs, Ecole polytechnique de l'Université de Nantes, 2000.

[418] A. Hénon, P.G. Mestayer, D. Groleau, J. Voogt, High resolution thermo-radiative modeling of an urban fragment in Marseilles city center during the UBL-ESCOMPTE campaign, Build. Environ. 46 (2011) 1747–1764. https://doi.org/10.1016/j.buildenv.2011.02.001.

[419] RayMan Pro, (n.d.). https://www.urbanclimate.net/rayman/ (accessed March 19, 2021).

[420] VDI 3789, Environmental meteorology - Interactions between atmosphere and surfaces - Calculation of spectral short-wave and long-wave radiation, Beuth, Berlin, Germany, 2019.

[421] A. Matzarakis, D. Fröhlich, RayMan Pro - Manual, 2017.

[422] G. Jendritzky, W. Nübler, A model analysing the urban thermal environment in physiologically significant terms, Arch. Meteorol. Geophys. Bioclimatol. Ser. B. 29 (1981) 313–326. https://doi.org/10.1007/BF02263308.

[423] A. Matzarakis, F. Rutz, H. Mayer, Modelling radiation fluxes in simple and complex environments: basics of the RayMan model, Int. J. Biometeorol. 54 (2010) 131–139. https://doi.org/10.1007/s00484-009-0261-0.

[424] G. Jendritzky, G. Menz, W. Schmidt-Kessen, H. Schirmer, Methodology for the Spatial Assessment of the Thermal Components in the Human Bioclimate: Updated Climate Michel Model, Beitr. Akad. Für Raumforsch. Landesplan. 114 (1990).

[425] C.V. Gál, N. Kántor, Modeling mean radiant temperature in outdoor spaces, A comparative numerical simulation and validation study - Annex A, Urban Clim. 32 (2020) 100571. https://doi.org/10.1016/j.uclim.2019.100571.

[426] T.R. Oke, Boundary Layer Climates, 1st ed., Routledge, 1987. https://doi.org/10.4324/9780203407219.

[427] F. Lindberg, T. Sun, S. Grimmond, Y. Tang, N. Wallenberg, Thermal Comfort - Introduction to SOLWEIG, (2018). https://umep-docs.readthedocs.io/projects/tutorial/en/latest/Tutorials/IntroductionToSolweig.html# (accessed March 29, 2023).

[428] F. Lindberg, C.S.B. Grimmond, The influence of vegetation and building morphology on shadow patterns and mean radiant temperatures in urban areas: model development and evaluation, Theor. Appl. Climatol. 105 (2011) 311–323. https://doi.org/10.1007/s00704-010-0382-8.

[429] F. Lindberg, S. Onomura, C.S.B. Grimmond, Influence of ground surface characteristics on the mean radiant temperature in urban areas, Int. J. Biometeorol. 60 (2016) 1439–1452. https://doi.org/10.1007/s00484-016-1135-x.

[430] J. Bogren, T. Gustavsson, M. Karlsson, U. Postgård, The impact of screening on road surface temperature, Meteorlogical Appl. 7 (2000) 97–104. https://doi.org/10.1017/S135048270000150X.

[431] E. Badino, L. Shtrepi, A. Astolfi, L'uso di Odeon per simulazioni a scala microurbana: un confronto con misure in campo, in: 49th Congr. Ital. Acoust. Assoc., Ferrara, Italy, 2023.

[432] E. Badino, L. Shtrepi, A. Astolfi, Façade design through parametric modelling for environmental noise mitigation in a courtyard, in: Proc. Euronoise, Madeira, Portugal, 2021: p. 10.

[433] E. Badino, L. Shtrepi, A. Astolfi, Studio parametrico sulla riduzione del rumore ambientale in vari scenari urbani, in: 48th Congr. Ital. Acoust. Assoc., Matera, Italy, 2022.

[434] F. Theakston, ed., Burden of disease from environmental noise: quantification of healthy life years lost in Europe, World Health Organization, Regional Office for Europe, Copenhagen, 2011.

[435] European Environment Agency., Environmental noise in Europe, 2020., Publications Office, LU, 2020. https://data.europa.eu/doi/10.2800/686249 (accessed August 31, 2022).

[436] E. Ottoz, L. Rizzi, F. Nastasi, Recreational noise: Impact and costs for annoyed residents in Milan and Turin, Appl. Acoust. 133 (2018) 173–181. https://doi.org/10.1016/j.apacoust.2017.12.021.

[437] S. Alves, L. Estévez-Mauriz, F. Aletta, G.M. Echevarria-Sanchez, V.P. Romero, Towards the integration of urban sound planning in urban development processes: the study of fourtest sites within the SONORUS project, Noise Mapp. 2 (2015). https://doi.org/10.1515/noise-2015-0005.

[438] Y.G. Tong, S.-K. Tang, Acoustical Benefits of Plenum Window as Facade Device - A Parametric Study, in: 2017. https://doi.org/10.1051/matecconf/201710303021.

[439] H. Hossam Eldien, The influence of an inclined line source close to building facades with balconies, Noise Control Eng. J. 60 (2012) 363–373. https://doi.org/10.3397/1.3701016.

[440] G. Guillaume, B. Gauvreau, P. L'Hermite, Numerical study of the impact of vegetation coverings on sound levels and time decays in a canyon street model, Sci. Total Environ. 502 (2015) 22–30. https://doi.org/10.1016/j.scitotenv.2014.08.111.

[441] T. Van Renterghem, D. Botteldooren, Reducing the acoustical façade load from road traffic with green roofs, Build. Environ. 44 (2009) 1081–1087. https://doi.org/10.1016/j.buildenv.2008.07.013.

[442] T. Van Renterghem, Improving the noise reduction by green roofs due to solar panels and substrate shaping, Build. Acoust. 25 (2018) 219–232. https://doi.org/10.1177/1351010X18776804.

[443] L. Savioja, U.P. Svensson, Overview of geometrical room acoustic modeling techniques, J. Acoust. Soc. Am. 138 (2015) 708–730. https://doi.org/10.1121/1.4926438.

[444] M. Vorländer, Auralization: Fundamentals of Acoustics, Modelling, Simulation, Algorithms and Acoustic Virtual Reality, 1st ed., Springer International Publishing, Cham, 2008. https://doi.org/10.1007/978-3-030-51202-6.

[445] L. Savioja, Room Acoustics Modeling with Interactive Visualizations, (2016). https://interactiveacoustics.info/ (accessed April 17, 2023).

[446] S. Siltanen, T. Lokki, L. Savioja, Rays or Waves? Understanding the Strengths and Weaknesses of Computational Room Acoustics Modeling Techniques, (2010) 6.

[447] H.H. El Dien, P. Woloszyn, The acoustical influence of balcony depth and parapet form: experiments and simulations, Appl. Acoust. 66 (2005) 533–551. https://doi.org/10.1016/j.apacoust.2004.09.004.

[448] E. Bo, L. Shtrepi, D. Pelegrín Garcia, G. Barbato, F. Aletta, A. Astolfi, The Accuracy of Predicted Acoustical Parameters in Ancient Open-Air Theatres: A Case Study in Syracusae, Appl. Sci. 8 (2018) 1393. https://doi.org/10.3390/app8081393.

[449] ISO 140-5:1998, Acoustics - Measurement of sound insulation in buildings and of building elements. Part 5: Field measurements of airborne sound insulation of facade elements and facades, International Organization for Standardization, Geneva, Switzerland, 1998.

[450] A. Farina, Simultaneous measurement of impulse response and distortion with a swept-sine technique, J. Audio Eng. Soc. (2000).

[451] P. Guidorzi, L. Barbaresi, D. D'Orazio, M. Garai, Impulse Responses Measured with MLS or Swept-Sine Signals Applied to Architectural Acoustics: An In-depth Analysis of the Two Methods and Some Case Studies of Measurements Inside Theaters, Energy Procedia. 78 (2015) 1611–1616. https://doi.org/10.1016/j.egypro.2015.11.236.

[452] A. Farina, Advancements in impulse response measurements by sine sweeps, J. Audio Eng. Soc. (2007).

[453] The Audacity Team, Audacity, (n.d.). https://www.audacityteam.org/ (accessed October 5, 2022).

[454] A. Farina, Aurora for Audacity, (n.d.).

[455] Odeon, (n.d.). https://odeon.dk/.

[456] I. Bork, Report on the 3rd round robin on room acoustical computer simulation–Part II: Calculations, Acta Acust. United Acust. 91 (2005) 753–763.

[457] I. Bork, Report on the 3rd round robin on room acoustical computer simulation–Part I: Measurements, Acta Acust. United Acust. 91 (2005) 740–752.

[458] I. Bork, A comparison of room simulation software-the 2nd round robin on room acoustical computer simulation, Acta Acust. United Acust. 86 (2000) 943–956.

[459] C.L. Christensen, G.B. Nielsen, J.H. Rindel, Danish Acoustical Society Round Robin on room acoustic computer modelling, (2008).

[460] A. Nowoświat, M. Olechowska, Experimental Validation of the Model of Reverberation Time Prediction in a Room, Buildings. 12 (2022) 347. https://doi.org/10.3390/buildings12030347.

[461] J.H. Rindel, Diffraction around corners and over wide barriers in room acoustic simulations, in: ICSV16, Krakow, Poland, 2009.

[462] L. Aspöck, Validation of room acoustic simulation models, Logos Verlag GmbH, Berlin, 2020.

[463] A. Van der Harten, Benchmark 2: PTB Round Robin 2, (2015). http://www.perspectivesketch.com/pachyderm/index.php/pachyderm/benchmarks/13-benchmark-2-ptb-round-robin-2 (accessed February 5, 2019).

[464] A. Van der Harten, Benchmark 1: PTB Round Robin 3, (2015). http://www.perspectivesketch.com/pachyderm/index.php/pachyderm/benchmarks/12-benchmark-1-ptb-round-robin-3 (accessed February 5, 2019).

[465] Building Bulletin 93, Acoustic design of schools: performance standards, 2015.

[466] H.-S. Yang, J. Kang, C. Cheal, Random-Incidence Absorption and Scattering Coefficients of Vegetation, Acta Acust. United Acust. 99 (2013) 379–388. https://doi.org/10.3813/AAA.918619.

[467] M. Vorländer, Computer simulations in room acoustics: Concepts and uncertainties, J. Acoust. Soc. Am. 133 (2013) 1203–1213. https://doi.org/10.1121/1.4788978.

[468] M. Hodgson, When is diffuse-field theory applicable?, Appl. Acoust. 49 (1996) 197–207. https://doi.org/10.1016/S0003-682X(96)00010-2.

[469] S.R. Bistafa, J.S. Bradley, Predicting reverberation times in a simulated classroom, J. Acoust. Soc. Am. 108 (2000) 1721–1731. https://doi.org/10.1121/1.1310191.

[470] J.H. Rindel, C.L. Christensen, G. Koutsouris, Simulations, measurement and auralizations in architectural acoustics, in: Acoust. 2013, New Delhi, India, 2013.

[471] E. Murphy, E.A. King, Principles of Environmental Noise, in: Environ. Noise Pollut.,

Elsevier, 2014: pp. 9–49. https://doi.org/10.1016/B978-0-12-411595-8.00002-1.

[472] D.A. Bies, C.H. Hansen, Engineering Noise Control: Theory and practice, 4th ed., CRC Press, 2017. https://doi.org/10.1201/9781315273464.

[473] G.L.M. Rossignol, N.M.M. Lagrange, Investigating the perception of soundscapes through acoustic scene simulation, (2018).

[474] L. Maffei, M. Masullo, Electric Vehicles and Urban Noise Control Policies, Arch. Acoust. 39 (2014) 333–341. https://doi.org/10.2478//aoa-2014-0038.

[475] International Collegium of Rehabilitative Audiology, ICRA Noise, (n.d.). https://icra-audiology.org/Repository/icra-noise (accessed August 6, 2021).

[476] Y. Liu, B. Yang, X.J. Zhang, Q.X. Xu, Research on Correlation between Urban Low-Noise Pavement Air Voids and Sound Absorption Coefficient, Appl. Mech. Mater. 303–306 (2013) 2898–2901. https://doi.org/10.4028/www.scientific.net/AMM.303-306.2898.

[477] Henning Larsen, WOC - Masterplan Concept, 2020.

[478] Henning Larsen, Signa, Wolfsburg Connect, n.d.

[479] Technische Akustik, Schalltechnische Untersuchung zum Bebauungsplan Heinrich-Nordhoff-Straße Ost der Stadt Wolfsburg, (2020).

[480] DIN 18005-1:2002-07, Noise abatement in town planning - Part 1: Fundamentals and directions for planning, Beuth, 2002.

[481] Danish Road Institute, Traffic Noise prediction with Nord2000 - An update, 2011.

[482] EN 1793-3:1998, Road traffic noise reducing devices - Test method for determining the acoustic performance - Part 3: Normalized traffic noise spectrum, European Commitee for Standardization, Brussels, Belgium, 1998.

[483] EN 16272-3-1:2012, Railway applications - Track - Noise barriers and related devices acting on airborne sound propagation - Test method for determining the acoustic performance Part 3-1: Normalized railway noise spectrum and single number ratings for diffuse field applications, European Commitee for Standardization, Brussels, Belgium, 2012.

[484] Odeon Application Note - Restaurants, (2012).

[485] ANSI/ASA S3.5-1997, Methods For Calculation Of The Speech Intelligibility Index, Acoustical Society of America, 1997.

[486] DIN 4109-1:2018-01, Sound insulation in buildings - Part 1: Minimum requirements, 2017.

[487] H. Lee, H. Mayer, D. Schindler, Importance of 3-D radiant flux densities for outdoor human thermal comfort on clear-sky summer days in Freiburg, Southwest Germany, Meteorol. Z. 23 (2014) 315–330. https://doi.org/10.1127/0941-2948/2014/0536.

[488] A. Salvati, M. Kolokotroni, Microclimate Data For Building Energy Modelling: Study On ENVI-Met Forcing Data, in: Rome, Italy, 2019: pp. 3361–3368. https://doi.org/10.26868/25222708.2019.210544.

[489] F. Salata, I. Golasi, R. de Lieto Vollaro, A. de Lieto Vollaro, Urban microclimate and outdoor thermal comfort. A proper procedure to fit ENVI-met simulation outputs to experimental data, Sustain. Cities Soc. 26 (2016) 318–343. https://doi.org/10.1016/j.scs.2016.07.005.

[490] P. Weihs, H. Staiger, B. Tinz, E. Batchvarova, H. Rieder, L. Vuilleumier, M. Maturilli, G. Jendritzky, The uncertainty of UTCI due to uncertainties in the determination of radiation fluxes derived from measured and observed meteorological data, Int. J. Biometeorol. 56 (2012) 537–555. https://doi.org/10.1007/s00484-011-0416-7.

[491] H. Simon, Modeling urban microclimate - Development, implementation and evaluation of new and improved calculation methods for the urban microclimate model ENVI-met, 2016.

[492] C. Piselli, V.L. Castaldo, I. Pigliautile, A.L. Pisello, F. Cotana, Outdoor comfort conditions in urban areas: On citizens' perspective about microclimate mitigation of urban transit areas, Sustain. Cities Soc. 39 (2018) 16–36. https://doi.org/10.1016/j.scs.2018.02.004.

[493] T.E. Morakinyo, A. Lai, K.K.-L. Lau, E. Ng, Thermal benefits of vertical greening in a high-density city: Case study of Hong Kong, Urban For. Urban Green. 37 (2019) 42–55. https://doi.org/10.1016/j.ufug.2017.11.010.

[494] A. Banfi, A. Tatti, M. Ferrando, D. Fustinoni, F. Zanghirella, F. Causone, An experimental technique based on globe thermometers for the measurement of mean radiant temperature in urban settings, Build. Environ. 222 (2022) 109373. https://doi.org/10.1016/j.buildenv.2022.109373.

[495] Brown, Correcting the Error in Measuring Radiation Received by a Person: Introducing Cylindrical Radiometers, Sensors. 19 (2019) 5085. https://doi.org/10.3390/s19235085.

[496] ARPA Piemonte, Il Clima in Piemonte - Estate 2022, Agenzia Regionale per la Protezione Ambientale, Turin, Italy, 2022.

[497] ASTM G173-03, Tables for Reference Solar Spectral Irradiances: Direct Normal and Hemispherical on 37 Tilted Surface, ASTM International, West Conshohocken, PA, United States, 2020. https://doi.org/10.1520/G0173-03R20.

[498] ENVI_MET GmbH, ed., ENVI-met - Decoding Urban Nature, (2017).

[499] C. Hoffmann, A. Geissler, M. Mutti, A. Wicki, F. Schwager, Building Materials for Cities and Climate Change – a Material Catalogue with Recommendations, J. Phys. Conf. Ser. 2042 (2021) 012057. https://doi.org/10.1088/1742-6596/2042/1/012057.

[500] Knauf, SM700, n.d. https://www.knauf.it/backoffice/userfiles/files/documentiAllegati/523/[8711]SM700.pdf (accessed February 2, 2023).

[501] A.H. Amir, H.Z. Alibaba, Comparison between Heat Conductivity of EPS (Expanded Polystyrene) and XPS (Extruded Polystyrene), 4 (2017).

[502] T. Dilmaç, XPS and EPS comparison, (n.d.). https://www.karplus.com.tr/EN/xpsandepscomparison.html#:~:text=Thermal%20conductivity%20depends%20on%20the,remain%20constant%20throughout%20the%20lifetime. (accessed February 2, 2023).

[503] L.E. Juanicó, Thermal insulation of roofs by using multiple air gaps separated by insulating layers of low infrared emissivity, Constr. Build. Mater. 230 (2020) 116931. https://doi.org/10.1016/j.conbuildmat.2019.116931.

[504] Expanded Polystyrene (EPS): Ultimate Guide on Foam Insulation Material, (n.d.). https://omnexus.specialchem.com/selection-guide/expanded-polystyrene-eps-foam-insulation#:~:text=The%20thermal%20conductivity%20of%20expanded,K)%20at%2010%20%C2%B0C. (accessed February 2, 2023).

[505] Poroton, P800 - technical datasheet, n.d. https://www.poroton.it/mattoni-laterizi/blocchi-semipieni-p800/ (accessed February 2, 2023).

[506] Rockwool, Frontrock Pro - technical datasheet, n.d. https://www.rockwool.com/syssiteassets/rw-it/documentazione-tecnica/schede-tecniche---gamma-edilizia/frontrock-pro.pdf (accessed February 2, 2023).

[507] Stabilia, Hollow bricks- technical datasheet, n.d. https://www.stabila.it/wp-content/documentazione/Comune/Mattone%20forato%20VI%20VR%20TV/ST_R_mattone_forato_2.pdf (accessed February 2, 2023).

[508] WUFI, (n.d.). https://wufi.de/en/ (accessed March 24, 2023).

[509] F. Salata, I. Golasi, R. de Lieto Vollaro, A. de Lieto Vollaro, Outdoor thermal comfort in the Mediterranean area. A transversal study in Rome, Italy, Build. Environ. 96 (2016) 46–61. https://doi.org/10.1016/j.buildenv.2015.11.023.

[510] A. Matzarakis, H. Mayer, Another kind of environmental stress: Thermal stress, (1996).

[511] F. Leccese, M. Rocca, G. Salvadori, E. Belloni, C. Buratti, Towards a holistic approach to indoor environmental quality assessment: Weighting schemes to combine effects of multiple environmental factors, Energy Build. 245 (2021) 111056. https://doi.org/10.1016/j.enbuild.2021.111056.

[512] C. Buratti, E. Belloni, F. Merli, P. Ricciardi, A new index combining thermal, acoustic, and visual comfort of moderate environments in temperate climates, Build. Environ. 139 (2018) 27–37. https://doi.org/10.1016/j.buildenv.2018.04.038.

[513] R.J. Cureau, Multi-domain human-oriented approach to evaluate human comfort in outdoor environments, Int. J. Biometeorol. (2022).

[514] A. Radicchi, Combined Sound- and Lightwalks. A Novel, Mixed Method to Assess Sound and Artificial Light of the Urban Environment at Night, in: B.E.A. Piga, D. Siret, J.-P. Thibaud (Eds.), Exp. Walks Urban Des., Springer International Publishing, Cham, 2021: pp. 77–91. https://doi.org/10.1007/978-3-030-76694-8_5.

[515] M. Manso, J. Castro-Gomes, Green wall systems: A review of their characteristics, Renew. Sustain. Energy Rev. 41 (2015) 863–871. https://doi.org/10.1016/j.rser.2014.07.203.

[516] A.B. Besir, E. Cuce, Green roofs and facades: A comprehensive review, Renew. Sustain. Energy Rev. 82 (2018) 915–939. https://doi.org/10.1016/j.rser.2017.09.106.

[517] I. Susorova, Green facades and living walls, in: Eco-Effic. Mater. Mitigating Build. Cool. Needs, Elsevier, 2015: pp. 127–153. https://doi.org/10.1016/B978-1-78242-380-5.00005-4.

[518] M. Manso, I. Teotónio, C.M. Silva, C.O. Cruz, Green roof and green wall benefits and costs: A review of the quantitative evidence, Renew. Sustain. Energy Rev. 135 (2021) 110111. https://doi.org/10.1016/j.rser.2020.110111.

[519] Z. Azkorra, G. Pérez, J. Coma, L.F. Cabeza, S. Bures, J.E. Álvaro, A. Erkoreka, M. Urrestarazu, Evaluation of green walls as a passive acoustic insulation system for buildings, Appl. Acoust. 89 (2015) 46–56. https://doi.org/10.1016/j.apacoust.2014.09.010.

[520] M.J.M. Davis, M.J. Tenpierik, F.R. Ramírez, M.E. Pérez, More than just a Green Facade: The sound absorption properties of a vertical garden with and without plants, Build. Environ. 116 (2017) 64–72. https://doi.org/10.1016/j.buildenv.2017.01.010.

[521] R. Djedjig, R. Belarbi, E. Bozonnet, Green wall impacts inside and outside buildings: experimental study, Energy Procedia. 139 (2017) 578–583. https://doi.org/10.1016/j.egypro.2017.11.256.

[522] V. Serra, L. Bianco, E. Candelari, R. Giordano, E. Montacchini, S. Tedesco, F. Larcher, A. Schiavi, A novel vertical greenery module system for building envelopes: The results and outcomes of a multidisciplinary research project, Energy Build. 146 (2017) 333–352. https://doi.org/10.1016/j.enbuild.2017.04.046.

[523] T. Van Renterghem, D. Botteldooren, K. Verheyen, Road traffic noise shielding by vegetation belts of limited depth, J. Sound Vib. 331 (2012) 2404–2425. https://doi.org/10.1016/j.jsv.2012.01.006.

[524] N.H. Wong, A.Y. Kwang Tan, P.Y. Tan, K. Chiang, N.C. Wong, Acoustics evaluation of vertical greenery systems for building walls, Build. Environ. 45 (2010) 411–420. https://doi.org/10.1016/j.buildenv.2009.06.017.

[525] W. Yang, H.J. Moon, Combined effects of acoustic, thermal, and illumination conditions on the comfort of discrete senses and overall indoor environment, Build. Environ. 148 (2019) 623–633. https://doi.org/10.1016/j.buildenv.2018.11.040.

[526] M. Ryan, M. Lanchester, S. Pugh, Noise Reduction through Facades with Open Windows, (2011).

[527] Bruag, Acoustic test report, (n.d.). https://www.bruag.com/downloads-2/.

[528] Diasen, DIATHONITE ACOUSTIX+, (n.d.). https://www.diasen.com/wp-content/uploads/2021/10/data-sheet-ST140EN21082407-DiathoniteAcoustixplusvs52.pdf (accessed April 27, 2023).

[529] Pyrok, Pyrok Acoustement 40 - Decorative/Acoustical Surfacing Material Product Dat, (n.d.). https://www.acoustement.com/wp-content/uploads/2014/12/Pyrok-Acoustement-40-Product-Data.pdf (accessed April 27, 2023).

[530] Pyrotek, VITEROLITE 900, (n.d.). https://www.pyroteknc.com/dmsdocument/203/VITEROLITE-900-TDS-227-2IP.pdf.

[531] Pyrotek, SORBERSCREEN, (n.d.). https://www.pyroteknc.com/dmsdocument/125/SORBERSCREEN-TDS-214IP.pdf (accessed April 27, 2023).

[532] Pyrotek, SORBERSCREEN MICRO, (n.d.). https://www.pyroteknc.com/dmsdocument/60/SORBERSCREEN-MICRO-TDS-224IP.pdf (accessed April 27, 2023).

[533] Pyrotek, REAPOR, (n.d.). https://www.pyroteknc.com/dmsdocument/162/REAPOR-TDS-217IP.pdf (accessed April 27, 2023).

[534] Quietstone, Quietstone Standard, (n.d.). https://www.quietstone.co.uk/wp-content/uploads/2014/06/Quietstone-standard-brochure-2016.pdf (accessed April 27, 2023).

[535] Quietstone, Acoustic Performance - Quietstone Light, (n.d.). https://www.quietstone.co.uk/wp-content/uploads/2014/05/Absorption-charts.pdf (accessed April 27, 2023).

[536] Brampton Brick, SOUNDBLOX, (n.d.). https://bramptonbrick.com/sites/default/files/resource_file/MD2129_Soundblox_8p_Brochure_web.pdf (accessed April 27, 2023).

[537] Sound Seal, Soundcell, (n.d.). https://www.soundseal.com/soundcell.html (accessed April 27, 2023).

[538] Sound Seal, Acoustade, (n.d.). https://www.soundseal.com/acoustade (accessed April 27, 2023).

Appendix 3B

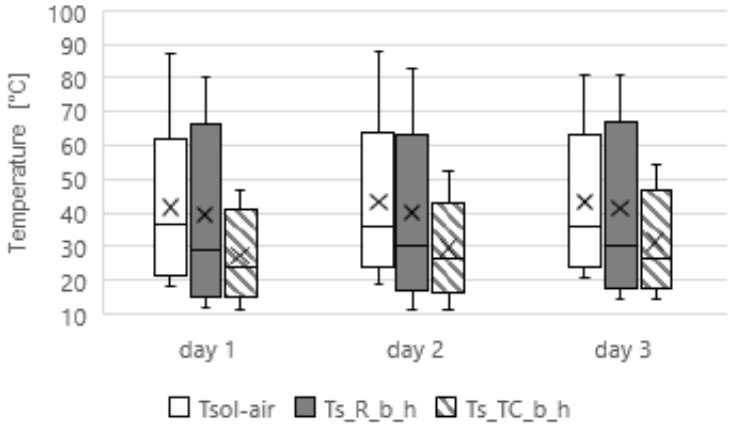

Figure 124. Boxplots showing the sol-air temperature and the surface temperature of the TC and reference roof panels (*Ts_TC_b_h* and *Ts_R_b_h*, respectively) during the first three day of outdoor experimentation.

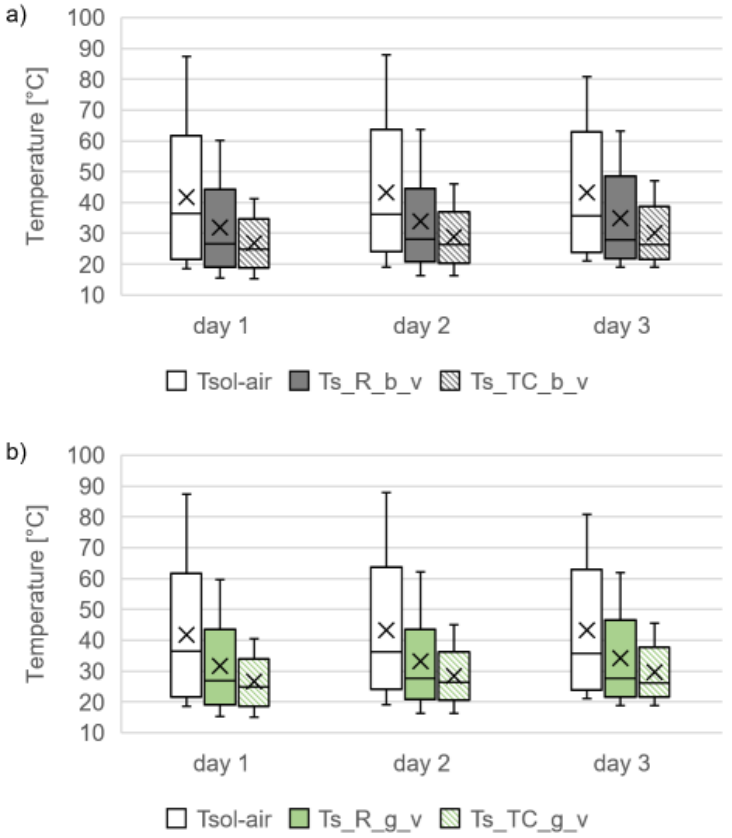

Figure 125. Boxplots showing the sol-air temperature and the surface temperature of the TC and reference façade panels in a) black color (*Ts_TC_b_*v and *Ts_R_b_v*, respectively) and b) in green color (*Ts_TC_g_v* and *Ts_R_g_v*, respectively) during the first three day of outdoor experimentation.

Appendix 5A

Table 47 reports the octave band and overall *SPL* [dB] measured in indoor positions with open windows, at the different building floors. The corresponding outdoor *SPL*s are reported in Table 48. The difference between the overall *SPL* in indoor and outdoor position is in line with the values in [526].

Table 47. Indoor *SPL* [dB] measured at 2 m distance from the façade at the different building floors.

	Octave band center frequency [Hz]								Overall
	63	125	250	500	1000	2000	4000	8000	
1st floor *SPL* [dB]	43.5	52.2	60.1	60.6	59.4	59.8	57.4	49.0	66.8
2nd floor *SPL* [dB]	45.5	51.6	58.2	58.2	57.4	57.8	54.7	47.7	64.7
3rd floor *SPL* [dB]	48.9	53.9	58.9	58.4	56.4	56.6	54.3	46.1	64.7

Table 48. Outdoor *SPL* [dB] measured at 2 m distance from the façade at the different building floors.

	Octave band center frequency [Hz]								Overall
	63	125	250	500	1000	2000	4000	8000	
SPL in G1 [dB]	54.3	58.2	64.1	65.7	66.5	67.5	65.1	60.9	73.1
SPL in G4 [dB]	54.6	59.0	65.8	69.0	68.0	68.6	66.8	63.1	74.9
SPL in G5 [dB]	54.2	57.5	64.6	66.3	65.0	68.0	66.0	61.5	73.3
SPL in G8 [dB]	50.3	58.2	63.2	63.1	62.6	65.3	64.0	58.3	71.0
SPL in G9m [dB]	53.6	58.0	63.0	65.8	65.9	65.9	64.9	59.8	72.4
1st floor *SPL* [dB]	49.9	58.1	67.1	67.7	67.8	69.7	67.9	64.9	75.2
2nd floor *SPL* [dB]	52.0	58.6	67.0	67.0	65.9	67.2	65.8	59.5	73.8
3rd floor *SPL* [dB]	52.7	56.4	64.6	64.4	65.0	66.0	63.7	58.0	72.0

Table 49. Measured *SPL* at 1 m from the source and calculated *SWL* of the sound source set-up used the *SPL* measurement in courtyard positions.

	Octave band center frequency [Hz]								Overall
	63	125	250	500	1000	2000	4000	8000	
SPL at 1m distance [dB]	56.1	70.7	79.2	79.4	79.7	81.7	83.2	80.7	88.0
SWL [dB]	67.1	81.7	90.2	90.4	90.7	92.7	94.2	91.6	99.0

Table 50. Measured *SPL* at 1 m from the source and calculated *SWL* of the sound source set-up used the *SPL* measurement in façade positions.

	Octave band center frequency [Hz]								Overall
	63	125	250	500	1000	2000	4000	8000	
SPL at 1m distance [dB]	54.9	68.7	76.9	77.6	77.2	82.2	81.0	78.0	86.6
SWL [dB]	65.9	79.7	87.9	88.6	88.2	93.2	92.0	89.0	97.6

Table 51. Sound absorption coefficients of the surfaces of the virtual environment for the model before the calibration, with the corresponding scattering properties.

Layer name	description	ref	Octave band sound absorption coefficient [-]								Scattering properties
			63	125	250	500	1000	2000	4000	8000	
00_bitumen	Smooth concrete, painted or glazed	[465]	0.01	0.01	0.01	0.01	0.02	0.02	0.02	0.02	LS
01_bricks	standard brickwork	[465]	0.05	0.05	0.04	0.02	0.04	0.05	0.05	0.05	MS
02_vegetation	100% cover	[466]	0.49	0.49	0.76	0.87	0.97	0.91	0.73	0.73	MS
03_grid	4mm glass	[465]	0.30	0.30	0.20	0.10	0.07	0.05	0.02	0.02	LS
04_walls	smooth brick, 10mm deep	[444]	0.08	0.08	0.09	0.12	0.16	0.22	0.24	0.24	MS
05_double glazing windows	double glazing	[465]	0.15	0.15	0.05	0.03	0.03	0.02	0.02	0.02	LS
06_single glazing windows	4mm glass	[465]	0.30	0.30	0.20	0.10	0.07	0.05	0.02	0.02	LS
07_open windows / outer enclosure	total abs		1.00	1.00	1.00	1.00	1.00	1.00	1.00	1.00	LS
08_cobblestones	smooth brick, 10mm deep	[465]	0.08	0.08	0.09	0.12	0.16	0.22	0.24	0.24	MS

Table 52. Sound scattering properties of the virtual model in the two simulation tools, before the calibration.

	Octave band sound scattering coefficient [-] (Pachyderm)								Single value (Odeon)
Description	63	125	250	500	1000	2000	4000	8000	
Low scattering (LS)	0.03	0.03	0.05	0.05	0.06	0.07	0.1	0.15	0.1
Medium scattering (MS)	0.03	0.08	0.28	0.35	0.42	0.45	0.47	0.5	0.4

Table 53. Sound absorption coefficients of the surfaces of the virtual environment after the calibration in Odeon, with the corresponding scattering properties.

Layer name	description	Octave band sound absorption coefficient [-]								Scattering properties
		63	125	250	500	1000	2000	4000	8000	
00_bitumen	Smooth concrete, painted or glazed	0.01	0.01	0.01	0.01	0.02	0.02	0.02	0.02	LS
01_bricks	standard brickwork	0.05	0.05	0.04	0.02	0.04	0.05	0.05	0.05	MS
02_vegetation	100% cover	0.39	0.39	0.61	0.87	0.78	0.73	0.87	0.87	MS
03_grid	4mm glass	0.30	0.30	0.20	0.10	0.07	0.05	0.02	0.02	LS
04_walls	Smooth brickwork with flush pointing	0.02	0.02	0.04	0.04	0.04	0.05	0.10	0.10	MS
05_double glazing windows	double glazing,2-3mm,10mm	0.08	0.08	0.07	0.05	0.03	0.02	0.02	0.02	LS
06_single glazing windows	single pane glass	0.06	0.06	0.04	0.03	0.03	0.02	0.02	0.02	LS
07_open windows / outer enclosure	total abs	1.00	1.00	1.00	1.00	1.00	1.00	1.00	1.00	LS
08_cobblestones	Smooth brickwork with flush pointing	0.06	0.06	0.07	0.09	0.12	0.16	0.31	0.31	MS

Table 54. Sound absorption coefficients of the surfaces of the virtual environment after the calibration in Pachyderm, with the corresponding scattering properties.

Layer name	description	Octave band sound absorption coefficient [-]								Scattering properties
		63	125	250	500	1000	2000	4000	8000	
00_bitumen	Smooth concrete, painted or glazed	0.01	0.01	0.01	0.01	0.02	0.02	0.02	0.02	LS
01_bricks	standard brickwork	0.05	0.05	0.04	0.02	0.04	0.05	0.05	0.05	MS
02_vegetation	100% cover	0.49	0.49	0.76	0.87	0.78	0.73	0.87	0.87	MS
03_grid	4mm glass	0.30	0.30	0.20	0.10	0.06	0.05	0.02	0.02	LS
04_walls	smooth brick, 10mm deep	0.08	0.08	0.10	0.12	0.13	0.18	0.29	0.29	MS
05_double glazing windows	double glazing	0.15	0.15	0.05	0.03	0.03	0.02	0.02	0.02	LS
06_single glazing windows	4mm glass	0.30	0.30	0.20	0.10	0.06	0.05	0.02	0.02	LS
07_open windows / outer enclosure	total abs	1.00	1.00	1.00	1.00	1.00	1.00	1.00	1.00	LS
08_cobblestones	smooth brick, 10mm deep	0.08	0.08	0.10	0.12	0.13	0.18	0.29	0.29	MS

Table 55. Sound scattering properties of the virtual model in the two simulation tools, after the calibration.

	Octave band sound scattering coefficient [-] (Pachyderm)								Single value (Odeon)
Description	63	125	250	500	1000	2000	4000	8000	
Low scattering (LS)	0.03	0.03	0.05	0.05	0.06	0.07	0.1	0.15	0.1
Medium scattering (MS)	0.03	0.05	0.28	0.28	0.28	0.28	0.34	0.36	0.4

Appendix 5B

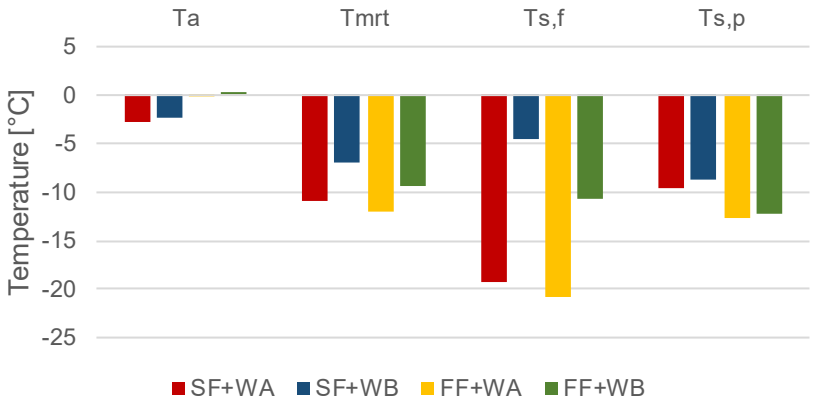

Figure 126. Summary of the peak error found for T_a, T_{mrt}, $T_{s,f}$ and $T_{s,p}$ for the four simulation methods.

Table 56. Evaluation metrics of the simulated directional radiative fluxes for SF+WA.

	N	R^2	MAE	MAPE	RMSE
L_{north}	20	0.714	106.46	0.16	117.46
L_{south}	20	0.845	46.78	0.09	47.73
L_{east}	20	0.732	61.25	0.11	65.01
L_{west}	20	0.879	59.43	0.11	62.14
L_{up}	20	0.745	35.63	0.07	41.48
L_{down}	20	0.902	75.63	0.13	77.22
K_{north}	10	0.952	46.66	2.75	52.01
K_{down}	20	0.926	19.96	0.58	28.14

Table 57. Evaluation metrics of the simulated directional radiative fluxes for SF+WB.

	N	R^2	MAE	MAPE	RMSE
L_{north}	20	0.906	71.24	0.11	76.01
L_{south}	20	0.850	45.07	0.09	46.08
L_{east}	20	0.854	39.39	0.07	44.41
L_{west}	20	0.968	41.77	0.08	42.58
L_{up}	20	0.924	16.95	0.03	19.81
L_{down}	20	0.941	66.84	0.11	67.81
K_{north}	10	0.952	46.66	2.75	52.01
K_{down}	20	0.926	19.96	0.58	28.14

Table 58. Evaluation metrics of the simulated directional radiative fluxes for FF+WA.

	N	R^2	MAE	MAPE	RMSE
L_{north}	20	0.741	109.63	0.17	121.91
L_{south}	20	0.815	50.92	0.10	51.89
L_{east}	20	0.732	65.44	0.11	68.68
L_{west}	20	0.882	62.57	0.11	66.05
L_{up}	20	0.739	37.42	0.07	43.85
L_{down}	20	0.898	81.75	0.14	83.91
K_{north}	10	0.977	48.87	3.31	52.25
K_{down}	20	0.945	17.74	0.59	26.13

Table 59. Evaluation metrics of the simulated directional radiative fluxes for FF+WB.

	N	R^2	MAE	MAPE	RMSE
L_{north}	20	0.889	82.90	0.13	91.44
L_{south}	20	0.822	49.60	0.09	50.56
L_{east}	20	0.816	48.07	0.09	51.26
L_{west}	20	0.951	49.18	0.09	51.16
L_{up}	20	0.889	23.11	0.04	28.05
L_{down}	20	0.932	74.96	0.13	76.50
K_{north}	10	0.977	48.87	3.31	52.25
K_{down}	20	0.945	17.74	0.59	26.13

Appendix 6

Given the noise reduction potential of the application of sound absorbing materials on urban facets, a database of available material options for such application was prepared. While most sound absorbing materials are developed for indoor application, some commercial solutions for outdoor application, often meant to treat noise barriers, are available. The material database, presented in Table 60 collects a series of common construction materials and commercial solutions suitable for outdoor application and compares them based on their potential effect on outdoor comfort conditions. The selection of materials collects products from various manufacturers, where some of them are only available in certain countries or regions. While the proposed database is very limited and does not aim to be comprehensive, it represents an attempt to collect the specifications of materials suitable for outdoor applications and support their comparison based on performance.

Besides the sound absorbing performance, also some other useful information, such as the finishing aspects, the color options, etc., are detailed. All the information were collected during February 2022 from the official website and resources; when needed, personal communication with the product dealers was also used to clarify some aspects and to collect more information on the laboratory measurement from the official lab certifications.

The sound absorbing performance of the materials, described by the octave band sound absorption coefficient, were collected from the official documentation provided by the manufacturers; other information, such as the type of lab measurement performed and the mounting conditions, were detailed. Besides, the frequency dependent sound absorption coefficients, also the weighted sound absorption coefficient a_w was calculated, according to ISO 11654:2017 Standard [158]. This coefficient is a single value indicator that is defined by comparing the measured frequency dependent sound absorption coefficient with a reference absorption curve and can ease the comparison of materials' performance. Moreover, the type of test is detailed, to highlight whether the sound absorption coefficient is obtained for random incidence (RI) or normal incidence (NI), considering that the random incidence properties are closer to real-world application and are those required by acoustic simulation tools.

The presented database, although not comprehensive, can support designers in the selection of the exterior materials for façade application, by allowing for quick performance comparisons, and potentially represent a starting point for further material integrations.

Table 60. Conventional and sound absorbing materials suitable for outdoor application, collecting information on the materials, the mounting conditions, the type of test and the sound absorbing properties.

Manufacturer	Name / Model	Description	Type	Configuration	Overall thickness [m]	Finishing aspect	Finishing color	Octave band sound absorption coefficients [-]							a_w	test type	link to specs
								125	250	500	1k	2k	4k	8k			
	Double glazing	2-3mm glass, >30mm air gap	glass pane		0.03	glass	-	0.15	0.05	0.03	0.03	0.02	0.02	0.02	0.05	RI	[444]
	Double glazing	2–3 mm glass, 10 mm air gap	glass pane		0.01	glass	-	0.10	0.07	0.05	0.03	0.02	0.02	0.02	0.05	RI	[444]
	Brick wall	stuccoed with a rough finish	bricks		-	bricks	brick color	0.03	0.03	0.03	0.04	0.05	0.07	0.07	0.05	RI	[444]
	Smooth brickwork	10 mm deep pointing, pit sand mortar	bricks		-	bricks	brick color	0.08	0.09	0.12	0.16	0.22	0.24	0.24	0.15	RI	[444]
	Smooth brickwork	with flush pointing, painted	bricks		-	bricks	brick color	0.01	0.01	0.02	0.02	0.02	0.02	0.02	0.05	RI	[444]
	Standard brickwork		bricks		-	bricks	brick color	0.05	0.04	0.02	0.04	0.05	0.05		0.05	RI	[465]
	Glazed bricks/ Ceramic tiles	with a smooth surface	bricks		-	glazed bricks	multiple options	0.01	0.01	0.01	0.02	0.02	0.02	0.02	0.05	RI	[444]
	Limestone walls		stone pane		-	limestone	light grey	0.02	0.02	0.03	0.04	0.05	0.05	0.05	0.05	RI	[444]
	Green façade	10 cm soil + ferns	green modules	10 cm on solid backing	0.1	vegetation	-	0.39	0.90	1.15	1.21	1.23	1.19		1.00	RI	[520]
	Green façade	10 cm soil + ferns	green modules	10 cm+10 cm airgap	0.2	vegetation	-	0.44	1.00	1.17	1.29	1.33	1.27		1.00	RI	[520]
Bruag		Formboard top pine (40% perforation) + 3 cm rockwool layer	custom sized panels	0.018+0.03+5 cm airgap	0.07	perforated wood	multiple options		0.40	0.80	0.93	0.85	0.75		0.70	RI	[527]
Bruag		Formboard top pine (40% perforation) + 3 cm rockwool layer	custom sized panels	0.018+0.03+10 cm airgap	0.12	perforated wood	multiple options		0.70	1.00	0.95	0.90	0.80		0.90	RI	[527]
Bruag		Formboard top pine (40% perforation) + 3 cm rockwool layer	custom sized panels	0.018+0.03+20 cm airgap	0.22	perforated wood	multiple options		0.82	1.00	0.95	0.90	0.73		0.90	RI	[527]
Bruag		Formboard top pine (20% perforation) + 3 cm rockwool layer	custom sized panels	0.018+0.03+50 cm airgap	0.52	perforated wood	multiple options		0.49	0.90	0.79	0.60	0.55		0.65 M	RI	[527]
Bruag		Formboard top pine (20% perforation) + 3 cm rockwool layer	custom sized panels	0.018+0.03+10 cm airgap	0.12	perforated wood	multiple options		0.80	1.00	0.75	0.65	0.60		0.70 L	RI	[527]
Bruag		Formboard top pine (20% perforation) + 3 cm rockwool layer	custom sized panels	0.018+0.03+20 cm airgap	0.22	perforated wood	multiple options		0.82	0.90	0.80	0.60	0.55		0.65 L	RI	[527]

Diasen	Diathonite Acoustix+	cork based sound absorbing plaster	plaster	0.03	0.03	porous plaster	multiple options	0.25	0.65	0.70	0.80	0.75	0.60	0.75	RI	[528]
Lecablocco	Fonoleca Quadro	holed blocks made of expanded clay	blocks	0.15	0.15	holed blocks	multiple options	0.19	0.61	1.10	1.04	1.03	1.10	0.90	RI	personal communication
Lecablocco	Fonoleca Nervato	holed blocks made of expanded clay	blocks	0.15	0.15	holed blocks	multiple options	0.17	0.54	1.00	0.91	0.88	0.95	0.80	RI	personal communication
Lecablocco	Fonoleca a doghe	holed blocks made of expanded clay	blocks	0.25	0.25	holed blocks	multiple options	0.22	0.53	0.68	1.11	1.06	1.05	0.75 MH	RI	personal communication
Lecablocco	Sound Leca Normale	holed blocks made of expanded clay	blocks	0.2	0.20	holed blocks	multiple options	0.34	0.71	0.53	0.52	0.62	0.52	0.55 L	RI	personal communication
Lecablocco	Sound Leca Super	holed blocks made of expanded clay	blocks	0.2	0.20	holed blocks	multiple options	0.67	0.96	0.77	0.48	0.62	0.52	0.55 L	RI	personal communication
Lecablocco	Sound Leca Architettonico	holed blocks made of expanded clay	blocks	0.12	0.12	holed blocks	multiple options	0.50	0.40	0.75	0.85	0.91	0.87	0.70 H	RI	personal communication
Lecablocco	Sound Leca Architettonico	holed blocks made of expanded clay	blocks	0.25	0.25	holed blocks	multiple options	0.58	0.45	0.49	0.65	0.74	0.75	0.55 H	RI	personal communication
Pyrok	Acoustement 40	sound absorbing plaster	plaster	0.01	0.01	porous plaster	multiple options	0.17	0.20	0.29	0.34	0.56	1.00	0.35 H	RI	[529]
Pyrok	Acoustement 40	sound absorbing plaster	plaster	0.012	0.01	porous plaster	multiple options	0.01	0.20	0.43	0.68	0.75	0.80	0.45 H	RI	[529]
Pyrok	Acoustement 40	sound absorbing plaster	plaster	0.025	0.03	porous plaster	multiple options	0.18	0.35	0.64	0.73	0.73	0.77	0.60 H	RI	[529]
Pyrok	Acoustement 40	sound absorbing plaster	plaster	0.038	0.04	porous plaster	multiple options	0.36	0.51	0.64	0.74	0.84	0.91	0.70 H	RI	[529]
Pyrok	Acoustement 40	sound absorbing plaster	plaster	0.041	0.04	porous plaster	multiple options	0.24	0.59	0.74	0.81	0.91	0.97	0.80 H	RI	[529]
Pyrotek	Viterolite 900	panels	panels	0.17	0.17	porous block	grey cement	0.39	0.81	0.71	0.76	0.76	0.72	0.75 L	RI	[530]
Pyrotek	Sorberscreen ST with Sorbertextile ST	perforated metal panels with sound absorbing layer	panels	50 mm airgap	0.05	perforated metal	multiple options	0.17	0.19	0.42	0.86	0.78	0.32	0.40 MH	NI	[531]
Pyrotek	Sorberscreen micro with Sorberpoly 2D	microperforated metal panels with sound absorbing layer	panels	50 mm airgap	0.05	microperforated metal	multiple options	0.07	0.29	0.66	0.90	0.81	0.55	0.60 M	RI	[532]
Pyrotek	Sorberscreen micro with Sorberpoly 2D	microperforated metal panels with sound absorbing layer	panels	100 mm airgap	0.10	microperforated metal	multiple options	0.21	0.50	0.89	0.79	0.75	0.59	0.75	RI	[532]
Pyrotek	Sorberscreen micro	microperforated metal panels	panels	50 mm airgap	0.05	microperforated metal	multiple options	0.03	0.11	0.36	0.65	0.69	0.40	0.35 MH	RI	[532]
Pyrotek	Sorberscreen micro	microperforated metal panels	panels	100 mm airgap	0.10	microperforated metal	multiple options	0.05	0.31	0.61	0.65	0.51	0.44	0.55	RI	[532]

Pyrotek	Reapor		panels	25 mm	0.03	porous panel	light grey	0.06	0.16	0.51	1.03	0.98	0.97	0.45 MH	RI	[533]
Pyrotek	Reapor		panels	50 mm	0.05	porous panel	light grey	0.16	0.62	1.19	1.01	1.07	1.04	0.90	RI	[533]
Pyrotek	Reapor		panels	63 mm	0.06	porous panel	light grey	0.26	0.79	1.11	0.96	1.03	1.01	1.00	RI	[533]
Quietstone	Quietstone Standard	panels (no info on materials) with rockwool layer	panels	30 mm thick, 50 mm rockwool, 40 mm air gap	0.12	porous panel	multiple options	0.80	1.05	0.95	0.75	0.80	0.85	0.80 L	RI	[534]
Quietstone	Quietstone Standard	panels (no info on materials) with rockwool layer	panels	30 mm thick, 50 mm rockwool, 100 mm air gap	0.18	porous panel	multiple options	1.00	1.10	0.95	0.75	0.80	0.95	0.85 L	RI	[534]
Quietstone	Quietstone Standard	panels (no info on materials) with rockwool layer	panels	30 mm thick, 50 mm air gap, 50 mm rockwool	0.13	porous panel	multiple options	0.50	0.70	0.80	0.85	0.85	0.95	0.85	RI	[534]
Quietstone	Quietstone Light	expanded glass beads panel	panels	25mm thick + 50 mm air gap	0.08	porous panel	multiple options	0.10	0.30	0.75	0.85	0.65	0.90	0.6 MH	RI	[535]
Quietstone	Quietstone Light + mineral fibre	expanded glass beads panel with mineral wool layer	panels	25mm thick + 50 mm mineral fiber	0.08	porous panel	multiple options	0.55	1.05	1.10	0.90	0.80	0.90	0.9 L	RI	[535]
Quietstone	Quietstone Light	expanded glass beads panel	panels	50 mm thick	0.05	porous panel	multiple options	0.10	0.35	0.85	0.95	0.85	0.85	0.65 MH	RI	[535]
Quietstone	Quietstone Light	expanded glass beads panel	panels	50 mm thick +25 mm air gap	0.08	porous panel	multiple options	0.20	0.60	1.00	0.90	1.00	1.00	0.90	RI	[535]
Quietstone	Quietstone Light	expanded glass beads panel	panels	85 mm thick + 12 mm airgap	0.10	porous panel	multiple options	0.30	0.75	1.00	0.90	0.90	0.85	0.95	RI	[535]
Sound Seal	Soundblox A-1	painted holed blocks	blocks	0.1	0.10	holed blocks	multiple options	0.12	0.85	0.36	0.36	0.42	0.45	0.40 L	RI	[536]
Sound Seal	Soundblox A-1	painted holed blocks	blocks	0.15	0.15	holed blocks	multiple options	0.62	0.84	0.36	0.43	0.27	0.50	0.35 L	RI	[536]
Sound Seal	Soundblox A-1	painted holed blocks	blocks	0.2	0.20	holed blocks	multiple options	0.97	0.44	0.38	0.39	0.50	0.60	0.40 H	RI	[536]
Sound Seal	Soundblox A-1	painted holed blocks	blocks	0.25	0.25	holed blocks	multiple options	0.62	0.84	0.36	0.43	0.27	0.50	0.35 L	RI	[536]
Sound Seal	Soundblox A-1	painted holed blocks	blocks	0.3	0.30	holed blocks	multiple options	0.62	0.84	0.36	0.43	0.27	0.50	0.35 L	RI	[536]
Sound Seal	Soundblox RSC/RF	painted holed blocks with fibrous filler in the cavity	blocks	0.2	0.20	holed blocks	multiple options	0.18	0.64	1.02	0.72	0.80	0.58	0.75 M	RI	[536]
Sound Seal	Soundblox RSC/RF	painted holed blocks with fibrous filler in the cavity	blocks	0.25	0.25	holed blocks	multiple options	0.18	0.64	1.02	0.72	0.80	0.58	0.75 M	RI	[536]
Sound Seal	Soundblox RSC/RF	painted holed blocks with fibrous filler in the cavity	blocks	0.3	0.30	holed blocks	multiple options	0.48	1.14	0.91	0.76	0.67	0.51	0.65 LM	RI	[536]

Sound Seal	Soundcell	holed blocks	blocks	0.2	0.20	holed blocks	multiple options	0.70	0.91	0.55	0.73	0.76	0.69	0.65 L	RI	[537]
Sound Seal	Soundcell	holed blocks	blocks	0.3	0.30	holed blocks	multiple options	1.04	0.69	0.56	0.74	0.78	0.73	0.65	RI	[537]
Sound Seal	Soundcell Acoustade	holed block on the side with porous filling	blocks	0.2	0.20	holed blocks	multiple options	0.70	0.91	0.55	0.73	0.76	0.69	0.65 L	RI	[538]

Publication list

The main publications of the candidate that are relevant for this thesis are grouped referring to the previous chapters.

Chapter 3A

- L. Shtrepi, A. Astolfi, E. Badino, G. Volpatti, D. Zampini, *More Than Just Concrete: Acoustically Efficient Porous Concrete with Different Aggregate Shape and Gradation*, Appl. Sci. 11 (2021) 4835. https://doi.org/10.3390/app11114835.
- L. Shtrepi, A. Astolfi, E. Badino, G. Volpatti, D. Zampini, *Acoustically efficient concrete: acoustic absorption coefficient of porous concrete with different aggregate size*, in: Forum Acusticum 2020 e-Conference (2020). https://doi.org/10.48465/FA.2020.0721.

Chapter 3B

- E. Badino, G. Autretto, S. Fantucci, M. Zinzi, V. Serra, *Laboratory and In-situ assessment of thermochromic coatings for building application: Testing on dynamic properties and photodegradation*, in: COBEE 2022, Montreal, Canada, 2022.
- E. Badino, G. Autretto, S. Fantucci, M. Zinzi, V. Serra, *Development of testing procedures for assessing the thermal and optical performance of thermochromic coatings for buildings*, submitted to Solar Energy Journal.

Chapter 4A

- E. Badino, L. Shtrepi, A. Astolfi, *Acoustic Performance-Based Design: A Brief Overview of the Opportunities and Limits in Current Practice*, Acoustics. 2 (2020) 246–278. https://doi.org/10.3390/acoustics2020016.

Chapter 4B

- E. Badino, M. Ferrara, L. Shtrepi, E. Fabrizio, A. Astolfi, V. Serra, *Modelling mean radiant temperature in outdoor environments: contrasting the approaches of different simulation tools*, J. Phys. Conf. Ser. 2069 (2021) 012186. https://doi.org/10.1088/1742-6596/2069/1/012186.

Chapter 5A

- E. Badino, L. Shtrepi, A. Astolfi, *Façade design through parametric modelling for environmental noise mitigation in a courtyard*, in: Proc. Euronoise, Madeira, Portugal, 2021.
- E. Badino, L. Shtrepi, A. Astolfi, *Studio parametrico sulla riduzione del rumore ambientale in vari scenari urbani*, in: Convegno Naz. Dell'Associazione Ital. Acust., Matera, Italy, 2022.

- E. Badino, L. Shtrepi, A. Astolfi, V. Serra, *An evaluation of geometrical room acoustic simulations in outdoor settings,* submitted for presentation at Forum Acusticum 2023 Conference, Turin, Italy, 2023
- E. Badino, L. Shtrepi, A. Astolfi, *L'uso di Odeon per simulazioni a scala microurbana: un confronto con misure in campo*, in 49th Congress of the Italian Acoustician Association, Ferrara, Italy, 2023

Chapter 6

- E. Badino, L. Shtrepi, A. Astolfi, V. Serra, *Parametric study on outdoor acoustic and thermal comfort in different urban scenarios*, submitted for presentation at IC2UHI 2023 Conference, Melbourne, Australia, 2023

Other publications by the author

- E. Badino, R. Manca, L. Shtrepi, C. Calleri, A. Astolfi, *Effect of façade shape and acoustic cladding on reduction of leisure noise levels in a street canyon*, Build. Environ. 157 (2019) 242–256. https://doi.org/10.1016/j.buildenv.2019.04.039.
- L. Shtrepi, T. Mendéz Echenagucia, E. Badino, A. Astolfi, *A performance-based optimization approach for diffusive surface topology design*, Build. Acoust. 28 (2021) 231–247. https://doi.org/10.1177/1351010X20967821.
- L. Shtrepi, T. Mendéz Echenagucia, E. Badino, A. Astolfi, *Optimizing diffusive surface topology through a performance-based design approach*, Proceedings of ISRA 2019 Conference, Amsterdam, the Netherlands, 2019
- T. Mendéz Echenagucia, L. Shtrepi, E. Badino, A. Astolfi, *Investigating the importance of geometrical accuracy acoustic simulation: A comparison of NURBS and mesh-based approaches*, Proceedings of ISRA 2019 Conference, Amsterdam, the Netherlands, 2019
- E. Badino, R. Manca, L. Shtrepi, C. Calleri, A. Astolfi, *Progettazione acustica delle superfici urbane per la riduzione del rumore ambientale*, Rivista Italiana di Acustica, 2019
- V. Tsiokou, L. Shtrepi, E. Badino, A. Astolfi, A. Karatza, *Exploratory Acoustic Investigation of Customizable 3D-Printed Hybrid Acoustic Materials (HAMs) through Interlaboratory Impedance Tube Measurements*, Acoustics. 5 (2023) 653–675. https://doi.org/10.3390/acoustics5030040.